

(4)

AD-A202 376

**VIRGINIA TECH
CENTER FOR ADHESIVE AND SEALANT
SCIENCE**

VPI-E-88-30
CASS/ESM-88-10

October 1988

**AN INTERDISCIPLINARY STUDY OF CATHODIC DEBONDING
IN ELASTOMER/METAL ADHESIVE BONDS**

FINAL REPORT

RAMZI F. HAMADEH
ENGINEERING SCIENCE AND MECHANICS

D. A. DILLARD, ASSOCIATE PROFESSOR
ENGINEERING SCIENCE AND MECHANICS

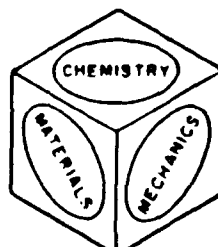
Support for this work was provided by the Office of Naval Research (Contract No. N00014-85-K-0145-P00003)
Dr. Larry H. Peebles, Jr., Project Monitor
Code 431
800 N. Quincy Street
Arlington, VA 22217

DTIC
ELECTED
S NOV 08 1988
D
H CxJ

**VIRGINIA POLYTECHNIC INSTITUTE
AND STATE UNIVERSITY**

216 NORRIS HALL
BLACKSBURG, VIRGINIA 24061

Telephone: (703) 961-6824
TLX: EZLINK 910331861
VPI-BKS



DISTRIBUTION STATEMENT A
Approved for public release; Distribution Unlimited

88 11 08 003

REPORT DOCUMENTATION PAGE

1a. REPORT SECURITY CLASSIFICATION Unclassified		1b. RESTRICTIVE MARKINGS	
2a. SECURITY CLASSIFICATION AUTHORITY		3. DISTRIBUTION/AVAILABILITY OF REPORT Distribution Unlimited	
2b. DECLASSIFICATION/DOWNGRADING SCHEDULE			
4. PERFORMING ORGANIZATION REPORT NUMBER(S) VPI-E-88-30 CASS/ESM-88-10		5. MONITORING ORGANIZATION REPORT NUMBER(S)	
6a. NAME OF PERFORMING ORGANIZATION Virginia Polytechnic Institute and State University	6b. OFFICE SYMBOL (If applicable)	7a. NAME OF MONITORING ORGANIZATION Office of Naval Research	
6c. ADDRESS (City, State, and ZIP Code) Center for Adhesive & Sealant Science 216 Norris Hall Blacksburg, VA 24061-0201		7b. ADDRESS (City, State, and ZIP Code) Code 431 800 N. Quincy Street Arlington, VA 22217	
8a. NAME OF FUNDING/SPONSORING ORGANIZATION Office of Naval Research	8b. OFFICE SYMBOL (If applicable)	9. PROCUREMENT INSTRUMENT IDENTIFICATION NUMBER	
8c. ADDRESS (City, State, and ZIP Code) 800 N. Quincy St. Arlington, VA 22217		10. SOURCE OF FUNDING NUMBERS	
		PROGRAM ELEMENT NO.	PROJECT NO.
		TASK NO.	WORK UNIT ACCESSION NO.
11. TITLE (Include Security Classification) An Interdisciplinary Study of Cathodic Debonding in Elastomer/Metal Adhesive Bonds			
12. PERSONAL AUTHOR(S) Hamadeh, Ramzi F., Dillard, D. A.			
13a. TYPE OF REPORT Final	13b. TIME COVERED FROM 1/85 TO 10/88	14. DATE OF REPORT (Year, Month, Day) 1988 October 17	15. PAGE COUNT 283
16. SUPPLEMENTARY NOTATION			
17. COSATI CODES		18. SUBJECT TERMS (Continue on reverse if necessary and identify by block number)	
FIELD	GROUP	SUB-GROUP	
19. ABSTRACT (Continue on reverse if necessary and identify by block number) An interdisciplinary study concerning the durability of adhesively elastomer/metal bonded joints in marine environments is reported. The generation of OH-ions at the bondline due to an imposed cathodic current from an external source is suspected to be the predominant cause of failure. A surface analysis study was performed early in this research for the purpose of identifying the cause(s) of failure. Characterization of the rubber and the metal failure surfaces with XPS (X-ray Photoelectron Spectroscopy) showed similar composition on both sides and to that of the bulk degraded primer component of the adhesive. Saponification of the adhesive and the leaching of chlorine (forming HCl that attacks the oxide) are identified as two possible failure mechanisms. The locus of failure is believed to be very close to the adhesive/oxide interface. The exposure of bulk adhesive free-standing films to different environments showed that the hydroxyl is detrimental in the environmental durability of these specimens judging by the percentage of net mass uptake. An alternate interfacial failure mechanism is also			
20. DISTRIBUTION/AVAILABILITY OF ABSTRACT <input checked="" type="checkbox"/> UNCLASSIFIED/UNLIMITED <input type="checkbox"/> SAME AS RPT. <input type="checkbox"/> DTIC USERS		21. ABSTRACT SECURITY CLASSIFICATION <i>S-51</i>	
22a. NAME OF RESPONSIBLE INDIVIDUAL		22b. TELEPHONE (Include Area Code)	22c. OFFICE SYMBOL

19. ABSTRACT (continued)

presented where the neutralization of the adhesion-promoting attachment sites (A.S.) at the interface leads to de-adhesion and whereby OH-ions chemically break-up the -COOH-Fe bond forming a non-operative activated complex at the degraded crack tip.

Debond, or loss of adhesion, can exist in two modes. Weakening denotes debond growth which takes place undetected to the naked eye, and is governed by a diffusion-control degradation process that gives a straight line when plotted against the square root of time. Delamination, on the other hand, is a "post weakening" process. Debond rates in this mode are influenced by the applied total strain energy release rate, G_T , and by the environment and can be described by an exponential function in G_T . The effect of shear stress on debond acceleration was determined to be minimal. While compressive stresses seem to be beneficial in slowing the ingress of the bulk hydroxyl into the bondline, no noticeable improvement was detected when an imposed current was used. The use of zinc phosphate-coated steel substrates is shown to improve bond durability significantly at low voltages. Similar trends are observed when silane (γ -aminopropyltrimethoxy) modified primer were used in bonding.

Two approaches are used in order to model debonding: empirical and analytical. Statistical Analysis System (SAS) is used to fit the empirical model which draws heavily on the functional dependencies of debond rates on the accelerating parameters, i.e., temperature, stress, and applied voltage. An Arrhenius relationship is shown to model the effect of temperature very well. Also, voltage effect is correlated with the corresponding current densities which, in turn, were found to obey an exponential relationship with debonded rates. SAS fits of the experimental data are shown to model the process accurately and could be utilized for life predictions. Integration of delamination rates in real time is a feasible method to predict durability as well.

A generalized analytical model for debonding is also developed, and it draws on the similarities between this application and corrosion fatigue of metals. The model is based on the conservation of mass of the involved species and is composed of a system of partial equations and their associated boundary conditions. Furthermore, temperature and voltage-dependent diffusion coefficients and reaction rate constants were used. The resulting boundary value problem amounts to a diffusion-chemical reaction mechanism into which a mechano-chemical failure mechanism is incorporated. A simplified version of the full scale analytical model is solved numerically and some interesting conclusions concerning the failure criterion are drawn. The model also simulates the weakening and delamination behavior and allows for temperature and voltage treatment as well. Delay times are also predicted as a function of the applied voltage and temperature. A particularly important conclusion is that the "marching boundary" phenomena seems to account for most of the accelerating influence of applied G .



Accession For	
NTIS GRA&I	<input checked="" type="checkbox"/>
DTIC TAB	<input type="checkbox"/>
Unannounced	<input type="checkbox"/>
Justification	
By	
Distribution/	
Availability Codes	
AVAIL AND/or	
DTIC Special	
A-1	

ACKNOWLEDGEMENTS

The authors wish to acknowledge their gratitude to the Office of Naval Research (ONR) and to the Naval Research Laboratory - Underwater Sound Reference Detachment for their financial support of this work. The monitors from these organizations were Dr. L. Peebles and Dr. R. Timme, respectively. Thanks are also due to the president, Dr. J. S. Thornton, and staff of Texas Research Institute for their financial support and friendship. The authors are also grateful to Dr. K. M. Liechti at the University of Texas at Austin, Dr. F. J. Boerio at the University of Cincinnati, and Dr. W. van Ouij at the Colorado School of Mines for their invaluable help and support.

Table of Contents

1. INTRODUCTION	1
1.1 BACKGROUND	1
1.2 OBJECTIVES	3
2. A STUDY OF THE MECHANISM OF CATHODIC DEBONDING OF ADHESIVELY BONDED NEOPRENE RUBBER FROM STEEL	6
2.1 ABSTRACT	6
2.2 INTRODUCTION	7
2.3 EXPERIMENTAL	9
2.4 RESULTS	12
2.5 DISCUSSION	27
2.6 CONCLUSIONS	36
2.7 ACKNOWLEDGEMENTS	36
3. A MECHANISTIC EVALUATION OF CATHODIC DEBONDING OF ELASTOMER TO METAL BONDS	38
3.1 ABSTRACT	38

3.2 INTRODUCTION	39
3.3 EXPERIMENTAL: MATERIALS AND SPECIMENS	41
3.3.1 Durability Specimens	43
3.3.2 Neat Film Specimens	43
3.3.3 Bonded Diffusion Specimens	45
3.3.4 Strip Blister Specimens	45
3.4 RESULTS AND DISCUSSION	46
3.4.1 Mass Uptake Studies	53
3.4.2 Accelerating Parameters	55
3.4.3 Stress Effects	64
3.4.4 Silane Effects On Durability	68
3.5 INSIGHTS INTO THE DEBONDING PROCESS	70
3.6 CONCLUSIONS	75
3.7 ACKNOWLEDGMENTS	76
4. WEAKENING MODE: CHARACTERISTICS AND MODELLING	77
4.1 INTRODUCTION	77
4.2 ACCELERATING PARAMETERS	82
4.2.1 Influence of Temperature	83
4.2.2 Influence of Voltage	87
4.3 MODELLING WEAKENING	90
4.3.1 Discussion	90
4.3.2 Temperature	98
4.3.3 Voltage	100
4.3.4 Model Formation	104
4.4 STRESS EFFECTS ON WBPR: COMPRESSION AND SHEAR	115
4.4.1 Compressive Stress	115
4.4.2 Shear Stress	123

4.5 CONCLUSIONS	125
5. DELAMINATION MODE: CHARACTERISTICS AND MODELLING	128
5.1 INTRODUCTION	128
5.2 DELAMINATION DATA	129
5.2.1 Influence of Temperature	130
5.2.2 Influence of Voltage	133
5.3 MODELLING DELAMINATION	136
5.3.1 Influence of G on the DBPR	139
5.3.2 Durability Predictions	151
5.4 CONCLUSIONS	156
6. ANALYTICAL MODELLING OF DEBONDING	157
6.1 INTRODUCTION	157
6.2 KINETIC EQUATIONS	158
6.3 CHEMICAL DEGRADATION	161
6.4 THE B.V.P.	163
6.5 FAILURE CRITERION	167
6.6 A SCHEME FOR NUMERICAL SIMULATIONS	176
6.7 NUMERICAL PREDICTIONS	178
6.7.1 Weakening	178
6.7.2 Delamination	187
6.8 CONCLUSIONS	189
7. INSIGHTS INTO THE MECHANISM(S) OF FAILURE	195
7.1. INTRODUCTION	195
7.2 THEORIES OF ADHESION	196
7.3 DISCUSSION	197

7.4 THE ATTACHMENT SITE THEORY	202
7.4.1 Geometry	202
7.4.2 Chemical Bonds	206
7.4.2.a Aluminum Substrates	208
7.4.2.b Steel Substrates	209
7.5 LOCUS AND MECHANISM OF FAILURE	210
7.6 CONCLUSIONS	212
8. SUMMARY AND CONCLUSIONS	213
8.1 INTRODUCTION	213
8.2 MECHANISM(S) OF DEBONDING	214
8.3 ACCELERATING PARAMETERS	215
8.4 DEBOND MODELLING	218
8.4.1 Semi-empirical Model	218
8.4.2 Numerical Model	219
BIBLIOGRAPHY	221
1. POLARIZATION STUDIES OF ANSI-1026 MILD STEEL	227
2. DURABILITY DATA	234
2.1 Discrepancies in Debond Data	250
3. THE FORTRAN PROGRAM USED IN THE ANALYTICAL MODEL	255
4. DEBONDING: A PROPOSED ANALYTICAL MODEL	263
4.1 Chemical And Electrochemical Reactions	263
4.2 Mathematical Modelling of the Environment	264
4.3 Initial and Boundary Conditions	270
4.4 Assumptions and Simplifications	272
4.5 Characterization of parameters	274

4.6 A Posed Sample Problem	276
5. MATHEMATICAL TREATMENT OF CONCENTRATIONS	281

List of Illustrations

Figure 1. A Schematic of the Bonded Diffusion Specimen (BDS).	11
Figure 2. AES depth profile of mild steel, a) degreased and grit-blasted b) degreased, grit blasted, and exposed to 1M NaOH for 4 days.	14
Figure 3. Neat primer components as a function of exposure time to alkaline environment: 1M NaOH, 30 C.	15
Figure 4. Curve fitting of the Cl 2p spectrum of the neat primer a) before and b) after 1 week exposure to 1M NaOH, 30 C.	16
Figure 5. Curve-fit of the C 1s spectrum of the primer a) before, b) after 20 hour, and c) after 1 week exposure to 1M NaOH, 30 C.	18
Figure 6. Sorption curves for neat primer films at 33 C showing exposure, drying, and resorption response.	20
Figure 7. Net weight gain of neat primer films plotted vs square root of time.	22
Figure 8. Interfacial failure components of the rubber and steel sides after exposure to 1M KOH, natural potential of zinc, and 30 C.	23
Figure 9. Analysis of the metal interfacial failure surface after exposure to 1M NaOH, natural potential of zinc, and 30 C.	25
Figure 10. Curve-fit of the C 1s peak of a shot-blasted surface after failure ; environment: 1M NaOH, natural potential of zinc, 30 C.	26
Figure 11. Auger profile of degreased and grit-blasted steel a) before sputter b) after 20 min. sputter.	28
Figure 12. Polished steel fracture surface components after exposure to 1M NaOH, natural potential of zinc, and 30 C.	29
Figure 13. Polished rubber failure surface components after exposure to 1M NaOH, natural potential of zinc, and 30 C.	30

Figure 14. Polished rubber failure surface components after exposure to artificial sea water, -1.02 V, and 30 C.	31
Figure 15. Curve fitting of the C1s band from a polished failure rubber surface; environment: ASW, -1.02 V, 30 C, 3 weeks.	32
Figure 16. Schematic of the Durability Specimen (DS).	44
Figure 17. The Strip Blister Specimen (SBS); Note the Self Loading Capacity.	47
Figure 18. A Photograph Showing the Intersfacial (External) Failure Zone and the Cohesive Zone in the DS as a Function of Exposure Time.	48
Figure 19. A Photograph Showing the Rubber Legaments on the Steel side of the Failure Surface.	49
Figure 20. Strength Decay of the DS, Control System A, as a Function of Exposure Time.	51
Figure 21. A Schematic Illustrating the Weakening and Delamination Modes.	52
Figure 22. Absorption in 1N NaOH solution, drying, DIW exposure, and re-drying Neat Film of Primer A.	56
Figure 23. WBPR for various concentrations of NaOH solutions with and without potential.	58
Figure 24. Potential effects on the WBPR in different environments.	59
Figure 25. Temperature effects on the WBPR.	60
Figure 26. Substrate effects on the WBPR.	61
Figure 27. Delamination Distances Plotted vs. Time for the SBS in ASW, 30 C, at -1020 mV and -1210 mV (SCE); Control A System.	66
Figure 28. Delamination Distances Plotted vs. Time for the SBS in 1N NaOH, 30 C, at -900 mV and -1310 mV (SCE); Control A System.	67
Figure 29. Silane Effects on Bulk Chemical Reaction rates and on the DBPR.	69
Figure 30. Mass Uptake Results for the Silane-Modified-Primer.	71
Figure 31. Comparison of the "diffusion" front in neat film, BDS, and SBS Specimens.	73
Figure 32. Comparison of Diffusion Fronts in BDS, SBS, and Free Film; Environment: 1M NaOH, and 0 mV; BDS and SBS: 25 C; Bulk: 33 C.	80
Figure 33. Temperature Effect on the WBPR; Control A; Environment: 1M NaOH, current density 4.	84

Figure 34. Temperature Effect on the WBPR; Control A; Environment: ASW, current density 4.	85
Figure 35. Temperature Effect on the WBPR; Modified B; Environment: ASW/1M NaOH, current density 4.	86
Figure 36. Voltage Effect on the WBPR; Control A; Environment: ASW, 25 C.	83
Figure 37. Voltage Effect on the WBPR; Control A; Environment: 1M NaOH, 25 C	89
Figure 38. Shrinking Core Model; The General Model showing the fluid and solid concentration profiles (taken from Wen [29])	92
Figure 39. Shrinking Core Model; The Truly Homogeneous Model (taken from Wen [29])	93
Figure 40. Shrinking Core Model; The Heterogeneous Model (taken from Wen [29])	94
Figure 41. Temperature Dependence of Diffusivity; BDS Data.	99
Figure 42. Polarization Data for 4130 Steel in Dearthed ASW (from	102
Figure 43. Voltage Dependence of the WBPR; BDS Data; Temperature = 25 C. .	106
Figure 44. Multiplicative Model SAS Fits of Weakening Data; Voltage effect; BDS Data; 1M NaOH, 25 C.	110
Figure 45. Multiplicative Model SAS Fits of Weakening Data; Temperature effect; BDS Data; 1M NaOH, Current Density 4.	111
Figure 46. Additive Model SAS Fits of Weakening Data; Voltage effect; BDS Data; 1M NaOH, 25 C.	112
Figure 47. Additive Model SAS Fits of Weakening Data; Temperature effect; BDS Data; 1M NaOH, Current Density 4.	113
Figure 48. SAS (Multiplicative Model) Fits of Weakening Data; Temperature effect; BDS Data; ASW, Current Density 4.	116
Figure 49. SAS (Multiplicative Model) Fits of Weakening Data; Voltage effect; BDS Data; ASW, 25 C.	117
Figure 50. Schematic of the Compression Fixture Used in conjunction with the BDS.	119
Figure 51. The Expected Compressive Stress Distribution.	120
Figure 52. Photograph Showing no Effect of Compression on WBPR with Applied Voltage; Control A, 1M NaOH, -1400 mV, 30C.	121

Figure 53. A Schematic of the Shear Specimen (SS) and the Expected Shear Stress Distribution.	124
Figure 54. Photograph showing negligible effect of Shear Stress on WBPR; ASW, -1020 mV, 30 C.	126
Figure 55. Temperature Effect on the DBPR; Control A; Current Density 4.	131
Figure 56. Temperature Effect on the DBPR; Modified B; Current Density 4.	132
Figure 57. Voltage Effect on the DBPR; Control A; ASW, 25 C.	134
Figure 58. Voltage Effect on the DBPR; Control A; 1M NaOH, 25 C.	135
Figure 59. Voltage Effect on the DBPR; Modified B; ASW, 25 C.	137
Figure 60. Voltage Effect on the DBPR; Modified B; 1M NaOH, 25 C.	138
Figure 61. Total G vs. Delamination Distance as a Function of Rubber Thickness and Dowel Diameter.	140
Figure 62. Typical Dependence of da/dt on G for Stress Corrosion Cracking of Adhesive Bonds (from [42]).	143
Figure 63. A Typical da/dt vs. G; Effect of Voltage on the DBPR.	144
Figure 64. Effect of Increased G on the DBPR; Control A; ASW, -1000 mV, 30 C; Note that Applied G Varies with Dowel Diameter.	146
Figure 65. Effect of Voltage, Temperature, and G on the DBPR; Control A; ASW.	147
Figure 66. Effect of Voltage, Temperature, and G on the DBPR; Modified B; ASW.	148
Figure 67. Effect of Voltage, Temperature, and G on the DBPR; Control A; 1M NaOH.	149
Figure 68. Effect of Voltage, Temperature, and G on the DBPR; Modified B; 1M NaOH.	150
Figure 69. An Illustration Describing the Different Regions of Delamination.	152
Figure 70. Pourbaix diagram showing the corrosion states of iron as a function of pH and cathodic and anodic voltage.	164
Figure 71. The Hydroxyl Concentration Profile for $W = 1.0$	168
Figure 72. The Critical Linkage Concentration Profile for $W = 1.0$	169
Figure 73. The Hydroxyl Concentration Profile for $W = 10.0$	170
Figure 74. The Critical Linkage Concentration Profile for $W = 10.0$	171

Figure 75. The Hydroxyl Concentration Profile for W = 100.0	172
Figure 76. The Critical Linkage Concentration Profile for W = 100.0	173
Figure 77. Variation of Applied and Critical G as a Function of Bondline Distance.	175
Figure 78. A Schematic of the Algorithm for Numerical Simulations.	177
Figure 79. Numerical Predictions of Weakening in ASW at 25 C; Control A.	180
Figure 80. Shifted Numerical Predictions of Weakening in ASW at 25 C; Control A.	181
Figure 81. Predictions of Weakening in SW at different voltages and temperatures; Control A.	183
Figure 82. Shifted Predictions of Weakening in SW at different voltages and temperatures; Control A.	184
Figure 83. Predictions of Weakening in 1M NaOH at 25 C; Control A.	185
Figure 84. Shifted Predictions of Weakening in 1M NaOH at 25 C; Control A.	186
Figure 85. Influence of Degradation on Critical G.	188
Figure 86. Shifted Delamination Data and the Apparent Fits; Control A; 1M NaOH, 25 C.	190
Figure 87. Delamination Predictions; Control A; 1M NaOH, 25 C.	191
Figure 88. Shifted Delamination Data and Apparent Fits; Control A; ASW, 25 C.	192
Figure 89. Delamination Predictions; Control A; ASW, 25 C.	193
Figure 90. Semi-empirical Curve Representing the Adhesion (Joint Strength) as a Function of Surface Attachment (from [57]).	204
Figure 91. Semi-empirical Curve Representing the De-adhesion (Joint Strength) as a Function of Degraded Surface Attachment (from [57]).	207
Figure 92. Loading polarization curves for ANSI 1026 steel in 1M NaOH.	229
Figure 93. Unloading polarization curves for ANSI 1026 steel in 1M NaOH.	230
Figure 94. Loading polarization curves for ANSI 1026 steel in ASW.	231
Figure 95. Unloading polarization curves for ANSI 1026 steel in ASW.	232
Figure 96. Comparison of polarization curves for ANSI 1026 in various environments.	233

Figure 97. Delamination Data; Case A-2: ASW at 25 C and -1000 mV (SCE).	235
Figure 98. Delamination Data; Case A-3: ASW at 25 C and -1100 mV (SCE).	236
Figure 99. Delamination Data; Case A-4: ASW at 25 C and -1420 mV (SCE).	238
Figure 100. Delamination Data; Case A-5: ASW at 25 C and -1825 mV (SCE).	239
Figure 101. Delamination Data; Case D-1: 1M NaOH at 25 C and -960 mV (SCE).	240
Figure 102. Delamination Data; Case D-2: 1M NaOH at 25 C and -1150 mV (SCE).	241
Figure 103. Delamination Data; Case D-3: 1M NaOH at 25 C and -1250 mV (SCE).	242
Figure 104. Delamination Data; Case D-4: 1M NaOH at 25 C and -1420 mV (SCE).	243
Figure 105. Delamination Data; Case D-5: 1M NaOH at 25 C and -1560 mV (SCE).	244
Figure 106. Delamination Data; Case B-4: ASW at 40 C and -1310 mV (SCE).	247
Figure 107. Delamination Data; Case C-4: ASW at 55 C and -1250 mV (SCE).	248
Figure 108. Delamination Data; Case E-4: 1M NaOH at 40 C and -1360 mV (SCE).	249
Figure 109. Delamination Data; Case F-4: 1M NaOH at 55 C and -1310 mV (SCE).	251
Figure 110. Photograph showing the calcareous deposits on SBS #827.	252
Figure 111. pH profiles as a function of crack length.	280

List of Tables

Table 1. Weakened Bond Propagation Rate (WBPR); Control Adhesive System	63
Table 2. The Inter-institutional Test Matrix	78
Table 3. Recommended Potentials for the Test Matrix (in mV (SCE)).	81
Table 4. Kinetics of Water Reduction A-4: ASW, 25 C, -1420 mV.	105
Table 5. Influence of Compressive Stress on Bond Weakening; 1M NaOH, 30 C.	122
Table 6. Applied G variation with a (crack length);	141
Table 7. Average Debond Growth (mm); A-4: ASW, 25 C, -1420 mV.	253

Nomenclature

a	Debond length
A_1, A_2, A_3	Regression coefficients
b_0, b_1, b_2, b_3, b_4	Curve-fit coefficients
B	Material parameter
B^1	Transfer coefficient
c	Molar concentration
C_1	Coefficient
C_A	Molar concentration of fluid A
C_S	Molar concentration of solid S
$[C.L]$	Critical linkage concentration
c_f^o	Bulk concentration of hydroxyl
d	Rubber thickness
D	Diffusion coefficient
D_e	Effective diffusivity
ϵ	Strain
E	Young's modulus of rubber

E_{-}	Activation energy barrier associated with voltage
E_{-h}	Reference potential
E_{ext}	External potential
f	Body traction
F	Faraday constant
G_c	Critical G
G_T	Total applied G
G_I, G_{II}	Applied G for modes I and II respectively
h	Rubber block's height
i	Current
J	Diffusion flux
k	rate constant for water reduction, Boltzman constant
k^1	Rate constant for oxygen reduction
k_1	Chemical degradation rate
k_2	Water forward reduction reaction rate constant
k_2^-	Water backward reduction reaction rate constant
k_3	Bicarbonate forward reaction rate constant
k_3^-	Bicarbonate backward reaction rate constant
k_4	Iron forward reduction reaction rate constant
k_4^-	Iron backward reduction reaction rate constant
k^*	Ultimate "theoretical" strength of BL
L	Control length
l_p	Control length
m	Exponential coefficient
n	No. of electrons
q	Effective dimension of the AS growth model

r_A	Rate of reaction
r_c	Position of reactive interface
r_p	Thickness of pellet
R	Gas constant
R^2	Coefficient of determination
R_i	Chemical reaction rate
S_b	Strength of the boundary layer
S_c	Cohesive strength of the bulk adhesive
S_d	Cohesive strength of the adherend
t	Time
t^*	Non-dimensional time
t_R	Dowel diameter
T	Absolute temperature
U	Strain energy function
U_b	Activation energy barrier for weakening
U^*	Activation energy barrier for delamination
v	Stoichiometric factor, positive or negative
V	Applied cathodic voltage
V_M	Stoichiometric factor, positive or negative
V_0	Material parameter
v_t	Relative volume in a polymeric medium
2w	Rubber block's side dimension
W	Hardness factor
x	Distance
x^*	Non-dimensional distance
X	Conversion

z	Total debond distance
z_1	Weakened distance
z_2	Delaminated distance
z_I	Delamination rate in region II
Z_e	Density of effective sites
Z_0	Density of inoperative sites
Z_{e0}	Intersfacial density of AS
y	Molar activity coefficient

Greek:

α	No. of moles of hydroxyl that react with 1 mole of AS
β	Transfer coefficient
γ	Rate constant of AS
θ	Adhesive failure energy
σ_{\max}	Maximum compressive stress
∇	Laplacian operator
η_c	Non-dimensional length of the shrinking core
ϕ	Potential drop
ϕ^*	Thiele modulus
χ	Loss function
λ	Stretch
Λ	Conductivity
π	Potential energy

v	Stoichiometric coefficient
μ	Chemical potential
ρ_1	Molar density
ζ	Charge

1. INTRODUCTION

1.1 BACKGROUND

Concerns about the environmental durability of adhesives is the major reason why a big part of the industry is hesitant to incorporate adhesively bonded joints into primary load-bearing structures. Intrusion of moisture is a major concern when using adhesively bonded structures especially in marine conditions. The problem under investigation arose when some adhesively bonded sonar transducer units failed earlier than their 15 year design life. These units are subjected to harsh cycles of pressure, temperature, and environment during service. Although supposedly isolated, marine and other deposits eventually result in electrically connecting these units to the hull of the ship where zinc blocks have traditionally been used as sacrificial anodes. The sealant at the rubber/metal location is, apparently, only marginally successful and it is a matter of time before water diffuses into the bondline, thus starting the destructive chain of events that leads to failure. A corrosion cathodic voltage of about -1020 mV (with respect to a standard calomel electrode) is imposed by the zinc anodes generating

electrons at the bondline. The combination of several acting mechanism-accelerating parameters, i.e., applied stress, temperature, pH, voltage, etc. introduces a vicious cycle of diffusion and chemical degradation of the adhesive and the interface that leads to failure.

The problem described above is a widespread one since cathodic protection of offshore drilling rigs, vessels, and other marine structures is a common practice to minimize corrosion. One of two electrochemical reduction reactions can occur at the boundary of a defect in the coating or an exposed edge of the joint (cathode). At voltages less negative than -1020 mV (SCE), the oxygen reduction reaction



is favored, while the water reduction reaction



is dominant at more negative potentials. Debonding of organic coatings as a result of several electrochemical processes has been widely referred to as "cathodic debonding" and has been demonstrated to be controlled by a galvanic mechanism [1-4]. Cathodic debonding is also suspected to be the culprit in this study of adhesive bonds since current is provided for cathodic corrosion in a fashion similar to that in this application of concern.

Historically, different workers hold various opinions about the mechanism of cathodic debonding. For instance, Leidheiser [10] proposes the solubilization of the oxide as the major mechanism and that the dissolution of the oxide breaks the bond between the coating and the substrate and the high pH leads to localized attack on the polymer at the interface. On the other hand, Dickie et al [11] suggest that chemical degradation of the polymer is generally responsible for debonding.

The establishment the center for adhesion science (CAS) at VPI has created an interdisciplinary working environment where a meaningful interaction between mechanics, materials science, and chemistry can lead to a better understanding of the phenomena of adhesion and the subsequent de-adhesion. Consequently, this research is part of a larger effort that is being conducted in order to understand and model the delamination process and, if possible, to devise means to reduce the adverse effect of the corrosive environment on the adhesively bonded system. Two chapters (2 & 3) are presented in this dissertation in a paper format that is needed to meet the journal's (Journal of Adhesion Science and Technology) standards. This explains the apparent repetition in these two chapters.

1.2 OBJECTIVES

As a result of the above discussion, one can identify three major objectives for this study:

1. Identify and develop an understanding for the processes that are involved in the cathodic delamination process. This includes the identification of the principal mechanism(s) that result in failure. Generally, several competing and parallel mechanisms may take place in the process that eventually leads to bond failure. Diffusion through the adhesive or the adherend, wicking along the interface, or a combination of the above are all possible intrusion mechanisms. Cathodic action can only complicate the process further. Generation of hydroxyl ions at the exposed metal

increases the pH, thus accelerating the bond's failure. Several failure mechanisms are possible: degradation of the bulk adhesive, chemical attack on the interfacial adhesion-promoting linkages, and hydrolysis or reduction of the metal oxide. Obviously, a combination of rate-competing mechanisms can take place at the same time with the fastest process controlling debonding.

2. Investigate and analyze the effect of the accelerating parameters on debond rates, i.e., temperature, cathodic voltage, and stress. This requires that a test matrix which accounts for a wide range of accelerating parameters be devised and implemented.
3. The development of an empirical model that will accept all the experimental data base as input. The model will utilize a multiple regression scheme that makes use of the relevant independent variables in the given problem. This model will be capable of predicting the ensuing process and relevant accelerating parameters.
4. The objectives of this dissertation also include the development of a methodology by which an ultimate analytical model can be created. This model should include all the relevant physical parameters, i.e., diffusion coefficients, chemical degradation reaction rates, and geometric, interfacial, and bulk adhesive properties. Simulation requires that a numerical solution to a complex system of partial differential equations be found. A computer code that is available in the IMSL package utilizes a numerical scheme known as the "method of lines" (MOL) and a finite differences technique to solve similar systems.

Modelling of the debonding process using a valid physical and mathematical approach is a long term process. One can only hope that, given the implied limitations

of a dissertation, the effort presented here will shed some light and set some trends for more involved studies.

2. A STUDY OF THE MECHANISM OF CATHODIC DEBONDING OF ADHESIVELY BONDED NEOPRENE RUBBER FROM STEEL

2.1 ABSTRACT

The feasibility of applying surface analysis techniques to study adhesion has been well established. Some of these techniques were utilized in this study of cathodic debonding of neoprene to steel bonds to examine the interfacial failure surfaces. Auger Electron Spectroscopy (AES) showed the poor cleaning capabilities of vapor degreasing and the modest effect of alkali on the oxide layer. The neat phenol-formaldehyde-based primer exhibited a significant amount of degradation characterized by changes in the chemical composition as shown by X-ray Photoelectron Spectroscopy (XPS). The analysis of the cathodically debonded surfaces suggested cohesive failure in the primer close to the interface.

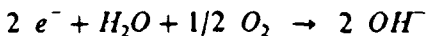
2.2 INTRODUCTION

The present study deals with the durability of neoprene/steel adhesively bonded joints in marine environments. The particular application of these joints includes a combination of environment and applied stress effects that tend to cause failure of the system after relatively short exposures. Cathodic debonding is suspected to be the culprit since current is provided for cathodic corrosion protection. This research is part of a larger effort that is being conducted in order to understand and model the delamination process and, if possible, to devise alternate means to minimize the adverse effect of the corrosive environment on the adhesively bonded system.

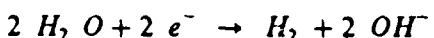
As to the mechanism of debonding, the formation of a Weak Boundary Layer has been suggested frequently in the literature as a cause for debonding ,i.e., hydrolysis of the polymer and simultaneous formation of a hydrated oxide layer at the interface serve to weaken the bond. Gledhill and Kinloch [5] suggested that the change from a positive to negative work of adhesion provides a driving force for the displacement of adhesive on the metal oxide surface by water. Kerr and MacDonald [6] suggested that the formation of a Weak Boundary Layer was due to the orientation of polar groups near the adherend surfaces resulting in a boundary layer with higher concentration of partially reacted functional groups than in the bulk polymer. They then proposed a failure mechanism when water accumulates at hydrophilic centers in the boundary layer and interferes with the metal oxide to adhesive hydrogen bonds thus creating a boundary layer. Stress hydrolysis of covalent bonds in the weakened boundary layer then occurs.

Considerable electrochemical work [7-9] has confirmed that cathodic delamination of organic coatings in corrosive environments is controlled by a galvanic process. Given that the electrolyte is present at the cathodic site, one of these two

reduction reactions, depending on the applied potential, can occur at the boundary of a defect:



Or



Either one of the above electrochemical reactions increases the OH^- ion concentration significantly in the immediate proximity of the exposed metal with the oxygen reduction reaction dominant at voltages less negative than -1000 mV (SCE). Different workers hold varying opinions about the mechanism of cathodic debonding. For instance Leidheiser [10] proposes the solubilization of the oxide as the major mechanism and that the dissolution of the oxide breaks the bonds between the coating and the substrate and the high pH leads to localized attack on the polymer at the interface. On the other hand, Dickie et al [11] suggest that chemical degradation of the polymer is generally responsible for debonding.

Several workers [7-9] have investigated the effect of electrochemical potential on the durability of adhesively bonded joints. Knowledge gained from cathodic debonding studies of coatings could be applied to adhesives keeping in mind that intrusion of moisture in adhesive bonds occurs in the lateral direction, as opposed to transverse in coatings.

In the marine environment under investigation, zinc blocks are provided for corrosion control purposes. If and when the zinc becomes electrically connected to the steel substrate, the flow of electrons to the cathodic site (steel) initiates the failure process. The rest of the elements needed for cathodic debonding are also available in

such an environment. The seawater electrolyte supplies the water molecules and oxygen that are necessary for the reaction and cations for charge neutralization. The steel substrate provides the catalytically active surface.

Some of the objectives of this study were to try to understand the mechanism(s) by which cathodic debonding fails the particular adhesively bonded system of interest and to determine the locus of failure. Testing was performed on adhesive joints as close to real life conditions as possible. A block of zinc was initially used to induce an electron supply. It was found, however, that debond rates were fairly slow and the use of zinc proved to be cumbersome due to passivation and to anode/cathode surface area ratio problems. Use of a power source and carbon electrode to provide a constant voltage provided a convenient solution. Another concern was whether accelerated testing could be achieved by using an alkaline solution for conditioning rather than seawater. Ritter and Kruger [13] reported pH values as high as 14 under a cellulose nitrate coating in a 5 percent NaCl environment. Such findings justify, in our opinion, the use of a concentrated alkaline solution to simulate the conditions at the metal/adhesive interface.

2.3 EXPERIMENTAL

The system under consideration is a proprietary two part vulcanizing adhesive system used in bonding elastomers to metal. The primer was found [14] to consist primarily of a blend of phenol formaldehyde and chlorinated isoprene, and includes titanium dioxide and zinc and lead compounds as additives, and carbon black as a filler. The adhesive is based on allylically brominated poly-2,3-dichloro-1,4-butadiene

containing 10-27 percent bromine. The material used for the substrate was ANSI 1026 steel and the rubber was 5109S Neoprene. The surface preparation of the substrate involved vapor degreasing with trichloroethane before and after grit-blasting with 40 grade steel grits at 275 kPa. A thin coat of metal primer was applied with a brush within 30 minutes of degreasing and two coats of adhesive followed after the primer had dried.

Following the adhesive application, the steel substrates were placed in a mold where pre-cut sheets of uncured neoprene were laid. Bonding and vulcanizing processes were performed simultaneously. The cure cycle involved a combination of temperature of 154 - 157° C and pressure of 3.4 MPa for 50 minutes. A post cure cycle of temperature at 177° C for about 3 hours followed. The bonded specimen shown in Fig. 1 was fabricated as such for another study of accelerated debonding as well as surface analysis. Two 6.35 mm thick neoprene layers were bonded to both sides of 1.6 X 25 X 72 mm pieces of steel that served as substrates.

Conditioning of the bonded specimens was done in a Napco model 220A water bath equipped with a temperature regulator. The specimens were placed in the electrolyte, becoming the working electrode of an electrochemical cell, with a graphite counter electrode and a standard calomel reference electrode also immersed in the solution. An HP model 6214B power supply was used to provide the desired voltage which was checked and adjusted occasionally. To provide the needed oxygen, room air was pumped into the bath after passing through a carbon dioxide trap that consisted of a flask full of a concentrated NaOH solution and another flask containing $\text{Ca}(\text{OH})_2$ solution serving as an indicator.

In addition to tests on actual bonded joints, neat primer and adhesive films were also studied. Some difficulties were encountered while preparing free films of primer due to the high solvent content. Thin films were cast on clean glass, exposed to the temperature cure cycle, and separated with a razor blade. The resulting films were about

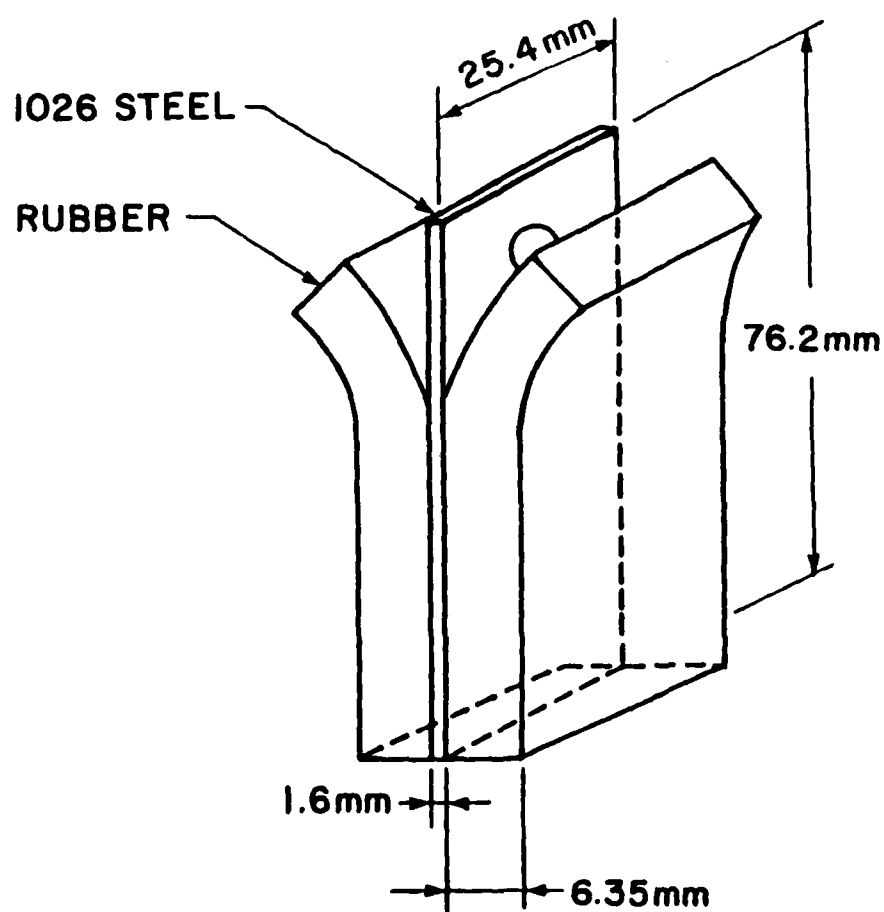


Figure 1. A Schematic of the Bonded Diffusion Specimen (BDS).

0.5 mm thick, brittle, and apparently pore-free. Fabricating thicker neat primer specimens needed for diffusion studies proved to be even more difficult. A technique was eventually developed for casting films of the primer on Teflon coated fiberglass peel cloth as used in the production of laminated composites. The cloth had enough flexibility that it could contract with the primer and did not produce cracking of the films.

The XPS used in the study was a Kratos instrument model XSAM-800 using X-rays Mg K_{α} (1.254 keV) and run at 260 watts under 10^{-9} torr vacuum. The other instruments were a Perkin-Elmer PHI multiprobe AES model 610 and a Philips 505 SEM.

2.4 RESULTS

Because all the evidence, based on the authors' observations, has pointed to the primer/steel interface as the locus of debonding, it was logical to concentrate on this region. In trying to address the question of delamination, an effort was made to analyze the steel substrate and the neat primer free films separately after exposure to concentrated NaOH solution and to contrast the results with the actual debonded failure surfaces in artificial seawater (ASW) or a high pH solution. The purpose was to see whether the respective analyses yield the same trends of reaction.

The effect of high pH solution on the oxide layer was investigated using AES. Two steel samples were degreased and grit-blasted, after which one was placed in a desiccator while the other was exposed to a 1M NaOH solution for 4 days at 25°C. AES

results are shown in Figs. 2a and 2b to reveal some changes in the composition of the oxide after exposure, perhaps some hydration of the original ferric oxide, Fe_2O_3 . The thickness of the original oxide layer was about 100 \AA and did not seem to change much after exposure. More work is necessary to determine the effect, if any, of such changes in the composition on the debonding process.

In order to determine the effect of the alkaline environment on the primer, thin films of primer were cast on glass substrates, as indicated before, and separated into three groups for exposure. One group was placed in a desiccator, and the other two groups were exposed to 1M NaOH for 20 hours and seven days, respectively. After rinsing the samples in distilled water, an XPS analysis was performed. The results are presented in Fig.3. The actual concentrations for the unexposed sample consist of about 74 percent carbon, 10 percent oxygen, 14 percent (organic) chlorine, and traces of silicone and metallic fillers. The results after 20 hr. exposure reveal a slight drop in the carbon content accompanied by an increase in oxygen, chlorine, and sodium. The results from the seven day exposure show a decline in the carbon and chlorine peaks and a sharp increase in oxygen and sodium.

The results from the peak deconvolution before and after exposure to 1M NaOH at room temperature are illustrated in Figures 4 and 5. They show that some linkages undergo chemical changes when exposed to a highly alkaline solution. The curve-fitting procedure was performed using standard XPS techniques utilizing a Gaussian peak shape.

Analysis of the Cl_{2p} peak is presented in Fig. 4 and shows peaks at 202.6 eV and 200.9 eV that was assigned to organic chlorine prior to exposure. The rise of a new inorganic peak at 200.5 eV and 198.8 eV could be seen in the figure after 1 week exposure to the alkali. The ratio of the newly formed inorganic chloride to the organic chlorine is about 2 to 1. The above increase of inorganic chloride was not accompanied by an increase

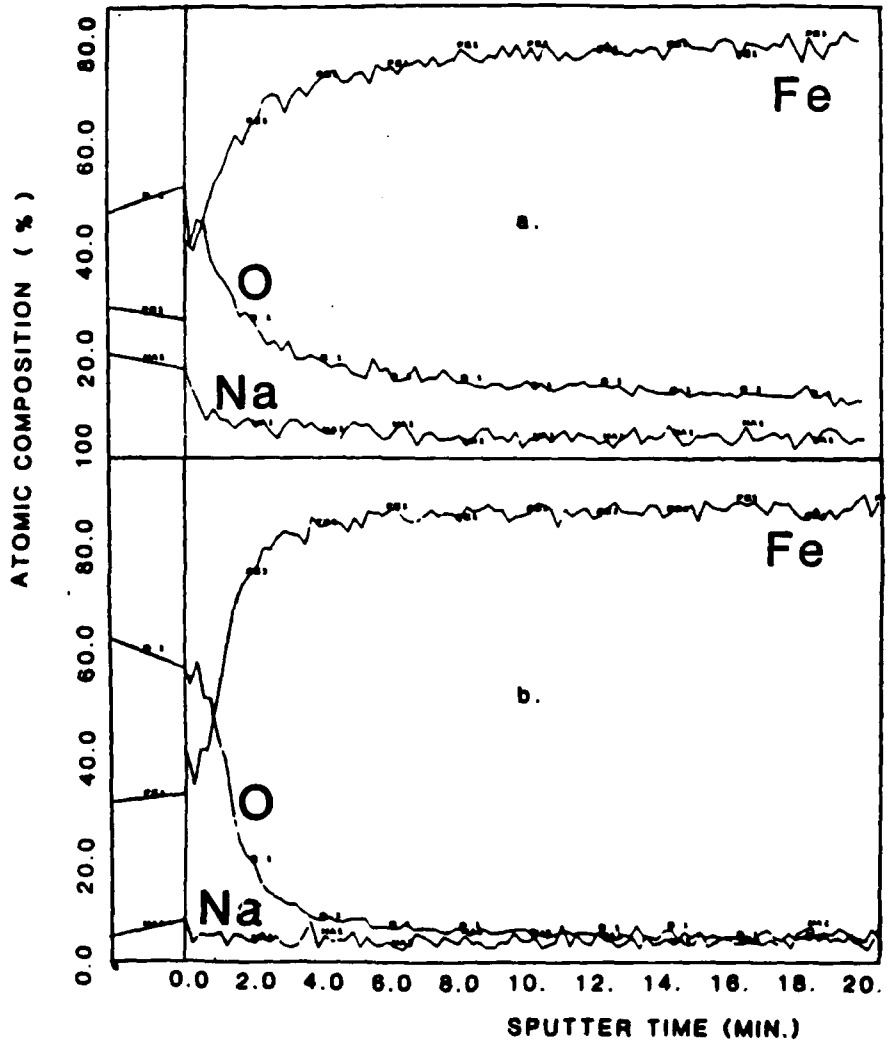


Figure 2. AFS depth profile of mild steel, a) degreased and grit-blasted b) degreased, grit blasted, and exposed to 1M NaOH for 4 days.

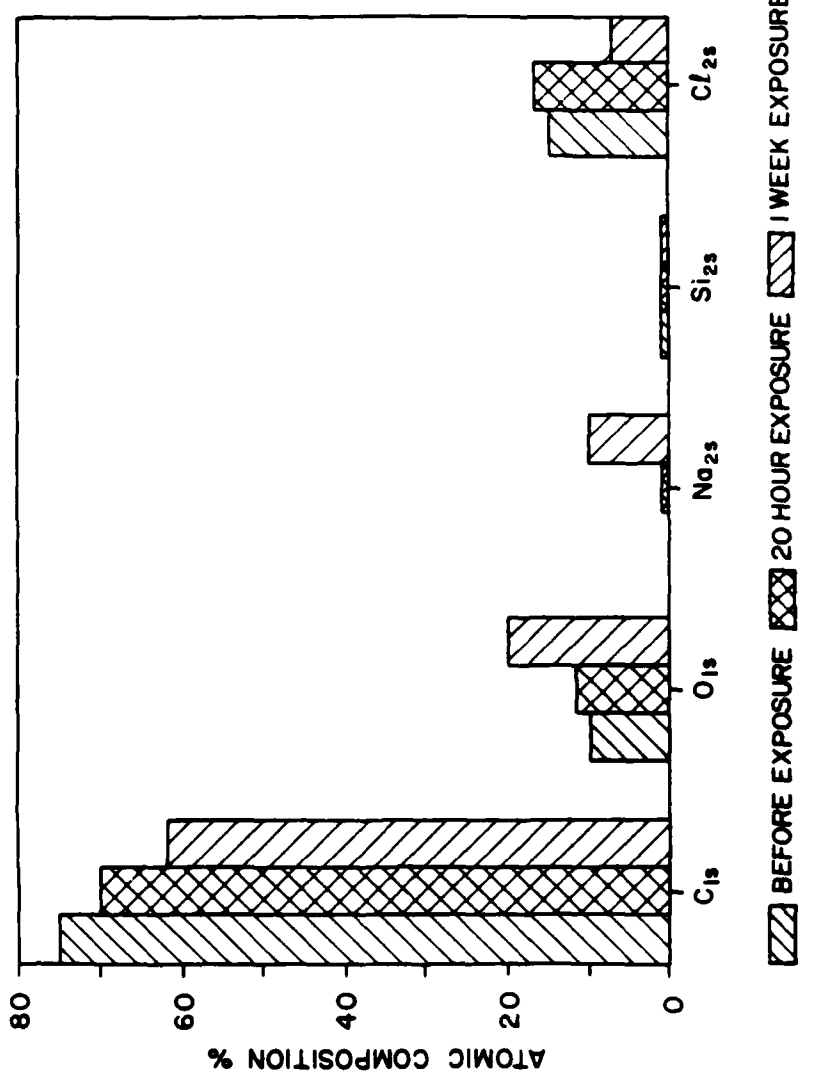


Figure 3. Neat primer components as a function of exposure time to alkaline environment: 1M NaOH, 30°C.

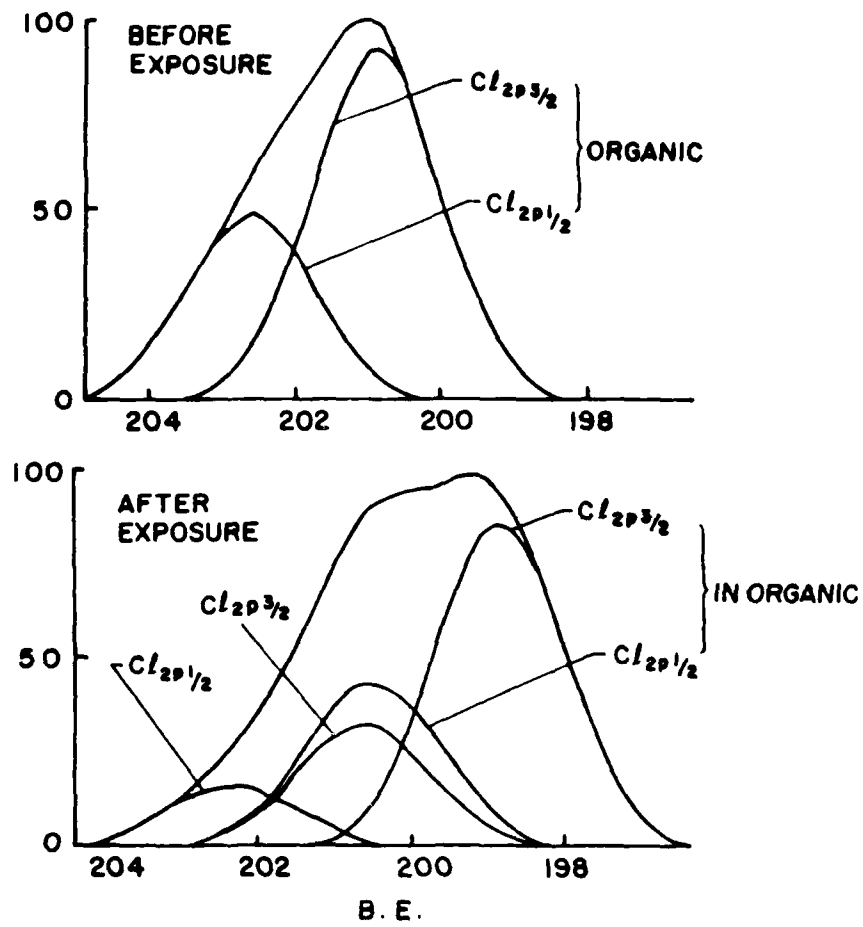


Figure 4. Curve fitting of the Cl 2p spectrum of the neat primer a) before and b) after 1 week exposure to 1M NaOH, 30 C.

of solids, i.e., zinc or lead. For the C_{1s} peak, the C-C peak position was corrected in Figure 5 , for sample charging, to 285.0 electron volts. The proprietary nature of the system and the uncertainty about the exact composition of the chlorinated rubber requires some speculation as to the nature of the remaining bands; all depending on whether the substitution of chlorine has occurred before or after polymerization of the rubber.

One explanation is that the peak at 286.4 eV corresponds to the C-O bonds while that at the 287.9 eV position is assigned to the C-Cl bonds. The other possibility assigns the C-O and C-Cl bonds to the former band and the C- Cl_2 bond to the latter. The C-O band is attributed to the formation of dibenzyl ether linkages between the benzene rings during the second stage polymerization of the resole [15] while the C-Cl and C- Cl_2 bonds are due to the presence of the chlorinated rubber. The above reasoning is dictated by the need to explain the fact that no significant shake-up satellite related to the aromatic groups in the resole has been detected in the spectra before exposure thus raising the possibility of phase separation or migration of the chloroprene to the surface. Exposure of the primer to the alkali for one week gave rise to two additional peaks at 289.9 and 291.5 eV that correspond to highly oxidized carbon states and are believed to be carboxylates and carbonates, respectively. The latter band position coincides with that of the shake-up satellite related to the benzene ring in the phenol-formaldehyde as well as that for carbonates. One possible explanation is that the band is a combination of the two above mentioned bands. One can argue that the chlorinated rubber has migrated to the surface of the free film during curing thus covering the resole resulting in no significant contribution of the satellite in the XPS spectra for the no-exposure and the 20 hour-exposure cases. On the other hand, hydrolysis of the ether linkages in the resoles, after exposure to the alkali, and that of the chlorinated rubber will in turn form carbonates as discussed later.

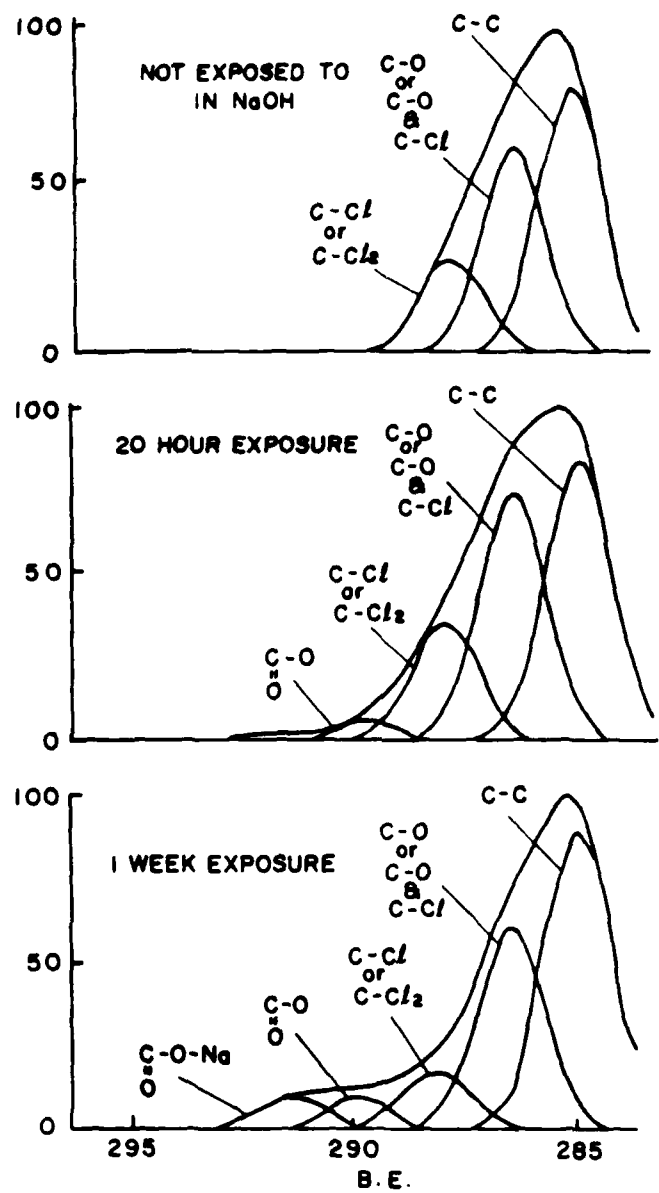


Figure 5. Curve-fit of the C 1s spectrum of the primer a) before, b) after 20 hour, and c) after 1 week exposure to 1M NaOH, 30 C.

A study of moisture intrusion into the neat primer was sought to better understand the mechanism involved, i.e., Fickian diffusion or chemical reaction, and to verify the effect of chemical degradation. Several films of neat primer were prepared using the teflon cloth technique mentioned above. The average thickness of the coupons was about 1.6 mm and the conditioning was done in several environments at 33° C. Results for these specimens are given in Fig. 6 and clearly indicate the significant effect that hydroxide has on the primer. In artificial seawater (ASW), the net weight gain at saturation is only about 2 percent; whereas in concentrated NaOH it approaches 50 percent.

At lower concentrations, the rate of weight gain is significantly less than for the concentrated environments and seems to indicate that these lower concentrations may result in saturation net weight gains which are below the 50 percent levels. There is an apparent reversal in the order for the effects of 3 and 10N NaOH which has not been explained, but could be due to a reduced thermodynamic activity of the solution at the extremely high concentrations.

The desorption data were collected in a convection oven maintained at the same temperature as the absorption. The weight loss occurs much more rapidly than the original weight gain. When the re-dried specimens were placed back in their respective environments, the net weight gain occurred very rapidly. The desorption in the specimen soaked in 10N NaOH shows a very slow rate which could be related to the accumulation of non-dissociated NaOH deposits in the bulk resin.

The net weight gain data are replotted against the square root of time in Fig. 7 and show that the intrusion is far from obeying Fick's law. In the figures with time as the horizontal axis, note that the experimental results indicate that the initial net weight gain is occurring at a constant rate and that there is an abnormally sharp knee in the curve. In the figures plotted against the root of time, the experimental results deviate

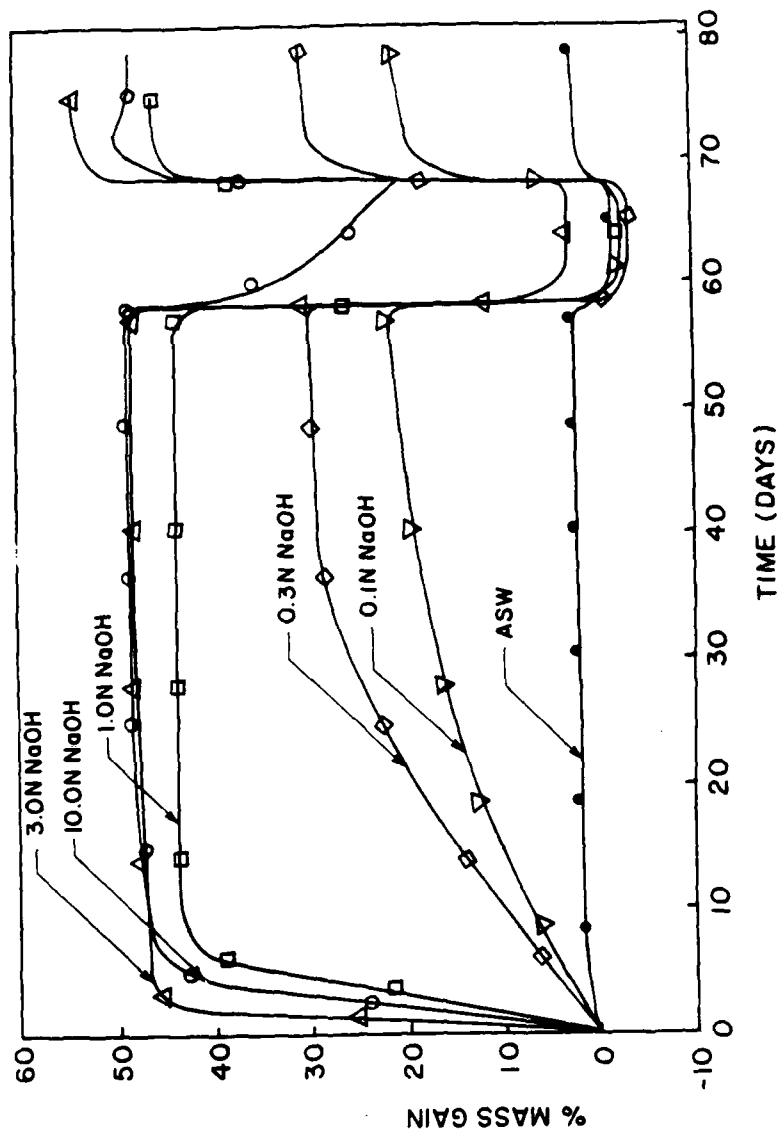


Figure 6. Sorption curves for neat primer films at 33°C showing exposure, drying, and resorption response.

substantially from the linear relationship expected from Fickian diffusion. It is believed that the intrusion is occurring as a front and that the net weight gain is not diffusion controlled, but rather is limited by the rate at which the polymer hydrolyzes. This data substantiates case II (chemical-reaction controlled) diffusion for these relatively thin primer samples.

For reasons stated above, it was decided to use XPS to analyze the actual debonded surfaces, i.e., steel and rubber sides of the fracture surface. Several specimens were conditioned in 1M KOH at 30° C and -1.40 V for 14 days in order to produce a weakened zone which could be easily separated by hand. Circular punchouts (9.5 mm dia.) from the steel and rubber in the interfacial failure zone were prepared for analysis. Figure 8 shows that the composition on both the steel and rubber side appear to be quite similar in the broad window of XPS even though the failure appears to be a clean interfacial failure to the naked eye. The compositions show the same trends as exhibited by the neat primer specimens when exposed to environment for long periods of time.

An interesting fact is the observation of very little iron on the steel surface. Two possible explanations are that the failure occurs within the primer layer, or that contaminants were left on the surface of the steel. In order to better understand the exact location of the debond, samples were cut from the steel substrate of a specimen exposed to the same conditions mentioned above. An XPS analysis was performed on samples cut directly from the failure surface and samples rinsed with distilled water, analyzed, and then sputtered with argon for four minutes and analyzed again. Fig 9 shows that rinsing tends to wash off sodium increasing the carbon and oxygen peaks and significantly reducing the sodium peak. Sputtering further increases the carbon peak and apparently reaches slightly into the metal oxide. The dominant elements, however, continue to be the carbon and oxygen. If the organic material on the steel were solely due to the residual contaminants on the surface and a true interfacial failure had

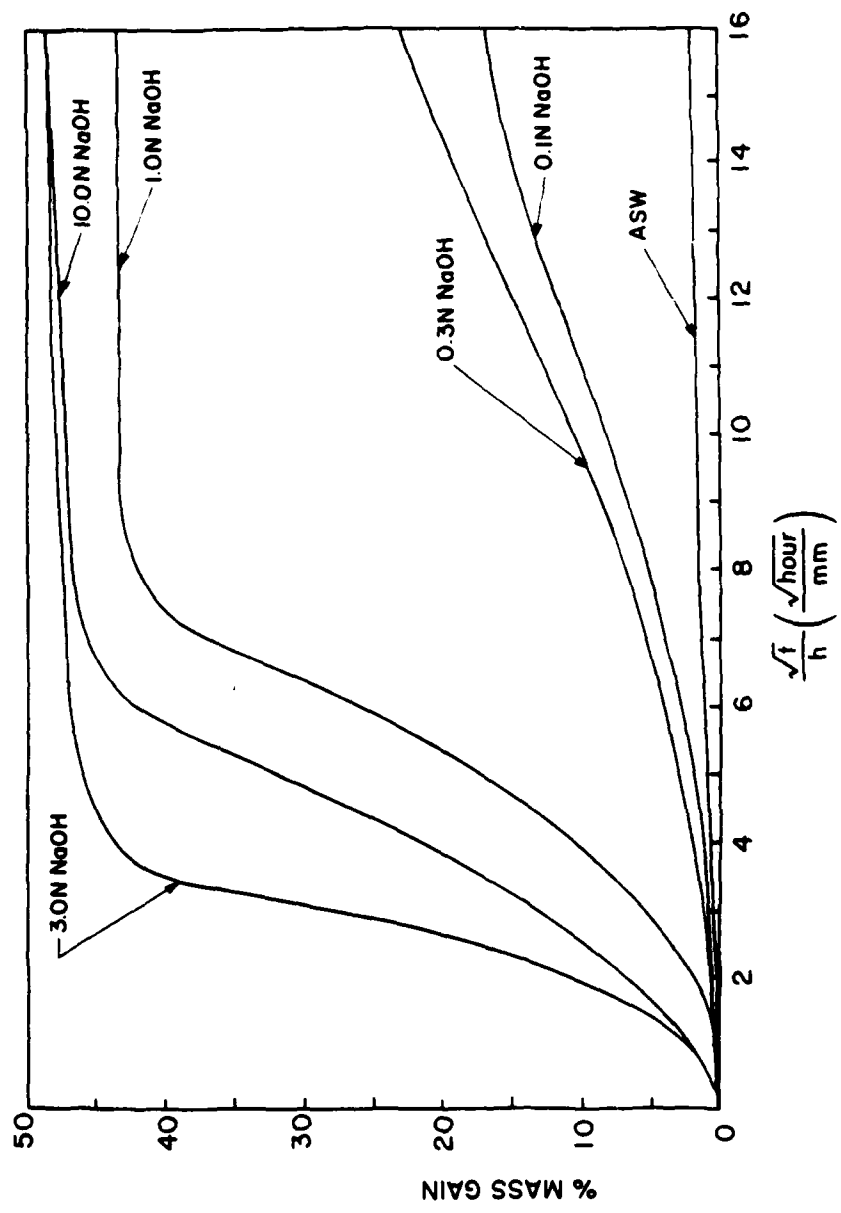


Figure 7. Net weight gain of neat primer films plotted vs square root of time.

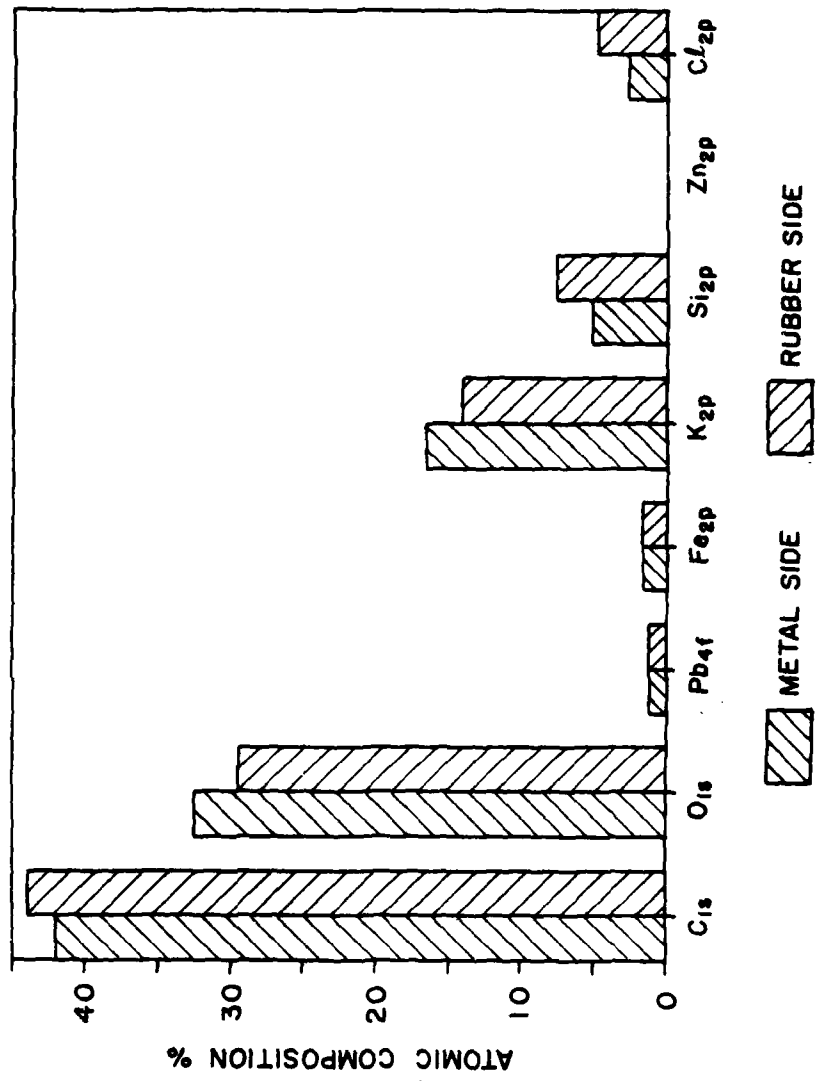


Figure 8. Interfacial failure components of the rubber and steel sides after exposure to 1M KOH, natural potential of zinc, and 30 C.

occurred, one would expect that the sputtering would have removed more of this layer and that more iron would have appeared.

Fig.10 shows the C_{1s} peak for the fracture surface of a bonded specimen after exposure to 1M NaOH for 3 weeks. The results appear to be quite similar to those obtained from neat primer samples except for a new smaller band at about 283.8 eV which is believed to arise from a differential charging effect that might have been caused by the presence of rubber ligaments on the steel side that will charge up thus altering the shift of the C-C peak associated with these regions. Again, curvefitting reveals the presence of the carboxyl group and the carbonate ion reinforcing the idea that most of the rubber failure surface contains degraded primer.

An experiment was carried out on the bonded specimens in order to answer a basic question about the role of the hydroxyl ion in the debonding process. Referring to the electrochemical reactions given above, one sees that the oxygen reduction reaction can not proceed if oxygen is not available. A sealed electrochemical cell was prepared into which nitrogen gas was injected continuously thus effectively purging the oxygen from the solution. The specimens were pulled out after conditioning for 11 days in ASW at 30 C and an applied cathodic voltage of -0.9 V (SCE). This particular potential was chosen in order to favor the desired reaction. The mechanical separation of the bond showed that the debond distance was insignificant in the absence of any considerable dissolved oxygen giving credibility to the proposed role of the hydroxide.

A point was raised as to whether mechanical interlocking at the rough surface is responsible for the presence of traces of primer on the fracture surface and whether contamination was indeed a factor in the analysis. In fact, AES results in Fig. 11.a show that some organic contamination was still present on the surface after vapor degreasing, judging by the large percentage of carbon and the small presence of iron. Fig. 11.b shows that the carbon was sputtered away after 20 minutes of sputter. Polishing and

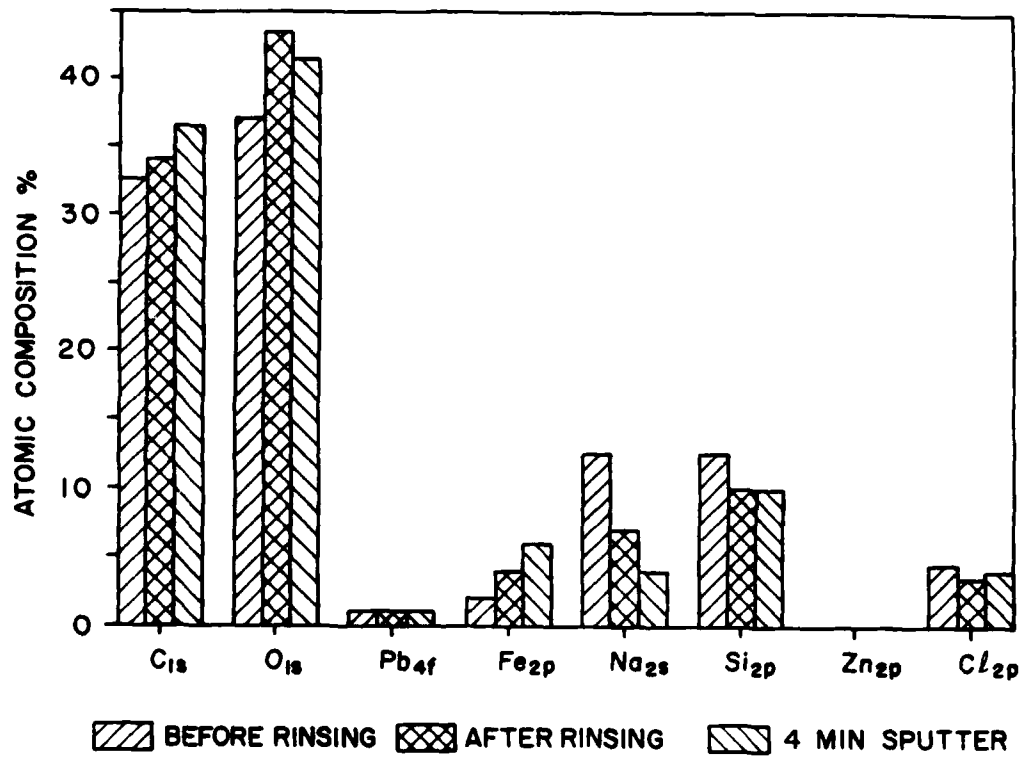


Figure 9. Analysis of the metal interfacial failure surface after exposure to 1M NaOH, natural potential of zinc, and 30 C.

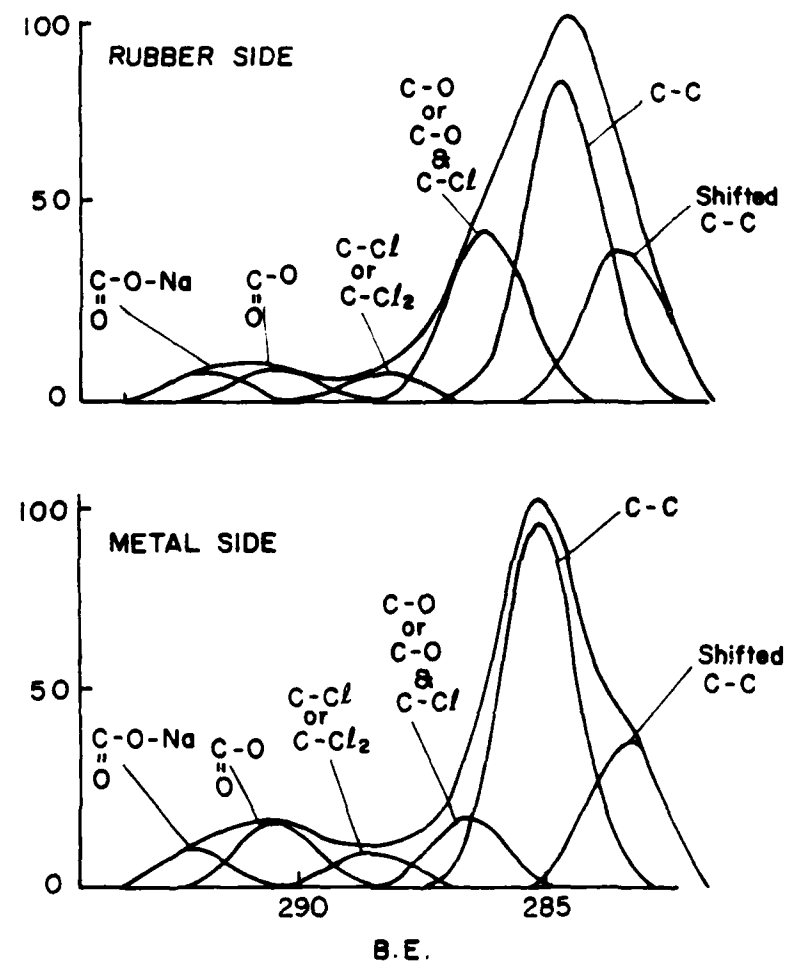


Figure 10. Curve-fit of the C 1s peak of a shot-blasted surface after failure ; environment: 1M NaOH, natural potential of zinc, 30 C.

cleaning of the steel was sought then as a way to answer these questions. Contrasting these two surfaces with results from grit-blasted specimens reveals a much cleaner break for polished specimens than for grit-blasted specimens. Figs. 12 and 13 show the opposite sides of the failure surface for a polished specimen exposed to 1M NaOH for one week at 30 C and -1.4 V (SCE).

Another concern has been whether exposure to seawater solution with applied potential would yield the same results as with the concentrated NaOH. The bond was delaminated after exposure in artificial seawater (ASW) at 30° C and -1.02 V (SCE). Fig. 14 shows basically the same components as in KOH or NaOH solutions except for less sodium , thus increasing the carbon peak. Understandably, sputtering reveals a significant increase in chlorine on the polished rubber side as one nears the adhesive. Contrasting these results with those for the harsher environments reveals the same locus of failure for both cases. A curve fit of the C_1 , peak from the polished surface above reveals (Figure 15) the same characteristics as those previously determined from the NaOH-conditioned specimens as far as degradation is concerned, thus giving this mechanism more credibility.

2.5 DISCUSSION

Chemical degradation of the above mentioned primer upon exposure to the alkali has been verified throughout this research. Saponification and leaching of chlorine are perhaps only two of several degradation processes that take place. The changes in composition of the various constituents of the primer along with the curvefitting analysis

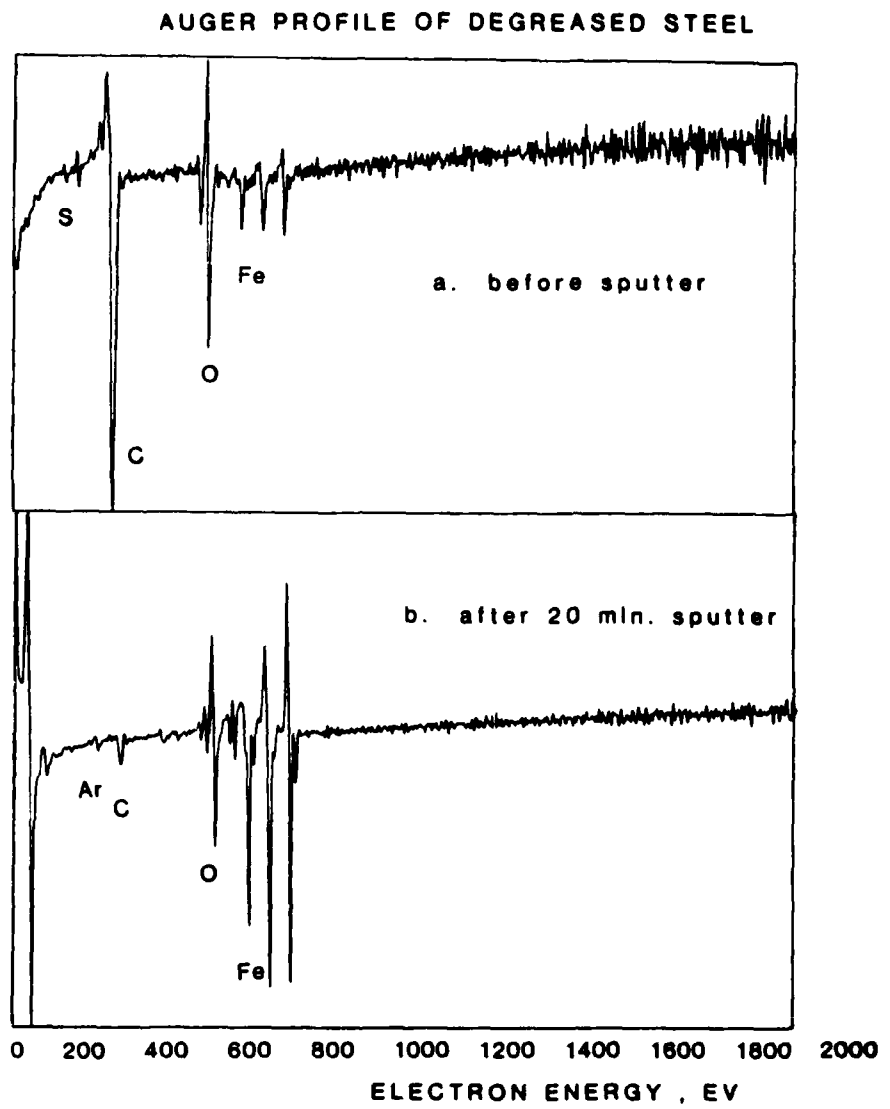


Figure 11. Auger profile of degreased and grit-blasted steel a) before sputter b) after 20 min. sputter.

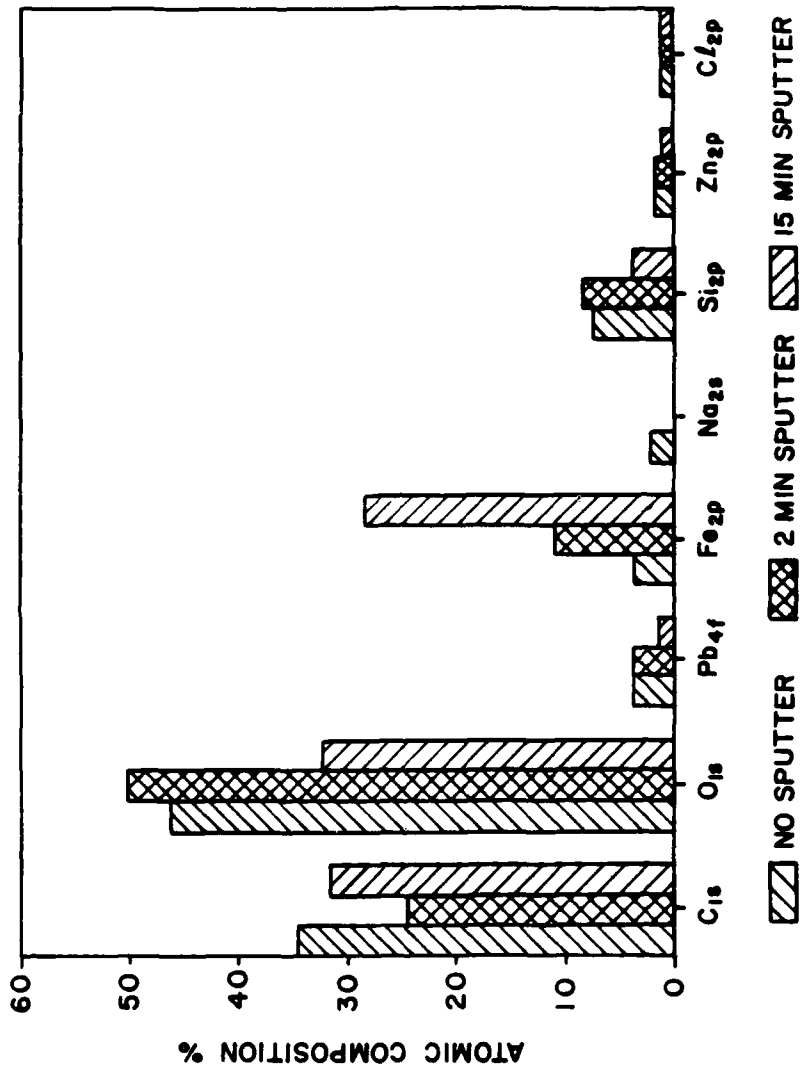


Figure 12. Polished steel fracture surface components after exposure to 1M NaOH, natural potential of zinc, and 30 C.

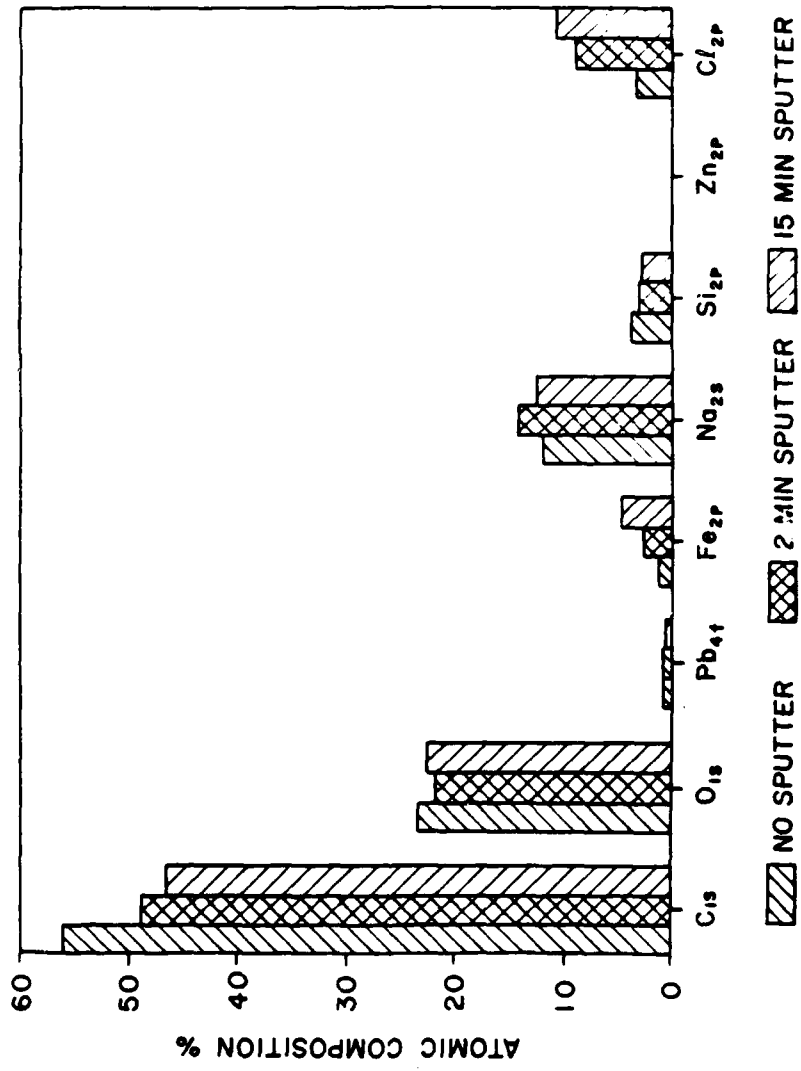


Figure 13. Polished rubber failure surface components after exposure to 1M NaOH, natural potential of zinc, and 30 C.

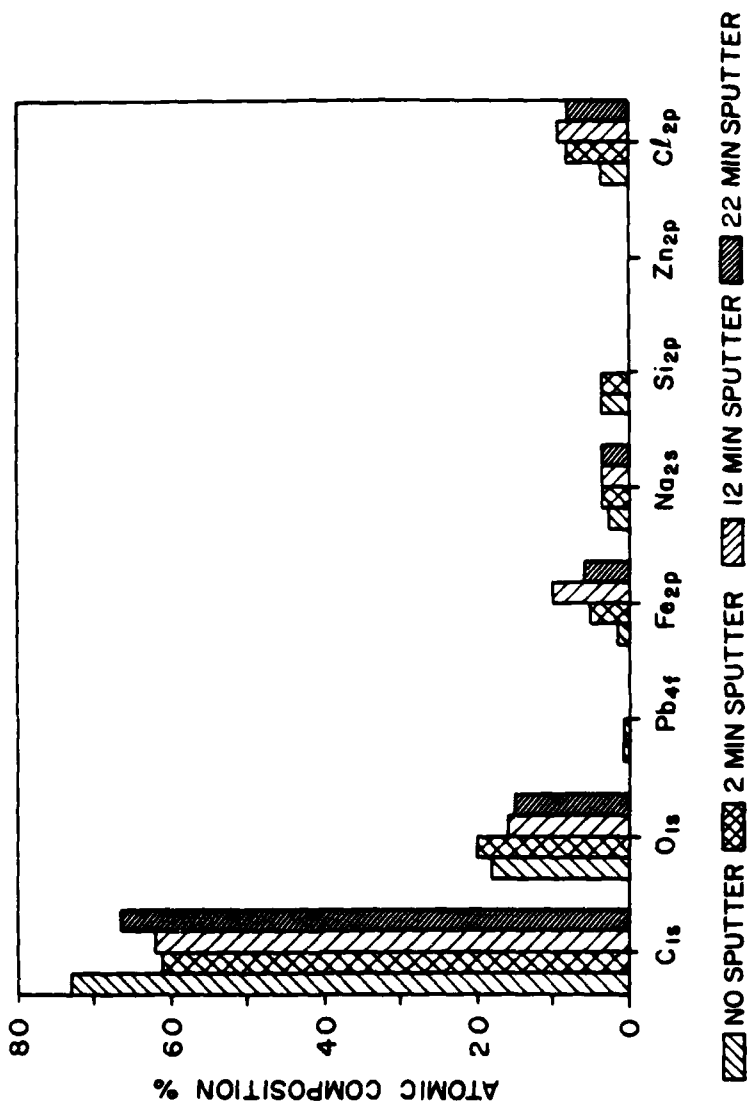


Figure 14. Polished rubber failure surface components after exposure to artificial sea water, -1.02 V, and 30 C.

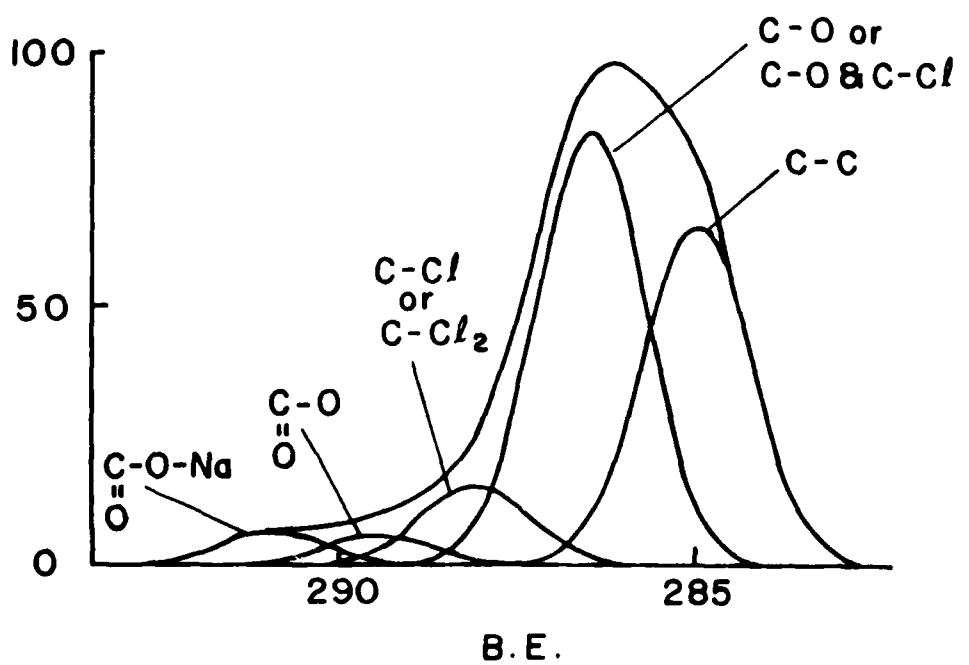


Figure 15. Curve fitting of the C1s band from a polished failure rubber surface; environment: ASW, -1.02 V, 30 C, 3 weeks.

of the respective peaks point to the hydrolysis of the adhesive. The weight gain studies point also to the apparent and significant change in the composition and nature of the adhesive after exposure. The fact that the sorption curves indicate a strong chemical reaction effect is further substantiated by observing the very steep rate at which re-sorption takes place indicating that the reaction is irreversible. Redrying and subsequent absorption processes occur rapidly because the chemical processes have already degraded the polymer and are no longer the rate limiting factor. The unusually high saturation level could be attributed to the hydrophilicity of the carboxylate ions that were formed in the resole and the chlorinated rubber. A similar effect could result from the hydration of the generated inorganic ions, i.e., Cl^- .

The chemical degradation of the adhesive may start when the hydroxide ions break up the resin resulting in the formation of the carboxylate ions at the ends of the broken chains. The ether (C-O-C) linkages have been shown [16,17] to be unstable when exposed to high pH where they hydrolyze and form metal salts. The presence of sodium (despite rinsing) could be due to the formation of carbonate groups on the polymer chain. The Na^+ ions would attach to the negatively charged oxygen as:



/



On the other hand, high pH is known to cause the release of the chlorine, as Cl^- , in the chlorinated rubber as in other chlorine-containing polymers [18] which, in turn, attack the iron oxide causing it to corrode. In alkaline conditions, the chlorinated isoprene splits off HCl which forms NaCl and which may explain the large percentage of sodium in the XPS spectra. The hydrolyzed chlorinated isoprene will also react with $OH^- + H_2O$ to form carboxylates. It is also possible, depending on how stable the bond is, that the Cl atom in the C-Cl is simply replaced by the OH^- resulting in the above

mentioned leaching. Leaching of chlorine could be deduced from the drop in its percentage after 1 week exposure of the primer to the corrosive environment and from the analysis of the Cl_{2p} peak that shows the rise of the new inorganic peak. Similarly, the net weight gain study shows that the primer has lost some of its original weight after sorption and subsequent drying which substantiates the leaching mechanism. It should be noted that the "net" expression refers to the total algebraic difference of the intruding species and the leached material. In light of the above, and if it is true that the chlorinated rubber migrates faster to the interface than the other constituents, then the degradation of these attachment sites and the subsequent corrosion of the steel by the chloride ions could be detrimental as far as durability of the bond is concerned. Phase separation during drying of the adhesive was found to exist in solvent-containing adhesives and it depends greatly on the rate of solvent evaporation.

The similarity of the composition of both sides of the rough failure surfaces and the cleaner break of the polished samples may be explained by the presence of a weak boundary layer. In the rough interface system, the peel front upon separating the rubber from the steel cannot follow the surface asperities and will jump into and out of the WBL leaving more organic material at the surface; while with the smooth surface the peel front propagates along the steel surface and remains in the WBL leaving very little organic material behind. It should be noted that XPS is a broad window technique, and the similarity of the two rough surfaces may only be true in an average sense. For instance, SEM results reveal more localized regions of homogeneous material. This is in line with the observations other workers have made. Koehler [19] reported that the cathodic debonding originates from a great number of distinct points that do not represent exposed metal but rather "regions in the coating of high ionic conductivity to provide cationic ingress". Hojo et al [20] reported on the effect of exposing vinyl ester resin to 10 percent NaOH and observed that "at an early stage of immersion, island

shaped white material is observed locally whilst at the same time hydrolysis occurs at or near the resin surface". All of the above indicates, perhaps, a current-induced hydrolysis that originates at regions of low ionic or current resistance, i.e., oxide filler concentrations at the interface.

The contribution of mechanical interlocking should not be underestimated. It has been observed that rubber ligament pull-outs often coincide with grit-blast crater tops. Most interesting is the fact that the weakened bond exists and its critical strain energy release rate, G_{σ} , has been measured to be of the order of 17.55 joules/m². On the polished specimens, however, the weakened bond has negligible strength and it often debonds spontaneously. The important implication is that the strength of the weakened bond is mechanical and in the absence of significant surface roughness, the failure is more interfacial than "island-like".

Finally, the OH^- ion, as determined from the analysis of the neat primer, the debonding of the bonded specimens, and the insignificant effect of the oxygen-free environment on the joint, is the main culprit in the cathodic delamination process. The success or failure of efforts to enhance the environmental durability of adhesive joints in marine applications lies in the effectiveness of preventing the hydroxyl from being generated in the first place or in minimizing its negative effects in case it reaches the neighborhood of the bond. Preliminary tests conducted on zinc phosphated steel show that this reduction in the surface activity may be one method to reduce hydroxide formation. The addition of silanes to the primer may improve its resistance to deterioration [21,22].

It is worth noting that another proof of chemical degradation, using IR, involving other linkages has been reported as well [23]. Further work is needed to answer some of the above raised questions concerning some of the proposed mechanism(s). SIMS is suggested as another useful technique that could be used in the

future because it is rapidly being utilized for polymer characterization and surface studies since it provides more molecular structures information than XPS does.

2.6 CONCLUSIONS

The authors, therefore, have arrived at the following conclusions:

- 1) We have provided evidence for a cathodic delamination of neoprene from steel in seawater in which the adhesive (phenol-formaldehyde resins and chlorinated rubber) is chemically attached by cathodically generated hydroxyl ions.
- 2) The chlorinated rubber splits off inorganic Cl^- ions which are corrosive to the steel substrate; saponification of the adhesive under formation of carboxylate ions also occurs.
- 3) Delamination is in a Weak Boundary Layer of degraded polymer
- 4) Combination of surface analysis techniques and sorption studies were proven to be very useful for the study of the interfacial phenomena in adhesively bonded systems.

2.7 ACKNOWLEDGEMENTS

The authors wish to express their gratitude to the Office of Naval Research and the Naval Research Laboratory - Underwater Sound Reference Detachment for their

support of this work. Acknowledgements are also due to Dr. David Dwight, Steve McCartney, and Naranjan Patel for their invaluable help and meaningful comments and to Zhiqiang Wang for his work on moisture uptake. The authors would also like to acknowledge the assistance of other participants in this joint study: Dr. F.J. Boerio at the University of Cincinnati, Dr. J.S. Thornton at Texas Research Institute, and Dr. K.M. Liechti at the University of Texas.

3. A MECHANISTIC EVALUATION OF CATHODIC DEBONDING OF ELASTOMER TO METAL BONDS

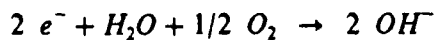
3.1 ABSTRACT

The durability of adhesively bonded Neoprene rubber to metal joints for marine applications is discussed. In order to simulate the local environment on cathodic surfaces, neat film specimens of various adhesive systems were fabricated and tested in NaOH aqueous solutions resulting in chemical degradation of the polymer accompanied by weight and volume changes. Neat film specimens exposed to artificial sea water (ASW) showed much smaller changes. The addition of a silane coupling agent to the primer component enhanced the chemical resistance of the free samples considerably. Actual bonded diffusion specimens were also utilized and it was found that the propagation of a weakened bond obeyed a linear relationship when plotted against the

square root of time, suggesting Fickian diffusion. The results suggest that the rate is very sensitive to temperature, cathodic current, and other accelerating parameters. It was also shown that the use of zinc phosphate coated steel substrates improve the durability especially at low cathodic potentials (currents). Stressed specimens were also tested and showed that tensile stresses accelerate bond delamination. The addition of relatively high concentrations of a silane coupling agent is correlated with reduced delamination rates.

3.2 INTRODUCTION

Cathodic protection of offshore drilling rigs, vessels, and other marine structures is a common practice to minimize corrosion. The present study deals with the environmental durability of adhesively bonded joints in marine applications under imposed cathodic current. Debonding of organic coatings as a result of several electrochemical processes has been widely referred to as "cathodic debonding" and has been demonstrated [1-4] to be controlled by a galvanic mechanism. In the current application the process occurs due to the presence of sacrificial zinc blocks (anodes) which protect the steel from corroding. One of two electrochemical reduction reactions can occur at the boundary of a defect in the coating or an exposed edge of the joint (cathode). At voltages less negative than -1.0V (with respect to a standard calomel electrode), the oxygen reduction reaction



is favored, while the water reduction reaction



is dominant at more negative potentials.

In the case of a coated surface or an adhesive joint, the concentration of the hydroxyl ion becomes excessive in the neighborhood of the metal substrate. Ritter and Kruger [13] reported pH values as high as 14 under a cellulose nitrate coating in a 5 percent NaCl environment as a result of localized anodic/cathodic regions. Turnbull [24-25] predicted crack tip pH values of at least 12 in his study of crack growth in seawater environment. Stevenson [7] demonstrated that under electrochemically inert conditions, the peel energy needed to separate a rubber to steel adhesive bond did not change after exposure to sea water for nearly two years and found that the failure was cohesive in the rubber and not interfacial. When electrochemical activity was imposed, however, significant interfacial failure was observed within a matter of weeks. Previous work [26,14] involved the use of several surface analysis techniques to identify the locus of failure and associated mechanism(s) of cathodically debonded joints using the same control adhesive system used in this study. It was concluded that the failure occurred mostly in the primer coat very close to the steel and mainly because of polymer degradation. Saponification of the primer, as a result of hydroxyl attack on the chemically unstable linkages (methylene or ether) was identified as a possible cause of failure.

In this study, two adhesive systems, different substrates, and other parameters were used in order to evaluate the durability. To facilitate evaluation of these material systems and relevant parameters, some type of accelerated characterization is desirable. Accelerated testing of adhesives is a valuable instrument by which the industry can evaluate the performance of a given system over extended periods of time. For example,

Williams [12] studied the effect of combined humidity, stress, and heat on several rubber to metal vulcanized bonded assemblies in the absence of cathodic activity and showed that butadine-styrene vulcanized assemblies showed no loss in bond strength while other systems did. That led him to conclude that accelerated testing can be used to select an adhesive bonding system that best suits a particular application. However, most, if not all, of the work involving vulcanized adhesive assemblies take up a considerable amount of time to collect real-life-like data. The use of accelerating parameters was sought in this study in order to be able to characterize a particular adhesive system in a reasonably short period of time. Such findings reported above about the pH, for instance, give some justification to the use of concentrated alkali as an accelerating environment. Similar arguments can be made about temperature, current, stress, etc. keeping in mind the obvious limitations such as when a different debond-causing mechanism evolves as a result. The use of some of these parameters will also be discussed herein.

3.3 EXPERIMENTAL: MATERIALS AND SPECIMENS

A specially formulated rubber for Navy applications known as 5109S Neoprene was used throughout this study. The "control" steel used in making the adherends is AISI-1026 and the principal control adhesive system is a proprietary, commercially available, two part vulcanizing adhesive system used in bonding elastomers to metal. The primer was found [14] to consist primarily of a blend of phenol formaldehyde and chlorinated isoprene, and includes titanium dioxide and zinc compounds as additives,

and carbon black as a filler. The adhesive is based on allylically brominated poly-2,3-dichloro-1,4-butadiene containing 10-27 percent bromine.

The surface preparation of the substrates involved vapor degreasing with trichloroethane before and after grit-blasting with 40 grade steel grits at 275 kPa. A thin coat of metal primer was applied with a brush within 30 minutes of degreasing and two coats of adhesive followed after the primer had dried. Following the adhesive application, the substrates were placed in a mold where pre-cut sheets of uncured neoprene were laid. Bonding and vulcanizing processes were performed simultaneously. The cure cycle involved a combination of temperature of 154 – 157° C and pressure for 50 minutes. A post cure cycle at 177° C for about 3 hours followed.

The bonded specimens were conditioned in Nalgene water tanks and the temperature was regulated with submergible heaters. The specimens were placed in the electrolyte, becoming the working electrode of an electrochemical cell, with a graphite counter electrode and a standard calomel reference electrode also immersed in the solution. An HP model 6214B power supply was used to provide the desired voltage which was checked and adjusted occasionally. To provide the needed oxygen, room air was pumped into the bath after passing through a carbon dioxide trap that consisted of a flask of a concentrated NaOH solution and another flask containing $\text{Ca}(\text{OH})_2$ solution serving as an indicator. It was found that, if CO_2 was not removed, problems were encountered because the electrolyte bulk solution turned acidic due to the generation of carbonic acid, resulting in slower debond rates.

In addition to the free-standing primer films, three types of adhesively bonded configurations were used throughout this study in order to provide complementary information concerning the various forms of debond and their associated rates. These specimens were namely the durability specimen, DS, the bonded diffusion specimen, BDS, and the strip blister specimen, SBS.

3.3.1 Durability Specimens

A bonded specimen was designed to capture the major features of the actual assembly of interest. The durability specimen (DS) is shown in Figure 16 and has evolved with geometrically attractive features. The specimen allows for both dry (creep and relaxation of rubber) and wet (durability of bond) testing. Results from the dry tests were used to determine some mechanical properties of the rubber, i.e. shear modulus, and were reported elsewhere [27]. The rubber can be strained in shear at different levels by introducing plastic shims of known thickness into the open slot between the adherends as shown and the specimens were tested loaded and exposed to cathodic activity. Such self-loading specimens are very convenient, especially when environmentally exposed. Because the steel is so much stiffer than the elastomer, the joint is essentially a thick adherend joint, giving a relatively uniform shear stress throughout.

3.3.2 Neat Film Specimens

Neat film samples of the primer were prepared to determine the extent of bulk degradation after exposure to the alkali. Some difficulties were encountered in trying to fabricate neat films of primer due to the high solvent content. Nonetheless, a technique was developed for casting films of the primer on Teflon coated fiber glass peel cloth as used in the production of laminated composites. The cloth had enough flexibility that

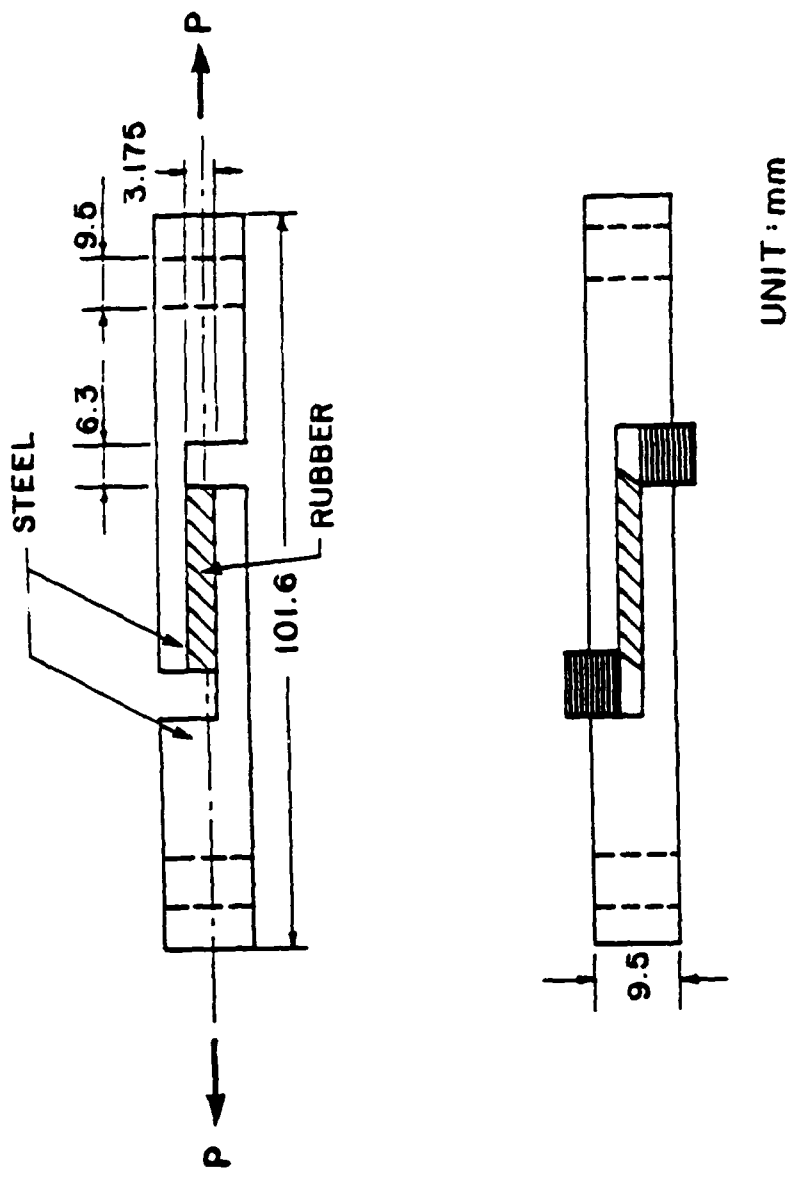


Figure 16. Schematic of the Durability Specimen (DS).

it could contract with the primer and did not produce much cracking of the film. The samples were then cured at 157°C and 275 kPa. The resulting coupons had an average thickness of about 1.6 mm and testing was done in several environments at 33°C.

3.3.3 Bonded Diffusion Specimens

The bonded diffusion specimens (BDS) were developed to measure the rate of bond deterioration in the absence of externally applied stresses. In fabricating the BDS, two 6.35 mm thick neoprene layers were bonded to both sides of 1.6 X 25 X 72 mm pieces of steel that served as substrates as shown in Figure 1. The bonding procedure followed the same cycle used for other geometries as described above.

3.3.4 Strip Blister Specimens

The strip blister specimens (SBS) were developed at the University of Texas-Austin [38] to measure debonding in the presence of an applied strain energy release rate. The SBS consists of a 152 X 25 X 1.6 mm steel substrate bonded to rubber strips of various thicknesses (6.35 mm in this paper) on both sides as shown in Figure 17. The SBS was fabricated following the same procedure as the BDS. An artificial debond in the center of the strip was introduced into which a dowel could be

inserted. Measurements were taken, using a specially sharpened calipers, along the four delaminated fronts : B,C,D, and E as marked in Figure 17.

3.4 RESULTS AND DISCUSSION

An initial effort was made to try to understand the nature of the failure regions within the degraded bond. It was observed that upon fracturing the durability specimens after cathodic conditioning, failure had occurred in two distinctive regions (see Figure 18). The boundary of the weakened front was defined by a distinctive "window" that separated the interfacial external zone from the cohesive, i.e. rubber, internal zone. The interfacial weakened region is indicative of bond degradation. Although the bond appeared intact prior to applying the additional load required to achieve separation, weakening could be detected after the bond is separated. Residual strength of the weakened region was sufficient to maintain a bond even under shear strains of nearly 100 percent. This residual strength could be partially due to mechanical interlocking at the interface. The critical strain energy release rate, G_{lc} , for the weakened region has been found to be in the neighborhood of 17 joules/m². It is interesting to note that rubber pull-out ligaments were observed (Fig. 19) on the metal surface after fracture of the weakened region and appear to coincide with the tops of grit blast craters. The larger the number of these ligaments, it seems, the higher the residual strength of the joint.

Figure 20 shows the effect of exposure under different conditions on shear strength of the durability specimen. Examination of the figure reveals that no

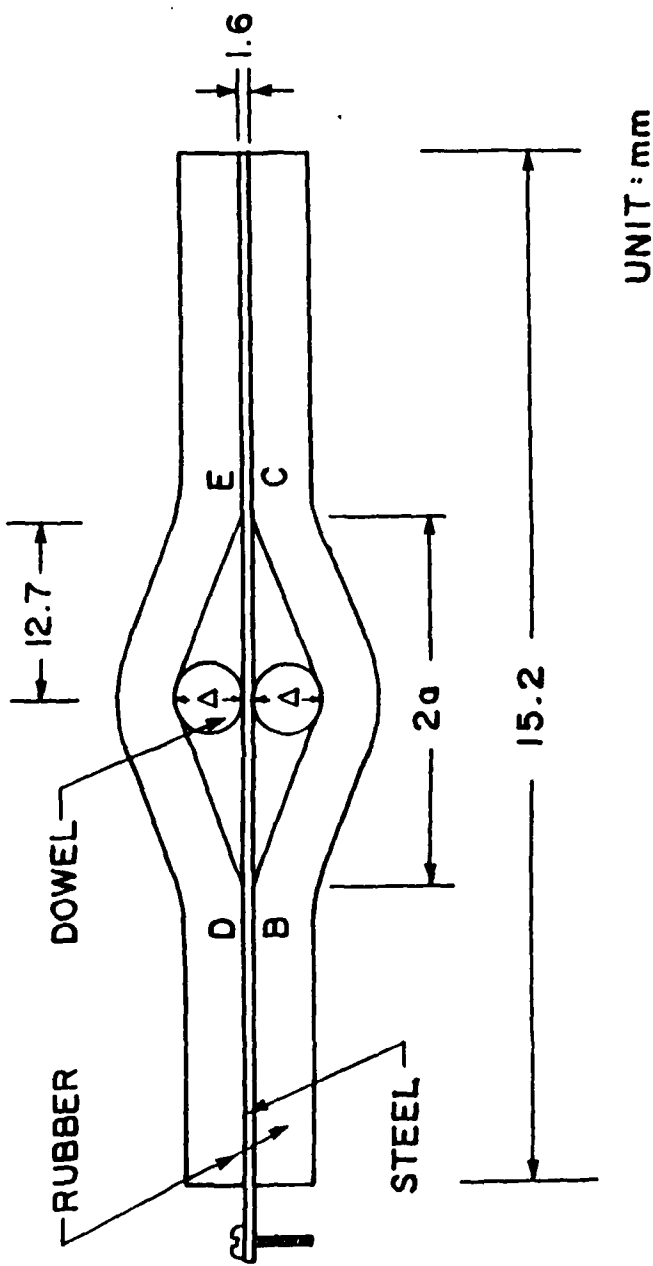


Figure 17. The Strip Blister Specimen (SBS); Note the Self Loading Capacity.



Specimens exposed to ASW, 60° C, -1.02 V, 0.1" disp.

G-1	G-7	G-4	G-10
8 days	14 days	20 days	43 days
870 lb	250 lb	250 lb	20 lb

Figure 18. A Photograph Showing the Interfacial (External) Failure Zone and the Cohesive Zone in the DS as a Function of Exposure Time.

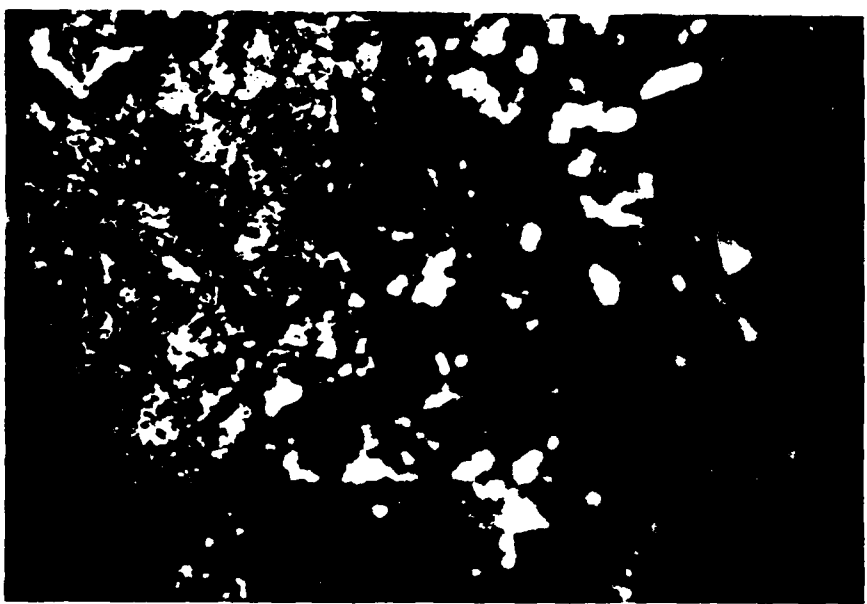


Figure 19. A Photograph Showing the Rubber Legaments on the Steel side of the Failure Surface.

degradation (strength decay) was observed when the bonded durability specimens were conditioned in ASW without cathodic activity for several months. On the other hand, the bond lost about 50 percent of its strength after 60 days of exposure to -1.02V (SCE) at 40°C in ASW and almost 100 percent after 45 days at 60°C at the same cathodic voltage and environment. Upon drying the specimens at 90°C under vacuum, the bond strength seemed to improve substantially. The improvement occurred in the weakened region where more traces of rubber pull-out ligaments were observed in that region than in those specimens that were fractured while wet. Drying of the interfacial components may have resulted in a dryer and stiffer adhesive layer, thus producing greater mechanical interlocking. It is also possible that some bonds may have re-formed after drying, although in light of the severe chemical degradation involved, this seems unlikely.

Because the integrity of the bulk adhesive (primer and topcoat) component of the joint may play a major role in the overall durability of the adhesive bond, the study of neat free-standing film coupons was conducted to answer questions about the bulk adhesive environmental stability when exposed to harsh conditions. Furthermore, the adhesively bonded specimens mentioned above were also used to study the environmental effects on the weak bond propagation rates (WBPR) and the delaminated bond propagation rates (DBPR).

We must mention that the difference between the weakened and the delaminated bonds is that the latter indicates actual separation of the rubber from the substrate, due to an applied load, *after* being weakened. Therefore, weakening data was collected from the BDS while the SBS provided delamination data. Thus, the two specimens play complementary roles in providing both stress-free and loaded bond degradation data. The expression "debond" has been used in this study to include any form of degraded bond whether weakened or delaminated. The total debond distance, z , was assumed to be the algebraic sum of z_1 and z_2 as illustrated in Fig. 21.

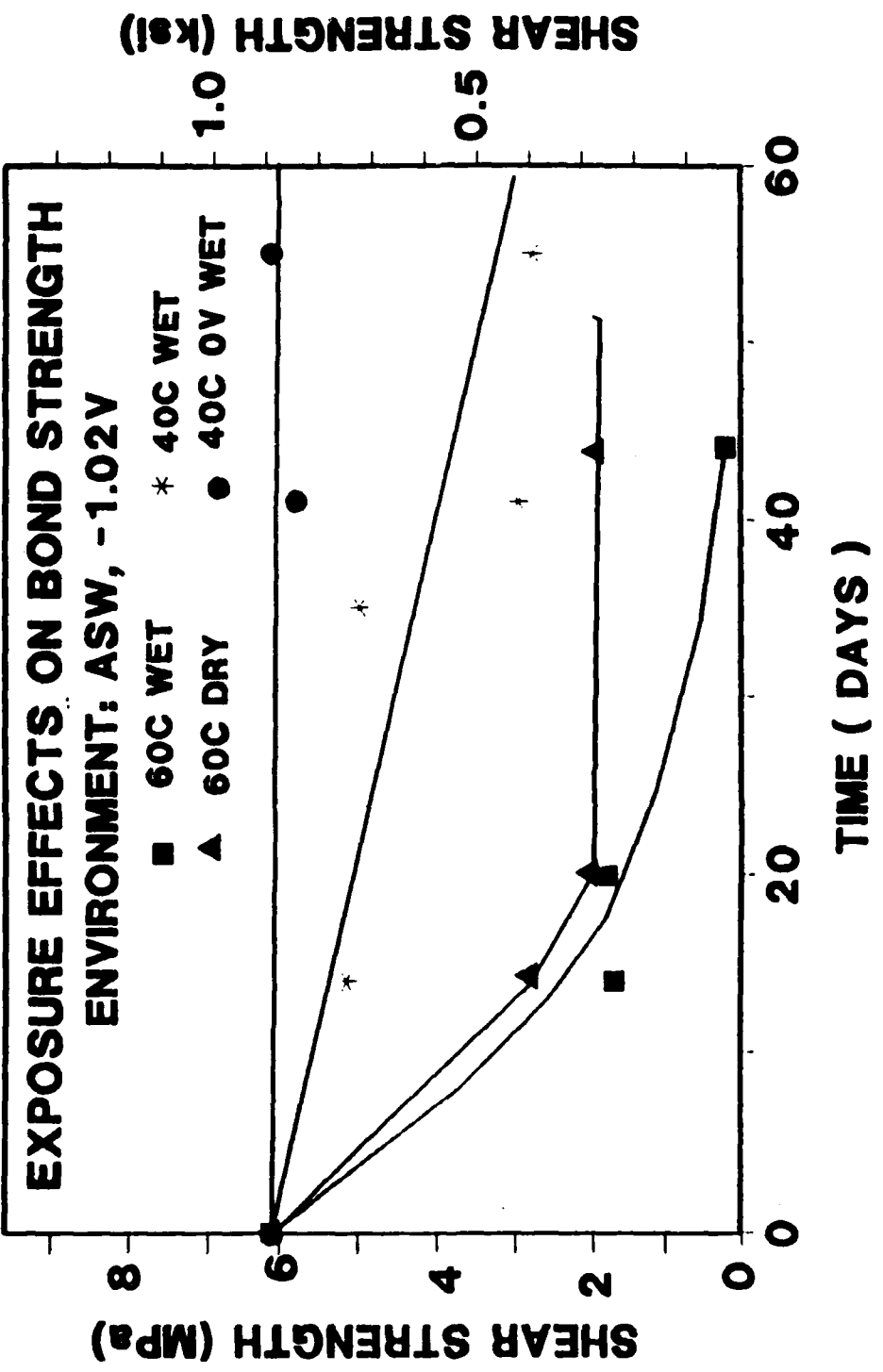


Figure 20. Strength Decay of the DS, Control System A, as a Function of Exposure Time.

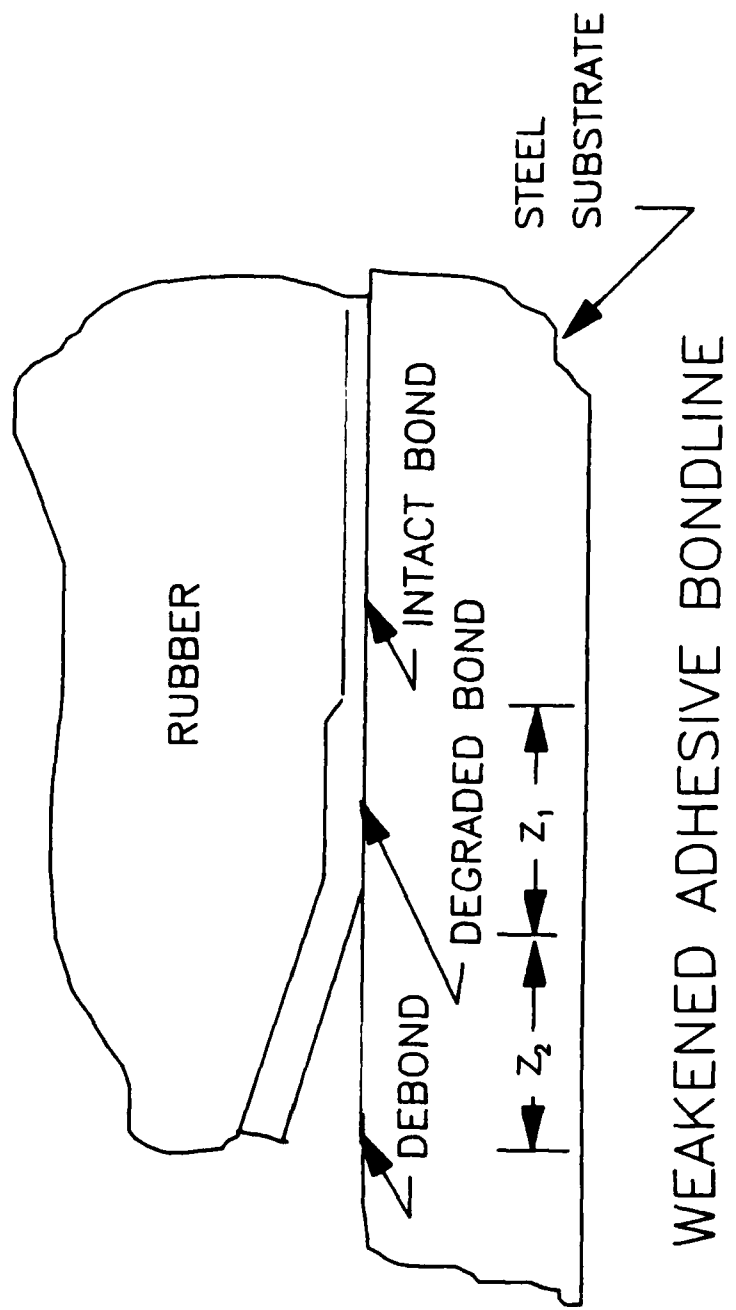


Figure 21. A Schematic Illustrating the Weakening and Delamination Modes.

Ways to improve the durability of the control adhesive system were also taken into consideration. Zinc phosphate coated steel substrates, for example, were investigated in an attempt to minimize the electrochemical activity of the metal surface. If the oxide role as a catalyst for the electrochemical reaction(s) can be removed or suppressed by a surface coating, then the contribution of the other available species needed for hydroxyl generation, namely water, oxygen, electrons, and cations, becomes somehow limited. In a separate series of tests, a silane coupling agent, γ - amino propyltrimethoxy silane (Union Carbide A-1100), was blended with the primer in several concentrations. Free films and several SBS's were fabricated and tested using the modified primer.

The following discussion deals with test results from the neat film and the bonded diffusion specimens in addition to some preliminary work on the strip blister specimen.

3.4.1 Mass Uptake Studies

Coupon films of control neat primer A were used to better understand the diffusion mechanisms involved. Both Fickian-like diffusion and chemical reaction are, generally, two possible mechanisms by which moisture and other species intrude into polymers. Results for these specimens were given in Figure 6 and clearly indicate the significant effect that hydroxide has on the primer. The effect of chemical degradation is shown clearly to be a result of OH^- concentration (environmental harshness). Note that the actual data in Figure 6 was collected much more frequently than indicated in the figure and that the data points on the graphs serve only as identifying markers. We

need to emphasize the fact that the uptake curves for high NaOH concentrations are very linear. In artificial seawater (ASW), the net weight gain at saturation is only about 2 percent; whereas in concentrated NaOH it approaches 50 percent. The rate of net weight gain decreases for lower concentrations of bulk alkali and may result in saturation net weight gains which are below that of high concentrations (3,10N).

The desorption data were collected in a convection oven maintained at the same temperature as the absorption process. The weight loss occurs much more rapidly than the original weight gain. When the re-dried specimens were placed back in their respective environments, the net weight gain occurred very rapidly. Apparently, the severe degradation of the primer has resulted in a permanent "sponge-like" structure that allowed the moisture to diffuse in and out very rapidly. It should be noted that the saturation levels following the second exposure to environment are essentially the same level as before drying, suggesting a characteristic damage state. The desorption in the specimen soaked in 10N NaOH shows a very slow rate which could be related to the accumulation of non-dissociated NaOH deposits in the bulk resin.

Leaching of some components in the adhesive has been shown [26] to occur in the primer following exposure to the alkali. Similarly, the net weight gain study shows that the resin has lost some of its original weight after absorption and subsequent drying which substantiates the leaching mechanism. It should be noted that the "net" expression refers to the total algebraic difference of the intruding species and the leached material. Figure 22 presents the percentage of mass change of a neat film specimen conditioned in 1N NaOH, dried, and then exposed to de-ionized water (DIW), and finally re-dried again. The mass uptake in the specimen in DIW was quite fast, but the equilibrium level was less than would have been achieved in the original alkaline bath. Upon re-drying, a very large amount of mass was lost, suggesting that perhaps NaOH within the specimen had leached out. One might speculate that a substantial amount

of the specimen may have leached out during the first exposure, only to be replaced by NaOH, thus resulting in a very small mass change between the original sample mass and the mass of the redried samples in Figure 6. The net weight gain data from Fig. 6 were replotted against the square root of time and showed that the intrusion is far from obeying Fick's law. Our belief is that the intrusion in the neat film samples is occurring as a front and that the net weight gain is not diffusion controlled, but rather is limited by the rate at which the polymer hydrolyzes. Such process is often referred to as Case II diffusion. One may suspect that as the front propagates and the distances for species diffusion increase, diffusion will be the limiting mechanism rather than chemical reaction as will be seen in the following discussion.

3.4.2 Accelerating Parameters

A weakened region, similar to the one reported above, was observed in the bonded diffusion specimens exposed to cathodic current in ASW or to the alkali even without applied current. On the other hand, no weakening was observed in these specimens after exposure to ASW without cathodic action for an extended period. A large number of BDS specimens were conditioned in their respective environments. Periodically, one was removed from the bath and pulled apart to measure the weakened distance (z_1). When plotted against the square root of time (Figures 23-26), the excellent fit suggests a Fickian process. The data shows a remarkable sensitivity to almost any change of parameters. The two parameters that were noticed to be most detrimental were the current and the bath temperature. Figure 23 compares the

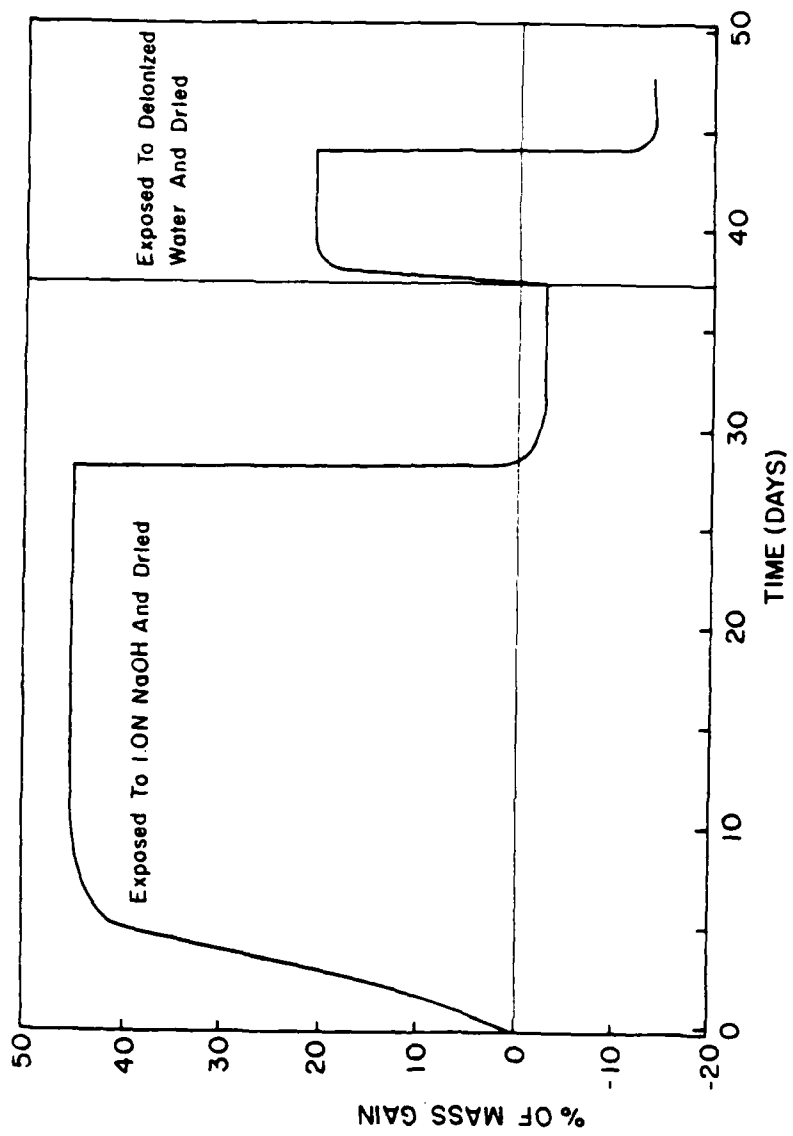


Figure 22. Absorption in 1N NaOH solution, drying, DIW exposure, and re-drying Neat film of Primer A.

weakened bond propagation rate (WBPR) for various concentrations of NaOH aqueous solutions with and without applied cathodic voltage. The propagation rate for the cathodically active specimens is about four times that of their counterparts in a voltage-free bath. It is worth noting that a line has been drawn through the origin which may, or may not, be realistic. An interesting conclusion can be drawn from Figure 24 which shows that at relatively high potentials, (-1.4 V), the nature and concentration of the environment play only a minor role in the WBPR. Presumably, at such high potential levels, the hydroxide ions are predominantly supplied by the cathodic current rather than the bath. Again excellent agreement for the square root of time dependence is seen.

Temperature also plays a significant role in the WBPR as is illustrated in Figure 25. Although the data is insufficiently little for the low temperature, this figure suggests that in a 1N NaOH environment with -1.4 V (SCE) potential, the WBPR at 2° C may be less than half that at 30° C. Again the data was connected through the origin. Results for ASW with -1.0V (SCE) potential at 30° C and 60° C are also shown. For these cases the presence of a "delay" or "incubation" period could be seen although the data is somewhat scattered. For the high temperature, the incubation period is about one day and increases to seven days for the lower temperature. It should be noticed that in ASW at higher voltages or in NaOH baths incubation periods appear to vanish and the effect of temperature seems to translate as an increase in the WBPR. Stevenson [7] reported the existence of such a delay time and has shown that it increases as the applied cathodic voltage decreases. The probable explanation is that in the relatively mild seawater environment the moisture and oxygen and the other species diffuse slowly through the primer and/or topcoat to the interface. The completion of the cathodic circuit increases the pH at the interface thus setting the interfacial debond mechanism in motion. Another explanation could be that the iron oxide next to the exposed edge

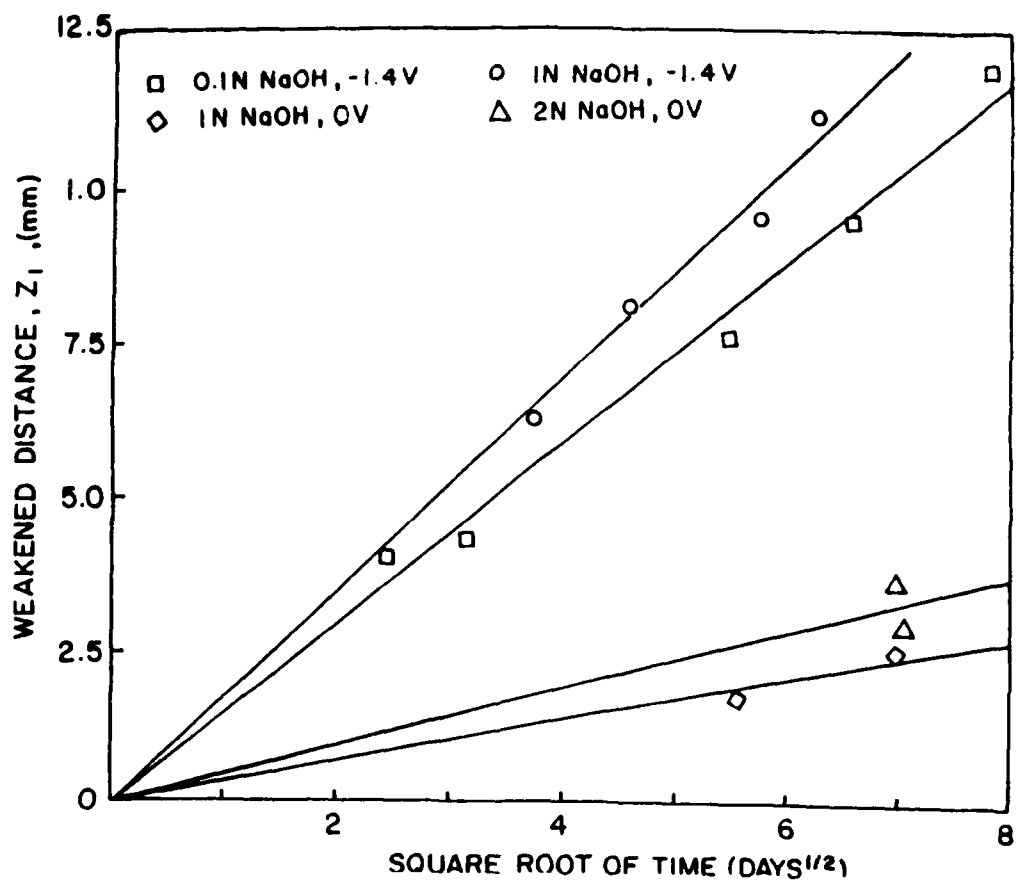


Figure 23. WBPR for various concentrations of NaOH solutions with and without potential.

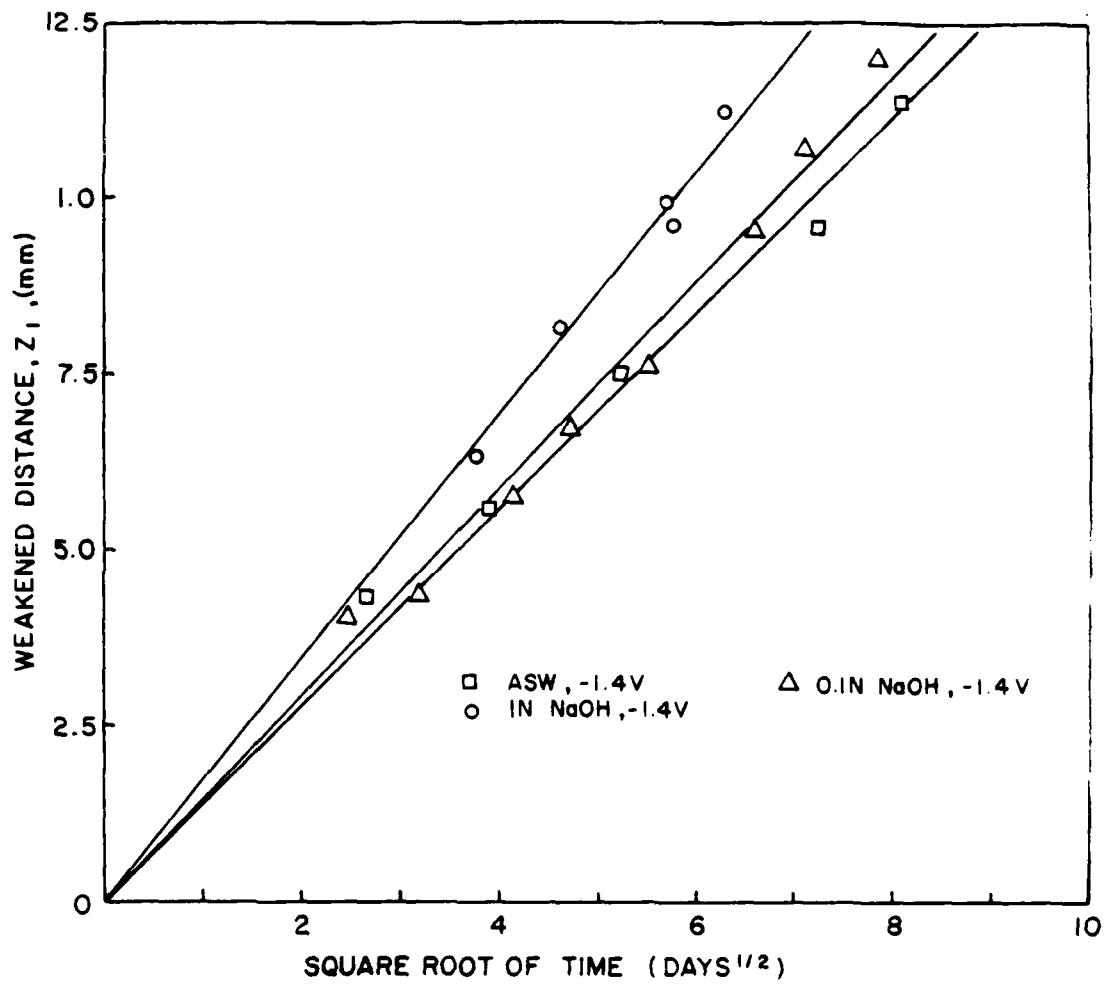


Figure 24. Potential effects on the WBPR in different environments.

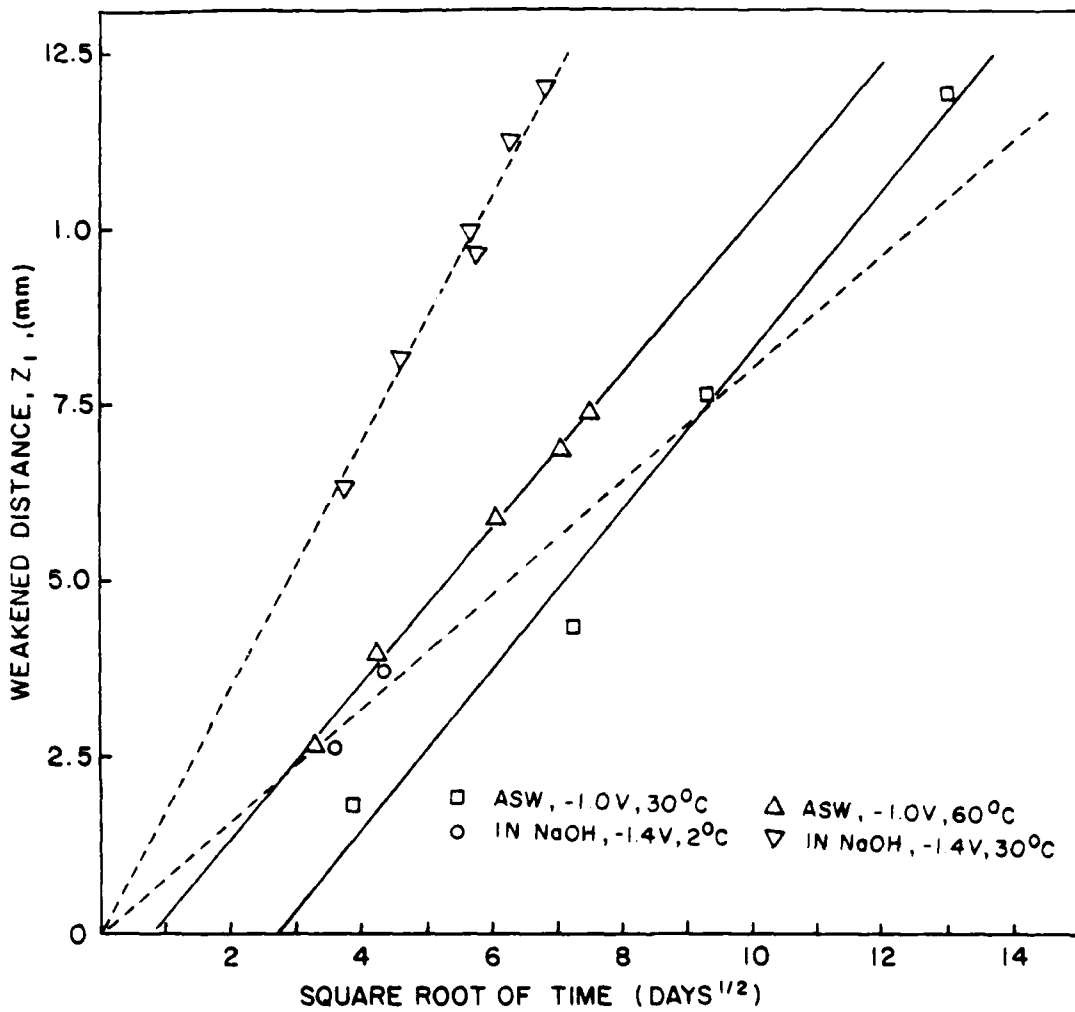


Figure 25. Temperature effects on the WBPR.

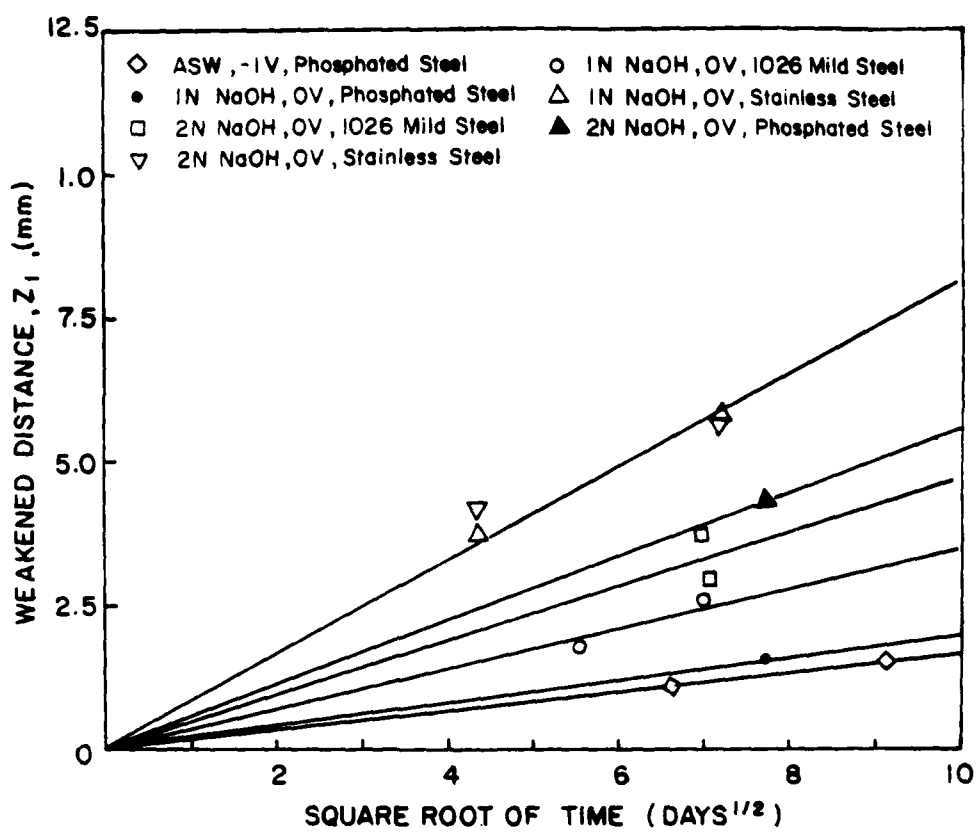


Figure 26. Substrate effects on the WBPR.

is being reduced. Watts and Castle [4] used XPS on a cathodically delaminated epoxy coated mil' steel and reported seeing a metallic iron component along with the more usual iron (III) in the outermost debonded region. That may indicate an initial reduction of the oxide after which the locus of failure moved to the oxide/polymer interface.

Other tests were carried out using BDS of zinc phosphate coated steel and stainless steel substrates as well as AISI-1026 mild steel with and without potential. Figure 26 illustrates the WBPR for those specimens. Surprisingly, stainless steel has the highest WBPR in concentrated NaOH. Phosphated specimens in 1N NaOH appear to be slightly better than the untreated ANSI 1026, but are perhaps worse in 2N NaOH. It has been speculated that the zinc phosphate is soluble in high pH and may be dissolving out from under the coating when placed in the higher pH. Interestingly, in ASW with -1.0V (SCE) of potential, the WBPR appears to be appreciably lower for phosphated specimens than for untreated specimens. The purpose of phosphatizing is to create a surface which is not catalytically active to the cathodic reaction. Indeed it may be effectively serving in this capacity when used in ASW at lower voltages. Table 1 summarizes the results from the above figures concerning the BDS.

WBPRs were clearly affected by any one or a combination of the accelerating parameters mentioned above. Obviously, if degradation was the culprit then one may suspect that the chemical reaction rate is concentration and temperature-dependent. The increase in potential means an increase in current which, eventually, will raise the pH. It is worth mentioning that an experiment was carried out on the BDS in a sealed electrochemical cell in which nitrogen gas was injected continuously thus purging the oxygen from the solution. The specimens were conditioned for 11 days in ASW at 30° C with -0.9V (SCE) after which no weakening was observed. The current density was insignificant, due to lack of oxygen; therefore, no appreciable amount of hydroxyl ions

Table 1. Weakened Bond Propagation Rate (WBPR); Control Adhesive System

Substrate	Solution	Temp. °C	Voltage, mV	WBPR × 10 ⁻³ mm/s ^{1/2}
AISI 1026	ASW	30	-1400	5.0
AISI 1026	ASW	30	-1000	3.8
AISI 1026	ASW	30	-670	2.6
AISI 1026	ASW	60	-1000	3.8
AISI 1026	0.1N NaOH	30	-1400	5.2
AISI 1026	1N NaOH	30	-1400	6.4
AISI 1026	1N NaOH	2	-1400	2.8
AISI 1026	1N NaOH	30	0	1.2
AISI 1026	2N NaOH	30	0	1.6
Phosphate Coated	1N NaOH	30	0	0.7
Phosphate Coated	2N NaOH	30	0	1.9
Phosphate Coated	ASW	30	-1020	0.6
Stainless Steel	1N NaOH	30	0	2.7
Stainless Steel	2N NaOH	30	0	2.7

was generated and the bond remained intact. This is compared with about 0.5mm of debond after exposure to ASW with -0.9 V (SCE) while dissolved oxygen is available. This illustrates that several apparently different environment factors are indeed interrelated. It is believed that the current density corresponding to a given voltage in a particular solution is very sensitive to any change in the surrounding conditions. A decrease in oxygen concentration in the bulk electrolyte, for example, could impair the mass transfer of that species to the cathode\electrolyte interface thus reducing the current density. The adaptation of a current density approach, rather than voltage, allows someone to evaluate the importance of several accelerating parameters as a function of their contribution to current generation. Due to the problems associated with monitoring current in durings times of increasing cathodic area and increasing passivation, however, voltage is used throughout the paper to express the potential with respect to SCE.

3.4.3 Stress Effects

Testing of the strip blister specimens (SBS) serves the purpose of identifying the effects, if any, of tensile stresses on a bonded joint. The complexity of bonding rubber to metal may result in variation of the debond rates; therefore, an initial attempt was made on a batch of four SBSs to determine the extent of data scatter and check the reproducibility between specimens. For that reason, testing was performed in two stages at two different voltages to eliminate discrepancies resulting from different bonding conditions. The tests were conducted in ASW and 1N NaOH environments for

approximately 80 days before the higher voltages were applied for 80-100 more days. The weakened zone ahead of the delaminated front, after the first stage, was pulled open by hand and the second phase of testing followed.

The delamination data for the control system in ASW and in 1M NaOH are presented in Figures 27 and 28 and show a considerable amount of scatter. The error bars show typical data spread for the four debond fronts B, C, D, and E (Fig. 17). The delaminated bond propagation rate for these loaded specimens was found to exceed that of the stress-free WBPR (under similar conditions) and to be initially constant but tends to decrease as delamination proceeds. Liechti [39] has shown that the applied strain energy release rate for the SBS decays rapidly with increasing z_2 . Delamination rates were higher in the NaOH environment than in ASW. Examining the above figures also shows that the weakened zone ahead of the crack tip was much more pronounced when ASW served as the conditioning solution. This could be inferred from both figures judging by the manually separated weakened distance just prior to voltage increase at about the 80 day mark in both figures. One possible explanation is that the concentration of the hydroxyl is, inherently, so much higher in the NaOH environment that the weakening process is faster than with ASW. One can picture the total debond distance as the product of the weak boundary layer and applied G. The strength of the interface itself is environment and exposure time dependent. Naturally, the harsher the environment and the higher the stress the smaller the ratio of the weakened zone with respect to the delaminated zone.

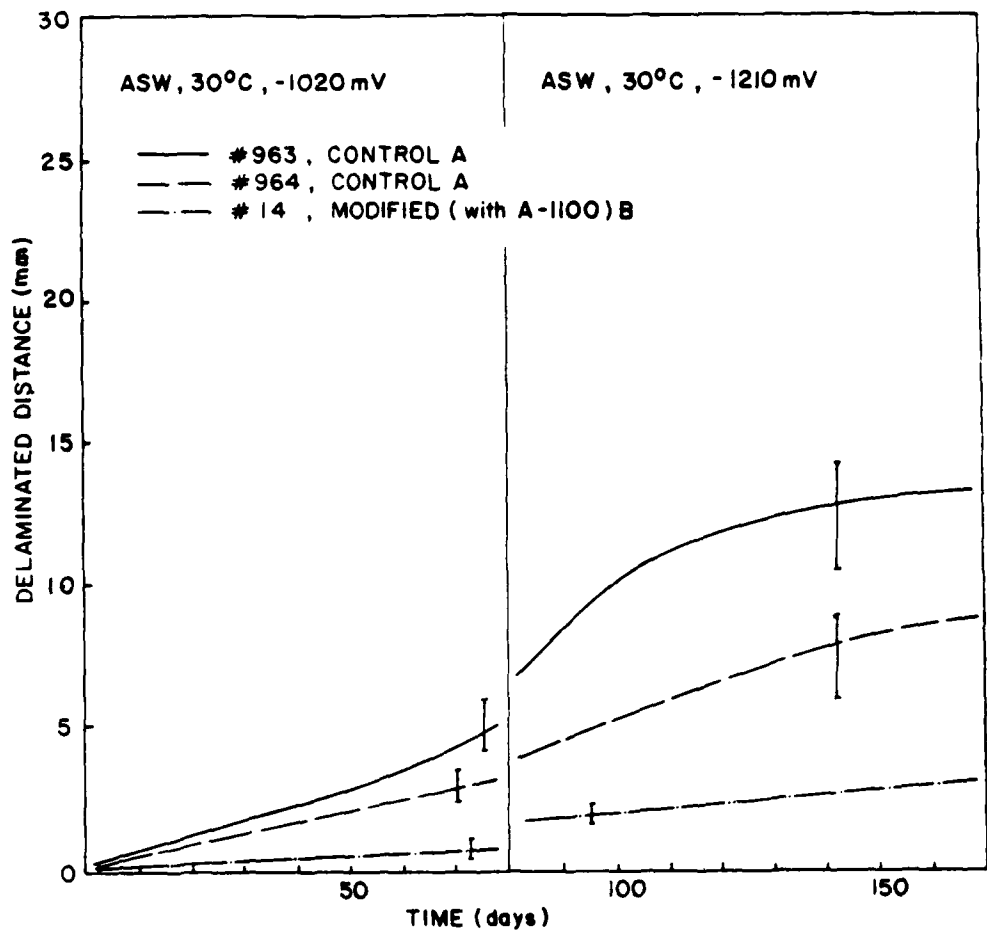


Figure 27. Delamination Distances Plotted vs. Time for the SBS in ASW, 30 C, at -1020 mV and -1210 mV (SCE); Control A System.

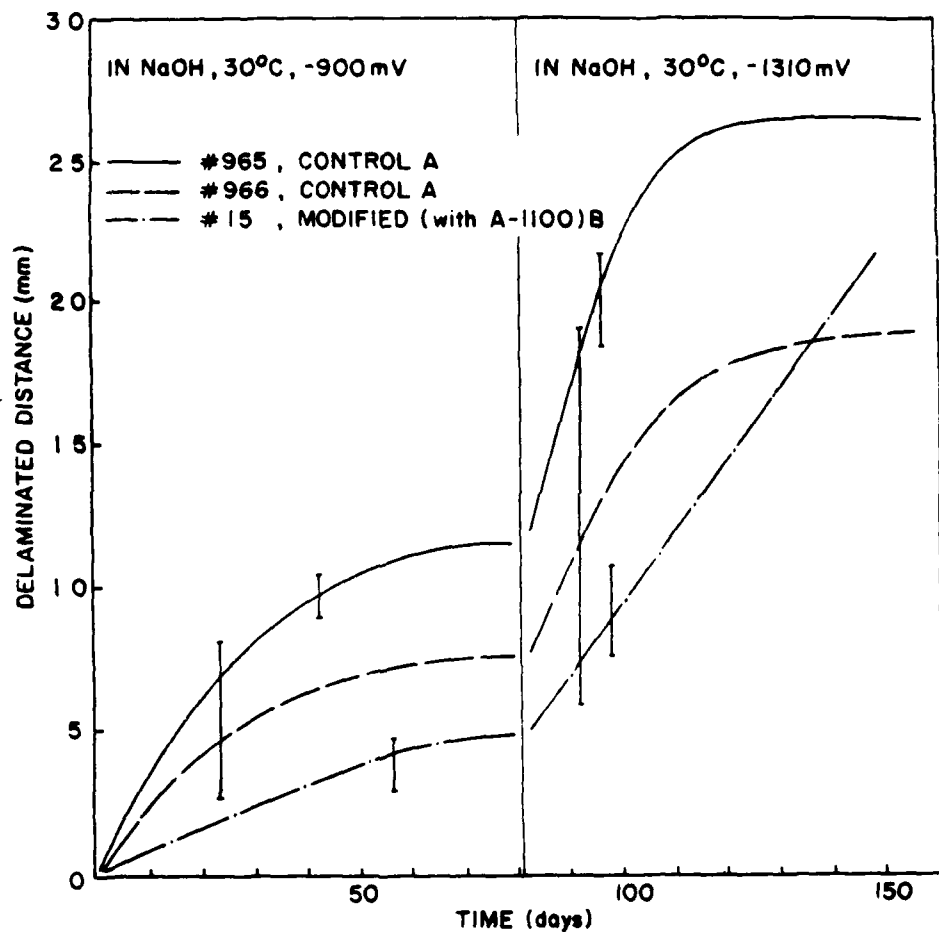


Figure 28. Delamination Distances Plotted vs. Time for the SBS in 1N NaOH, 30 C, at -900 mV and -1310 mV (SCE); Control A System.

3.4.4 Silane Effects On Durability

The enhancement of bond durability due to the addition of A-1100 silane coupling agent is clearly demonstrated in Figures 27 and 28. Although scatter is significant in control A specimens, the use of silane seem to have resulted in lower DBPR's: about three fold improvement in ASW at -1.02 V and two fold in 1N NaOH at -0.9 V. The durability improvement was quite noticeable at higher voltages in ASW, although it seems to disappear at higher cathodic potentials (-1.31 V) in NaOH. This behavior could be explained by a possible different debonding mechanism at those higher voltages.

The considerably reduced DBPR's may suggest an improved environmental durability at the crucial interface and, perhaps, a decrease in the bulk hydrophylicity thus resulting in lower diffusion coefficients. A number of silane-modified SBS's were fabricated and tested in 1M NaOH at -1.2V (SCE) and 30° C. The study involved several concentrations of A-1100 and aimed at quantifying the effect of that modification on delamination rates. Figure 29 shows an interesting decreasing trend for the DBPR's (representing the initial linear region) as a function of increasing silane concentration. A considerable improvement in durability occurred after the addition of 0.5 percent A-1100 (weight/weight of primer and solvent). DBPR has improved by 10 fold as a result of addition of a fairly high percentage (8 percent) of silane.

The unusually high percentage of A-1100 reported above prompted another round of mass uptake studies. This time, the primer was mixed with 0, 0.5, 2.0, 5.0, and 8.0 percent silane by weight (same as in DBPR study above) and thin free films were fabricated similar to those reported in section 3.3. Testing was conducted in a 1M NaOH solution at 42° C. in a fashion similar to that reported above. The results are

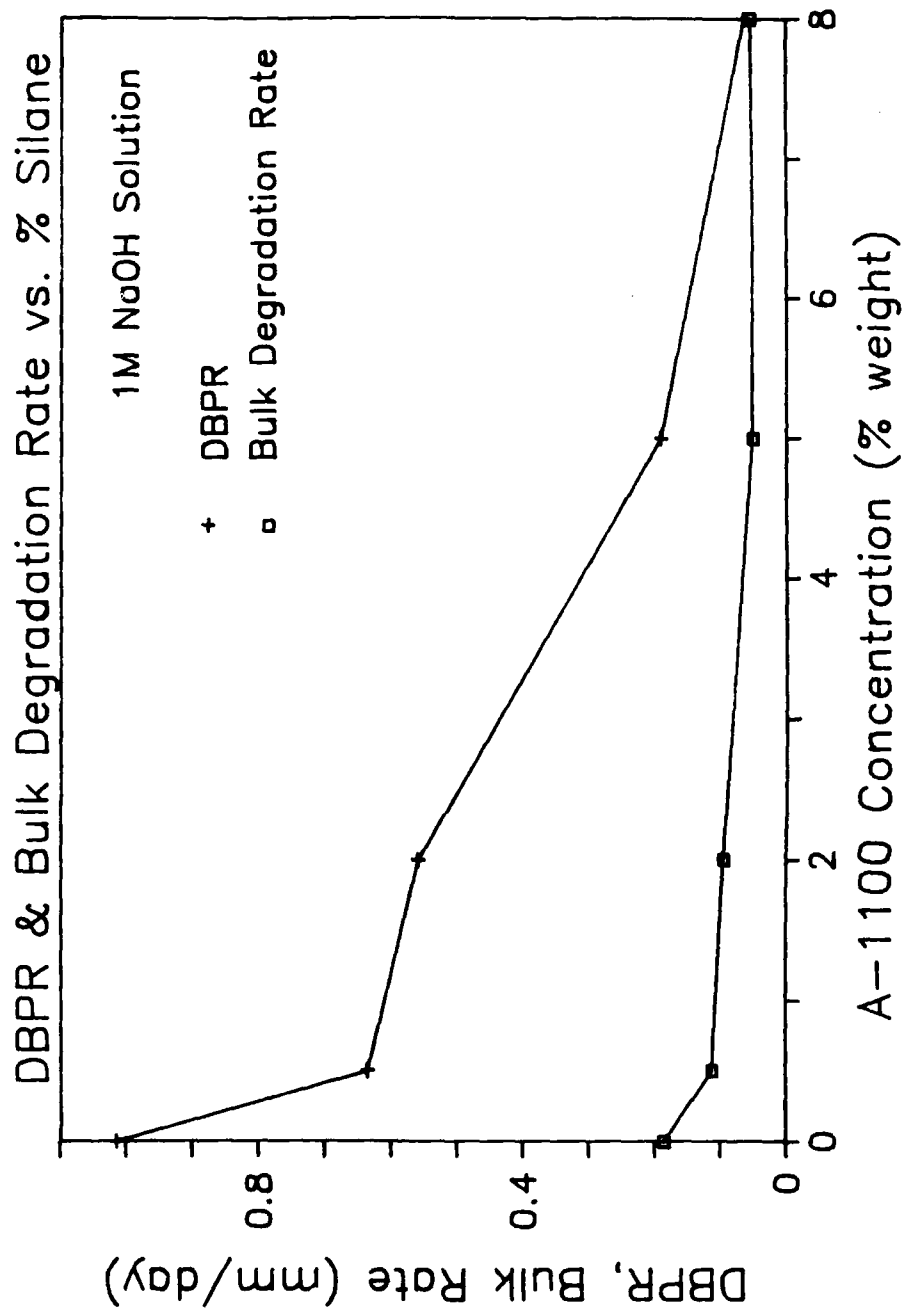


Figure 29. Silane Effects on Bulk Chemical Reaction rates and on the DBPR.

shown in Figure 30 and indicate that the saturation levels decreased as a function of increased silane concentration. Linear rates (mm/day) were determined based on the slopes (/day), saturation levels (mg/mg), and specimen thickness (mm) for every case. The degradation chemical reaction in the bulk primer was characterized, again, by a linear rate. The rates for different silane concentrations were plotted in Figure 29 and clearly illustrate the reduced bulk degradation. A large improvement occurred with 0.5 percent silane to primer ratio. A decrease of about 60 percent in saturation level was observed when 8 percent silane was added after which no further improvement was observed.

3.5 INSIGHTS INTO THE DEBONDING PROCESS

The results of the study on the neat film samples reinforce the idea that the adhesive itself is being attacked chemically. It remains to be seen in the course of this study if any correlations can be drawn between the way the bulk specimens performed and that of actual bond durability of various systems. The fashion by which the moisture intruded and the unusually high percentage of weight and volume changes in the coupons is a clear indication of chemical changes in the resin itself. The decrease in the net uptake rate and the saturation level after addition of silane suggests that some unstable linkages in the primer are being stabilized. The overall chemical resistance is improved as a result.

The primer next to the oxide layer in an actual bond is susceptible to degradation in a manner similar to that of the bulk resin in alkali. The actual concentration of the

MASS UPTAKE VS. A-1100 (BY WEIGHT)
PRIMER A FREE FILM, 1N NAOH, 42 C

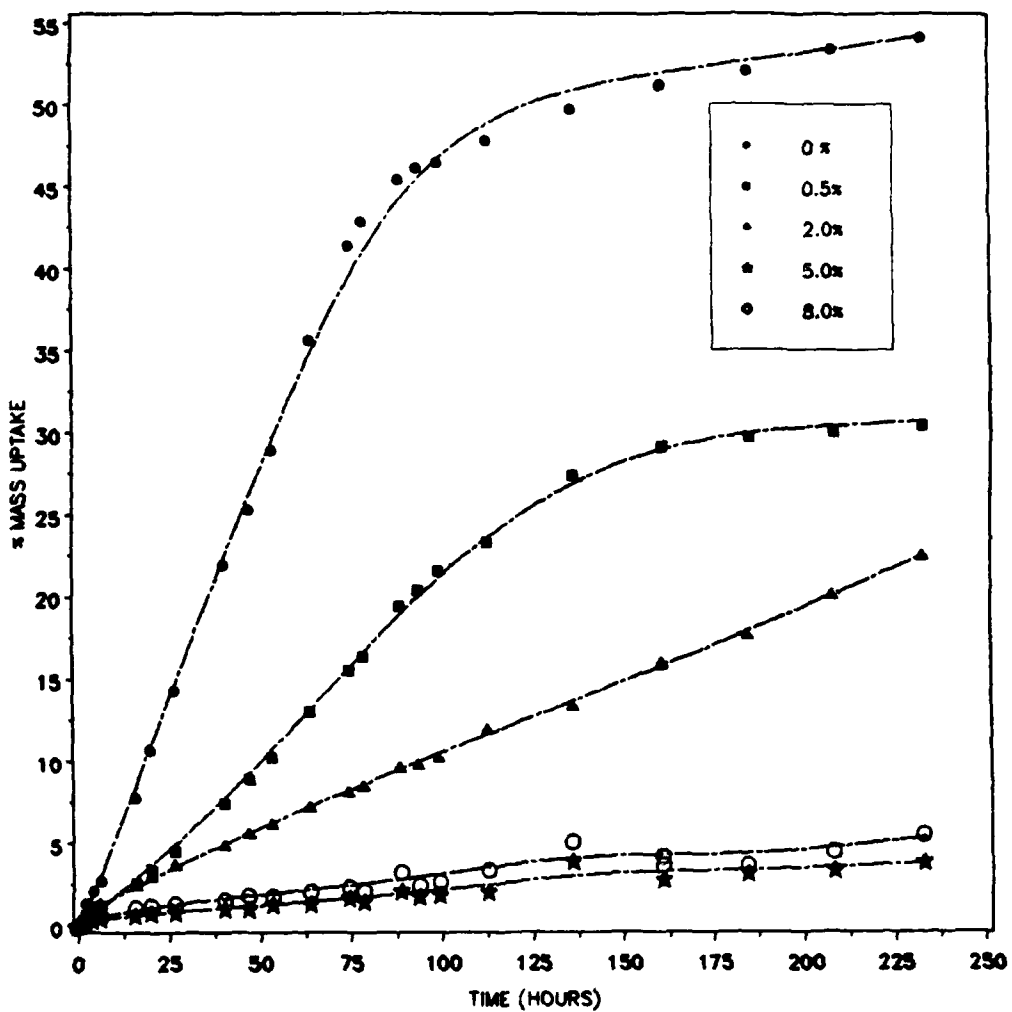


Figure 30. Mass Uptake Results for the Silane-Modified-Primer.

OH^- at the interface (crack tip) is believed to be high enough that the degraded portion of the adhesive layer in the bond resembles that of the bulk after conditioning in alkali [26]. That weakened distance, z_1 , which is occupied by degraded adhesive acts as a diffusion path for moisture and other species needed for the electrochemical reaction at the tip where the bond is being degraded.

The data from a non-opened stress-free BDS is substantially different from data collected recently from the loaded SBS. The loaded strip blister results tend to suggest that the debonding rates are faster and are moderately affected by applied G within the range of acquired data. While other mechanisms are also present, it appears that the dominant mechanism is associated with changing the boundary conditions of the diffusion process. A comparison of the intrusion (debond) front from neat film coupons, BDS, and SBS is presented in Figure 31. The initial intrusion rates for the free films and the bonded specimens without voltage are comparable. In the presence of more aggressive environments, applied stress, or impressed potential the weakening and delamination rates increase dramatically. The joint, obviously, delaminates the fastest when several of the accelerating parameters act simultaneously.

Comparing the BDS and SBS data at -1.4 V, the WBBR and DBPR are almost equal for very short debond distance while the latter becomes significantly larger as the debond front propagates. This is due to the relatively slow diffusion-control process that, we believe, governs weakening (BDS) at long distances. For the case of free primer film and a BDS exposed to 1M NaOH with no voltage, the similarity in initial "diffusion" rates may suggest that, perhaps, the same degradation mechanism in the bulk primer is responsible for bond weakening as well. The faster intrusion in bonded joints with potential than in the neat material could be due to several factors that accelerate the mechanism: faster diffusion along the interface (wicking), higher OH^- concentrations at the metal/adhesive interface due to confinement, an increased driving force which the

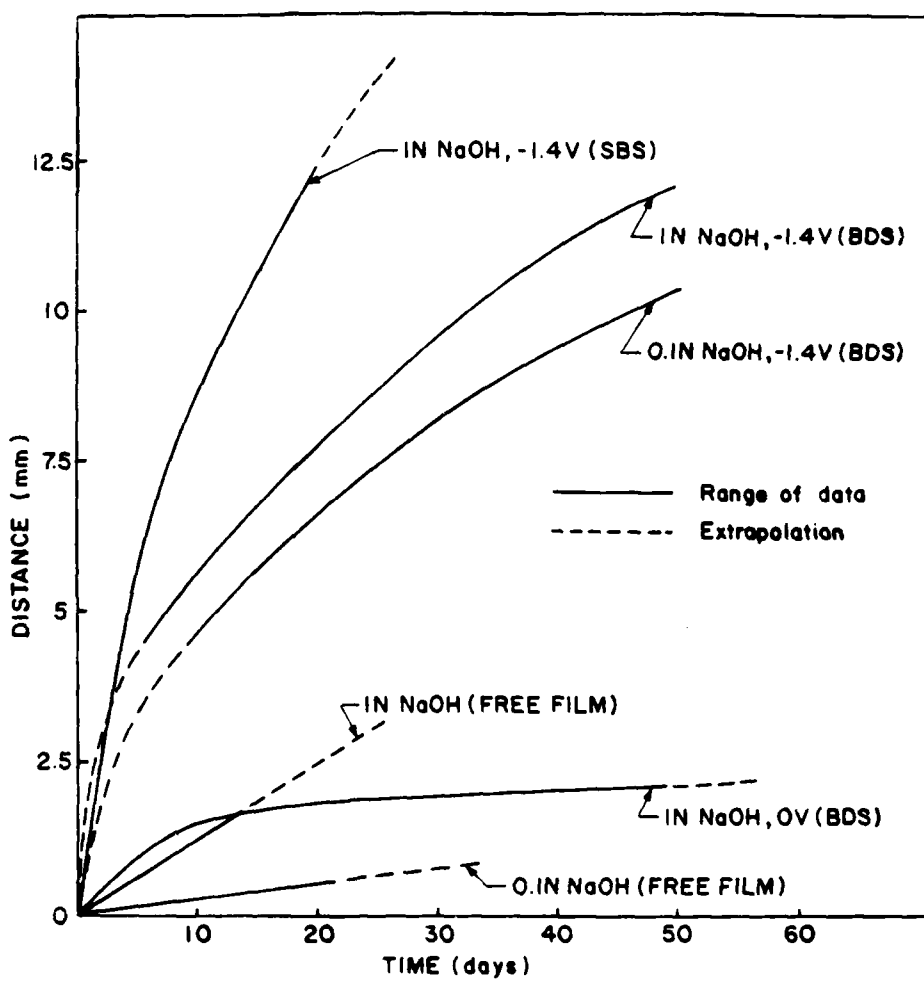


Figure 31. Comparison of the "diffusion" front in neat film, BDS, and SBS Specimens.

applied potential exerts on ions (electrophoresis), or, finally, the physical pressure added from the hydrogen gas evolution. For the stressed bonds, an additional factor to consider is bond separation which shortens the diffusion distance. The role of mass transport of moisture and other species from the mouth of the environmental crack to the tip is drastically reduced as the weakened region continuously delaminates. Tensile stresses may also contribute in a more direct fashion such as in reducing the activation energy barrier needed to break the bonds between the adhesive and the oxide, thus accelerating the degradation process.

The effect of silane coupling agents on durability is two fold: a more environmentally stable interface and a less porous, more hydroxyl resistant bulk primer. In a bonded joint under cathodic action, two parallel and, apparently, independent degradation-causing processes take place simultaneously. These are: relatively slow bulk chemical degradation reaction [26,23] and degradation of the interfacial bonds. When silane is added in moderate quantities, as shown in Figure 29, a big improvement in the DBPR is seen. The decreasing trend in the DBPR continues until large quantities (8 percent) of silane are added. Interestingly enough, the final DBPR is equivalent to that of the bulk degradation rate. Two possible explanations are: the rate of the interfacial mechanism has diminished to such a low level allowing the relatively slow bulk degradation process to take over; or that the rate of the acting interfacial mechanism has simply slowed down to a small value that is comparable with the bulk rate. However, one may need to take into consideration the slightly different temperatures at which the mass uptake and the delamination studies were carried out. The trend, nonetheless, has been established.

3.6 CONCLUSIONS

The study has revealed a number of insights into possible mechanistic interpretations for cathodic debonding of rubber to steel in marine environments, and allow us to draw the following conclusions.

- 1- The bulk degradation mechanism of the primer may be the same mechanism responsible for bond weakening. This process is hydroxyl related and is governed by a chemical-reaction-controlled mechanism for relatively short distances and by a diffusion-controlled mechanism as the front propagates longer.
- 2- The weak bond propagation rates (WBPR) is very sensitive to the accelerating parameters, i.e., temperature, applied cathodic current density.
- 3- The WBPR's are affected by substrate type (*mild steel outperformed stainless steel*), catalytic and morphological properties of the substrate (the use of zinc phosphate coated AISI-1026 steel adherends resulted in enhanced durability), and the primer (silane coupling agents seem to improve the durability at low voltages when mixed with the primer).
- 4- The existence of a "delay" time is a function of environmental harshness; temperature or voltage increase result in decreased incubation.
- 5- Delaminated bond propagation rates (DBPRs) are much larger than the WBPR's due, mainly, to a change in the boundary conditions for the weakening process.

3.7 ACKNOWLEDGMENTS

The authors wish to express their gratitude to the Office of Naval Research and the Naval Research Laboratory - Underwater Sound Reference Detachment for their support of this work. The monitors from these organizations were Dr. L. Peebles and Dr. R. Timme, respectively. We would like to thank Dr. Hal F. Brinson for his help and encouragement. We also acknowledge the suggestions and comments of Dr. Wim van Ooij, currently at the Colorado School of Mines. Thanks are due to Martin Marietta and Amchem Products for their help with phosphating. The authors would also like to acknowledge the work done by Zhiqiang Wang and Yeou Chang on mass uptake of free films.

4. WEAKENING MODE: CHARACTERISTICS AND MODELLING

4.1 INTRODUCTION

Based on many of the previous observations, a comprehensive test matrix (see Table 2) was devised in conjunction with TRI, University of Cincinnati, and The University of Texas at Austin for the purpose of collecting debond data. The completion of the test matrix has produced a wealth of weakening and delamination data covering a wide range of accelerating parameters. One feature of the experimental weakening data is that it obeys a linear relation when plotted against the square root of time. Incubation times associated with seawater environments at low cathodic voltages are also characteristic of weakening. Delamination, on the other hand, is faster and is linear in time at relatively high levels of strain energy release rates.

A comparison of typical bond weakening and delamination histories in 1M NaOH, at 25 C, with no applied potential are shown in Figure 32. Superimposed is an

Table 2. The Inter-institutional Test Matrix

Rubber thickness (mm)	Environment Temp. (° C)	#	Current Density (mA/ cm²)				
			1 0.59	2 1.0	3 1.475	4 14.75	5 73.3
3.75	ASW 25	A	a-1 b-1	a-1 b-1	a-1 b-1	a-1 b-1	a-1 b-1
3.75	ASW 40	B				a-1 b-1	
3.75	ASW 55	C				a-1 b-1	
3.75	1M NaOH 25	D	a-1 b-1	a-1 b-1	a-1 b-1	a-1 b-1	a-1 b-1
3.75	1M NaOH 40	E				a-1 b-1	
3.75	1M NaOH 55	F				a-1 b-1	
3.75	10⁻³M NaOH 25	G				a-1 b-1	
3.75	10⁻¹M NaOH 25	H				a-1 b-1	
0.625	ASW 25	I				a-1 b-1	
1.25	ASW 25	J				a-1 b-1	
0.625	1M NaOH 25	K				a-1 b-1	
1.25	1M NaOH 25	L		a-1 b-1	a-1 b-1		

a: Adhesive system Control A

b: Adhesive system Modified B

extrapolated line describing the propagation of the degraded front in free bulk adhesive (at 33 C), and the initial slopes of all three supposedly different modes are compared (although the temperatures are a little different). The WBPR, DBPR, and the bulk degradation rate are almost identical at short "diffusion" distances. The behavior of delamination is modelled by the SBS and the results show how deviations from a straight line come about due to the decaying of the driving force, G. Weakening, on the other hand, is dominated by the environmental parameters and the behavior is modelled using the data collected from the BDS.

As discussed in chapter 3, the relevant (and apparently independent) accelerating parameters were identified as stress, temperature, and current density. Cathodic current density was chosen as an independent parameter rather than voltage per say. The above assumption is directly derived from the physics of the problem and results in the elimination of some parameters by rendering them dependent, i.e., dissolved oxygen and electrolyte. Electrochemical work was done on ANSI 1026 mild steel in different solutions in order to determine the corresponding current densities at some designated potentials. Five current densities were eventually chosen including the level that corresponds to -1000 mV in ASW (1 mA/cm^2). Appendix A explains the experimental apparatus and the voltammetry data that was generated. The results are summarized in Table 3.

Similarly, in order to account for temperature variations under which the Navy sonar transducer units operate, three temperature levels, i.e., 25, 40, and 55 °C., were used in the test matrix. These temperatures were all higher than normal service, but were used to accelerate the debond process, and to determine temperature effect and the associated activation energy. Effects of shear and compressive stresses on weakening rates are also evaluated in this chapter. Tensile stresses were also shown to play a major

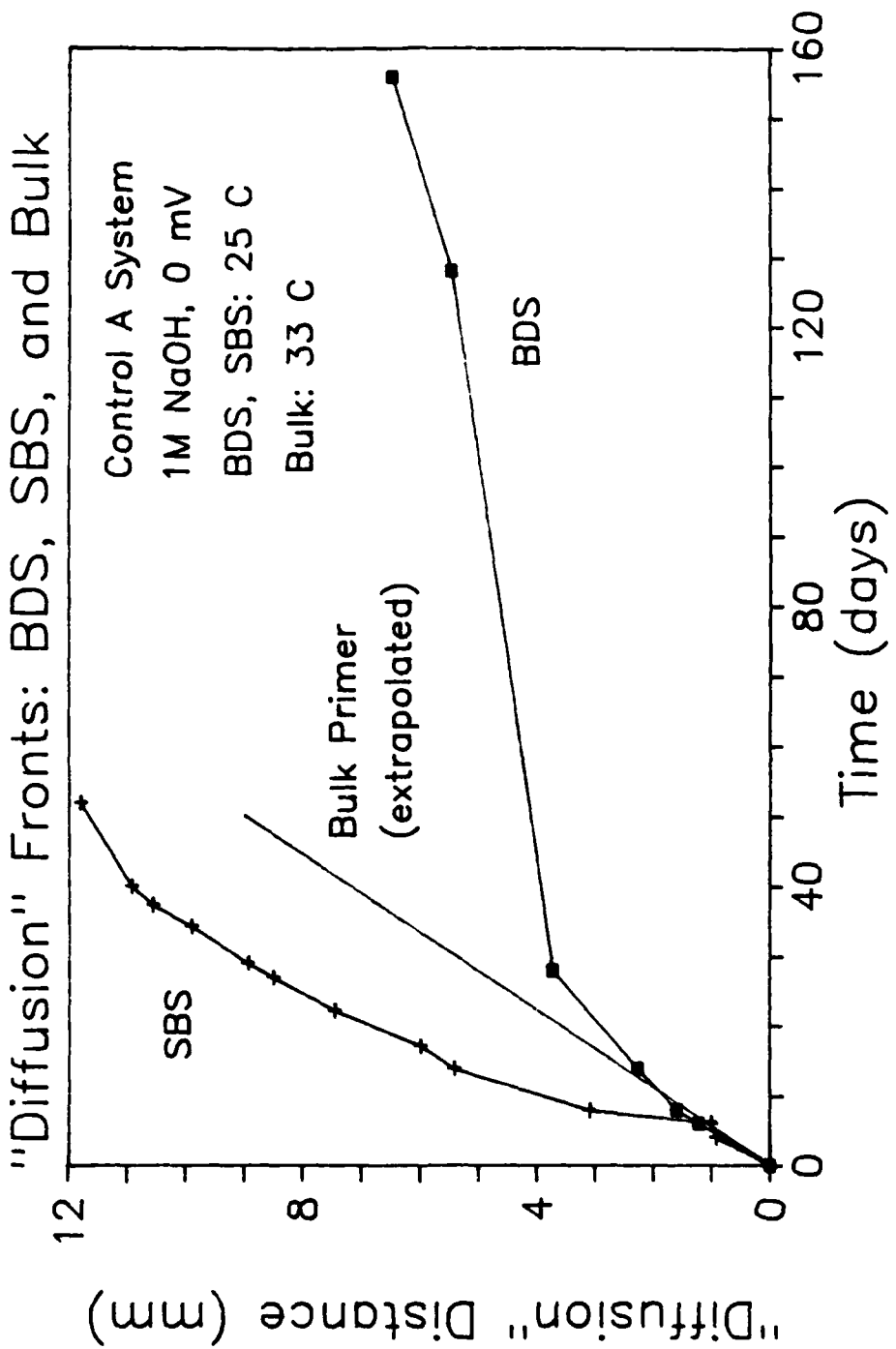


Figure 32. Comparison of Diffusion Fronts in BDS, SBS, and Free Film; Environment: 1M NaOH, and 0 mV; BDS and SBS: 25 C; Bulk: 33 C.

Table 3. Recommended Potentials for the Test Matrix (in mV (SCE)).

Environment/ Temperature (° C)	Current Density (mA/ cm ²)				
	1	2	3	4	5
	0.59	1.0	1.475	14.75	73.3
ASW 25	-830	-1000	-1100	-1420	-1825
ASW 40	-770	-970	-1020	-1310	-1620
ASW 55	-770	-930	-1000	-1250	-1520
1M NaOH 25	-960	-1150	-1250	-1420	-1560
1M NaOH 40	-920	-1000	-1200	-1360	-1500
1M NaOH 55	-890	-980	-1060	-1310	-1470
0.1M NaOH 25	-830	-930	-1130	-1480	-2020
0.001M NaOH 25	-1100	-1640	-	-	-

role in accelerating debonding. This effect is fully investigated in chapter 5 with particular emphasis on coupling with other accelerating parameters.

For this purpose, two BDS specimens (control A), along with one SBS specimen of each adhesive system, Control A (Chemlok 205/220) and Modified B (Chemlok 205 + A-1100/220), were tested for every corresponding test case. Another phosphate coated SBS was also tested in some ASW baths for comparison. The raw weakened and delaminated data are presented in Appendix 2. In this chapter, an effort was made to present the data in such a way so as to show the effect of temperature and voltage in ASW and 1M NaOH on the WBPR's. In addition, a linear regression model was developed and implemented in order to predict the propagation of the weakened mode.

4.2 ACCELERATING PARAMETERS

The data from the non-stressed BDS were shown (chapter 3) to obey a linear relationship when plotted against the square root of time. This is further substantiated in this chapter for the two adhesive systems under consideration under all conditions. No BDS were fabricated with System B, however, four side diffusion distances per SBS were averaged up, after the joints were pulled apart, and a straight line was drawn through the origin.

4.2.1 Influence of Temperature

The effect of temperature on the control system in 1M NaOH solution is clearly demonstrated in Figure 33. The WBPR's are considerably higher for elevated temperatures. An effort was made to vary the temperatures in the three different baths while maintaining the other parameters (current density and environment) constant. However, some scatter still exists mainly due to occasional variations in bath temperature and voltage (current density) from day to day.

In ASW, the temperature effect is noticeable even though the WBPR seems to be artificially low for the 55 C tank. At such high levels of temperature, calcareous deposit build-up becomes excessive and may retard ingressions. This may mask the time dependency of the true debond process. Figure 34 also shows that, all things considered, the WBPR for system A is doubled when the temperature is raised from 25 to 55 C.

System B seems to follow the same trends although, unfortunately, the number of data points is very limited as mentioned above. The data plotted in Figure 35 is from the SBS's which were bonded at TRI unlike their counterparts (BDS's) which were manufactured at VPI. Again, all the tests were run at the same current density level in attempting to isolate the temperature dependency. It is apparent from the figure that at such high current density outputs, the contribution of bulk pH becomes consistently smaller as seen by the comparable rates for both ASW and 1M NaOH. Supposedly, the pH at the crack tip may reach the same high levels in both solutions regardless of the electrolyte.

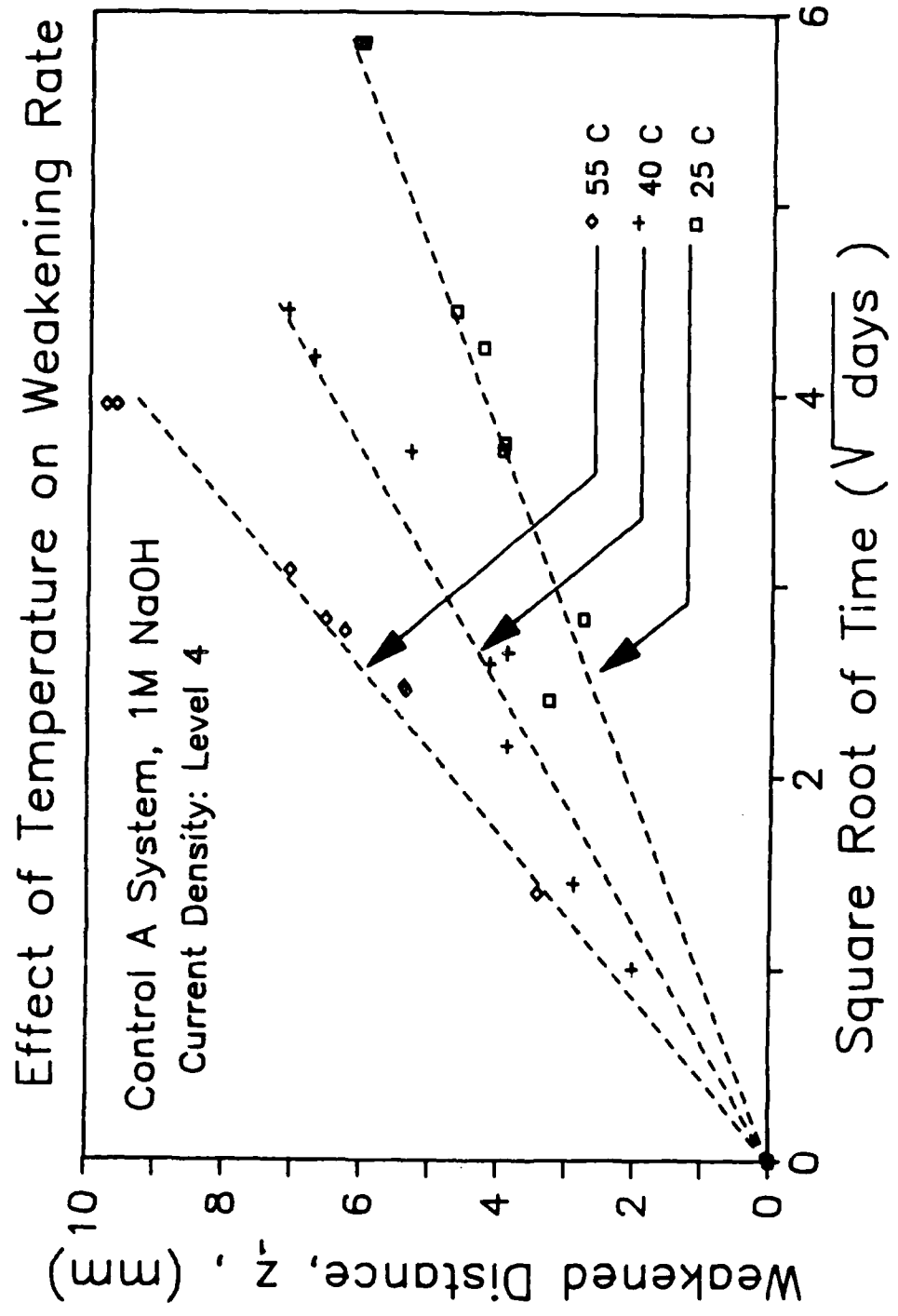


Figure 33. Temperature Effect on the WBPR; Control A; Environment: 1M NaOH, current density 4.

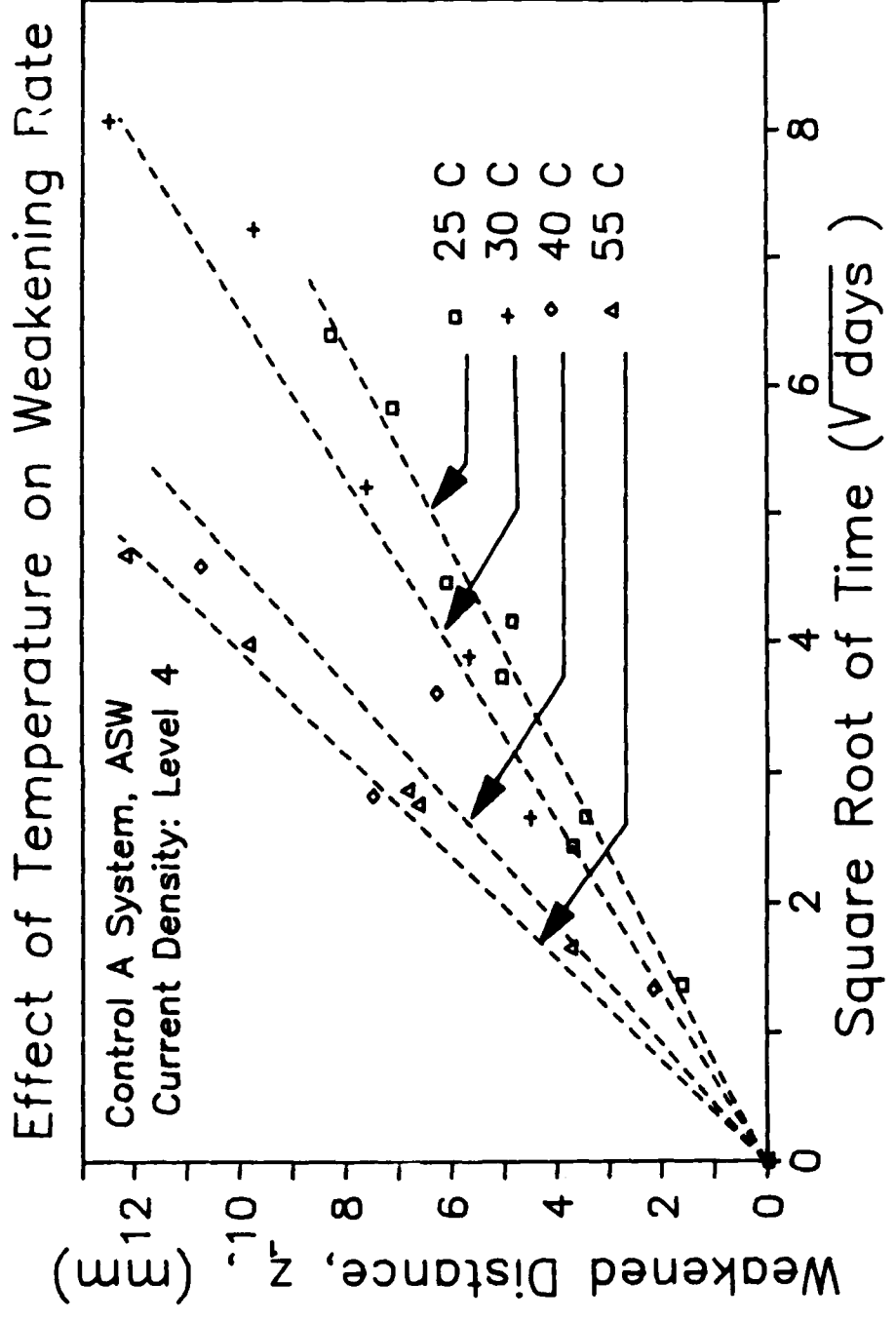


Figure 34. Temperature Effect on the WBPR; Control A; Environment: ASW, current density 4.

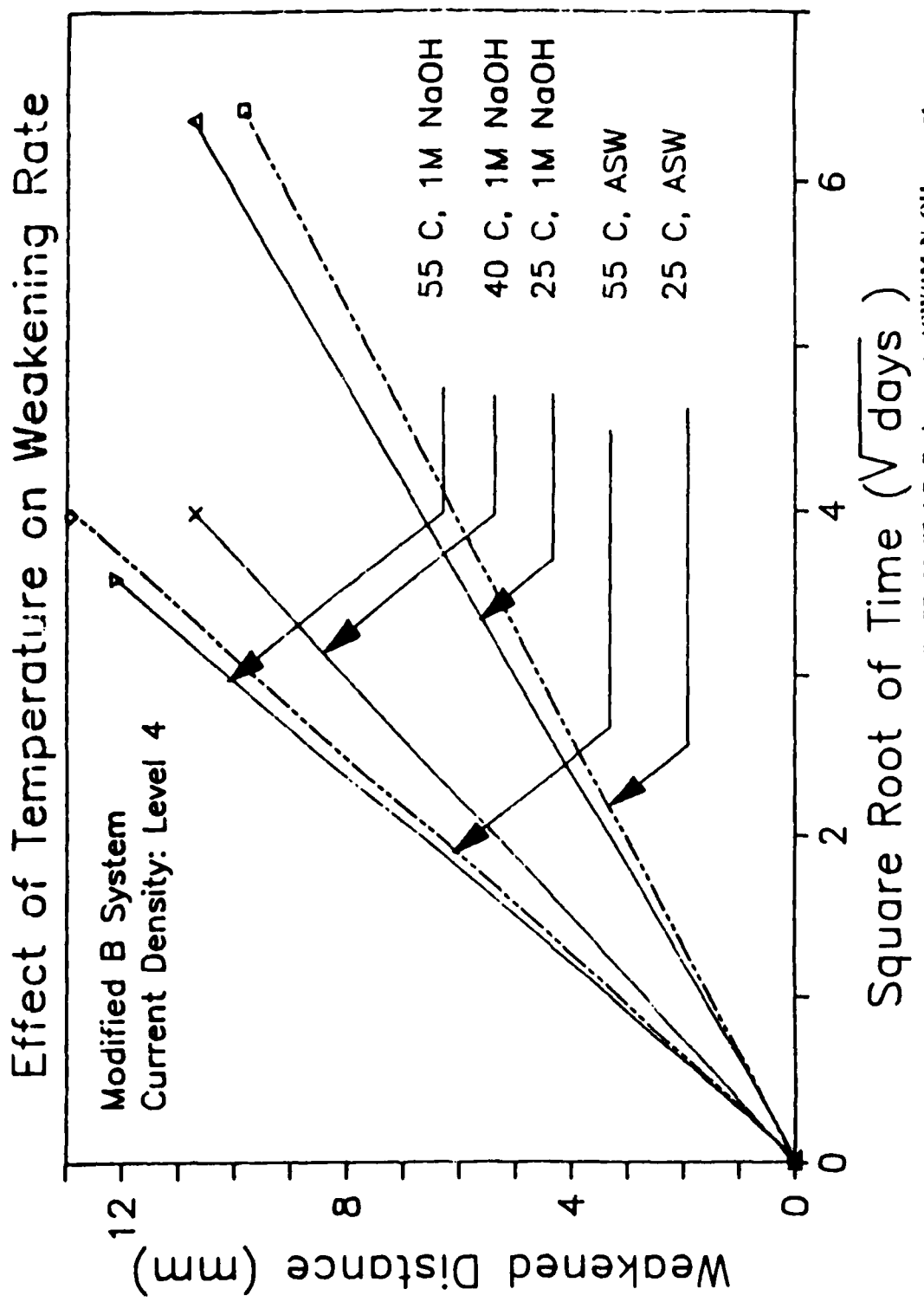


Figure 35. Temperature Effect on the WBPR; Modified B; Environment: ASW/1M NaOH, current density 4.

4.2.2 Influence of Voltage

Figure 36 illustrates the effect of applied cathodic potential on the WBPR. The respective potentials of -1000, -1100, -1420, and -1825 mV (SCE) in ASW at 25 C correspond to current density levels 2 through 5. An important observation here is the delay time which decreases as potential increases. A possible explanation for this phenomena was given in chapter 3. The weakening rates also increase as a function of cathodic potential supposedly because the crack pH varies in accordance with the applied voltage. The delay time all but disappears for voltages higher than -1100 mV. The build-up of thick calcareous deposits at higher voltages (and temperatures) seems to be the reason why the WBPR at -1825 mV declines rapidly. The hard build-up provides a natural barrier for diffusion of water and electrolyte into the crack tip where the electrochemical reactions take place.

In 1M NaOH at 25 C, Figure 37 shows that the hydroxyl ion attack on the adhesive bond results in an unavoidable loss of adhesion. Although voltage was not applied (0 mV), debonding has occurred and progressed, thanks to a reservoir of OH^- ions from which the aggressive species diffused into the adhesive. Delay time seems to have disappeared apparently due to the already available hydroxyl. Again, the voltages -1150, -1250, -1420, and -1550 mV correspond to current density levels 2 through 5.

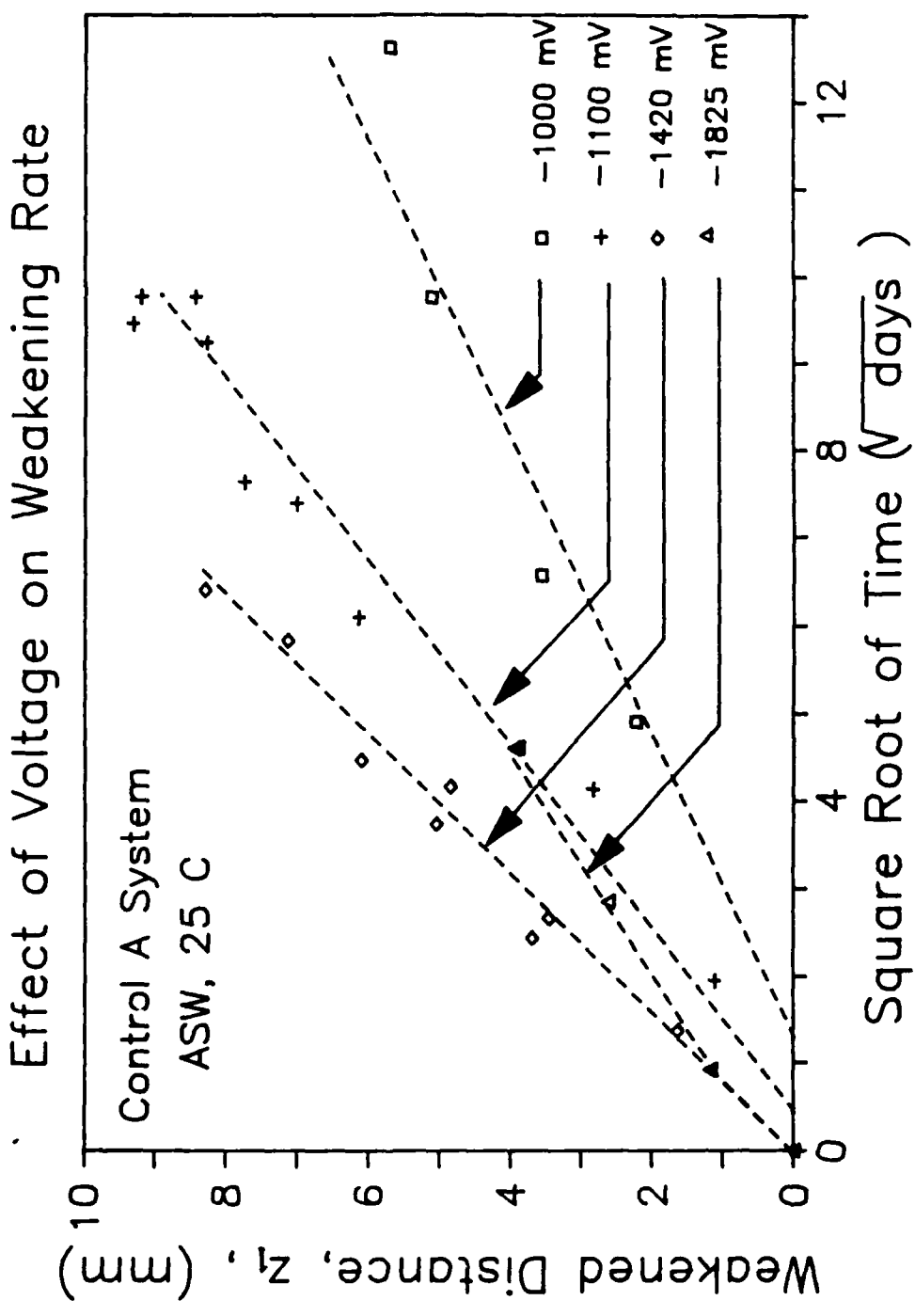


Figure 36. Voltage Effect on the WBPR; Control A; Environment: ASW, 25 C.

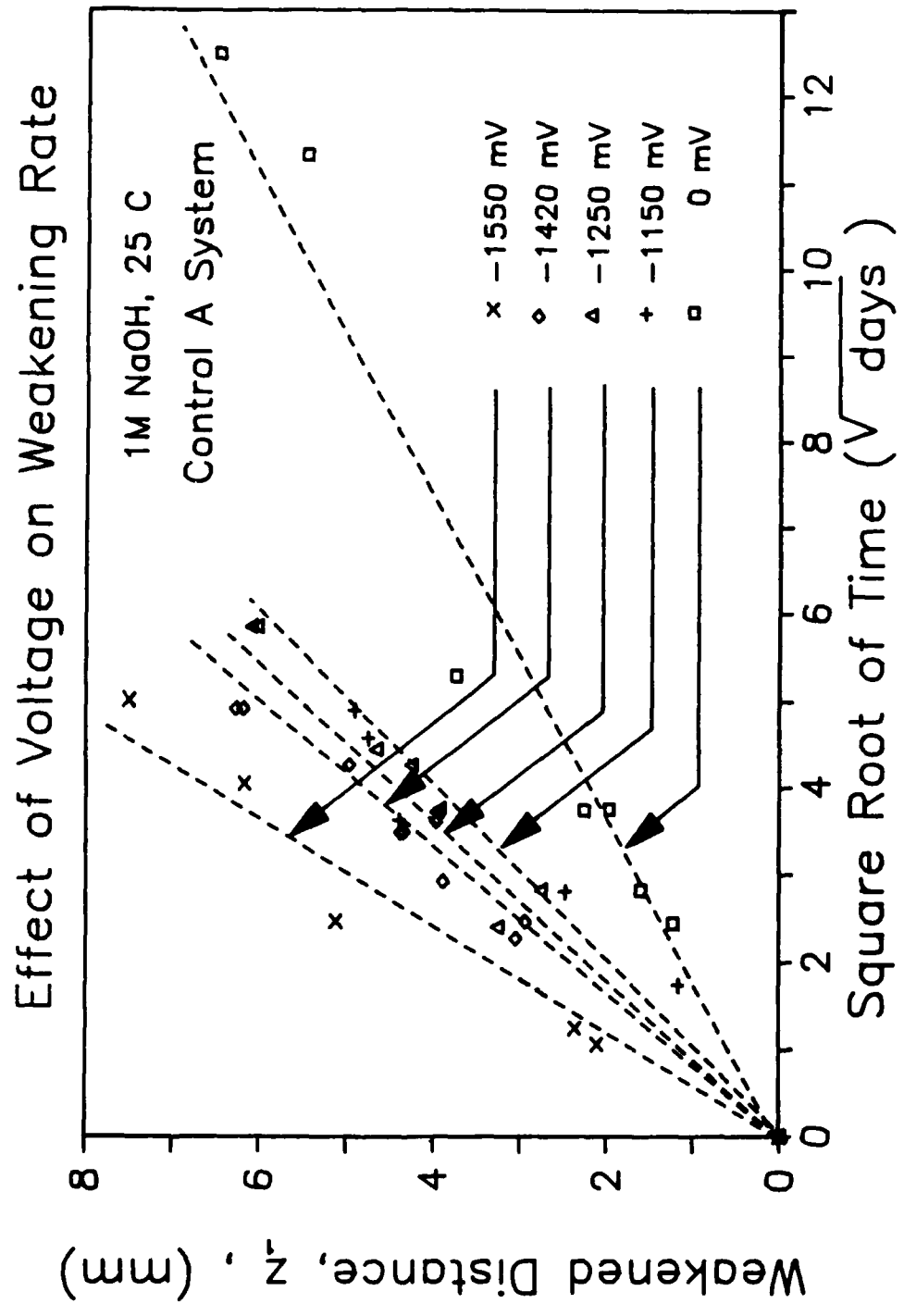


Figure 37. Voltage Effect on the WBPR; Control A; Environment: 1M NaOH, 25 C

4.3 MODELLING WEAKENING

Weakening could be described as an environmental crack growth due to the presence of an aggressive medium. The mechanism is conceptualized as a chemical reaction between the reactive OH^- and the unstable linkages of the adhesive (and perhaps other interfacial adhesion promoting bonds as will be discussed in chapter 7) at the crack tip. It seems at the first glance that the environmental crack will grow governed by the degradation reaction rate. However, the intermediate steps play important roles that lead to the reaction at the crack tip. The minute dimensions inside the resulting crack may dictate that mass transfer, possibly possessing the slowest rate of all processes, becomes the limiting process. A basic understanding of how weakening proceeds is a must, and hence, a brief discussion will be dedicated for this purpose.

4.3.1 Discussion

The shrinking core model presents an attractive explanation for the different competing processes. A fluid reacting with a solid of low porosity to yield a reacted layer may be a suitable approach to modelling weakening. While weakening progresses, the reactants (OH^- ions, water molecules, dissolved oxygen, Na^+ ions, etc.) must penetrate through the product layer in order for the electrons to flow and for the degradation reaction to proceed. Figures 38-40 clearly explains the relative progress of diffusion

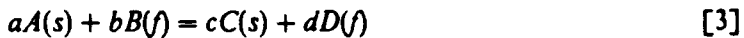
versus chemical reaction. According to Froment and Bischoff [28], three possible situations could arise as a result of the above:

1- The General Model: The rate of diffusion of the species is comparable to that of the chemical reaction between the polymer and the diffusing medium that the reaction takes place over the entire region where diffusion has occurred. Figure 38 shows typical concentration profiles for the fluid species (C_A) and the reacted solid species (C_S).

2- The Truly Homogeneous Model: The ratio of diffusion of the degrading species to chemical reaction is so high that degradation starts long after diffusion is finished. This is what is known as "chemical reaction control". As seen in Figure 39, the degraded solid concentration decays at a fairly uniform rate along the entire length of the reacted zone.

3- The Heterogeneous Model: The chemical reaction is much faster than the diffusion process, and degradation occurs in very thin surface regions (fronts) that propagate from the outer surface to the inner regions. The result is that a sharp interface exists between the reacted skin and the intact core as shown in Figure 40. We feel that this case resembles our application in what could be described as a "diffusion controlled" process. Given the similarity, we will make use of some of the concepts of the shrinking core model in the following.

Let us consider a chemical reaction of the form



where A (s) and B (f) represent the adhesive and the reacting fluid species, OH^- , and a, b, and c are the stoichiometric coefficients. The rate of reaction is often expressed as

$$r = kC_A^a C_B^b$$

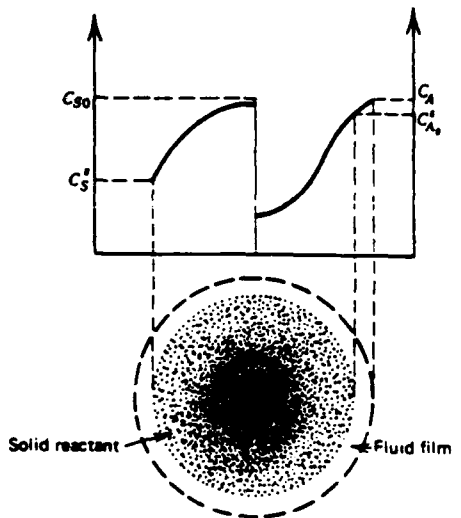


Figure 38. Shrinking Core Model; The General Model showing the fluid and solid concentration profiles (taken from Wen [29])

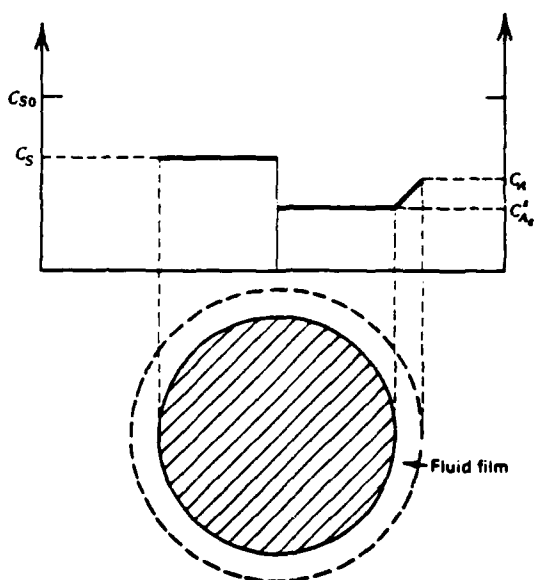


Figure 39. Shrinking Core Model; The Truly Homogeneous Model (taken from Wen [29])

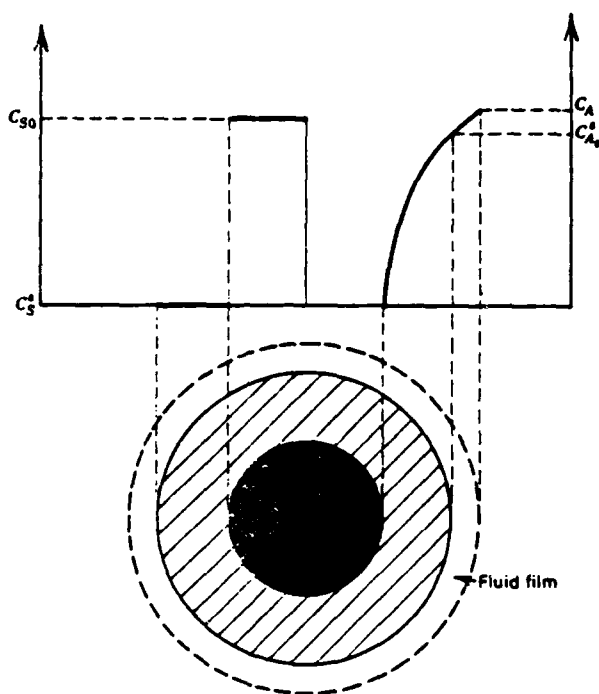


Figure 40. Shrinking Core Model; The Heterogeneous Model (taken from Wen [29])

The proportionality constant is called the rate coefficient, and C denotes concentration.

For a first order reaction, the previous equation leads to

$$r_A = - \frac{dC_A}{dt} k C_A$$

If a flat pellet of A reacts with the surrounding fluid, B, the conversion, X, is described by

$$X = 1 - \eta_c \quad [4]$$

where

$$\eta_c = r_c \frac{2}{l_p}$$

r_c is the position of the interfacial reactive zone and l_p is the length of the pellet's reactive path. One can see that

$$X = 0, \text{ at } r_c = l_p/2$$

$$\text{and } X = 1, \text{ at } r_c = 0.$$

For thin shrinking unreacted core samples, conversion (completed reaction distance) is predicted [30] as a linear function of time. The reason being that at short distances the overall rate is controlled by the rate of chemical reaction at the interface. X is related to time by the relation

$$X = \left(\frac{k_0 C_{A0}}{\rho_s l_p} \right) t = k_s t \quad [5]$$

where X is conversion, k is the heterogeneous rate constant, C_{A0} is the bulk concentration of the reactant, ρ_s is the molar density of the solid, and r_p is the thickness of the flat pellet.

In many fluid-solid systems with high chemical reaction rates, the overall rate is controlled by diffusion between the bulk and the reaction site. When diffusion controls the process, the relationship for a slab geometry can be expressed in the form

$$X^2 = \left(\frac{2C_{A0}}{\rho_s} \frac{D}{l_p^2} \right) t = D_e t \quad [6]$$

where D is the diffusivity constant. We can consider the term between the brackets to be the effective diffusivity and it can be regarded as analogous to (WBPR)².

Therefore, in the presence of resistance due to external mass transfer the X - t relationship takes on a linear form when X is plotted against the square root of time. The Thiele modulus for first order reactions is described by the relationship

$$(\phi^*)^2 = l_p^2 \frac{k_e}{D_0}. \quad [7]$$

This quantity incorporates both kinetic and structural parameters and is very helpful in the characterization of the system. When the modulus is high, the diffusion of fluid A through the solid is rate controlling. As a result, the concentrations of the diffused species, OH^- for instance, reach some minimal levels that "overall" rate coefficient dictates a continuously slower front propagation rate. On the other hand, when the modulus is large, no gradients exist inside the particle and the chemical reaction becomes rate controlling.

The similarity between the shrinking core model and the system of concern is obvious where the weakened bond propagation is analogous to the conversion, X . For

thin free standing primer films (chapter 3), the percentage of mass uptake in different concentrations of NaOH solutions (C_{40}) is equivalent to X and give straight lines with a slope of

$$\frac{k_0 C_{40}}{\rho_0 l_p}$$

and with units of days^{-1} . Considering the control case of 1M NaOH (where X vs. t gives a straight line) and that C_{40} to be 1 mole/l, the slope of the 1M NaOH-exposed primer film yields a value of $k_e = 1.1 \text{ days}^{-1}$ and $k_0 = 0.88 \rho_s (\text{mm}/\text{d})$ when a control length $l_p = 0.8 \text{ mm}$ was used. Note that the value of ρ_s is an unknown (mole/l).

The weakened distances for the BDS (Figure 32) were converted to the equivalent form X. This allowed us to treat the BDS as a thick specimen in order to extrapolate D_0 . Using the expression in Equation 7 with $l_p = 12.7 \text{ mm}$, we were able to calculate that $D_0 = 0.1643 \rho_s (\text{mm}^2/\text{d})$.

As seen from the above discussion, in order for the weakening process to be diffusion controlled, the Thiele modulus should be large. Using SI units, the values of k_e and D_0 become $1.273E-05 (\text{s}^{-1})$ and $1.9E-08 \rho_s (\text{cm}^2/\text{s})$ respectively. Considering the BDS of $l_p = 1.27 \text{ cm}$, the corresponding value of the modulus is 1080, which is indicative of diffusion control. We would also expect that the reaction rate will increase as a function of harshness (applied potential or higher temperature) at a higher rate than the diffusion coefficients. This is due to the fact that the activation energy of chemical reaction is usually higher than that of diffusion. That will favor, of course, more diffusion control as expected.

4.3.2 Temperature

In order to model the effects of temperature on the WBPR's, one needs to determine the diffusion coefficient's dependence functionality. For this purpose, the effects of voltage and solution were eliminated by choosing the appropriate current densities and using the same solution, and hence temperature dependence was segregated. Knowing that the D_s 's are the squares of the WBPR's, the slopes of Figures 33, 34, and 35 were plotted versus $1/T$ ($^{\circ}K^{-1}$), and the resulting dependency of the WBPR's is illustrated in Figure 41. We continue to see that temperature effects are better predicted in 1M NaOH solutions. In ASW, the slopes are distorted, we feel, because of the observed deposits along the diffusion path. The slopes of those lines were used to deduce an effective activation energy for the limiting diffusion process. Diffusion of hydrated Na^+ ions, dissolved oxygen, and other ions is both necessary and sufficient for OH^- production at the reaction site. The activation energy must then be associated with the slowest diffusion process of all. The calculated activation energy, E, in NaOH was found to be about 10 kcal/mol (42 kJ/mol). This value is relatively low and is comparable with activation energies of diffusion processes. Activation energies of reaction are much higher than those of the mass transfer and diffusion phenomena. Also note that the slopes of the Arrhenius plots, and hence activation energies of diffusion, are similar for both the control system and the silane-modified system.

Temperature effects, then, could be modelled according to the Arrhenius approach. The form for the exponential temperature dependency is universally recognized, in diffusion for example, as:

$$D = D_0 \exp - \left[\frac{U_D^x}{RT} \right] \quad [8]$$

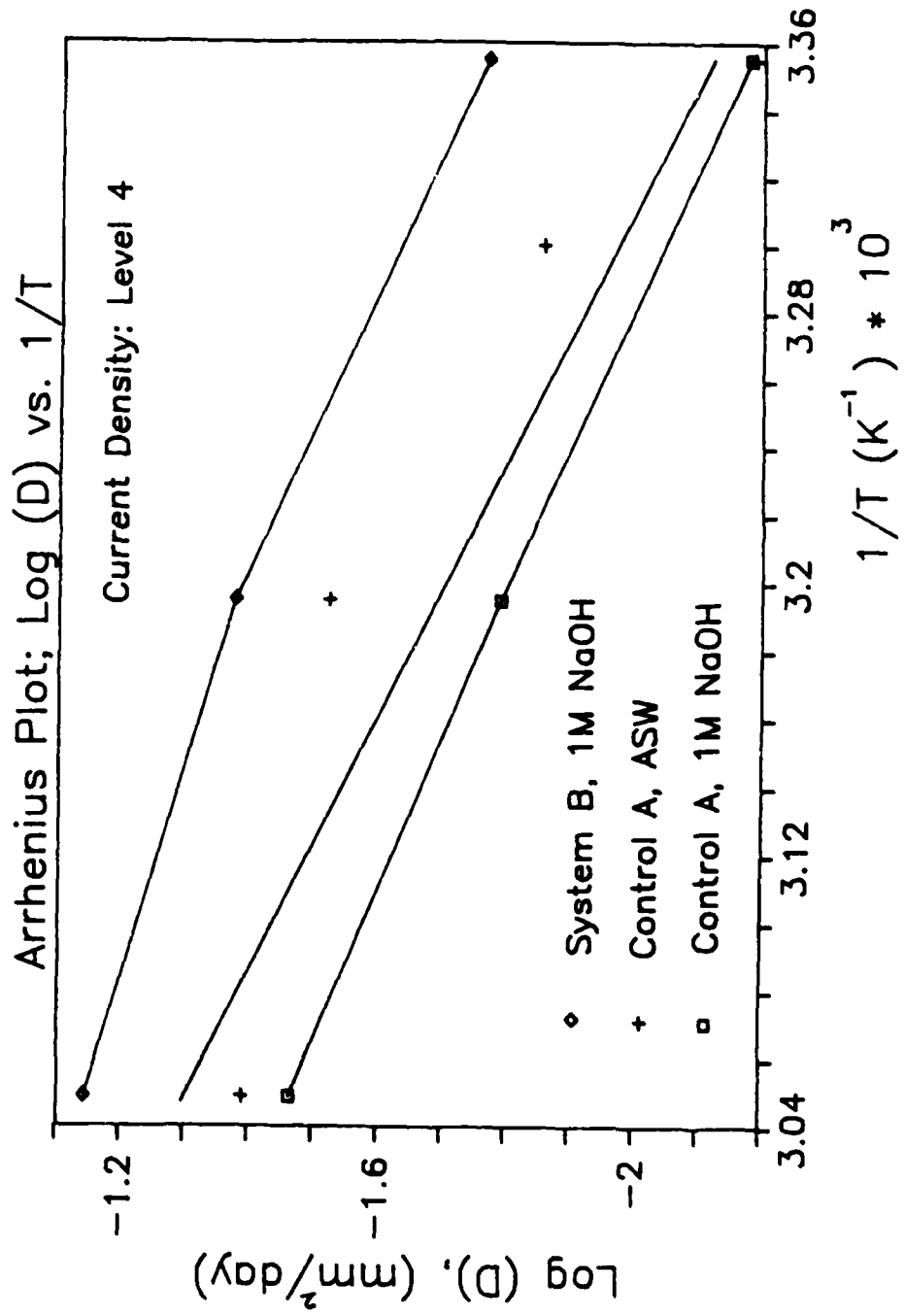


Figure 41. Temperature Dependence of Diffusivity; BDS Data.

where U_g is the activation energy for the diffusion process through the bondline medium. Also, higher temperature increases the thermal motion leading to an accelerated rate for the chemical breakage of the attachment sites.

$$k = k_0 \exp - \left[\frac{U^*}{RT} \right]. \quad [9]$$

Here U^* is the activation energy for the degradation reaction between the aggressive media and the adhesive. As we suggested above, high temperatures favor pure diffusion control, and thus the reaction rate dependence is of little interest to us at this time.

4.3.3 Voltage

As discussed above, cathodic voltage should be modelled through the corrosion current density. A question may be raised about the functional relationship between current density and pH. Unfortunately, the correlation between the former and crack pH can only be determined numerically and will be discussed later.

According to Vetter [31], the partial current density for a particular cathodic electrochemical reaction could be expressed as follows :

$$\begin{aligned} i_i &= -k^+ c_i \exp\left(-\frac{E}{RT}\right) \\ &= -k^+ c_i \exp\left(-\frac{E_{-h}}{RT}\right) \exp\left(-\left(\frac{\beta F E}{RT}\right)\right) \\ &= -k c_i \exp\left(-\left(\frac{\beta F E}{RT}\right)\right) \end{aligned} \quad [10]$$

where i_1 is the cathodic current density, k is a rate constant dependent on the ionic concentration (A cm⁻²), c_1 is the electrolyte concentration immediately at the electrode surface, E_- is the activation energy barrier (absolute potential), E_{-h} is a chosen reference potential, E is relative potential, β is transfer coefficient, $0 < \beta < 1$, F is Faraday constant, where $F = N * e_0$ is the total charge of "one mole of elementary charges", R is the gas constant, and T is absolute temperature.

Gangloff [32] studied the cathodic and anodic polarization kinetics for 4130 steel in deaerated 3 percent NaCl at pH 7.9 and a voltage scan rate = 360 mV/hr. He then employed the polarization data in Figure 42 for crack chemistry modelling.

Similarly, Turnbull [24] used comparable expressions to simulate the kinetics of water reduction. The electrode potential was related to the resulting cathodic current density as follows

$$i_{(H_2O)} = k(H^+) \exp\left\{-\frac{\beta(H^+)FE}{RT}\right\} \quad [11]$$

where k and β are constants dependent on the hydrogen ion concentration. The oxygen reduction kinetics were assumed to have the form

$$i_{(O_2)} = k^-[O_2] \exp\left\{-\frac{\beta^-FE}{RT}\right\} \quad [12]$$

Buck et al [33] developed a model which describes crack initiation and growth by the combined effects of a static stress and corrosion. They observed that the pits grow linearly in time under constant stress. Consequently, they were able to relate the corrosion pit depth, a_p , to exposure time, t , and to the corrosive environment and the potential, V , as

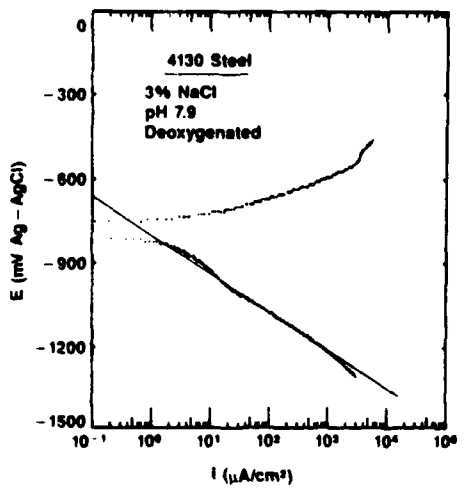


Figure 42. Polarization Data for 4130 Steel in Dearthed ASW (from Gangloff [32]).

$$a = B t \exp\left(\frac{V}{V_0}\right) \quad [13]$$

where B and V_0 are "material" parameters defined by:

$$B = \frac{V_M i_{corr}}{\zeta F}, \quad V_0 = \frac{RT}{\beta F} \quad [14]$$

ζ is the charge of the aggressive ion, V_M is the molar volume, and β is the symmetry factor. This time, the Butler-Volmer equation for anodic dissolution at the corrosion site was used with the potential versus current density measurement directly providing B and V_0 .

Dependence of crack propagation on current density has been demonstrated throughout this research. It is unclear at this point what the direct linkage between the latter and the WBPR's. However, two possible explanations are as follows:

1- A direct contribution of cathodic current density to crack pH that was found to be detrimental in adhesive degradation. However, the effect of concentration on the diffusion coefficient is where our interest lies as discussed above. If this is the case, a direct correlation between those two quantities is only possible through a comprehensive model of the type presented in the next chapter. Nonetheless, the above discussion allows us to properly assume a linear relationship between the current density and the total number of the generated OH^- ions, and hence, the crack pH. It is indeed feasible, and perhaps possible, that the proportionality constant is not unity.

2- An iron oxide dissolution mechanism at voltages more negative than -1000 mV (which is the case in most of our cases). A direct correlation between the current density and the rate of dissolution similar to those used above could be in order. However, the

work was focused primarily on polymer degradation which resulted in that this possibility not be investigated.

Accordingly, the polarization data of ANSI-1026 collected at VPI were fitted, using a least squares fit SAS routine, according to temperature and environment. The results of the parametric analysis used in this cathodic reduction study are summarized in Table 4. The effect of OH^- concentration on the diffusion coefficients, then, is modelled indirectly through current density dependence such as:

$$D_e = D_0[OH^-] \propto D_0 k(H^+) \exp\left(-\frac{\beta(H^+)FE}{RT}\right) \quad [15]$$

Figure 43 shows a typical WBPR dependence on applied voltage. The linear relationship between the log of WBPR's and the applied voltage is, perhaps, an indication to the validity of Equation 15. The implied conclusion is that diffusion through the degraded polymer is directly related to the concentration of the alkali which in turn is proportional to the applied current density.

4.3.4 Model Formation

Although we may be able to identify the independent variables to be included in the model, the actual relationship between the dependent and independent variables is still unknown. Two approaches could be used in a situation like this. The first one is to fit the data into an assumed model that accounts for the physical quantities such as temperature and voltage. The other approach is to assume a very general regression

Table 4. Kinetics of Water Reduction A-4: ASW, 25 °C, -1420 mV.

Environment	Temperature (° C)	k (mA/ cm²)	β
ASW	25	1.017E-05	0.3040
ASW	30	6.685E-06	0.3270
ASW	40	1.848E-06	0.3787
ASW	55	6.976E-07	0.4470
1M NaOH	25	5.837E-10	0.4940
1M NaOH	40	4.843E-09	0.5026
1M NaOH	55	5.297E-09	0.5494

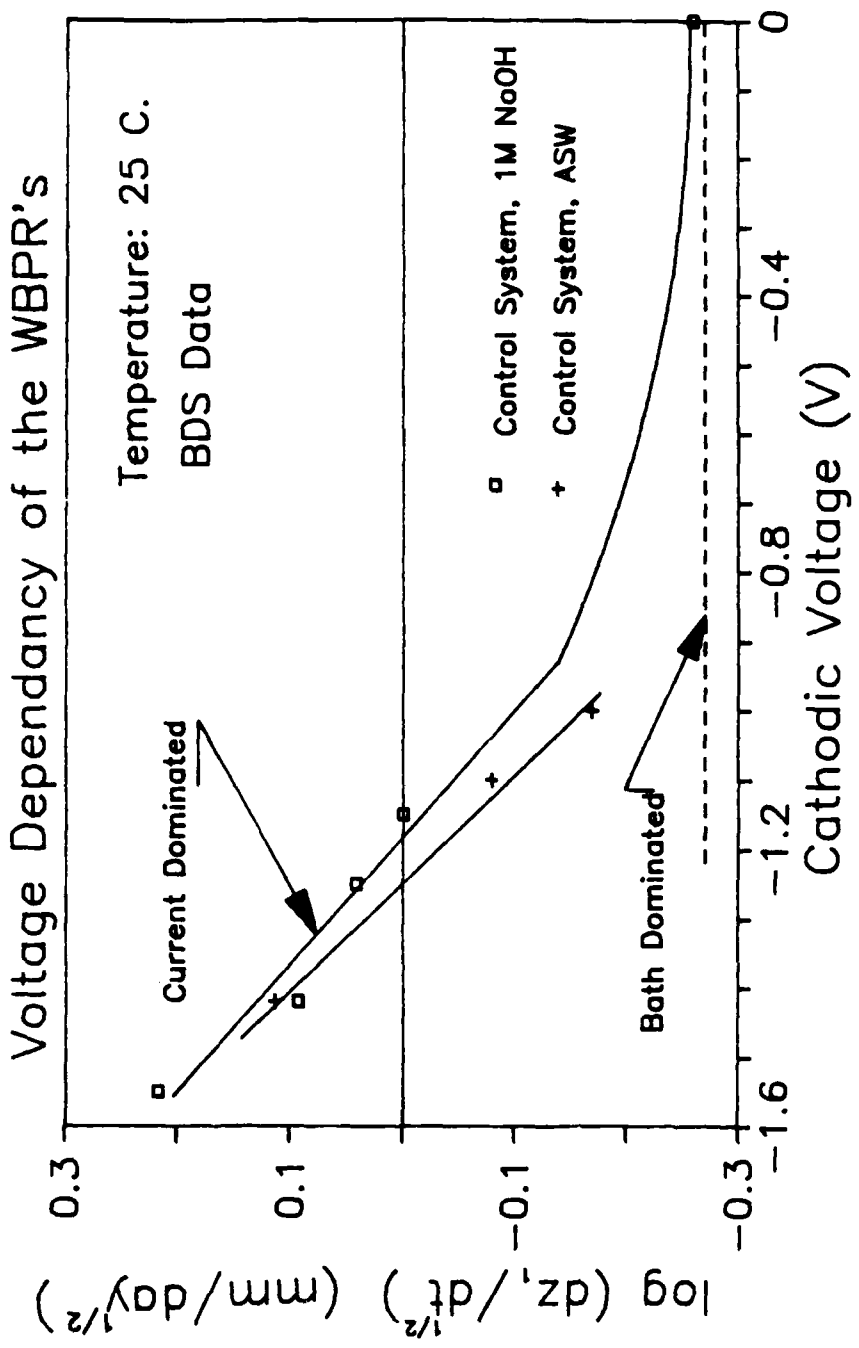


Figure 43. Voltage Dependence of the WBPR; BDS Data; Temperature= 25 C.

model (with constant coefficients) which contains all the independent variables and select the best fit using a number of procedures ,i.e., backward elimination method or step wise regression procedure. One must make use, in the process, of the known functional dependencies. AS mentioned earlier, the best information can be obtained by plotting log WBPR against each independent variable, and advantage should be taken from the apparent linearity.

Levi [34] has used a multiple regression analysis technique to model the effects of stress, temperature, and humidity on the durability of aluminum bonds. Reaction rate theory was used for theoretical basis in which the time to failure under constant stress is given by:

$$\log t_F = C - \log T + \frac{\Delta H}{RT} - b \frac{S}{T} . \quad [16]$$

where C and b are constants, T is absolute temperature, ΔH is activation energy, and S is stress. He suggested another empirical model where emphasis was put on individual plots that resulted in:

$$\log t_F = a_0 - a_1 S + a_2 H + a_3 T + a_4 H^2 \quad [17]$$

A general type model was suggested by Bussa et al [35] for metal life under random fatigue loads. For the same independent variables mentioned above, the model becomes:

$$\log t_F = \log C + a_1 \log S + a_2 \log H + a_3 \log T \quad [18]$$

Assuming that temperature and voltage effects on the diffusion coefficients are multiplicative, a semi-empirical model of the form

$$\begin{aligned}
 z_1^2(t) &= D_e(T,[OH^-])t \\
 &= D_0 f(T,[OH^-])t \\
 &= D_0 \left\{ \exp\left(\frac{-U_D^x}{RT}\right) \times k[H^+] \exp\left(\frac{-\beta(H^+)FV}{RT}\right) \right\} t
 \end{aligned} \tag{19}$$

where z_1 is the weakened bond distance, D_0 and D_e are diffusion and effective diffusion coefficients respectively, t is time, T is temperature, V is applied voltage, U_D^x is the apparent activation energy associated with diffusion, and β and k are pH-dependent constants. Although voltage is included in Equation 19, current density is what is really being used in the analysis since the parametric analysis assigns different values of k and β for different environments. Taking the square root of both sides of the equation yields:

$$\begin{aligned}
 z_1(t) &= WBPR_e t^{1/2} \\
 &= WBPR_0 \left\{ \exp\left(\frac{-U_D^x}{RT}\right) \times k[H^+] \exp\left(\frac{-\beta(H^+)FV}{RT}\right) \right\} t^{1/2}
 \end{aligned} \tag{20}$$

where $WBPR$ is the weakened bond propagation rate ($\text{mm}/\text{day}^{1/2}$). One may argue that the contribution of temperature and voltage is additive, and hence, resulting in an addition sign instead of multiplication in the r.h.s. of Equation 19 as follows

$$z_1^2(t) = D_0 \left\{ \exp\left(\frac{-U_D^x}{RT}\right) + k \exp\left(\frac{-\beta FV}{RT}\right) \right\} t. \tag{21}$$

Both of these options were investigated. To predict durability, a regression model similar to that in Equations 19 and 21 was built into the statistical analysis system (SAS) and the fit of the functional relationship was examined by the linear regression technique using the REG procedure of SAS.

Considering Equation 19, it is appropriate to linearize the model by taking the log of both sides to obtain

$$\log\left(\frac{z_1^2}{t}\right) = A_1 - A_2 \frac{1}{RT} + A_3 \frac{\beta FV}{RT} . \quad [22]$$

where A_1 is $\log D_0$, the coefficient A_2 should ideally estimate the apparent activation energy U_D^* , and A_3 is a proportionality constant. Based on the regression analysis, the optimum equation that was used to predict weakening of Chemlok 205/220 in 1M NaOH is

$$\log\left(\frac{z_1^2}{t}\right) = 14.964 - 4826.9 \frac{1}{T} + 0.3548 \frac{V}{T} . \quad [23]$$

The resulting coefficient of determination, R^2 , has a value of 0.895. Figures 44 and 45 illustrate the good fit of the multiplicative model for the 205/220 adhesive system in NaOH solution under various voltages and temperatures. Comparing some diffusivity values in SI units, $D_e = 1.32E - 07 \text{ cm}^2/\text{s}$ at $V = 1150 \text{ mV}$ and $T = 25 \text{ C}$ compared to $2.13E - 07 \text{ cm}^2/\text{s}$ for $V = 1550 \text{ mV}$ and $T = 25 \text{ C}$. Note that the estimated value of U_D^* is 40 kJ/mol and is, not surprisingly, close to the experimentally measured value of 42 kJ/mol.

Another equation of the form

$$\frac{z_1^2(t)}{t} = -0.2696 + 1.35 \times 10^7 \exp\left(-\frac{4826.9}{T}\right) + 4.43 \times 10^{-4} k \exp\left(\frac{11.6\beta V}{T}\right) \quad [24]$$

has resulted from the additive model with an R^2 value of 0.85. Note that this model, inherently, cannot estimate a value for U_D^* . Instead, the value from the multiplicative model was used as an input. Figures 46 and 47 show a good fit within the range of experimental data except perhaps for the case when no voltage was applied.

SAS Fit: Multiplicative Model

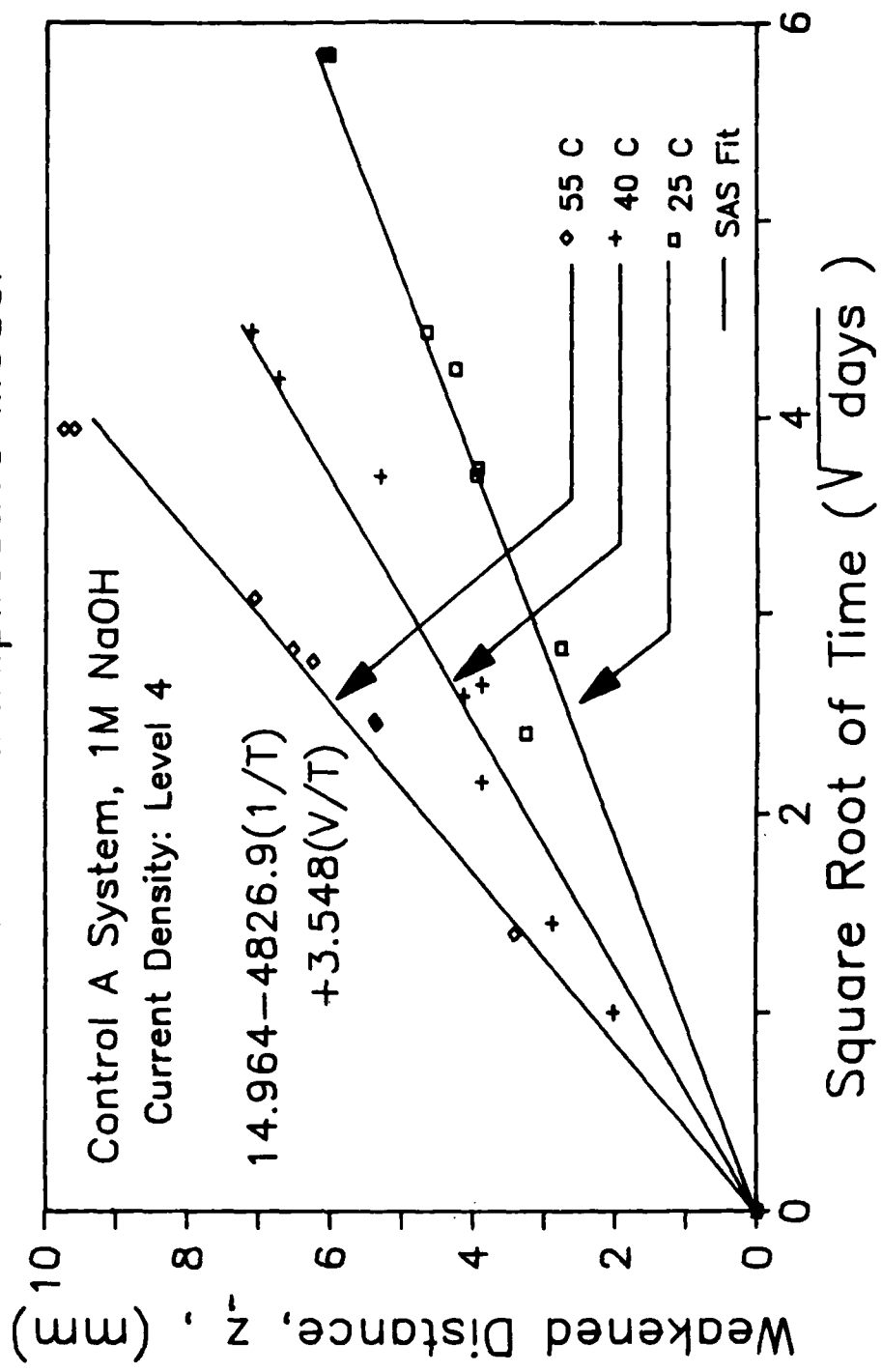


Figure 44. Multiplicative Model SAS Fits of Weakening Data; Voltage effect; BDS Data; 1M NaOH, 25°C.

SAS Fit: Multiplicative Model

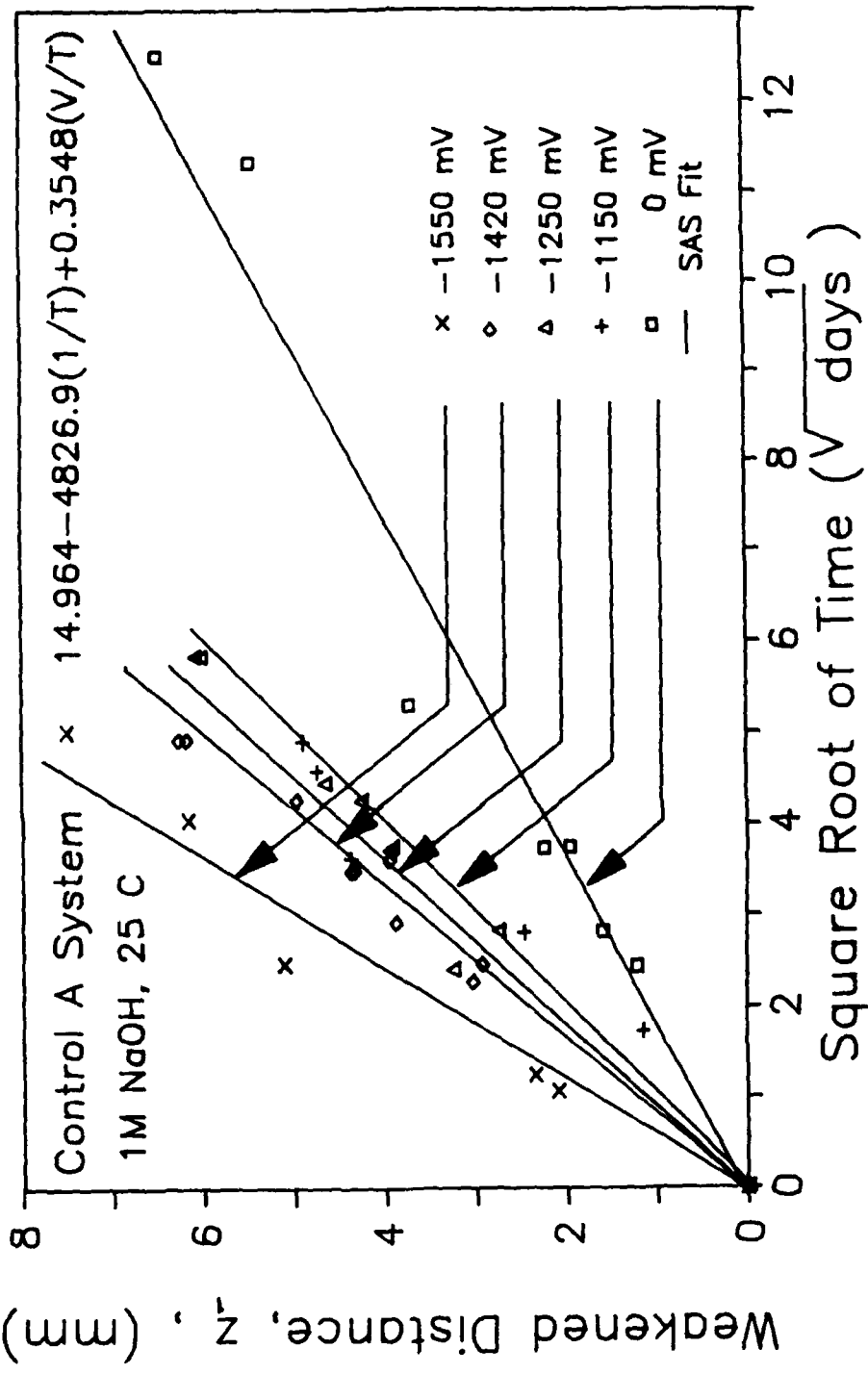


Figure 45. Multiplicative Model SAS Fits of Weakening Data; Temperature effect; BDS Data; 1M NaOH, Current Density 4.

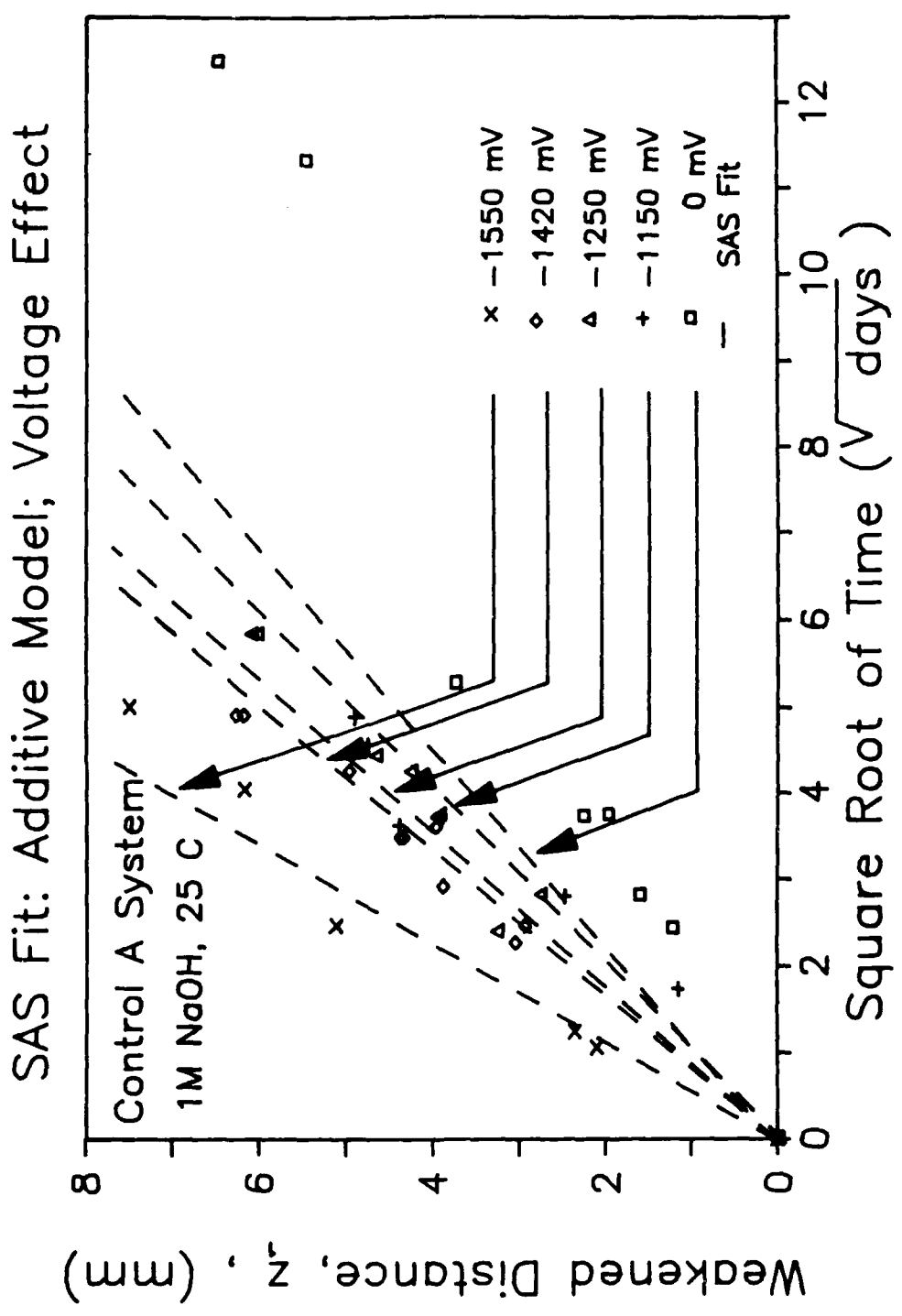


Figure 46. Additive Model SAS Fits of Weakening Data; Voltage effect; BDS Data; 1M NaOH, 25 C.

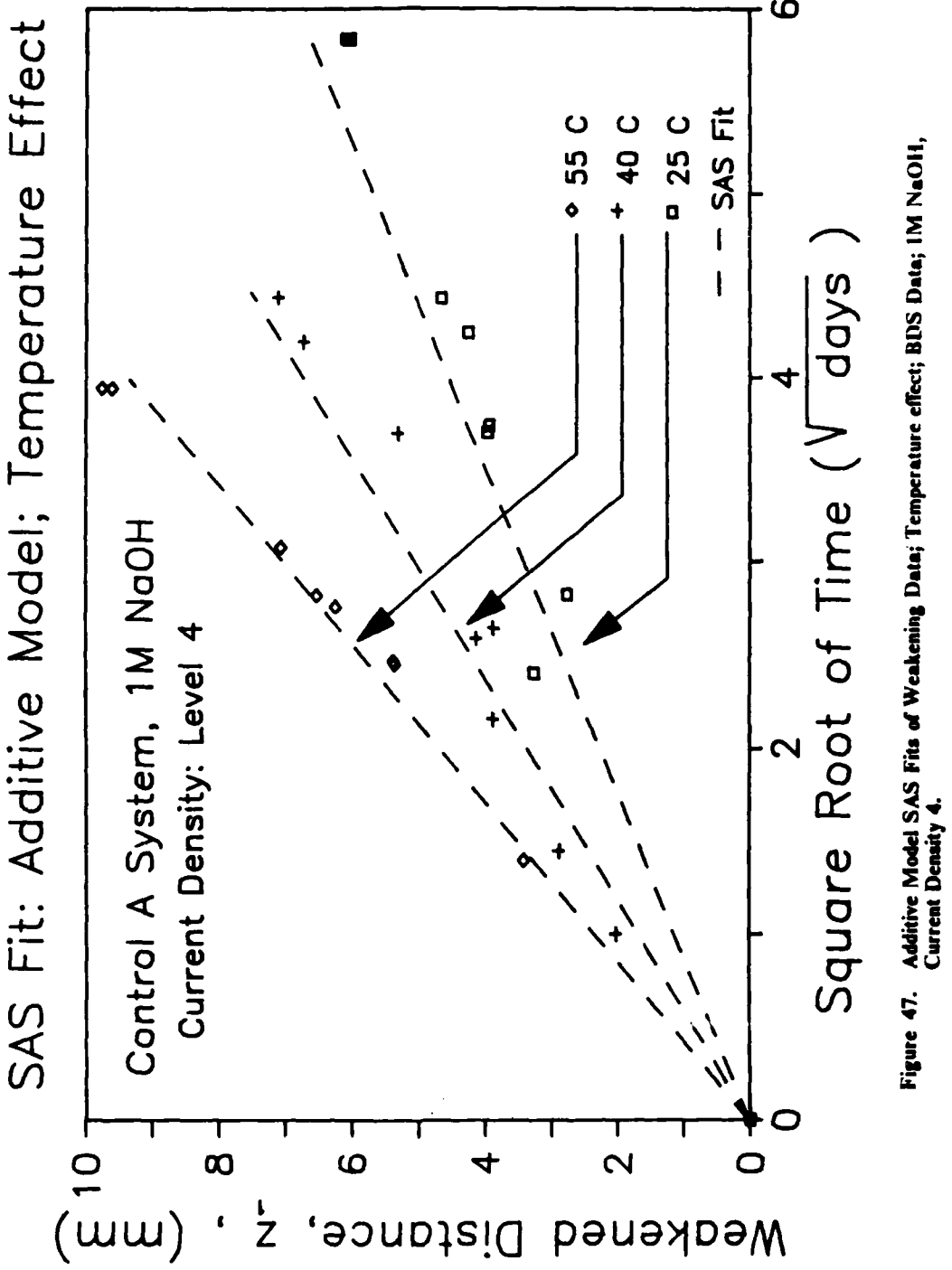


Figure 47. Additive Model SAS Fits of Weakening Data; Temperature effect; BDS Data; 1M NaOH, Current Density 4.

The fits from both approaches show the shifts due to temperature and voltage according to the above equations. However, the multiplicative model is clearly superior because:

- 1) It is capable of both: estimating the physical parameters and of predicting durability. It is also apparent that the coefficients associated with both accelerating parameters (temperature and potential) are statistically significant as expected.
- 2) From a statistical view point, the fit is superior judging by the larger value of the coefficient of determination corresponding to the multiplicative model. Furthermore, the sum of squares for error,

$$SSE = \sum_{i=1}^n (y_i - \hat{y}_i)^2$$

for the multiplicative model was smaller (5.6) than SSE for the additive (22.54) model.

- 3) The multiplicative model is sensitive to changes in the applied voltage as seen by the nice shifts at low or no voltage.

Similar equations were developed for debonding in ASW environment. The model gives the following relation between weakening distance, temperature, voltage, and time

$$\log\left(\frac{z_1^2}{t}\right) = 20.69 - 7564 \cdot \frac{1}{T} + 1.1195 \cdot \frac{V}{T}. \quad [25]$$

with a calculated $R^2 = 0.869$. The respective fits are presented in Figure 48 and 49. This time, the estimated value of the limiting diffusion process is estimated to be about 60 kJ/mole compared to a value of 40 kJ/mole for the NaOH environment. This may be due to the presence of already available OH^- ions in the bulk NaOH solution meaning

that the barrier for diffusion of non-reacting species (H_2O for example) is naturally higher.

4.4 STRESS EFFECTS ON WBPR: COMPRESSION AND SHEAR

The role of tensile stress as an accelerating parameter is discussed in chapter 3. But to summarize, separation of the rubber from the substrate is due mainly to tensile stresses. This is substantiated by the fact that degraded joints have exhibited shear strength (see the durability specimen results in chapter 3) but very low tensile strength. In the following, the discussion will focus on whether compression can be used as a decelerating parameter and to the effect of shear stresses on the WBPR's.

4.4.1 Compressive Stress

A constant load device was utilized to determine the effect, if any, of compression on the rate of cathodic debonding. A spring of constant $k = 91 \text{ kN/m}$ was used to produce the required load. Relaxation of the rubber may have resulted in some stress

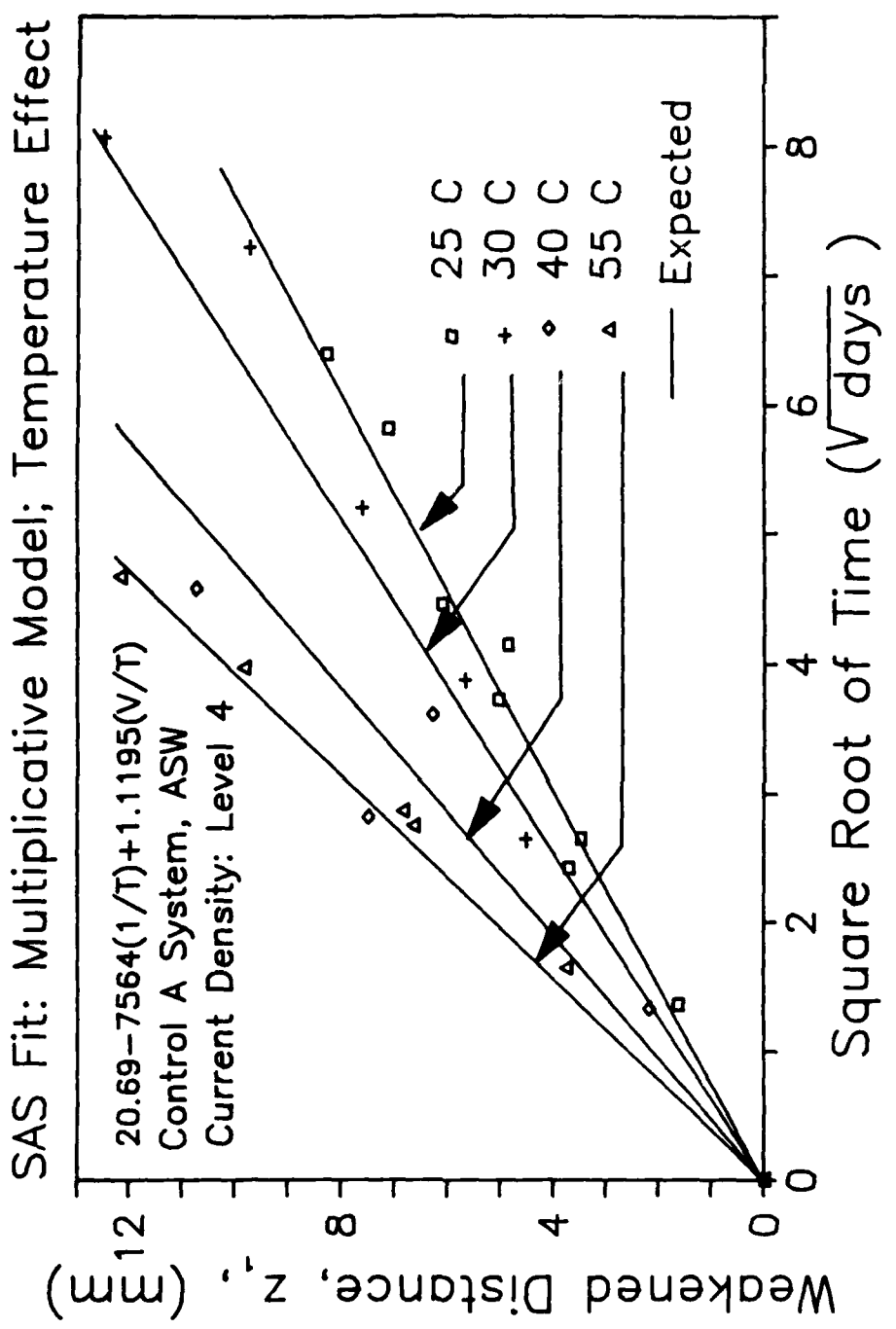


Figure 48. SAS (Multiplicative Model) Fits of Weakening Data; Temperature effect; BDS Data; ASW, Current Density 4.

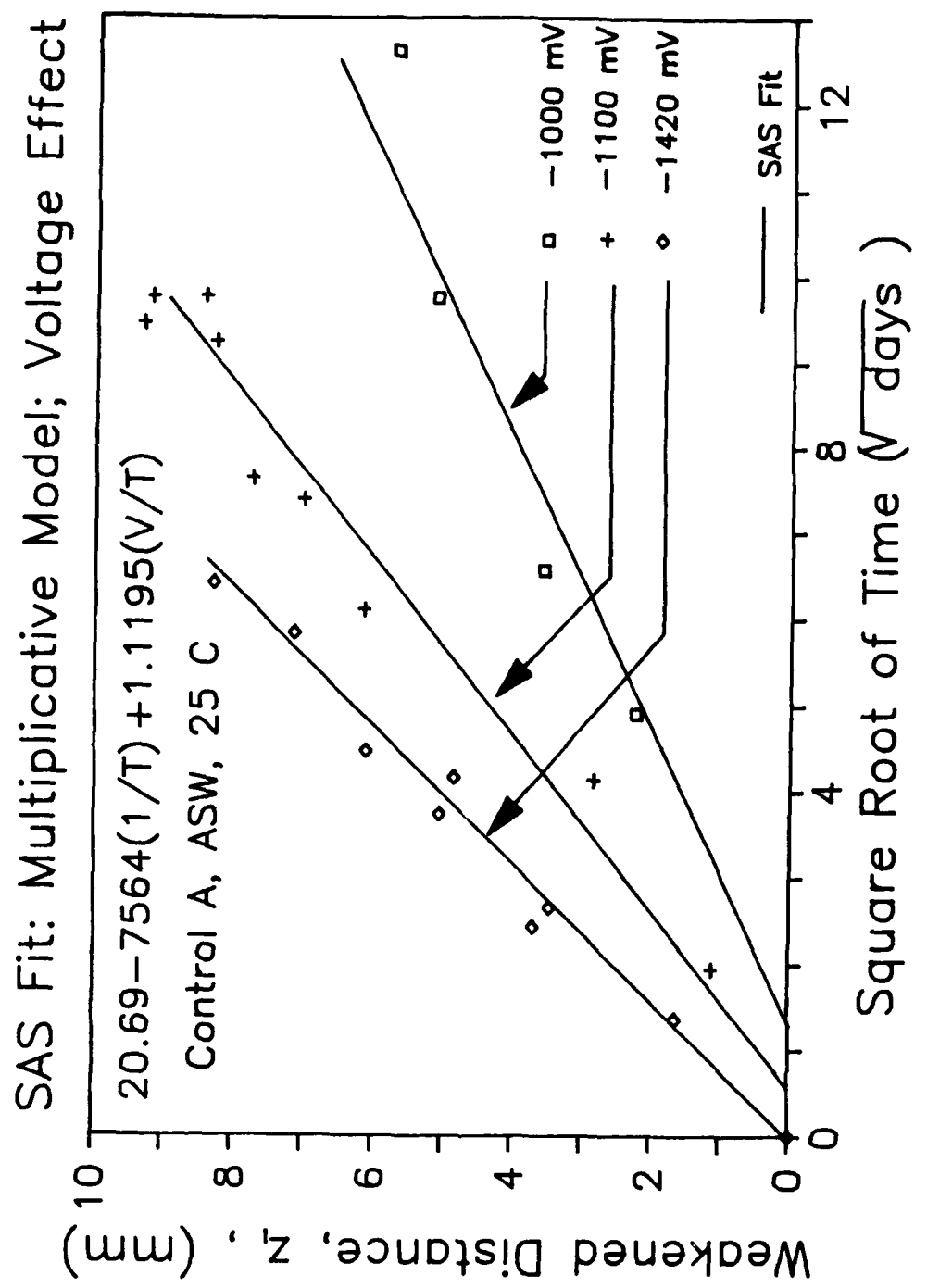


Figure 49. SAS (Multiplicative Model) Fits of Weakening Data; Voltage effect; BDS Data; ASW, 25 C.

decay over the testing period, but should have been very small. According to Gent [36], the compressive stress distribution is expressed by

$$\sigma_{\max} = Ee[1 + 1.179(\frac{w}{h})^2] \quad [26]$$

where E is the rubber modulus (taken to be 4.136 MPa), e is the compressive strain, the bonded block's side is $2w$ and h is the height. The concentrated load was applied at the kern resulting in a distribution of compressive stresses varying from 0 MPa to a maximum of 7.88 MPa (corresponding to $e=0.333$). Figures 50 and 51 show the compression fixture and the expected stress distribution respectively.

Out of a total of 6 BDS's that were tested in 1M NaOH at 30 C, three (#J2, J3, and I15) were exposed to a cathodic potential of -1400 mV. These specimens had a slot cut out through the middle in the longitudinal direction partly to increase the number of exposed edges while the first two were loaded to a maximum compressive stress $\sigma_{\max} = 7.88$ MPa, specimen #I15 was left free of stress for comparison. Figure 52 shows the weakened distances on these specimens after 7 and 10 day exposure times. Compression seems to have little effect on debonding since the weakened distances are fairly equal alongside any given edge for the stressed and the non-stressed specimens. Table 5 shows the outer (corresponding to external edge) and inner (edge of slot) debond distances for both cases.

For comparison sake, more tests were performed on additional BDS's (#J1, K4, and K11) in 1M NaOH with no applied cathodic voltage. Increasing maximum stress levels of 0, 7.88, and 9.5 MPa were applied on these specimens respectively. This time, a clear effect of compression is noticed where Table 5 shows that the average debond has decreased significantly as a function of applied stress. The inner debond profile of #K4 showed almost a complete inhibition of debond towards the regions where the

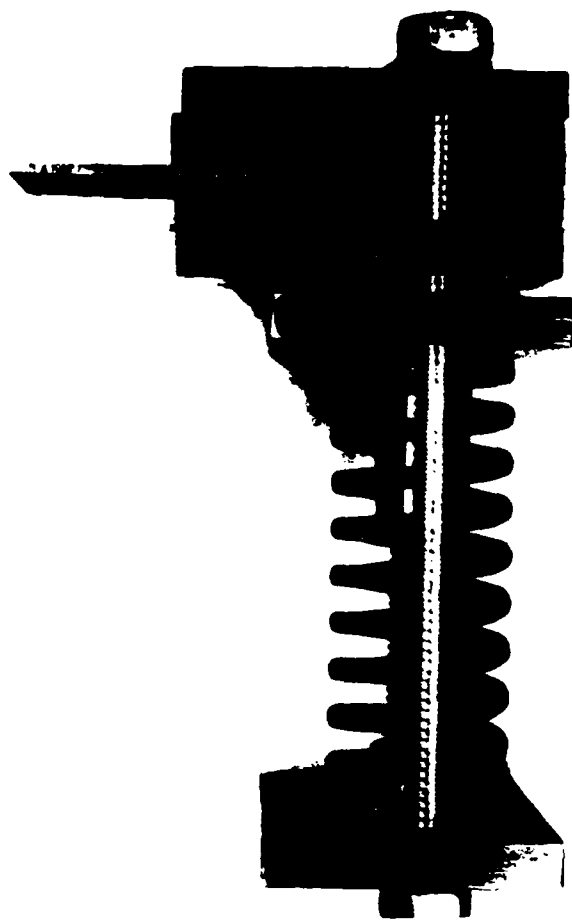


Figure 50. Schematic of the Compression Fixture Used in conjunction with the BDS.

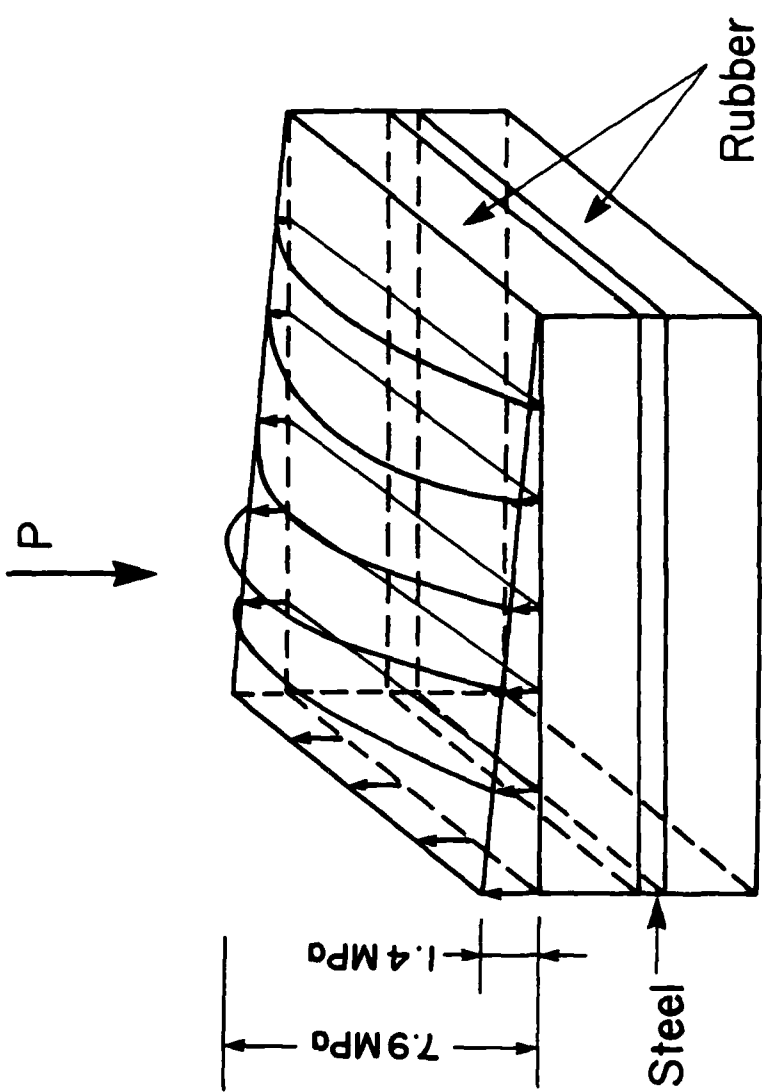


Figure 51. The Expected Compressive Stress Distribution.

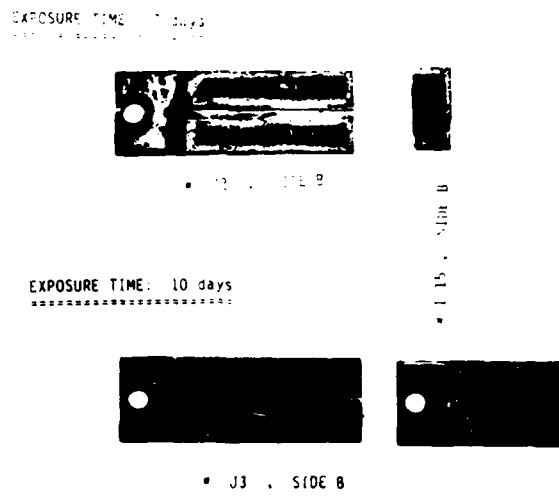


Figure 52. Photograph Showing no Effect of Compression on WBPR with Applied Voltage; Control A, 1M NaOH, -1400 mV, 30C.

Table 5. Influence of Compressive Stress on Bond Weakening; 1M NaOH, 30 C.

P_{max}	200 psi -1400 mV				0 psi -1400 mV	0 psi 0 mV	200 psi 0 mV		234 psi 0 mV
Voltage	#J2		#J3		#I15	#J1	#K4		#K11
Time (days)	Average outer	Average inner	Average outer	Average inner	Average	Average	Average outer	Average inner	Average
7	2.28	3.0	--	2.8	--	--	--	--	--
10	--	--	2.64	3.4	3.3	--	--	--	--
12	--	--	--	--	--	1.9	1.55	1.3	0.76

stresses are expected to be maximum. At the highest stress level, debond was so little after 12 days that we encountered difficulties in measuring the actual debond and in identifying the diffusion profile.

These results may indicate that compression is of little help in slowing cathodic debonding when potential is applied. For the case where mass transport from the bulk to the crack tip dominates, compression seem to play a significant role in slowing down the process. We must mention, however, that TRI [37] has observed an improvement in similar systems when compression was applied while Stevenson [8] reported no improvement after seawater exposure.

4.4.2 Shear Stress

A torsional type specimen was developed to evaluate the influence of shearing stresses on debond rates. Two steel disks were bonded using the control adhesive in a specially designed mold that allows for a non-bonded triangular region through which the bondline is exposed to the environment. After vulcanizing and bonding was completed, a torque is applied on one disk with respect to the other until a maximum shear strain of 152 percent (at the outer radius) was attained, afterwhich two bolts were inserted in a built-in hole in both disks to maintain the configuration. The geometry is not ideal since fairly large peel stresses are introduced at the bond corners due to the large shearing angles. Nevertheless, one would expect a linear distribution of shearing stresses along the bondline with a maximum at the outer radius. A schematic of the specimen and the expected shear stress distribution is shown in Figure 53.

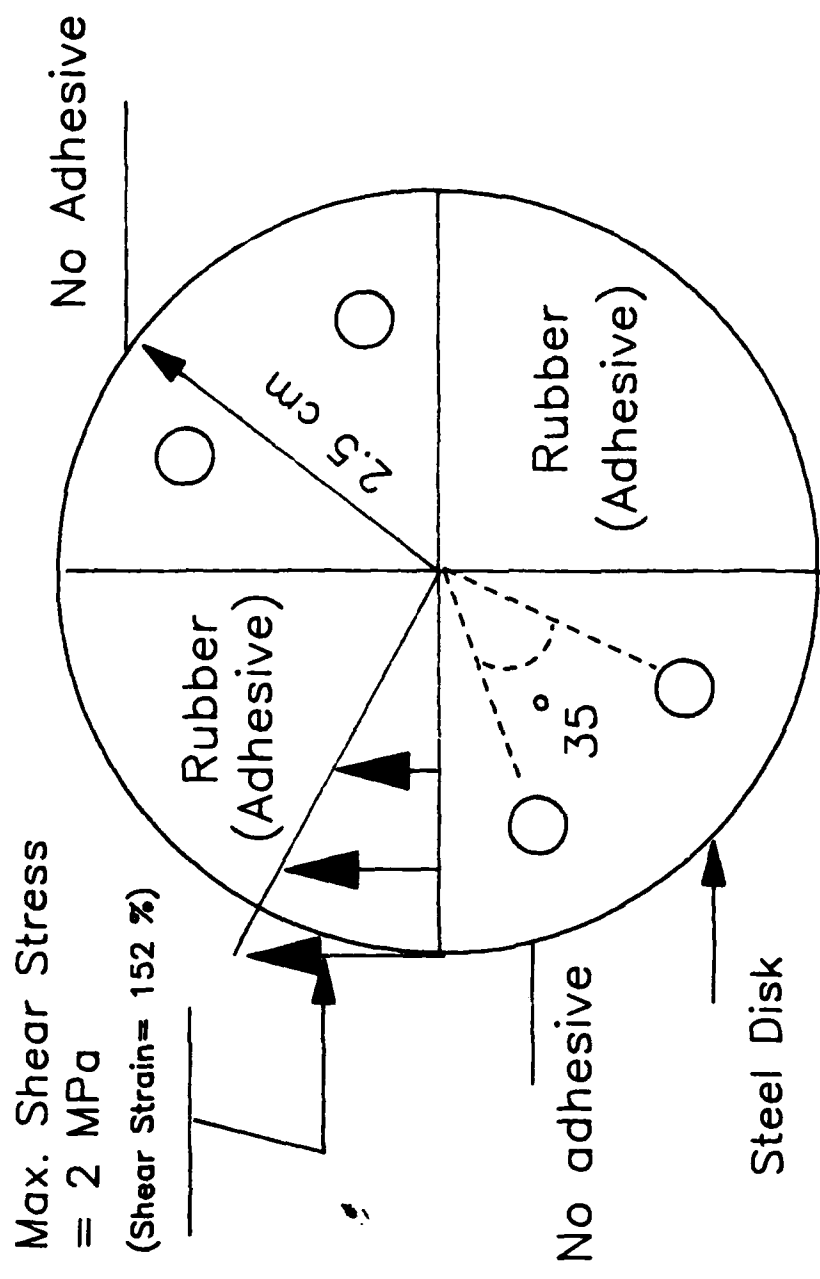


Figure 53. A Schematic of the Shear Specimen (SS) and the Expected Shear Stress Distribution.

Figure 54 shows that after 22 days in ASW, with -1020 mV, and at 30 C debond distances seem to have not been affected by shear. One might have expected to see a similar linear distribution of weakened distances along that line. This is in line with the weakening results from the DS (chapter 3) for which the WBPR's were similar for the loaded sides and for those edges where shear is negligible. The weakened window was of nearly equal width on all sides including the bondline side at about 152 percent shear strain. This may lead us to conclude that mode I is the dominant mode as far as debond propagation mainly, perhaps, due to a "marching boundary" effect.

4.5 CONCLUSIONS

From the above discussion, we have arrived at the following conclusions:

- 1- Voltage affects debond rates through an increase in the corresponding current density at the exposed metal surface. This in turn will increase the pH in the confined environmental crack between the adhesive and the substrate causing the degradation rate to increase. Similarly, diffusion coefficients are very concentration-dependent in this mass transfer controlled mechanism which may result in dramatic changes in the values of those coefficients.
- 2- Temperature seems to influence the diffusion coefficients for this diffusion-controlled process. During weakening, diffusion of OH^- ions, for instance, can increase according to the Arrhenius relationship as a result of an increase of bath temperature. This is witnessed in the substantial increase in the WBPRs following an increase in temperature.

SHEAR SPECIMENS:
ENVIRONMENT : 1 N NaOH, -1.4 V, 30 C.
TWIST ANGLE : 35°.

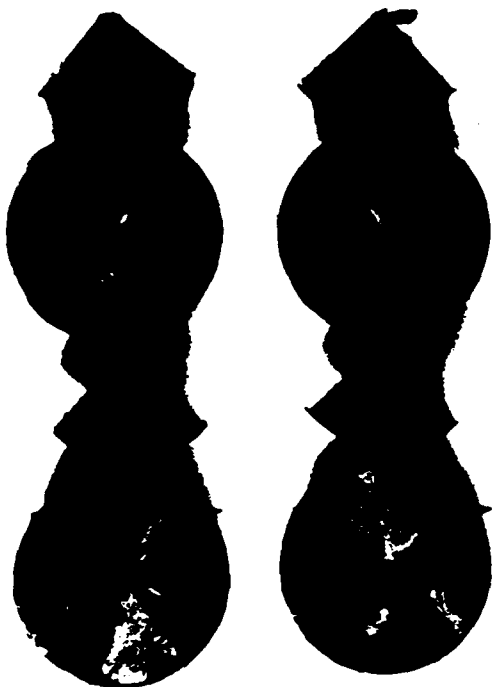


Figure 54. Photograph showing negligible effect of Shear Stress on WBPR; ASW, -1020 mV, 30 C.

3- In the absence of tensile stresses, the constituents of the adhesive bond stay relatively close following weakening, thus favoring a diffusion controlled process. This gives rise to a linear relationship between weakened distances and the square root of time. When tensile stresses are applied on the other hand, the separation (delamination) of these constituents leads to a chemical reaction controlled process and a linear relationship of delamination distances versus time ensues.

4- The application of moderate compressive stresses seems to have little effect on the WBPRs at high voltages in ASW or NaOH solutions. One explanation is that oxygen is not needed at such voltage outputs and any effect of compression (as far as oxygen is concerned) is perhaps innoticeable. At low voltages, however, these stresses seem to play an important role in slowing the diffusion of oxygen (being non-ionic) into the reaction site resulting, perhaps, in impairing the oxygen reduction reaction and ,consequently, weakening.

5- Shear stresses (within the range of data) appear to have no effect on debond rates. One possible explanation is that mode II stresses could not contribute to the "marching boundary" hypothesis. Another possibility is that friction at the rough interface plays an important role in minimizing the contribution of shear.

5. DELAMINATION MODE: CHARACTERISTICS AND MODELLING

5.1 INTRODUCTION

For modelling purposes, caution must be exercised when sorting out the variables of concern to us. As in chapter 4, temperature was treated as an independent variable because of its significant contribution as an accelerated parameter. Voltage, on the other hand, was looked upon in the context of number of generated electrons, and OH^- ions formation. Therefore, we were able to reduce the problem of characterizing the environment into two: current density and temperature.

Generally, environment assisted crack growth is influenced by the environment, the stress, or a combination of both parameters depending on their relative dominance. In conjunction with the environment, the effect of applied tensile stresses in accelerating debonding of adhesive joints is two fold:

1- A direct effect that comes about due to a decrease in the "resisting" strength of the bondline when acted upon by the environment. Consequently, a fracture parameter is needed to serve as a scale factor to define the magnitude of the crack tip active stress field. G , the strain energy strain rate, serves this purpose very well. One possible approach to model this phenomena is through a failure criterion dictated by a balance mechanism between the "resisting", and environmentally degraded, energy and the energy supplied by external stress.

2- An indirect effect due to the "marching boundary" phenomena that results in minimizing the resistance due to mass transfer. This will favor a chemical reaction control mechanism. This could best be modelled through a numerical procedure that will take into consideration the degradation kinetics, the diffusion parameters, and a failure criterion. This approach is explained in more details in chapter 6.

Input from the real life application needs to be taken into consideration to determine whether the environment, the applied loads, or a combined effect will determine the failure mode.

5.2 *DELAMINATION DATA*

G_c of the dry bond was determined [38] using a double cantilever beam (DCB) specimen to be about 15 kJ/m^2 (failure apparently interfacial) while that of a degraded bond is on the order of $.0175 \text{ kJ/m}^2$. One can assume that actual separation of the bond in the weakened state will take place given that G_T exceeds G_c over a finite region ahead of the crack tip. Such a failure criterion is reinforced by the fact that delamination

rates almost always decrease as a function of time (increasing crack length). A by-product of this is that diffusion distances become shorter, compared to those of a weakened bond, resulting in an accelerated delamination and in a minimized contribution of the mass transfer process. This failure criterion will be discussed in more details in chapter 6.

5.2.1 Influence of Temperature

Figure 55 shows temperature to play a major role in accelerating the DBPR in a fashion similar to that with the WBPR. Compared to the same conditions as in Figures 33 and 34, the severe effect of tensile stress when coupled with temperature is clear. After 5 days in 1M NaOH at 40 C, delamination totaled about 27 mm relative to about 4 mm of weakening. Again, we feel that the rapid build-up of calcareous deposits at the steel/rubber bondline is detrimental in masking the true contribution of temperature in ASW solution

Adhesive system Modified B seems to obey the same trends as the control as far as temperature dependency. Figure 56 clearly illustrates the influence of temperature on the DBPR of the modified system. For instance, after 10 days in a 1M NaOH solution at current density level 4, the delaminated distances were about 3, 9, and 14mm for 25, 40, and 55 C respectively. Similar trends can be seen in ASW solutions. Scatter was noticed to increase for higher temperatures (and understandably, higher DBPRs). Therefore, the arithmetic averages of the four delaminated fronts were plotted in a line for every specimen.

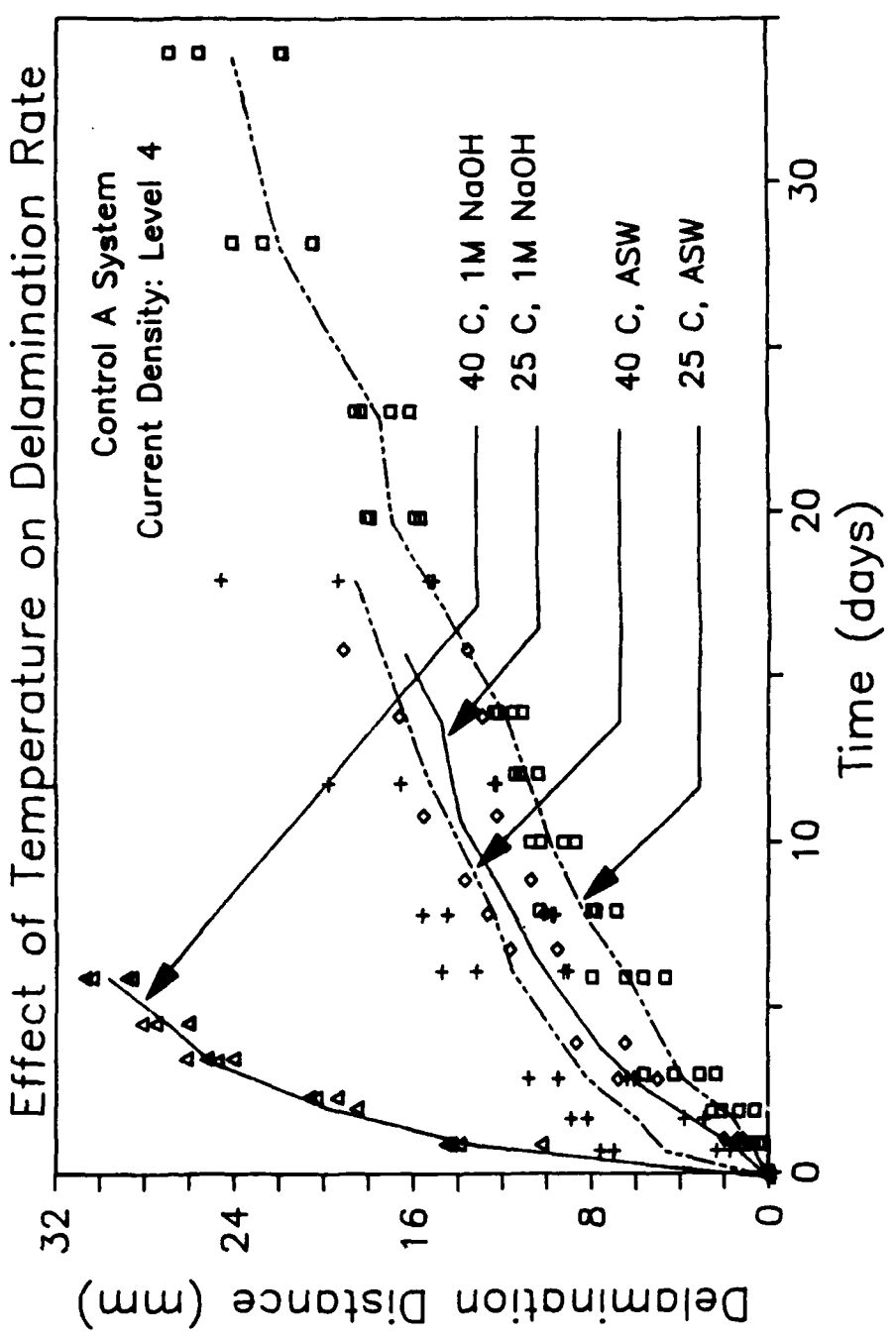


Figure 55. Temperature Effect on the DBPR; Control A; Current Density 4.

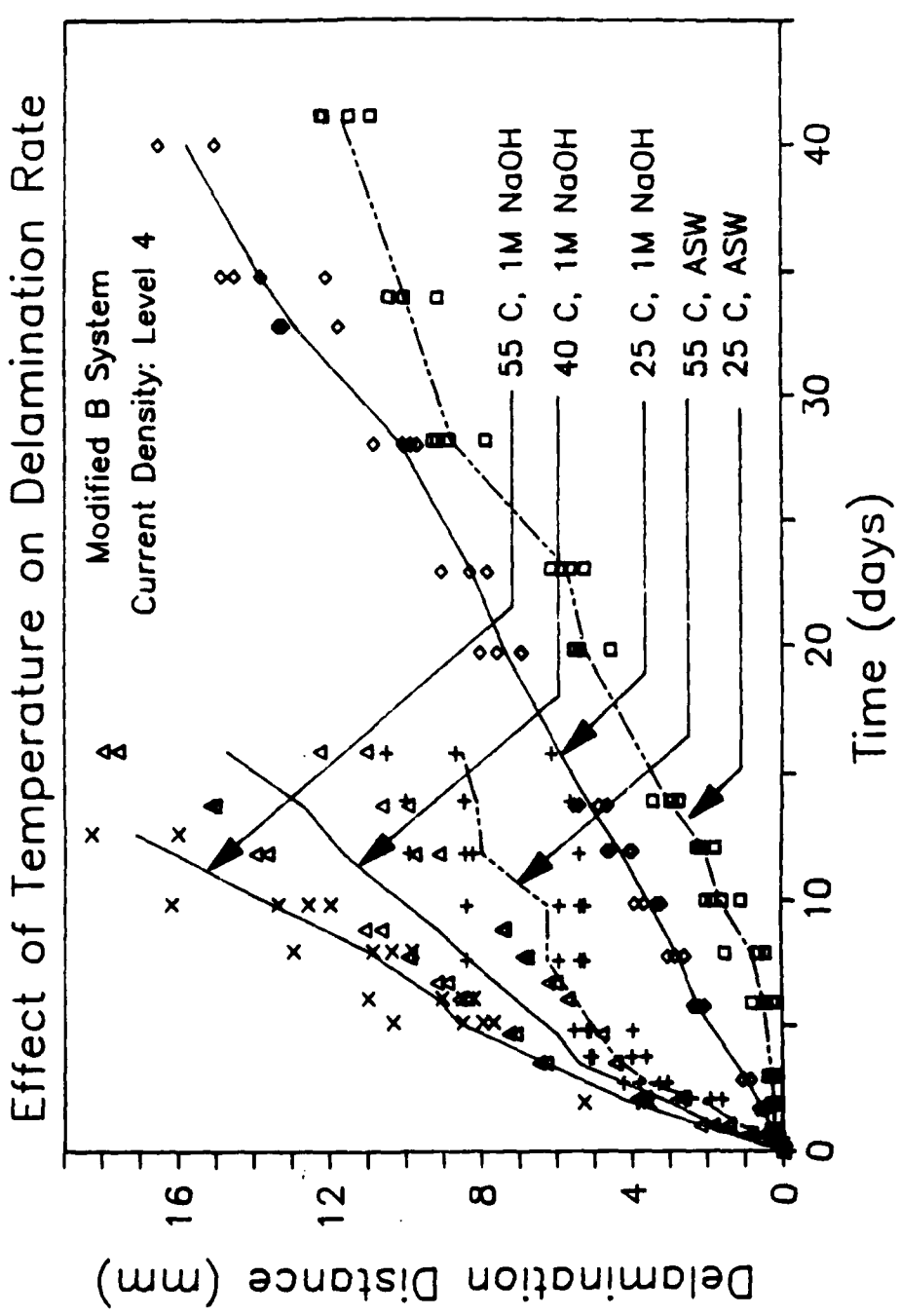


Figure 56. Temperature Effect on the DBPR; Modified B; Current Density 4.

5.2.2 Influence of Voltage

An interesting observation in Figure 57 is the sharp increase in the DBPR for a -100 mV increase in the cathodic potential. The current density ratio (from Table 3) for -1100 and -1000 mV is only 1.475 while the ratio of the initial slopes (DBPR's) is considerably higher for those potentials. As the potential increases to -1420 and -1825 mV, current density ratios increases while the ratios of the initial DBPR's lag behind. One possible reason for the lack of correspondence of DBPR to current ratios is that, at such high levels of current, most of the generated OH^- ions get buffered into the bulk solution away from the crack. Another explanation could be that the steel surface passivates rapidly at such high voltages resulting in a considerable decrease in the corresponding current densities. Contrasting Figure 57 (delamination) with Figure 36 (weakening), the delay times have almost vanished for the stressed bonds. To illustrate the strong influence of Mode I stresses, after 20 days the environment (voltage) assisted crack propagation was 0.7, 4, 16, and 22mm at -1000, -1100, -1420, and -1825 mV respectively.

Figure 58 shows the influence of voltage on delamination of the control system in 1M NaOH. This is most dramatically demonstrated when contrasting the data from the -900mV level and the remaining potentials. It is feasible to think that the control system is very sensitive to high pH concentrations, and that its environmental resistance diminishes considerably at higher pH levels (potentials over -900mV). The DBPR's tend to decrease as a function of time, supposedly because of a significant reduction in the value of G_c at such large delamination distances.

Delamination history of system (A-1100 modified) B in ASW at 25 C is presented in Figure 59. Similar trends to those of system A are observed, except, perhaps that the

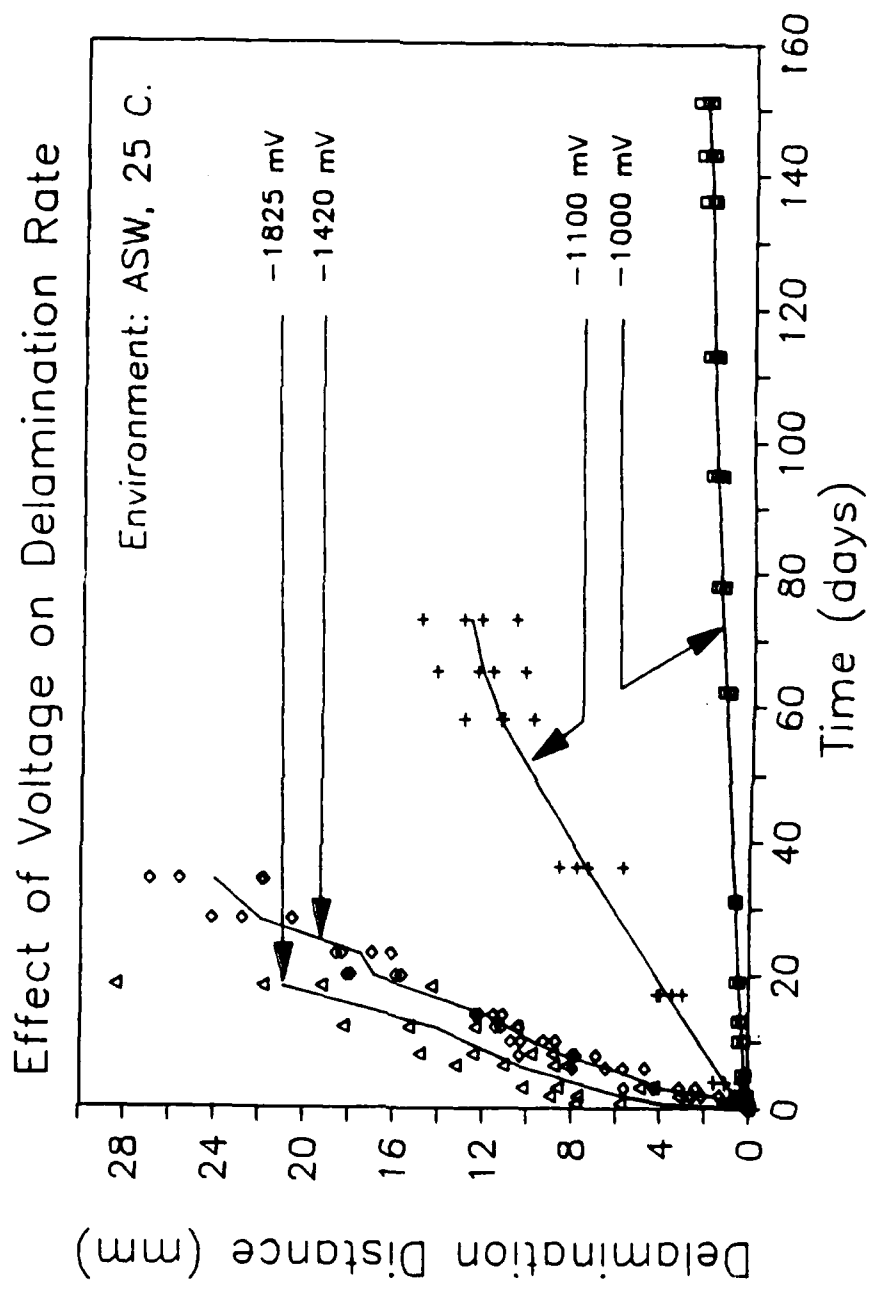


Figure S7. Voltage Effect on the DBPR; Control A; ASW, 25 C.

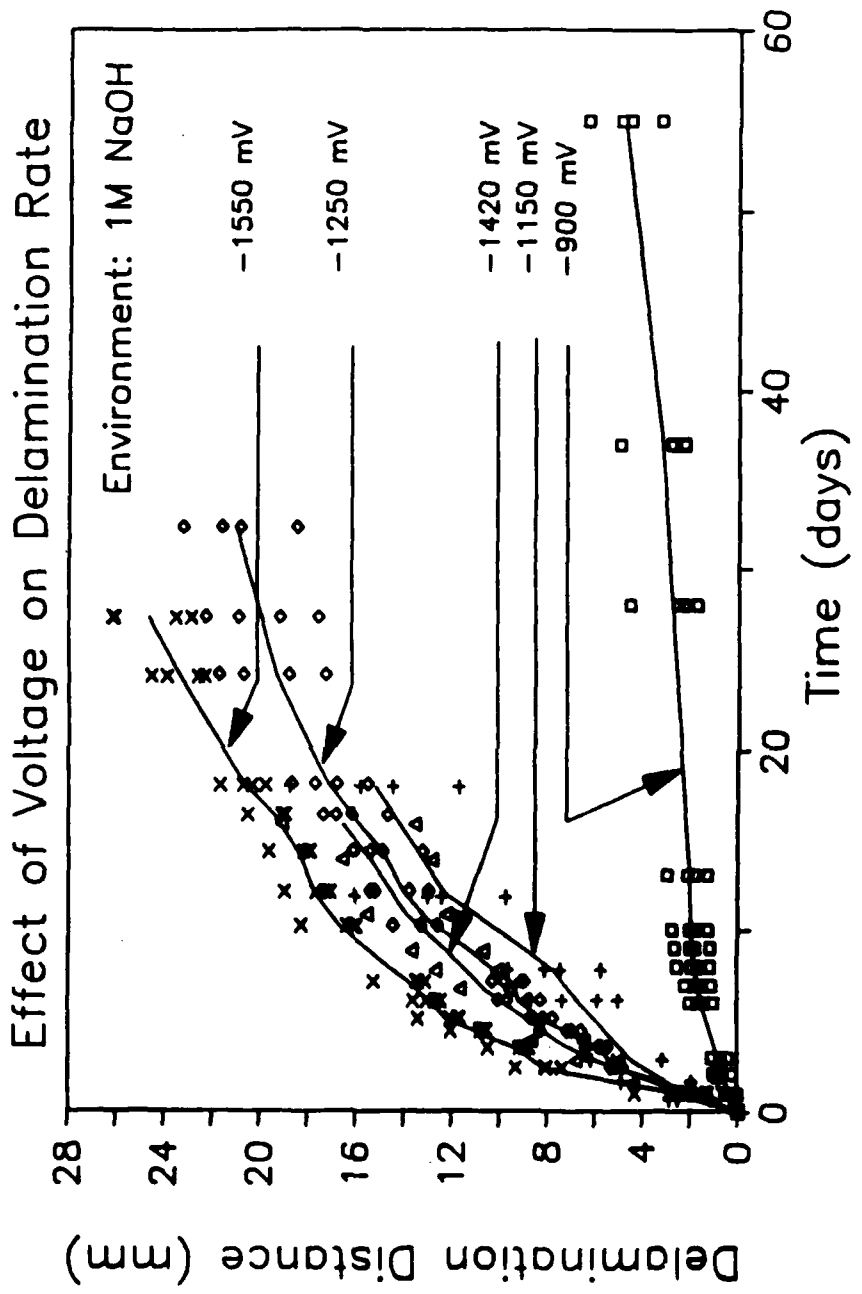


Figure 53. Voltage Effect on the DBPR; Control A; 1M NaOH, 25 C.

DBPR's are lower (meaning a better durability) and that the build-up problem is more pronounced. The slopes of the specimen at -1420 mV are the steepest after apparently anomalous data in the early stages. Figure 60 shows that the silane modified system is similarly affected by increasing potential. Dependency on voltage is somehow clearer in NaOH than in ASW possibly due to the absence of passivation. It seems, also, that the initial DBPR's are comparable for all the potentials.

5.3 MODELLING DELAMINATION

From the data in chapter 2 and above, the DBPR's seem to be very sensitive to externally applied tensile stresses. Liechti [39] has shown that G_T for the strip blister geometry is dominated by G_I for the entire crack path. Some question may be raised as to the validity of using $G_I + G_{II}$ as a fracture parameter rather than simply G_I . Nonetheless, Liechti [40] used the experimentally determined principal stretches, λ_i , of the neoprene rubber to determine the strain energy function, $U(\lambda_i)$, according to Peng [41]. From continuum mechanics, the total potential energy of the joint is expressed as

$$\pi(X, x) = \int_{V(x)} U(X, x) dV - \int_{V(x)} f(x - X) dV - \int_{S(x)} t(x - X) dS \quad [27]$$

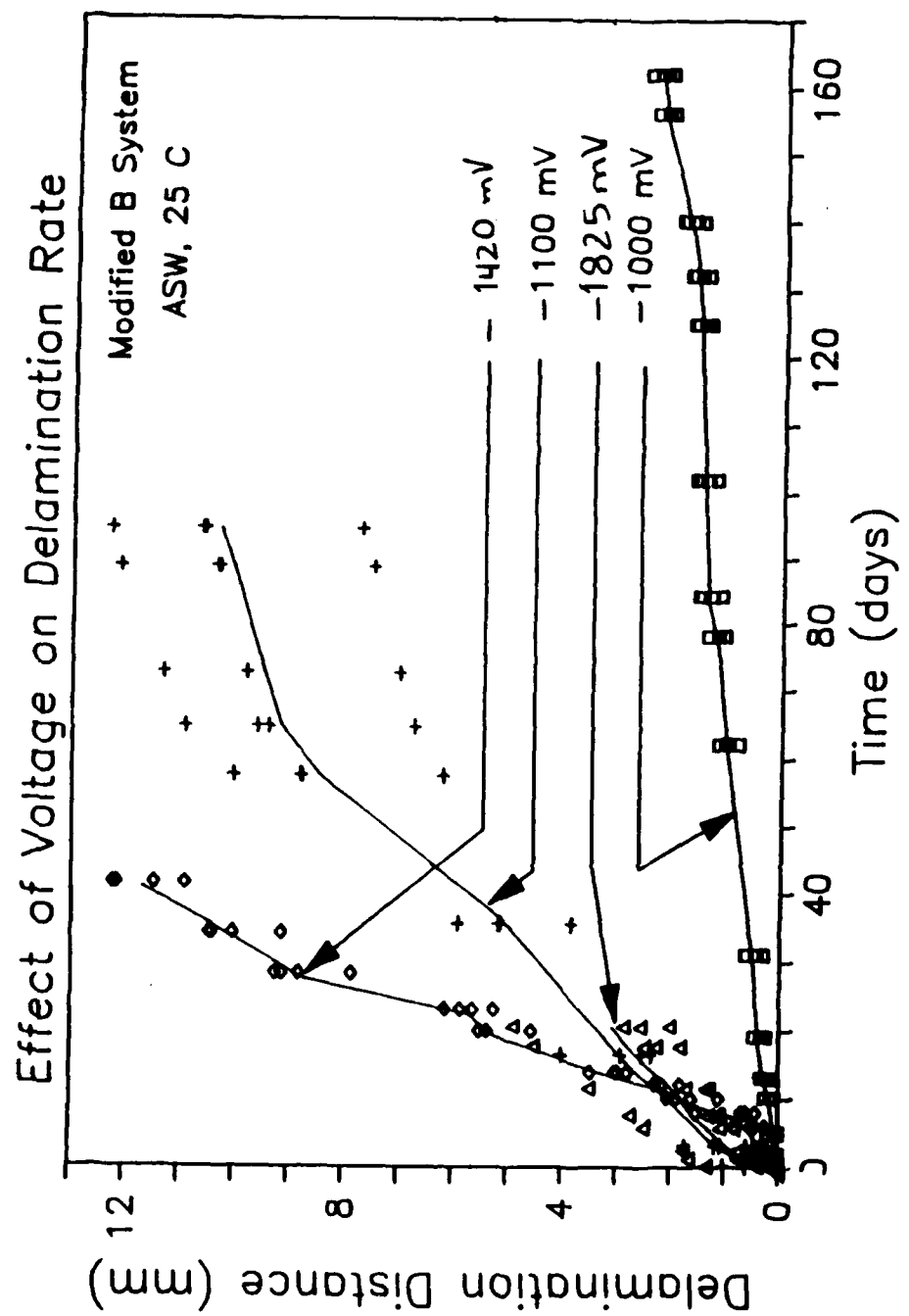


Figure 59. Voltage Effect on the DBPR; Modified B; ASW, 25 C.

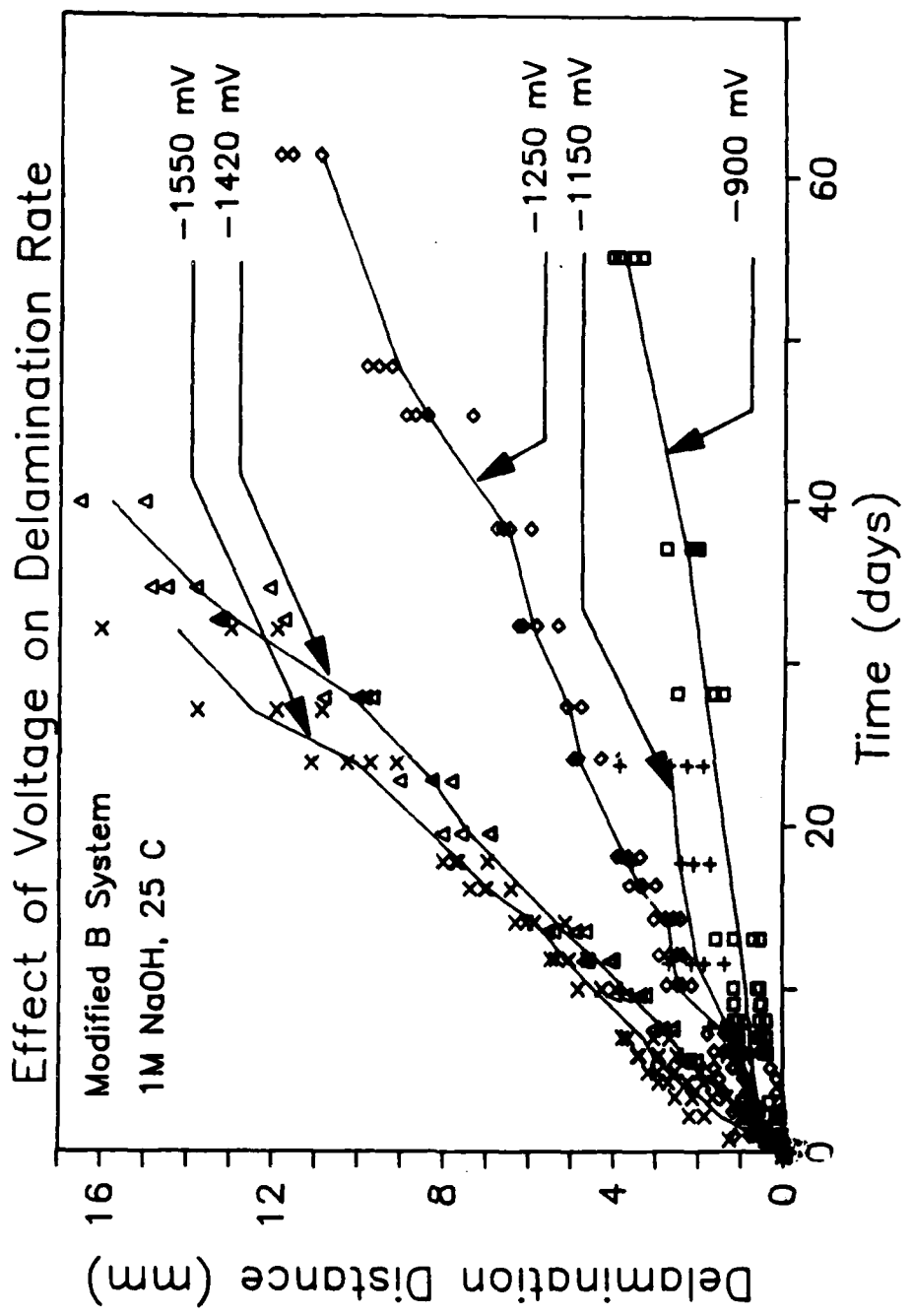


Figure 60. Voltage Effect on the DBPR; Modified B; 1M NaOH, 25 C.

where X and x are the undeformed and deformed nodal arrays, $V(x)$ and $S(x)$ are the deformed volume and surface of the body, and f and t are the body and surface tractions, respectively. He then incorporated the relationship

$$G_T(X,x) = \frac{1}{\delta a} \frac{\partial \pi(X,x)}{\partial X} \delta X \quad [28]$$

into the code TEXPAC-NL in order to calculate G_T as a function of delamination for the Strip Blister Specimen.

The resulting G_T solution is a function of rubber thickness (t_R) and the imposed deflection (d) and a graphic representation which describes the decay of G is shown in Figure 61. A fourth order least squares fit of the form

$$G_T = b_0 + b_1 a + b_2 a^2 + b_3 a^3 + b_4 a^4 \quad [29]$$

was obtained in order to interpolate. The coefficients for each load (dowel diameter) and rubber thickness are presented in Table 6.

5.3.1 Influence of G on the DBPR

Similar to crack growth in metals and glass, one needs to characterize the kinetics of crack growth rate as a function of fracture parameters and environmental effects. Because a singularity prevails at the crack tip and the stresses become theoretically infinite, a relationship involving the strain energy release rate, G , is desirable. A typical [42] da/dt vs. G relationship of an adhesively bonded system under stress corrosion

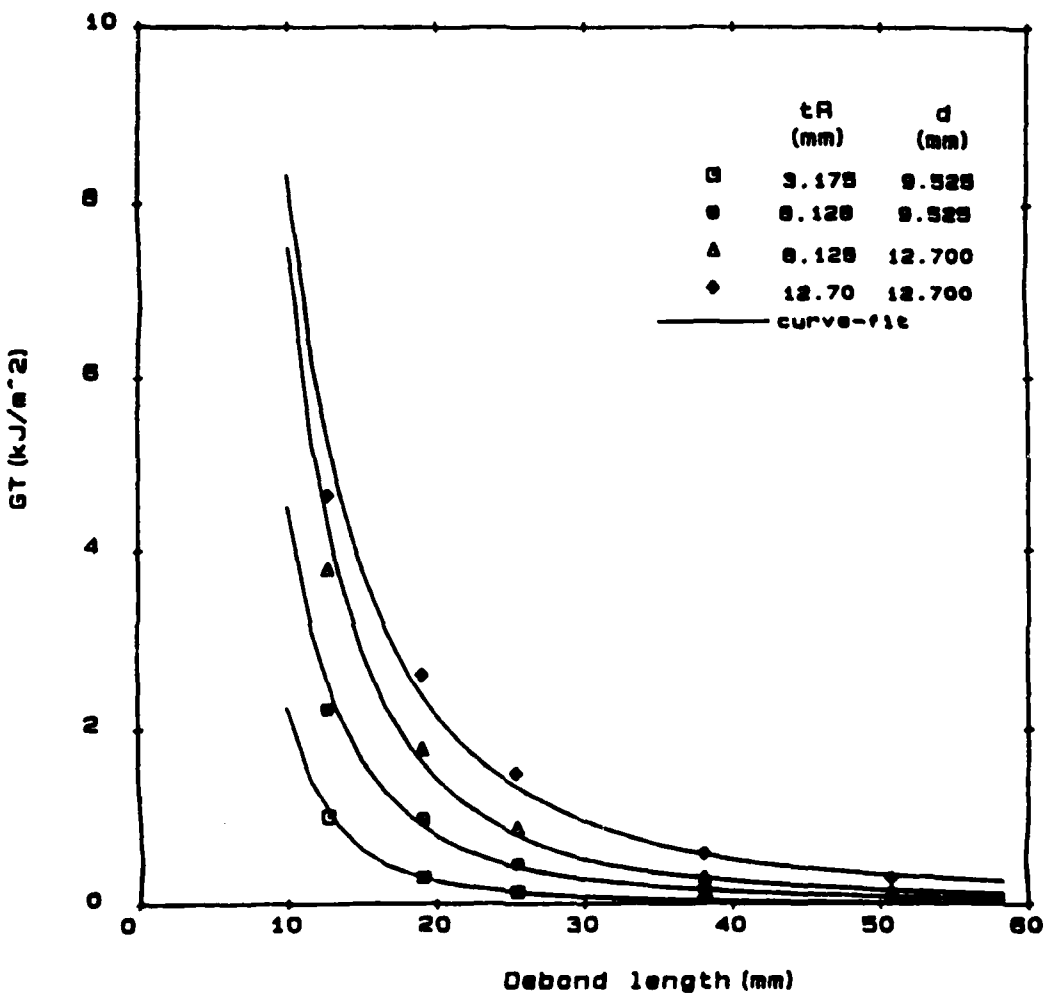


Figure 61. Total G vs. Delamination Distance as a Function of Rubber Thickness and Dowel Diameter.

Table 6. Applied G variation with a (crack length);

$$G = b_0 + b_1 a + b_2 a^2 + b_3 a^3 + b_4 a^4$$

t_R (mm)	d (mm)	G_0 kJ.m ²	b_0	b_1	b_2	b_3	b_4
3.175	9.525	1.044	6.462	-0.7627	0.03426	-6.76E-04	4.88E-06
8.128	9.525	2.241	9.341	-0.9302	0.03697	-6.66E-04	4.50E-06
8.128	12.7	3.798	14.99	-1.4498	0.05639	-1.0E-03	6.69E-06
12.7	12.7	4.625	13.712	-1.0912	0.03619	-5.63E-04	3.387E-06

cracking may take on any of the two forms shown in Figure 62. Three distinct regions exist in a fashion similar to that for other systems. However, some bonds apparently exert a G-dependent behavior in region II while others show no sensitivity. In the latter case, the environment (including temperature) exclusively determines the kinetics of the process of debonding in this region while stresses do not play any role within the second region.

Figure 63 shows a typical dz/dt vs. G curve where experimental delamination data was used. All four specimens were bonded using Chemlok 205/220 and exposed to ASW at 25 C but at different current densities, i.e., 2,3,4, and 5 corresponding to -1000, -1100, -1420, and -1825 mV (SCE). The scatter is typical of a "stair step" phenomena in which the degradation process is complemented by a stress influence resulting in a localized failure whenever $G_T \geq G_c$ is locally satisfied. The influence of voltage is apparent in that the higher the current density the harsher the pH and, thus, the faster the reaction kinetics. The increase in region II delamination rate with increasing voltage can be described mathematically in a form similar to that for diffusion in Equation 19 where the reaction rate, k_e , (or $DBPR_e$) becomes

$$k_e = k_0 \left\{ \exp\left(-\frac{U^*}{RT}\right) k \exp\left(-\frac{\beta FV}{RT}\right) \right\} \quad [30]$$

or,

$$DBPR_e = DBPR_0 \left\{ \exp\left(-\frac{U^*}{RT}\right) k \exp\left(-\frac{\beta FV}{RT}\right) \right\} \quad [31]$$

The tabulated G values in Table 6 indicate that one way to control the initial value of G is to modify the thickness of the rubber or the imposed deflection (dowel diameter). Considering the high value of G_c (about 15 kJ/m²), the SBS data is most suited to model region II. In order to better characterize region II's dependency on G,

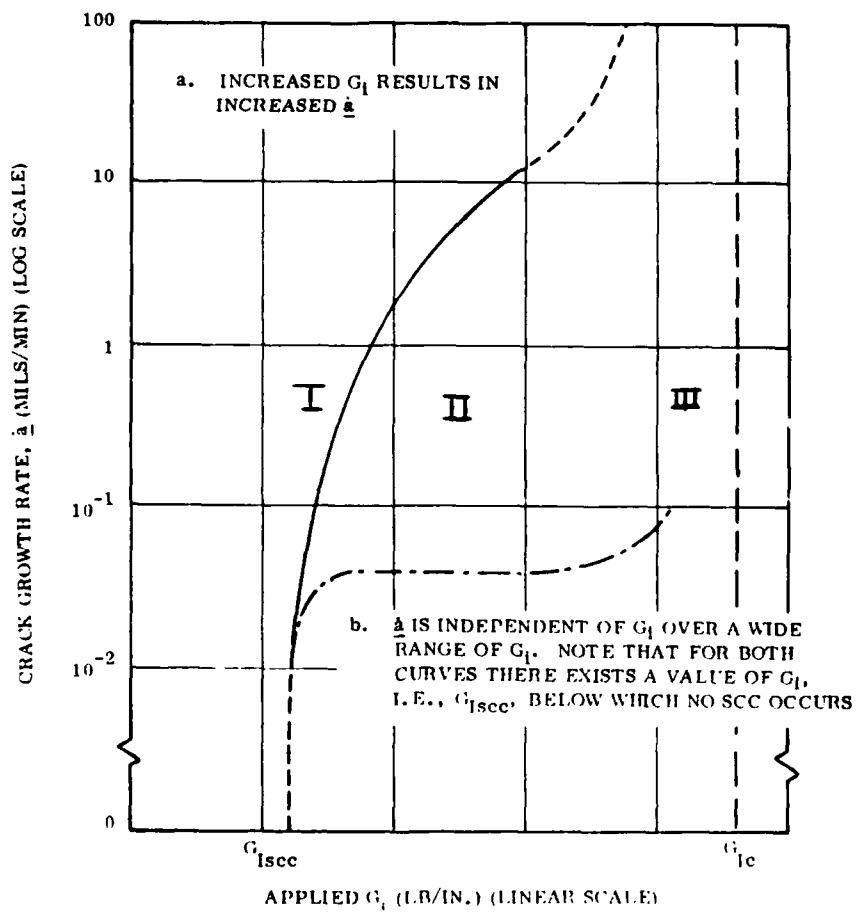


Figure 62. Typical Dependence of da/dt on G for Stress Corrosion Cracking of Adhesive Bonds (from [42]).

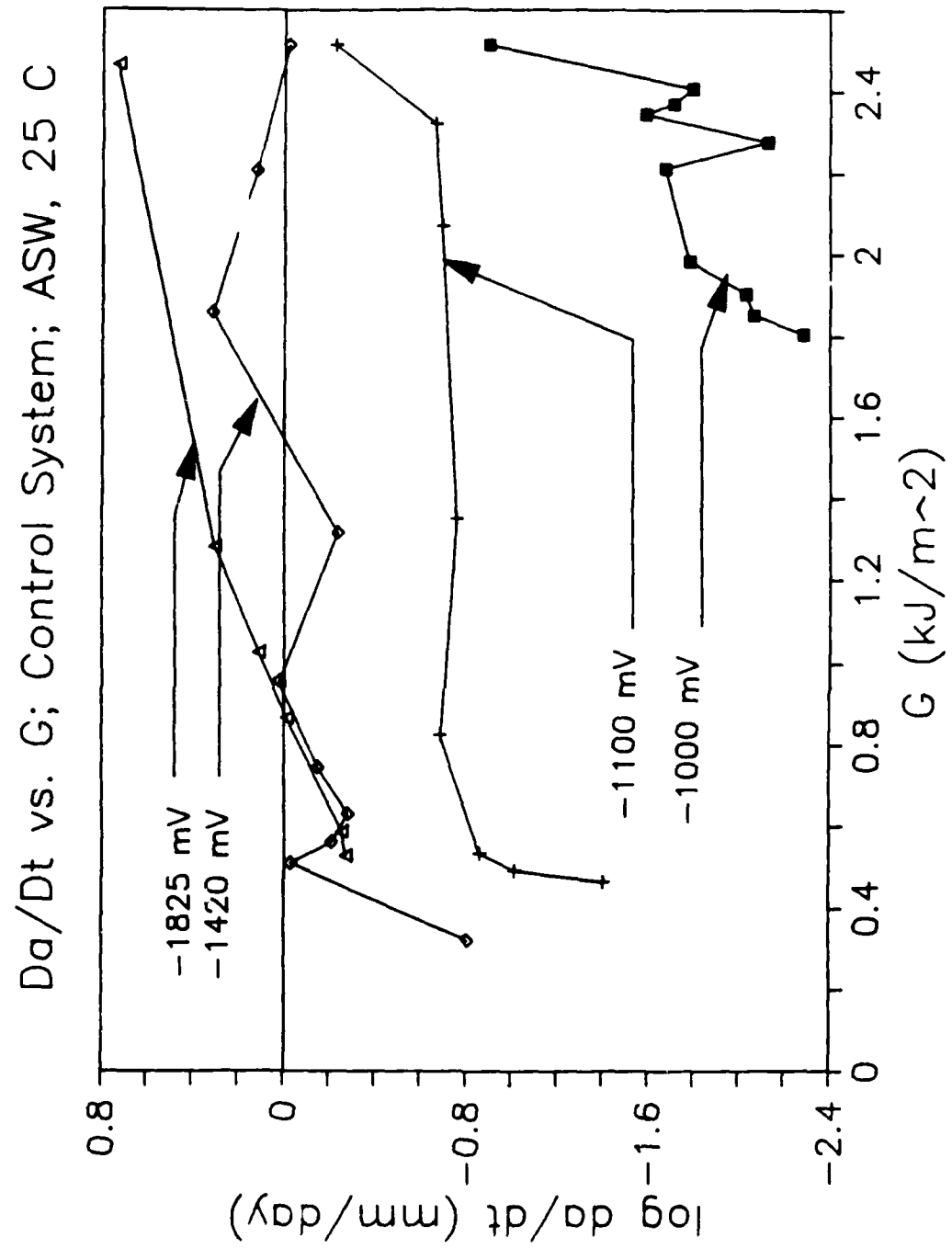


Figure 63. A Typical $d\alpha/dt$ vs. G; Effect of Voltage on the DBPR.

Dr. Liechti et al, at the University of Texas at Austin, have collected experimental data of up to about 4.6 kJ/m^2 . Figure 64 illustrates some of that data, and is presented along with a representative set of data collected at VPI for lower applied G range. This example figure reveals several interesting trends although the apparent scatter calls for some concern on our part. Repeatability is excellent in the same bath; however, the DBPR's within the same G range are about an order of magnitude larger for the two specimens #UT1025 and #UT1026 than their counterparts #UT27 and #UT904. Two possible explanations are: 1) the applied potentials were erroneously different or 2) the quality control during bonding is somehow flawed. Note that although "stair stepping" is almost unnoticeable at large G values, the phenomena is clearly identified (by the jagged line) at lower G's (for example in #UT1025 and #UT1026). Although some degree of built-in randomness exists in this data (due to the arbitrary nature of quality control and the duality of the testing institutions), the figure shows an increasing trend in the DBPR's with increasing applied G.

Following the above procedure, debond data for both systems in ASW and NaOH environments were plotted all temperature, voltage, and G ranges. Figures 65-68 present this data on a base chart for comparison. Different data sets are identified by their numbers, the testing institution, and the environment. Again, an increasing trend of the DBPRs with G is clear in all systems. These graphs could be used to determine the delamination rate under any condition, and integration in real time could be performed as will be discussed in the following discussion.

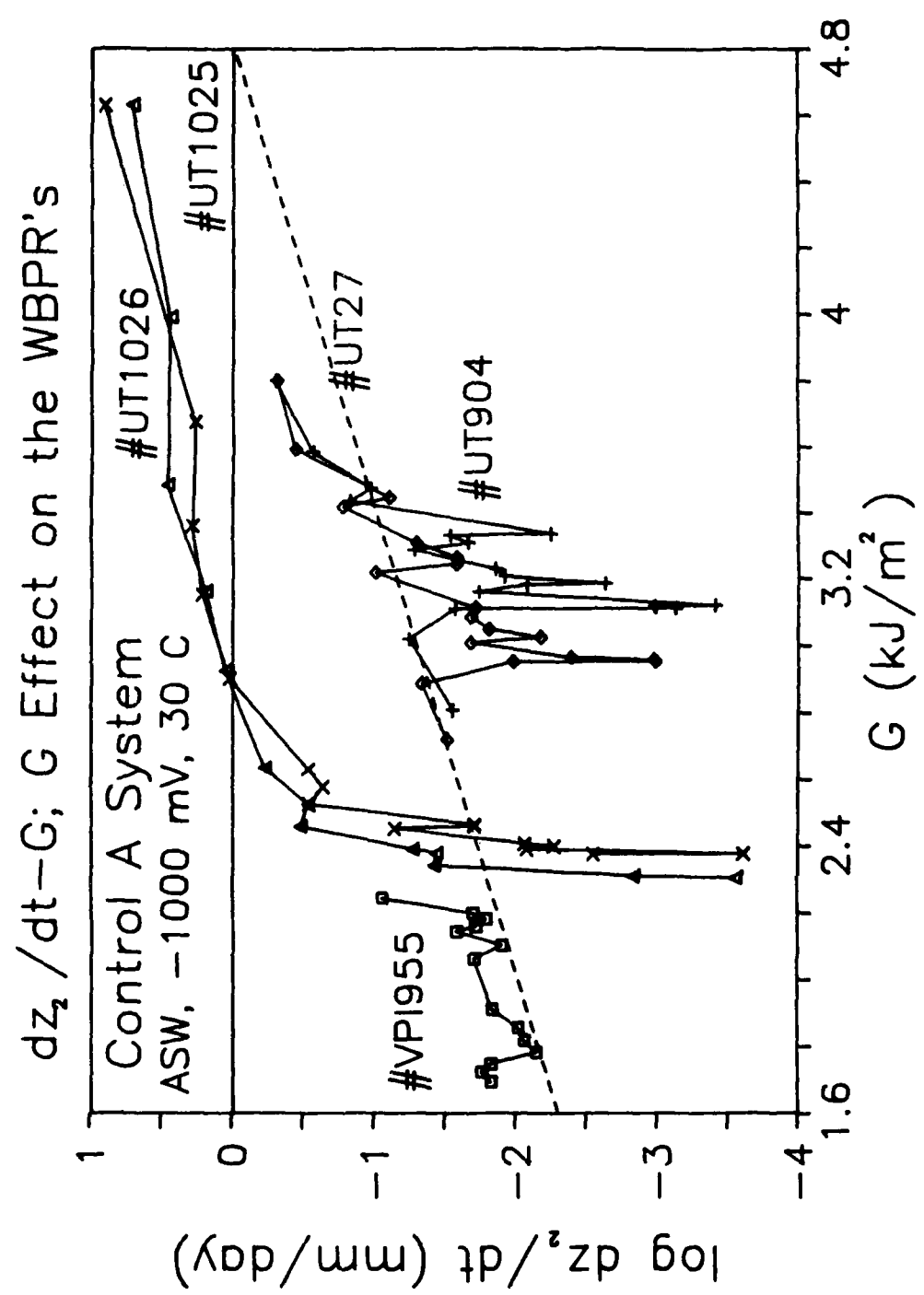


Figure 64. Effect of Increased G on the DBPR; Control A; ASW, -1000 mV, 30 C; Note that Applied G Varies with Dowel Diameter.

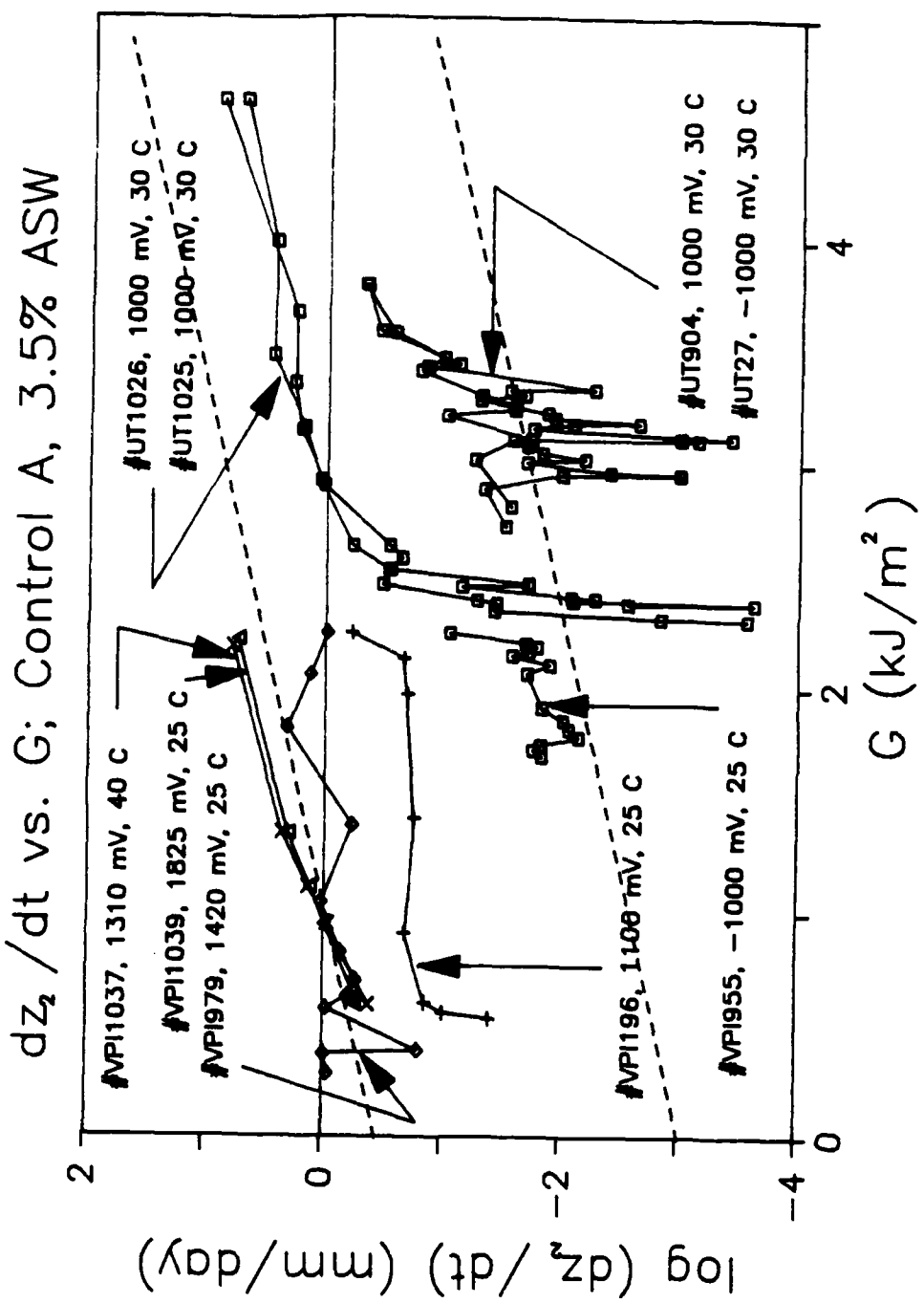


Figure 65. Effect of Voltage, Temperature, and G on the DBPR; Control A; ASW.

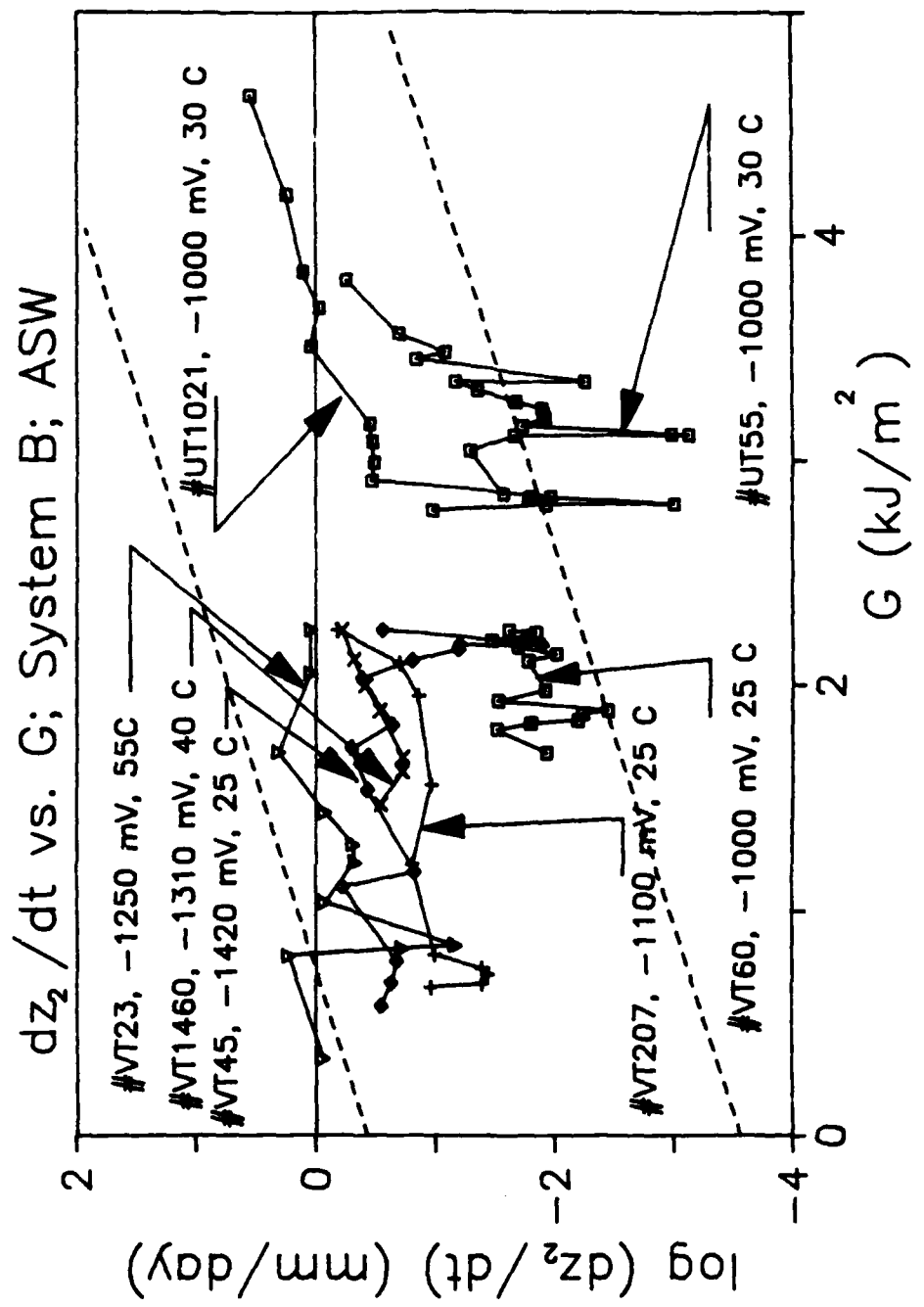


Figure 66. Effect of Voltage, Temperature, and G on the DBPR; Modified B; ASW.

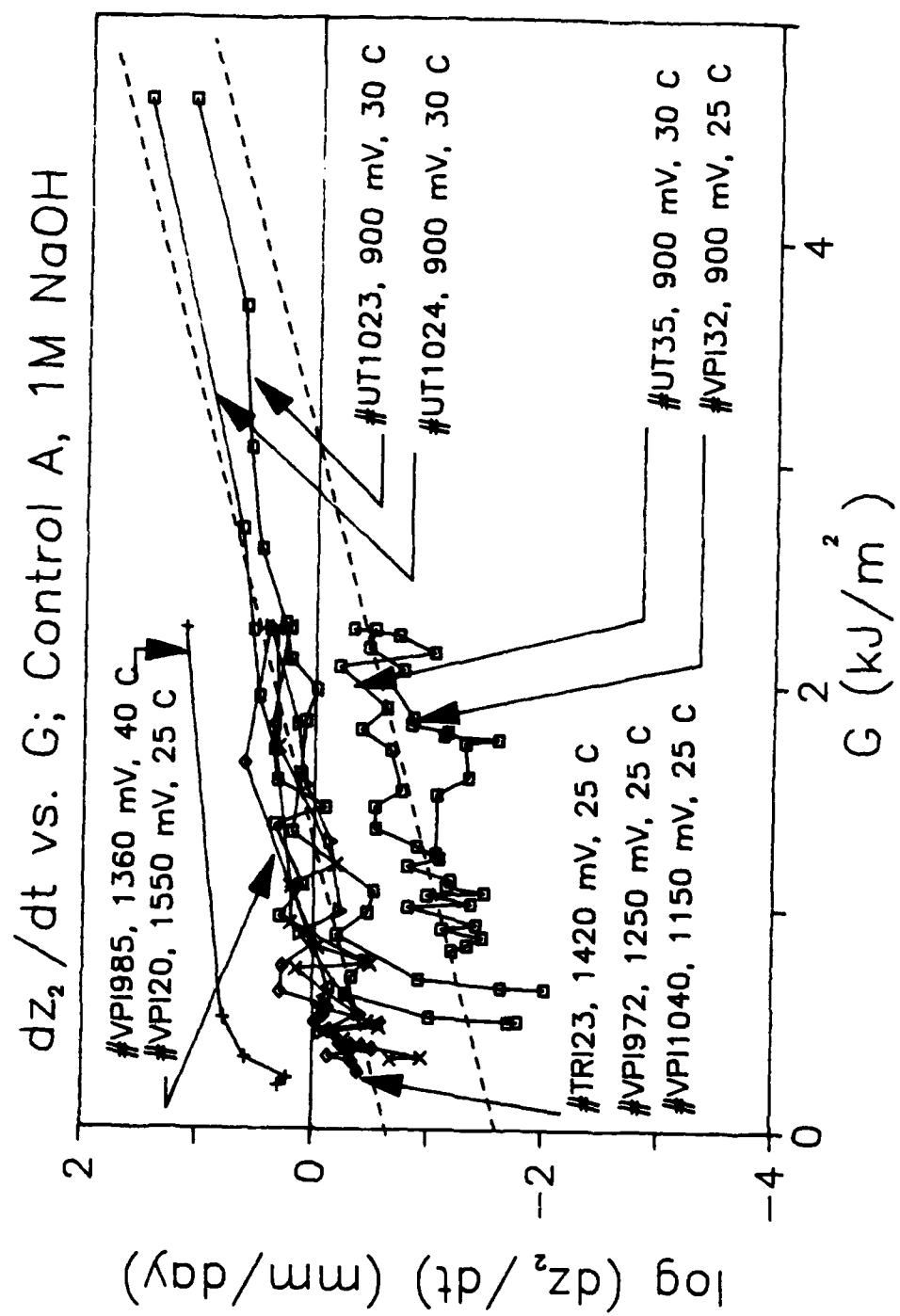


Figure 67. Effect of Voltage, Temperature, and G on the DBPR; Control A; 1M NaOH.

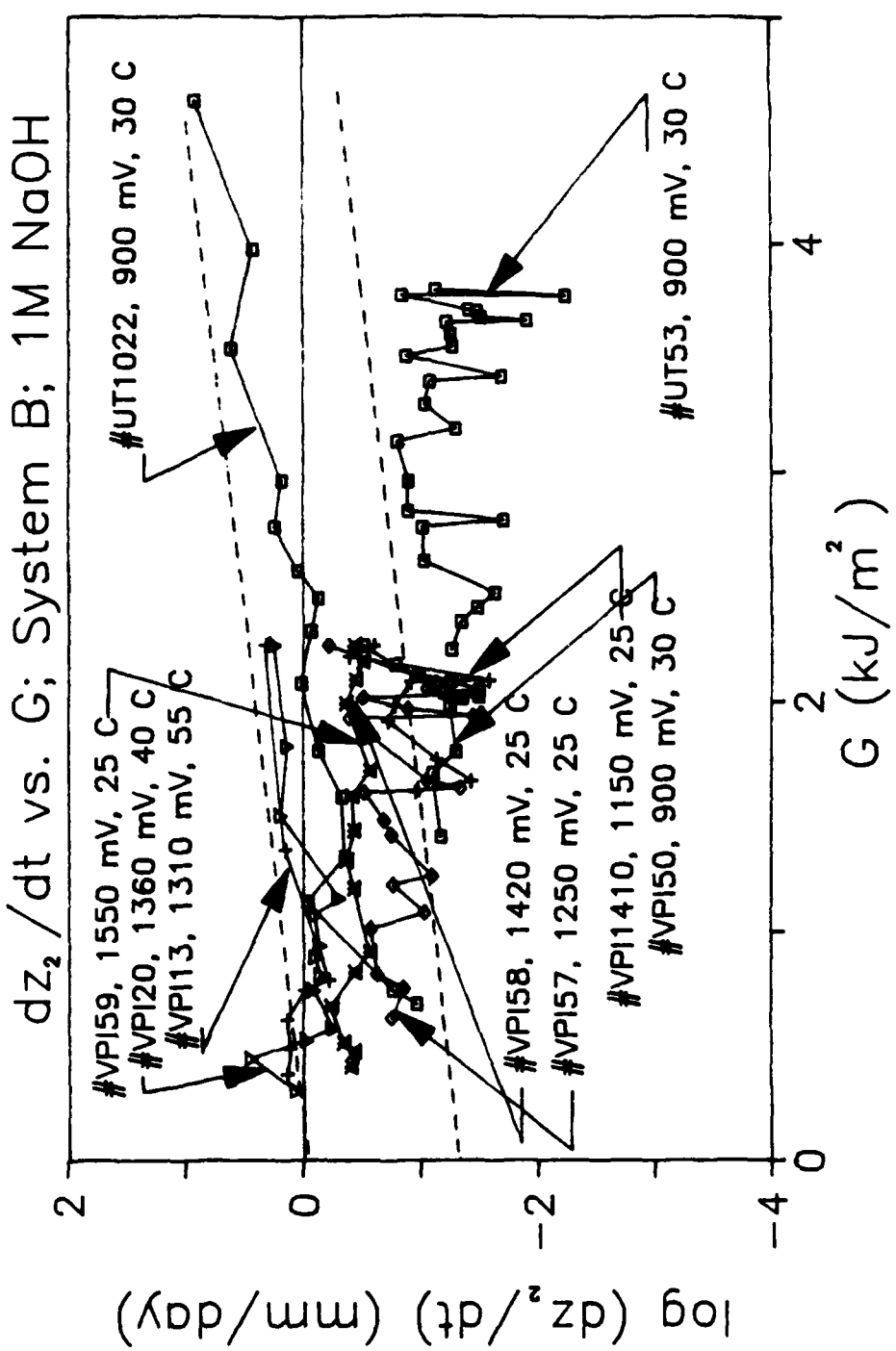


Figure 68. Effect of Voltage, Temperature, and G on the DBPR; Modified B; 1M NaOH.

5.3.2 Durability Predictions

As a result of the preceding discussion, a clearer picture about the total debond behavior is summarized and presented in Figure 69. A critical G value, G_c , of about 15 kJ/m² was measured at VPI [38]. At this value, crack propagation of the dry bond grew in an unstable manner. A value of about 0.02 kJ/m² was also measured for G_c of the degraded bond [38]. Similar to crack growth in other adhesive bonds, three distinct regions exist. Region III is totally dominated by the applied G while region II seems to be affected by both stresses and the environment as illustrated earlier. Region I seems to possess a very steep increasing (with increasing G) slope around the value of G = 0.3-0.5 kJ/m². Data collection from the SBS ceases when G_T becomes comparable to G_c of the weakened bond (at large crack lengths) that weakening becomes dominant.

According to Hertzberg [43], the kinetic crack growth data can be integrated to provide estimates of life and crack length as a function of time. Ignoring region III, it is clear from Figure 69 that one needs to account for region I and II. In this treatment, region I will also be neglected due to the exceptionally sharp knee in the dz_2/dt vs. G curves presented earlier, and because Liechti [40] has reported a rather steep drop in the region of about 0.3-0.5 kJ/m². Therefore, we will denote the rate for the remaining region by \dot{z}_{II} where the rate can best be described by

$$\frac{dz_2}{dt} = \dot{z}_2 = \dot{z}_{II} z_{II}(\text{environment}, G_T) \quad [32]$$

Integrating the above equation yields that the time needed for delamination to propagate a distance z_2 is given by

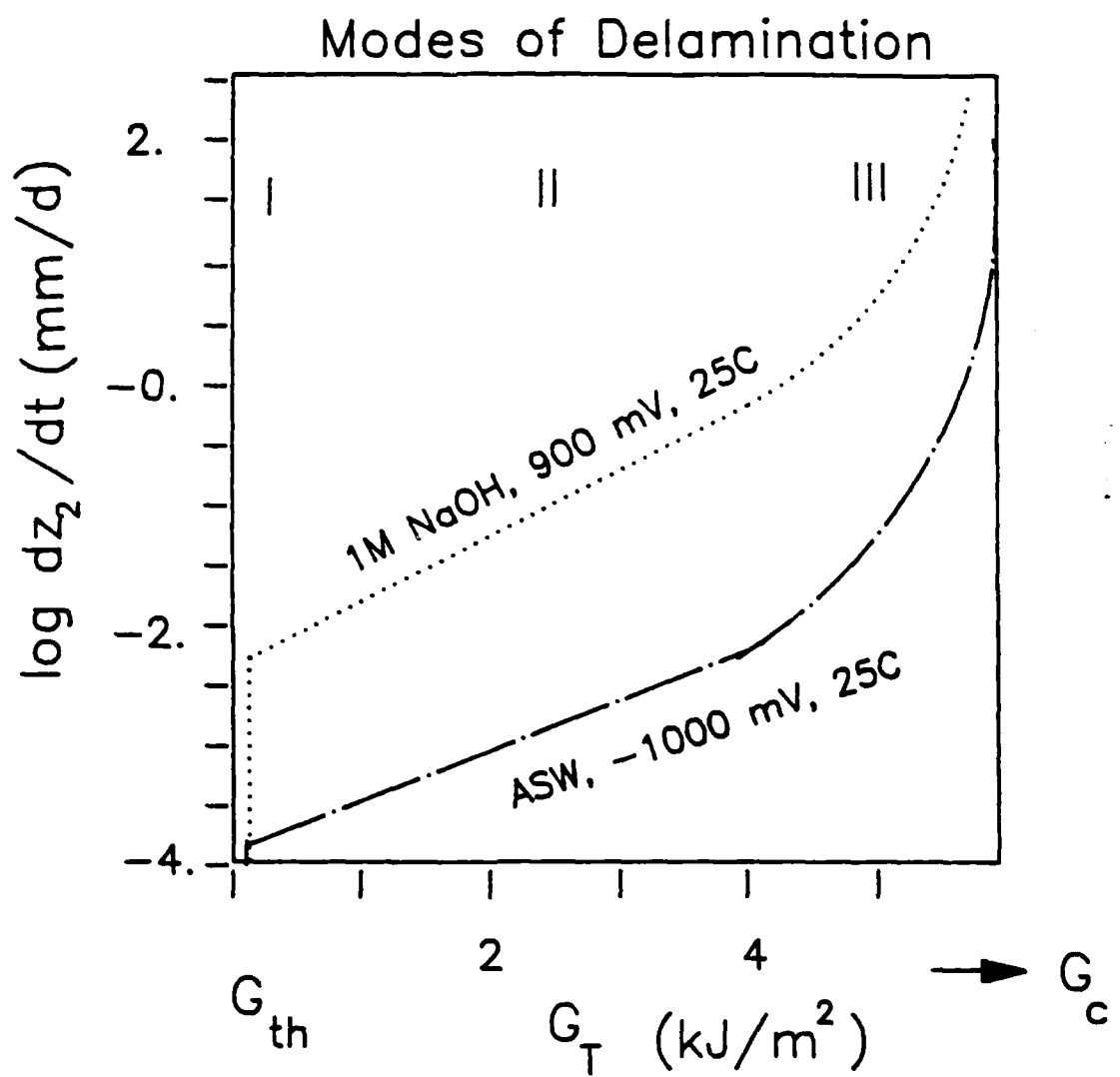


Figure 69. An Illustration Describing the Different Regions of Delamination.

$$t = \int_0^{t_i} dt = \int_{z_2}^{z_2} \dot{z}_2 dz_2. \quad [33]$$

The delamination rate can best be described [44] by the relation

$$\dot{z}_2 = C_1 \exp(mG_T) \quad [34]$$

where C_1 and m are environment-dependent constants and are determined from curve-fitted delamination data. In order to determine the time required for a desired bondline length to delaminate, it suffices to integrate Equation 33 (of which the r.h.s. is integrable in z_2) in conjunction with the above equation. G_T is an explicit function of z_2 for which the coefficients are tabulated in Table 6.

Since the constant C_1 in the above equation plays the role of an environmental shift factor it may as well be functionally similar to the expression for the reaction rate in Equation 30. This parameter serves as an indicator of the severity of the environment. The appropriate expression for the delamination rate then becomes

$$\dot{z}_2 = k_0 \left\{ \exp\left(\frac{-U^\times}{RT}\right) \exp\left(\frac{-\beta FV}{RT}\right) \right\} \exp(mG). \quad [35]$$

This yields the expression

$$z_2 = k_0 \left\{ \exp\left(\frac{-U^\times}{RT}\right) \exp\left(\frac{-\beta FV}{RT}\right) \right\} \exp(mG) t.$$

And upon linearizing the above equation, the delamination model becomes

$$\log \frac{z_2(t)}{t} = A_1 - A_2 \left(\frac{1}{T} \right) + A_3 \left(\frac{\beta FV}{T} \right) + A_4 G \quad [36]$$

Again, A_2 is an estimate of the activation energy of delamination. The SAS fit in what follows uses the test $H_0 : A_i = 0$ for the individual coefficients (A_1, A_2, A_3 and A_4) in order to determine the significance of these terms. In equations 37-40 listed below, all the coefficients were found to be significant. An example will be provided for a typical fit below.

The fact that the SBS represents a G-decaying geometry necessitates the use of SAS in order to account for the continuously decaying applied G. A semi-empirical model of the form presented in Eq.36 for the control system in ASW, considering all independent variables, has resulted in an excellent fit of the form

$$\log \frac{z_2(t)}{t} = 43.686 - 16500\left(\frac{1}{T}\right) + 2.3469\left(\frac{V}{T}\right) + 0.446G \quad [37]$$

Note also that the estimated value for the activation energy has risen from about 60 kJ/mole for the diffusion-control case to about 137 kJ/mole for the above reaction-controlled process. This is consistent with the notion that the activation energy barrier associated with chemical degradation reactions is usually larger than that for diffusion. Two representative straight lines were superimposed on Fig. 65 corresponding to a -1000 mV at 30 C and -1420 mV at 25 respectively. Note that Eq.37 fits the data best at relatively large G's and is in error for low values of applied G.

Similarly, a multiple linear regression fit for the delamination data for System B in ASW (presented previously in Figure 66) has resulted in the expression

$$\log \frac{z_2(t)}{t} = 25.97 - 10303\left(\frac{1}{T}\right) + 1.2659\left(\frac{V}{T}\right) + 0.6587G \quad [38]$$

The regression model seems to fit the data well and the goodness of fit test of $H_0: A_1 = 0$ is significant at the $p = 0.0326$ level, $A_2 = 0$ is significant at the $p = 0.0039$ level, $A_3 = 0$ is significant at the $p = 0.0002$ level, and $A_4 = 0$ is significant at the $p = 0.0032$ level

show that all the coefficients are significant. Again, two representative lines were superimposed on Fig. 67 corresponding to -1000 mV at 30 C and -1310 mV at 40 C respectively. The activation energy barrier for this case was estimated to be about 90 kJ/mole .

Another fit was calculated for the DBPR's for the Control A System in 1M NaOH, with the resulting fit as follows

$$\log \frac{z_2(t)}{t} = 37.16 - 13002 \left(\frac{1}{T} \right) + 1.376 \left(\frac{V}{T} \right) + 0.5418G \quad [39]$$

Again, U^* is estimated to be about 100 kJ/mole for this case compared to 40 kJ/mole for diffusion-control. It is interesting to note that the activation energy for the chemical-reaction in ASW is somehow higher than its counterpart in NaOH solutions which follows the same trend with the case of diffusion-control illustrated in chapter 4. Again, Fig.67 shows the good fit of the semi-empirical model. The two dotted lines now represent -900 mV at 30 C and -1250 mV at 25 C respectively.

Similar to the Chemlok 205/220 system, the delamination data for the silane modified system in 1M NaOH were also used in the same fashion resulting in the fit

$$\log \frac{z_2(t)}{t} = 29.4 - 10577 \left(\frac{1}{T} \right) + 0.984 \left(\frac{V}{T} \right) + 0.227G \quad [40]$$

An interesting observation is the moderate G dependency exerted by the modified system compared with the control as seen by the coefficient multiplying G in Eq.39 and the previous equation. Two representative lines corresponding to -1420 mV at 25 C, and -1360 mV at 40 C were superimposed on Fig. 68 to illustrate the influence of harshness (as seen by the intercept) and the relatively moderate effect of G (slope) as compared to the three previous cases.

5.4 CONCLUSIONS

As a result of the above discussion, the author has arrived at the following conclusions:

- 1- Delamination rates were found to be influenced by the temperature and current density in a fashion similar to that of weakening.
- 2- The effect of tensile stress on the DBPRs (in the SBS) is modelled using an exponential function in applied G. SAS to predict durability of the adhesive bonds
- 3- A multiple regression analysis (using the REG procedure of SAS) was successfully utilized to model the effect of all the accelerating parameters, i.e., temperature, current density, and stress on delamination rates.

6. ANALYTICAL MODELLING OF DEBONDING

6.1 INTRODUCTION

This model seeks to relate the effect(s) of applied tensile stress on debond rates of adhesive systems to the adverse conditions that are caused by the environment. The attack of the hydroxyl ion on the adhesive/metal bondline has been proven throughout this research to be the single most important factor in determining the environmental durability and stability of cathodically protected systems. The environmental attack on the critical linkages discussed earlier is, in fact, responsible for weakening the interfacial layer and eventually failing the bond. The overall production of the hydroxyl ions depends on several rate-dependent reactions that take place in the immediate proximity of the steel surface leading to the fact that the slowest of those reactions would control the outcome i.e. deterioration.

A multi-chain-of-events approach is presented which incorporates a non-linear diffusion boundary value problem, a degradation boundary value problem, and a mechano-chemical failure criterion. Special care was exercised when addressing the two similar-in-origin, yet different-in-consequences, problems of bond weakening and delamination. Updating the boundary conditions for the boundary value problem was incorporated as a possible means to modelling delamination.

6.2 KINETIC EQUATIONS

In order to understand the mechanism by which the adhesive bond deteriorates as a result of the environment, it is necessary to establish the kinetics of the process(es) by which ions migrate into a polymeric material or an environmental crack. Diffusion of the individual ions and their state within the medium (becoming hydrated, attacking the chemically unstable bulk linkages, or hydrolyzing the attachment sites at the polymer/metal interface) could determine the extent of damage to the bond. Assuming that adsorption of the aggressive medium on the reactive zone surface and desorption of the degraded products are governed by a rapid mass transfer mechanism, two important and parallel mechanisms remain to be accounted for. These processes are: diffusion of the aggressive species into the polymer or the crack, and the chemical reaction of these species with the attachment sites and with the chemically unstable groups in the adhesive itself (designated by "critical linkage, C.L").

Simple diffusion of particles within a medium could be expressed in a form of a flux vector

$$\vec{J}_i = - B_i \vec{\nabla} \mu_i \quad [41]$$

which relates the flow of some species i to its chemical potential through what is called the kinetic coefficient, B_i . The negative sign in the above equation is due to the fact that diffusion takes place in a direction opposite to that of increasing chemical potential. Because the chemical potential of a substance is not easy to utilize, an equivalent form can be obtained where concentrations can be used. Substitution of the expression for the chemical potential yields

$$\vec{J}_i = - D_i \left(1 + \frac{d \ln y_i}{d \ln c_i} \right) \vec{\nabla} c_i \quad [42]$$

where y_i is the molar activity coefficient, c_i is the concentration, and D_i is the diffusion coefficient of species i . The resulting form for D_i includes the kinetic coefficient and is stated as follows:

$$D_i = B_i k T \quad [43]$$

The expression between brackets in Equation 42 is known as the thermodynamic factor of B_i and will be set to unity in this study (for an ideal system $y_i = c_i$). The resulting form is widely known as Fick's first law of diffusion.

The continuity of mass governing equations introduce the time element into the simple diffusion process and for a single-component system it takes on the general form:

$$\frac{\partial c}{\partial t} = \vec{\nabla} \cdot \vec{J} \quad [44]$$

Substituting the expression for the flux (from Equation 42) into Equation 44 yields Fick's second law for simple diffusion:

$$\frac{\partial c}{\partial t} = \vec{\nabla} \cdot (D \vec{\nabla} c). \quad [45]$$

The general governing conservation equation of a multi-component ionic system in a crack or a polymeric material could be represented by a system of differential equations that accounts for the concentration changes in time and space of the n different components which the solution consists of. The above stated law, however, does not account for special features associated with the migration, advection or chemical reaction processes. Therefore, additional terms have to be added into Equation 45 in order to satisfy all the physical and chemical phenomena that are associated with debonding as seen in the following expression.

$$\frac{\partial c_i}{\partial t} = - \vec{v} \cdot \vec{\nabla} c_i + \vec{\nabla} \cdot (D_i \vec{\nabla} c_i) + \frac{z_i}{RT} F_i \vec{\nabla} \cdot (D c_i \vec{\nabla} \phi) + R_i \quad (i = 1, 2, \dots, n) \quad [46]$$

Here, the rate of change of concentration depends on

- 1) advection mechanism,
- 2) simple Fickian diffusion,
- 3) ion migration due to potential gradient effects,
- 4) and homogenous chemical reactions involving the generation or depletion of species as indicated by the three terms above, respectively.

In the above equations, v is the rate of movement of the volume of solution within the crack or the polymeric material due to fatigue loading or swelling, c_i is the concentration of species i, D_i is the effective diffusion coefficient of ions (molecules) of the ith species, z_i valency of the ith ion, ϕ potential drop = [E_{ext} - $E(x)$], and R_i the rate of production or depletion of species by chemical reaction. The advection term vanishes for a static crack because no replenishing of the electrolyte takes place and will be neglected throughout this research.

While a more involved treatment is proposed in Appendix 4, the first and third terms of the r.h.s. of the above equation will be neglected for the remainder of this chapter. This will result in a simplified form of the mass conservation equations as follows

$$\frac{\partial c_i}{\partial t} = \vec{\nabla} \cdot (D_i \vec{\nabla} c_i) + R_i \quad (i = 1, 2, \dots, I). \quad [47]$$

As we will see in the upcoming discussion, we have used nonlinear expressions for the degradation reaction rate constants and the diffusion constants in order to account for temperature and voltage.

6.3 CHEMICAL DEGRADATION

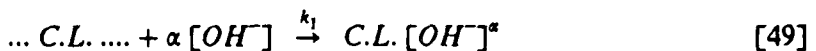
Degradation of the adhesive bond is a complex problem to model because several parallel mechanisms may take place simultaneously. The process of degradation is highly dependent on the particular system and may take place at various regions of the adhesive bond depending on the relative rates of the acting processes. In this specific application, however, the degradation takes place interfacially in fronts as discussed previously in chapter 4. This is responsible for what we describe as a "diffusion window" phenomena at the bond's boundary. The thickness of such a surface reactive zone cannot be determined experimentally but it is believed to be very thin for very high chemical reaction to diffusion ratios. The continuity of mass for such a system must be represented on a surface concentration basis and not on bulk concentrations. Therefore,

the solution of the coupled system of p.d.e's is essential to determine the actual "surface" concentration of the aggressive species (hydroxyl) at the sharp front. Taking this into consideration, one may write [45] the overall rate of the degradation of a heterogeneous polymer or an adhesive bondline as :

$$\sum_{i=1} \frac{\partial C_n}{\partial t} = \sum_{i=1} [- k(C_{n0} - C_n) c_1]_i v_i \quad [48]$$

where v_i is the relative volume of each region in the medium and C_n is the degraded linkage's concentration. The above equation shows that several degradation mechanisms can occur simultaneously in the different components of the polymer and could be accounted for with this model.

In an NaOH solution, the hydroxyl is readily available for degradation thanks to bulk concentrations. The attack on the critical linkages (interfacial bond-creating attachment sites or unstable bulk primer linkages) is believed to be chemically activated, with α molecules of OH ions reacting with those linkages at the crack tip to form an activated complex thus forming an inactive site according to:



where the value of α determines the order of reaction and k_1 is the degradation rate constant. If only one "culprit" mechanism is considered, Eq. 48 degenerates into

$$\frac{\partial C.L.}{\partial t} = - k_1(C.L._0 - C.L.) c_1 \quad [50]$$

Another complication may involve the hydrolysis or reduction of the iron oxide itself at high voltages and high pH. According to Pourbaix [46], the potential-pH

diagram for the $Fe - H_2O$ suggests that in the presence of 1N NaOH and coupled to zinc ($pH = 13.7$ and $E(h) = -0.9V$) corrosion of the iron is inevitable (Fig. 70). The hydrolysis of iron, for example, could be incorporated into the above model through the addition of an extra rate-dependent reaction equation



Similarly, the related flux and continuity equation should be taken into consideration. However, that avenue will not be investigated here for simplicity.

6.4 THE B.V.P.

The uncertainty in characterizing the "culprit" degradation mechanism has dictated that we use the experimentally determined kinetic parameters from chapters 4 and 5. The need to pin-point such a mechanism vanishes as a result because these rates are those of the "acting" mechanism under the specific conditions. For the case where an adhesive bond is exposed to NaOH or ASW with voltage, the diffusion B.V.P. and the degradation problem is expressed in two mass balance equations. Assuming that the reaction is first-order, an equation that accounts for mass balance of the reacting species (OH^-) that contains an accumulation term which comes about due to the transient term, a transport term that accounts for diffusion, and a consumptive reaction term that accounts for the degradation reaction as follows

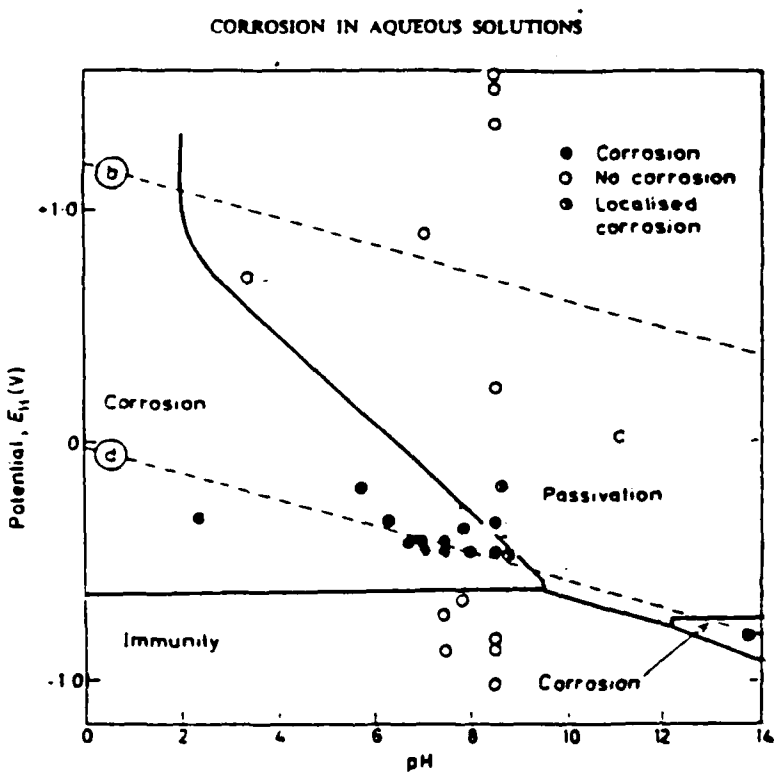


Figure 70. Pourbaix diagram showing the corrosion states of iron as a function of pH and cathodic and anodic voltage.

$$\frac{\partial c_1}{\partial t} = D_e \frac{\partial^2 c_1}{\partial x^2} - \alpha k_1 C.L. c_1 \quad [52]$$

where c_1 is $[OH^-]$ at the reaction site, k_1 is the first-order reaction rate coefficient $(l/s)/(mole/cm^3)$, C.L. is the concentration of the degradable adhesive ($mole/cm^3$), and α is a stoichiometric coefficient. The other equation accounts for the degraded bondline species (Equation 49) and is expressed as:

$$\frac{\partial C.L.}{\partial t} = - k_r C.L. c_1 \quad [53]$$

where the r.h.s. term is the rate of reaction, R.

The concentrations above were normalized with respect to the bulk concentration of the aggressive species as follows:

$$c_1^* = \frac{c_1}{c_1^\infty}, \quad C.L.^* = \frac{C.L.}{c_1^\infty}$$

(for example, c_1^∞ is equal to $1.0E+11$ mole/ cm^2 for an 1M NaOH solution). Using non-dimensional time and distance according to the relationship

$$t^* = \frac{D_e}{L^2} t, \quad x^* = \frac{x}{L}$$

gives rise to the non-dimensional system (where the superscript has been dropped for convenience in this treatment) as follows

$$\frac{\partial c_1}{\partial t} = \frac{\partial^2 c_1}{\partial x^2} - \alpha W C.L. c_1 \quad [54]$$

$$\frac{\partial C.L.}{\partial t} = - W C.L. c_1. \quad [55]$$

The reduced problem is subject to the BC's: at $t > 0$,

$x = 0$, at the crack mouth,

$$c_1 = 1, \quad \frac{\partial C.L.}{\partial x} = 0. \quad [56]$$

$x = 1$, at the crack tip,

$$\frac{\partial c_2}{\partial x} = 0, \quad \frac{\partial C.L.}{\partial x} = 0. \quad [57]$$

The non-dimensional quantity W above is of the form

$$W = \frac{k_e L^2}{D} c_1^\infty \quad [58]$$

and is analogous to the Thiele modulus, $(\phi^*)^2$, reported previously (chapter 4) which indicates whether diffusion or chemical reaction is rate controlling. At high values of W diffusion is nonlinear and is characterized by a propagating front. Indeed, at large values of the Thiele modulus, the diffusion coefficient becomes very species concentration-sensitive and can not be explained on the basis of linear Fickian diffusion relations.

Typical concentration profiles for $[OH^-]$ and $[C.L.]$ resulting from the above diffusion-chemical reaction system are shown in Figures 71-76. The normalized initial concentrations for $[OH^-]$ and $[C.L.]$ are 1.0 and 1.5 (section 6.7) respectively. Unlike the case where W is very low ($= 1, 10$; Figures 71, 73), the diffusion of the aggressive species (OH^-) becomes restricted to a fairly thin layer for the case where W becomes larger (Fig. 75). Consequently, the neutralization of the critical linkages proceeds in the shape of a wave. This trend continues for the case when chemical reaction seems to dominate ($W = 100$). Now the reaction becomes limited to a fairly sharp surface characterized by

a sharp front. The degree to which weakening proceeds in relationship to delamination is very much governed by the shape of such a front. Compared to Figure 72, one predicts that this weakened distance ahead of the crack tip in Figure 76 (corresponding to $W = 100$) is much shorter.

6.5 FAILURE CRITERION

An interesting formulation called the 'Generalized fracture mechanics' (GFM) was developed fairly recently by Andrews [47]. He showed that a function he called the adhesive failure energy is a function of surface treatment, the adhesive, and the adherend. He then developed a scheme by which the work of debonding, θ , is related to the environment and stresses through a "loss function" according to the relationship

$$\theta = \theta_0 \chi(da/dt, T, \epsilon). \quad [59]$$

θ_0 is the energy needed to break the adhesive bond across the fracture plane, χ is a loss function dependent on crack velocity, temperature, and strain.

In this treatment, we have assumed that debonding is a direct consequence of degradation. We will denote the degraded crucial linkage (attachment site, bulk primer linkage) at the bondline by [C.L.]. During exposure, the density of these interatomic bonds will decrease as a function of the local OH^- concentration and could be modelled through a similar loss function as follows

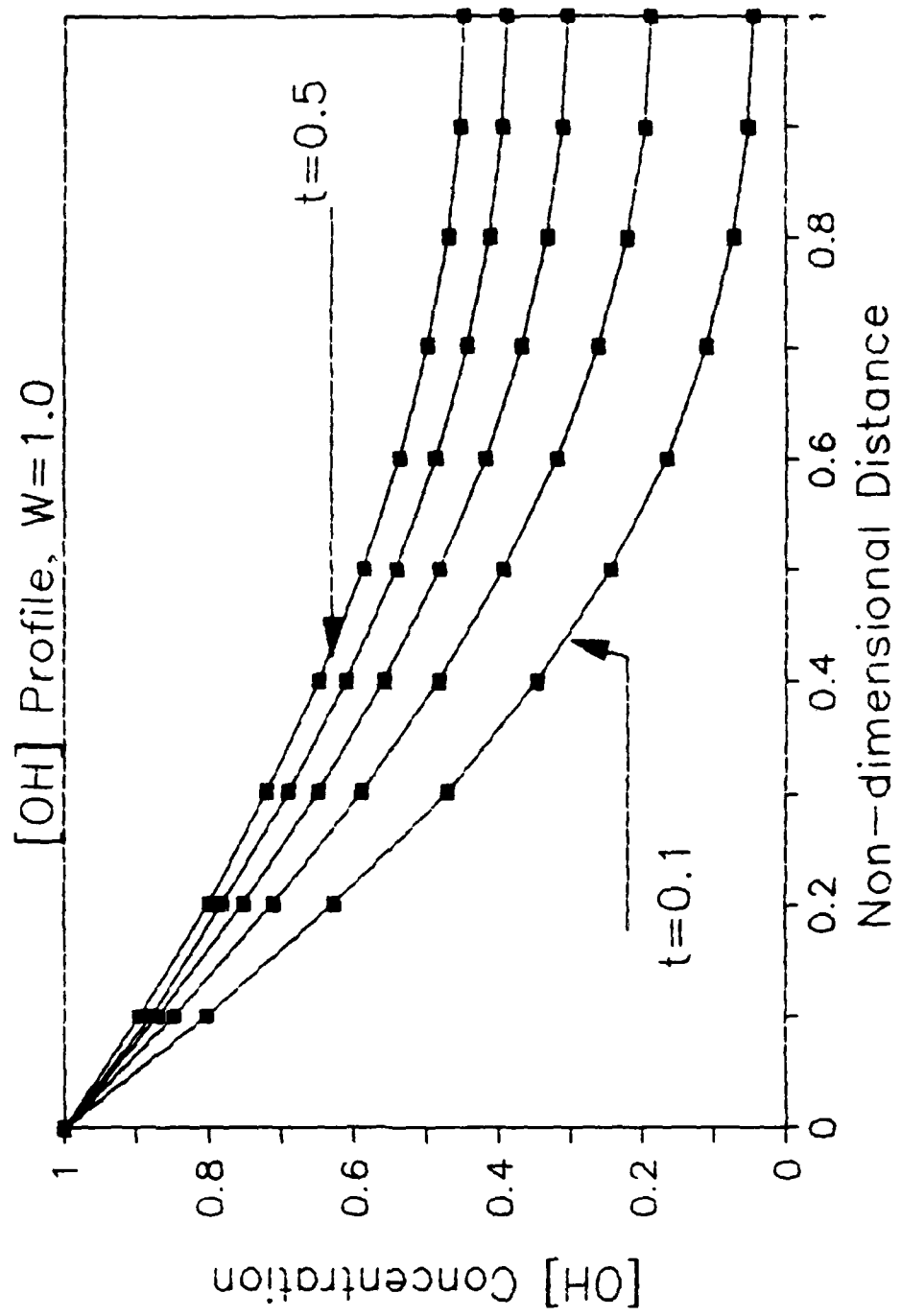


Figure 71. The Hydroxyl Concentration Profile for $W = 1.0$

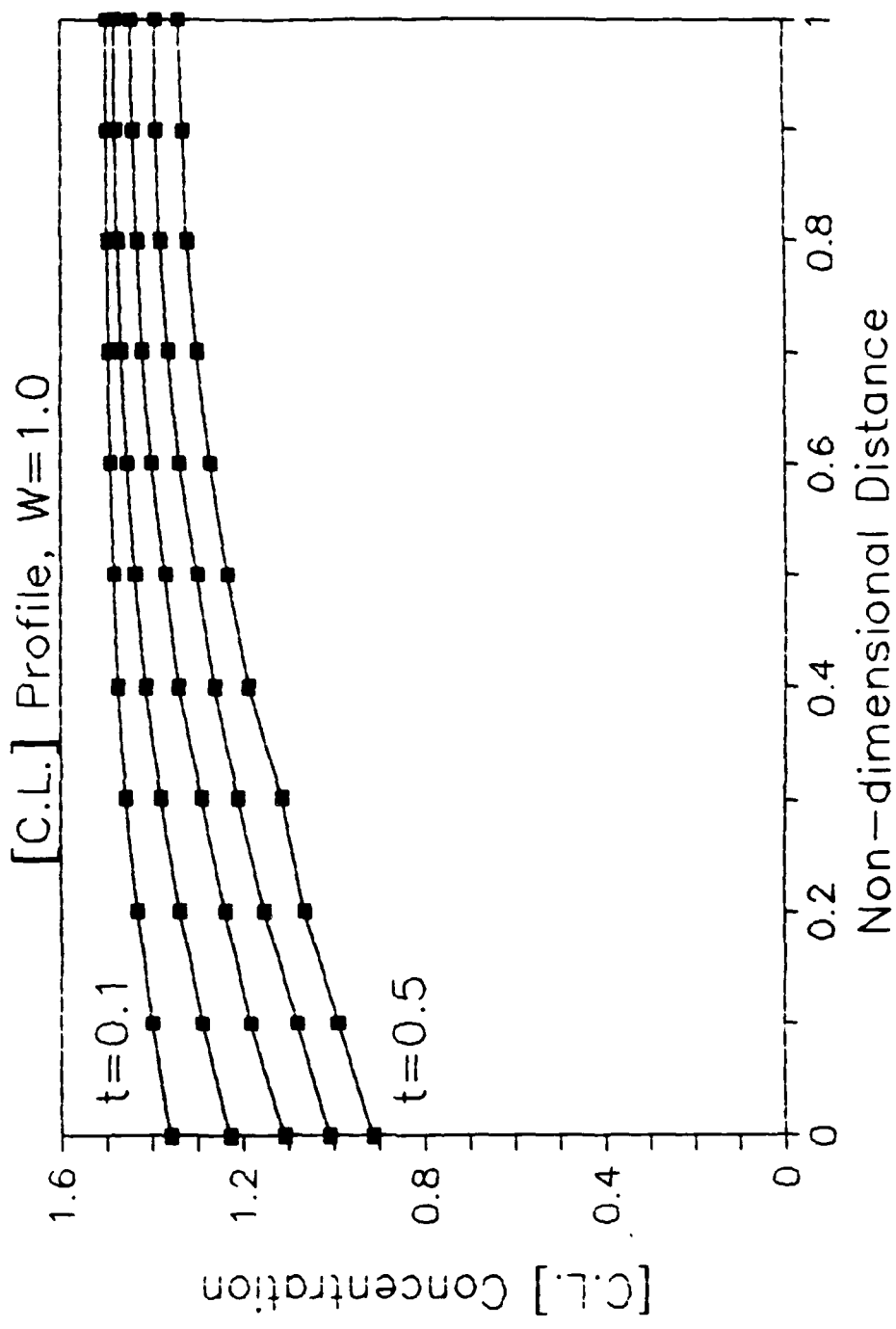


Figure 72. The Critical Linkage Concentration Profile for $W = 1.0$

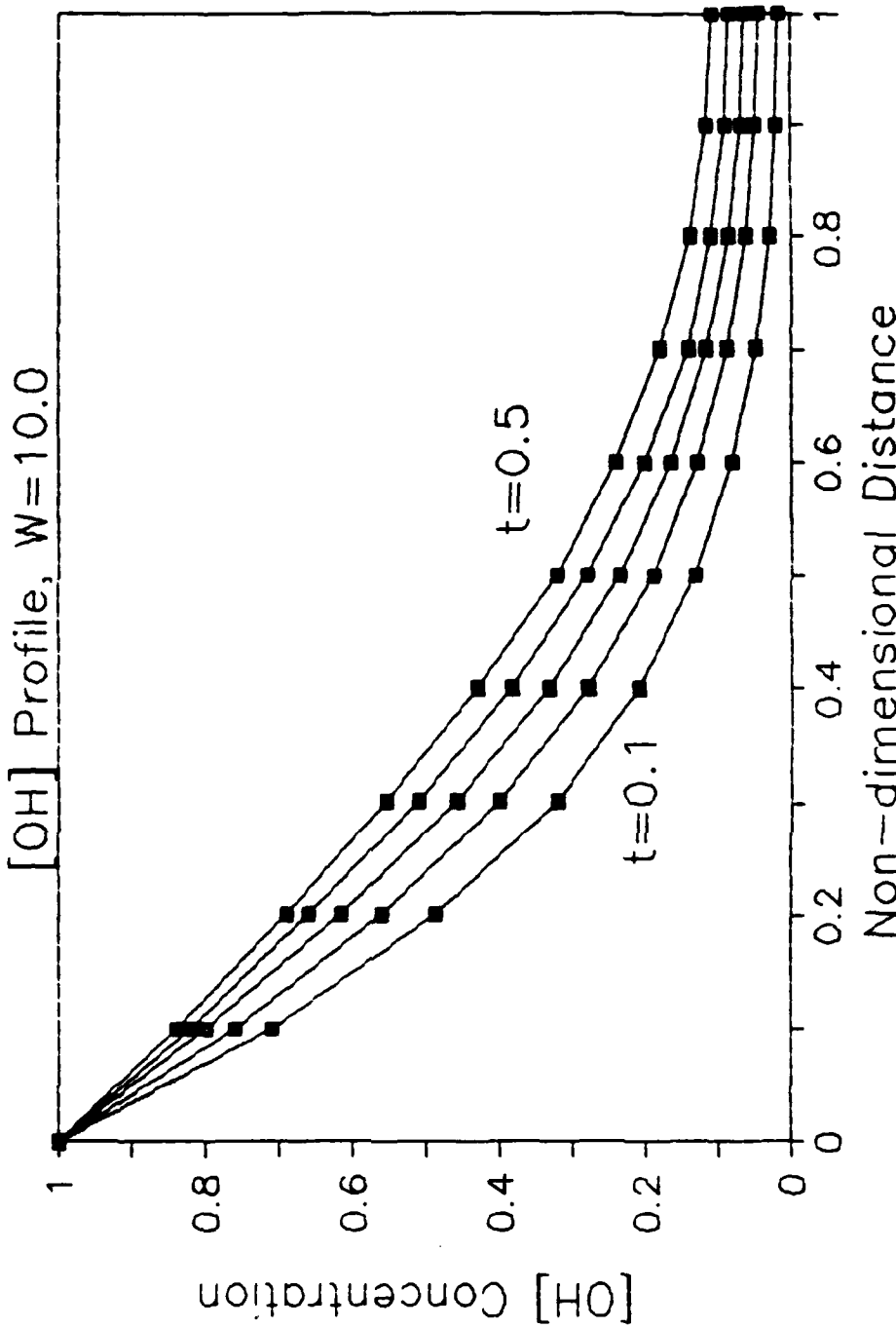


Figure 73. The Hydroxyl Concentration Profile for $W = 10.0$

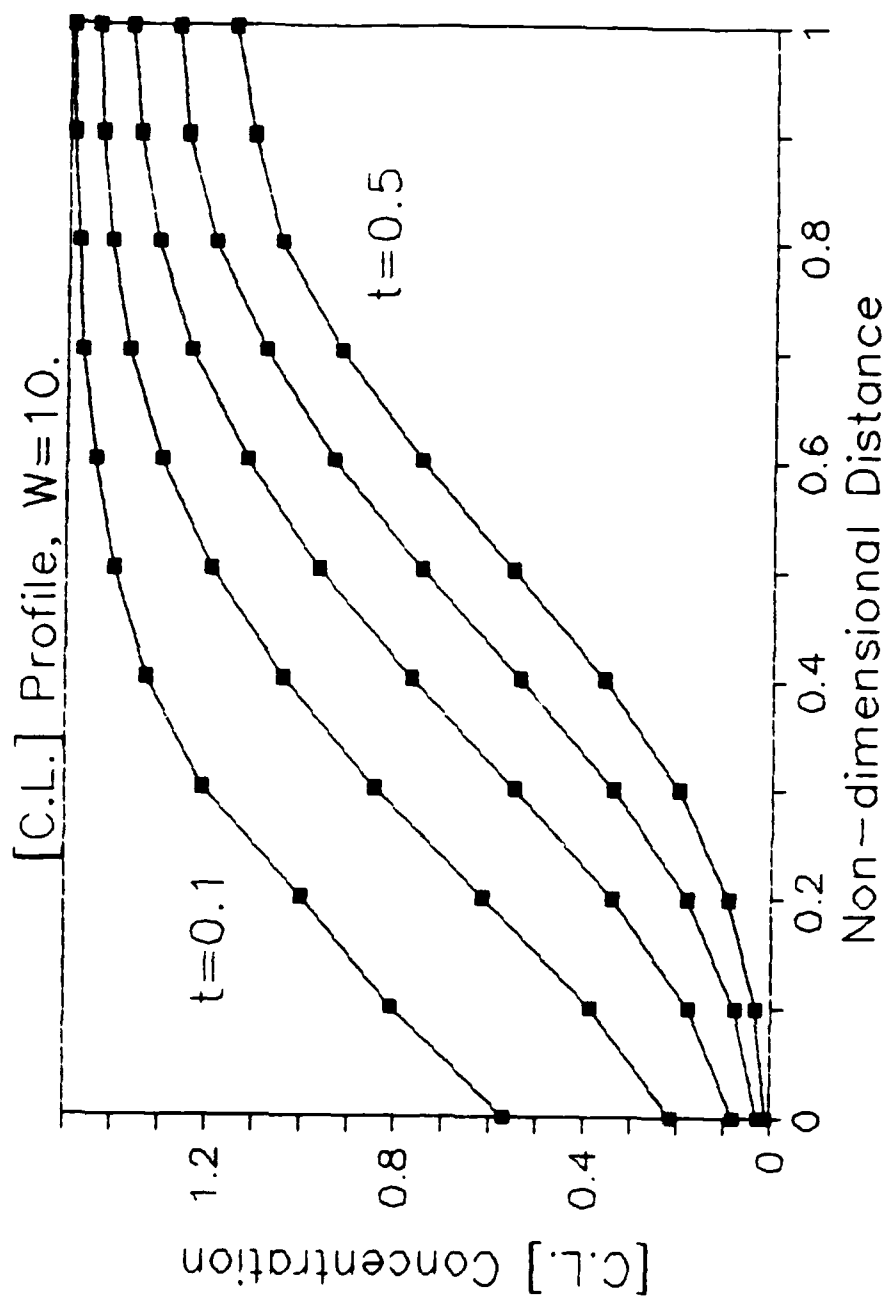


Figure 74. The Critical Linkage Concentration Profile for $W = 10.0$

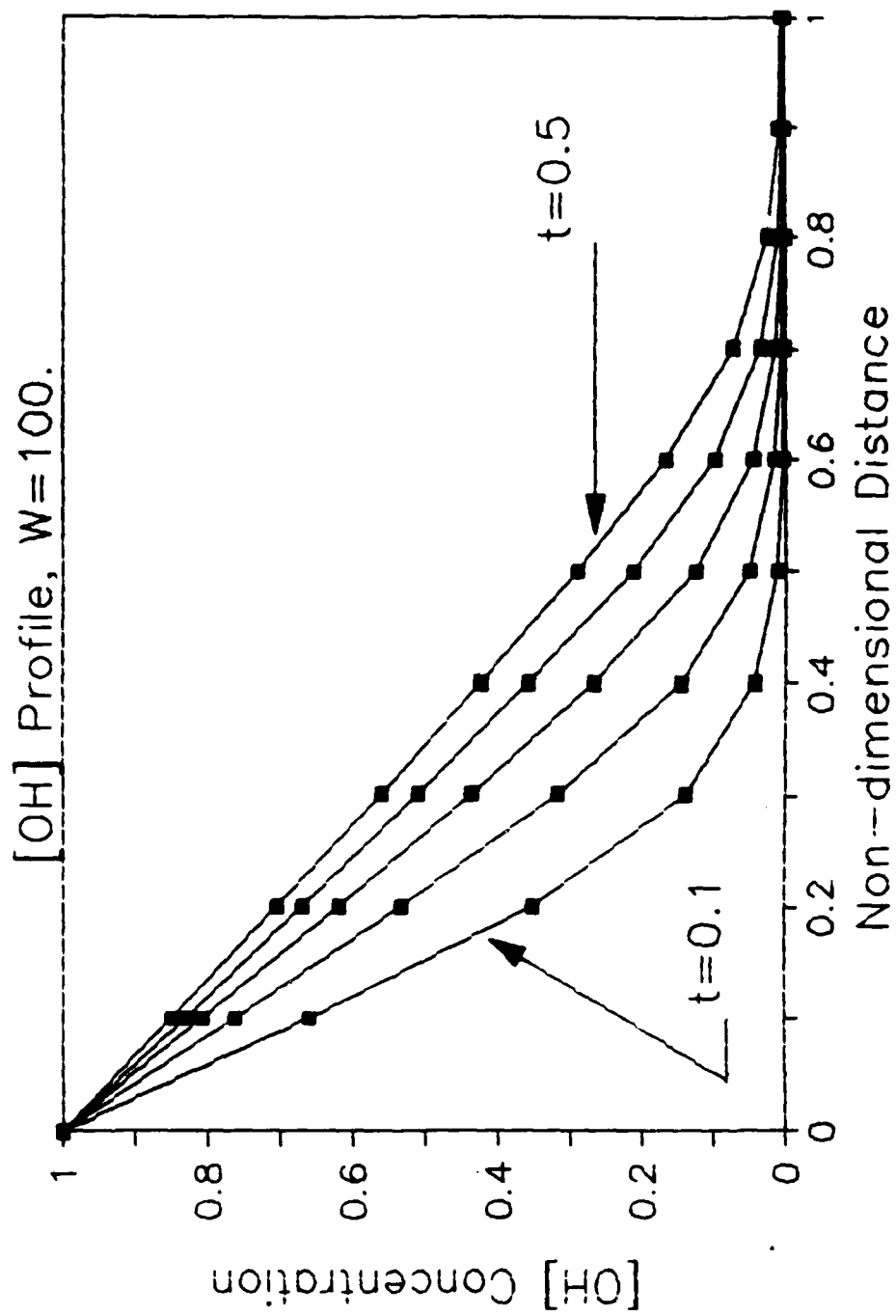


Figure 75. The Hydroxyl Concentration Profile for $W = 100.0$

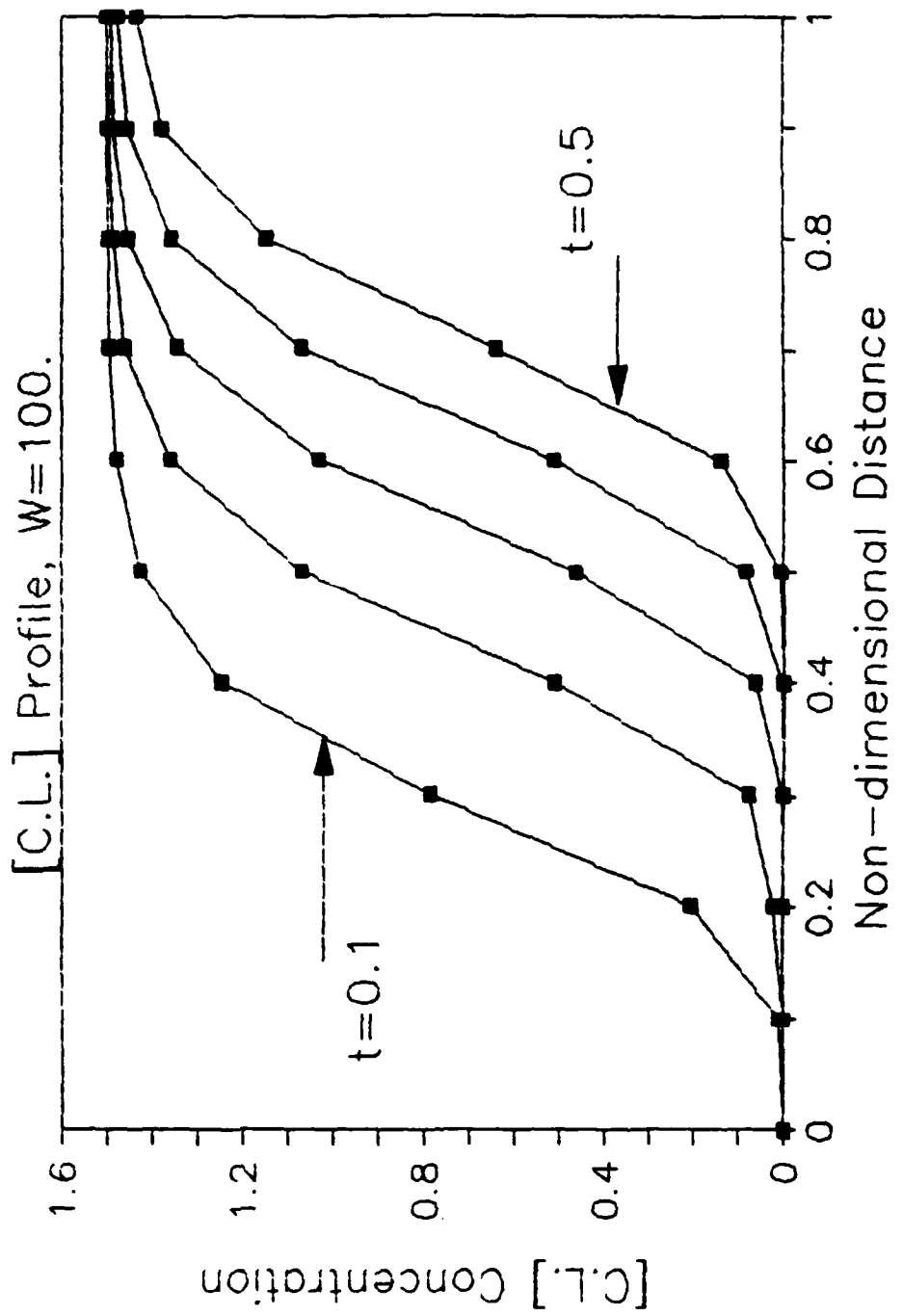


Figure 76. The Critical Linkage Concentration Profile for $W = 100.0$

$$[C.L] = C.L_0 \chi([OH^-]) \\ = C.L_0 \chi(c.d., pH, Temp., t) \quad [60]$$

where c.d. is the cathodic current density and t is time.

Essentially, G_c is a measure of the resistance of the bondline to the propagation of an existing crack and is an inherent property of any particular adhesive bond. Naturally, its value is system sensitive and is affected by such factors as surface preparation, the adhesive and adhesive compatibility. It is natural then to assume that the degraded bond will possess at any time a resisting G , G_c , that is directly related to the density of the operative interatomic bonds

$$G_c = G_c([C.L]). \quad [61]$$

where [C.L] for the adhesive bond is calculated at any point and at every time increment according to Equation 60. A failure mechanism is completed by considering that

$$z_2 = z_2(G_T, G_c). \quad [62]$$

Figure 77 shows how we envision that this criterion will function. As the bond weakens (assuming that a linear relationship exists between χ and [C.L]) the loss function, χ , will follow the same wave-like shape as in Figure 76. G_c is proportional to χ and is similarly influenced by the rate-governing kinetics. Notice that the lines representing G_c in Figure 77 correspond to large times ($t = 0.1-0.5$). Delamination will pursue when the failure criterion is satisfied. It is, therefore, necessary and sufficient that G_T exceeds G_c for the crack to propagate locally.

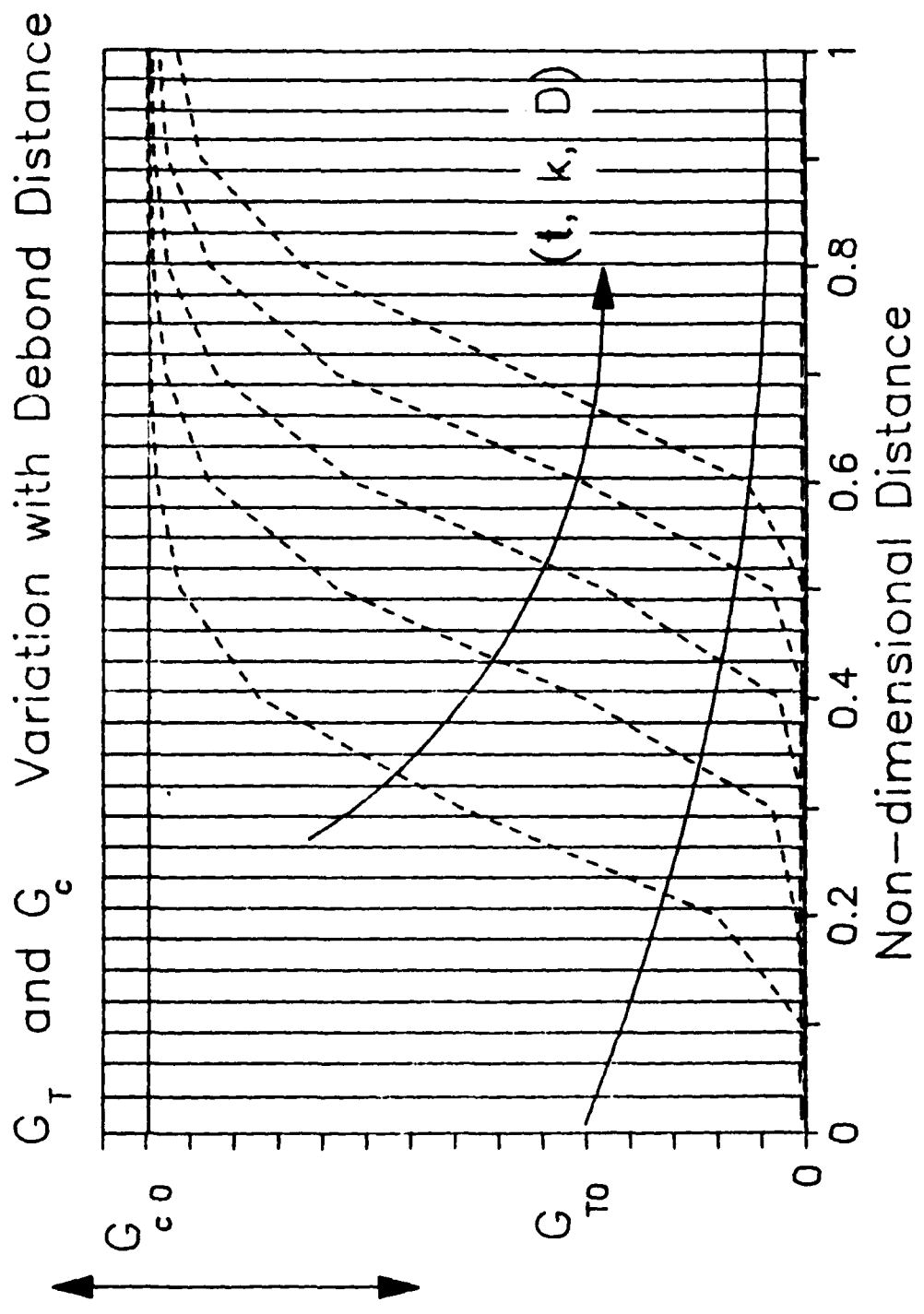


Figure 77. Variation of Applied and Critical G as a Function of Bondline Distance.

6.6 A SCHEME FOR NUMERICAL SIMULATIONS

The proposed algorithm is set up in such a way to allow one to take full advantage of the numerical scheme in order to solve the system for both weakening and delamination. Figure 78 illustrates the algorithm that operates according to a closed-chain-of-events complete with a failure mechanism. The latter being either a critical concentration of the degraded linkage density, $[C.L]_{c0}$, for weakening progress or a fracture mechanism similar to that discussed above. The primary input data includes

- The geometric parameters that may contain the bond line's length for example
- initial conditions associated with the aggressive and degradable species
- the environment including applied voltage and temperature
- the kinetic parameters for the involved processes
- loading parameters, G_T , for the tension loaded case

The kinetic parameters above are assumed to be functionally similar to those determined from the regression analysis. And note that both temperature and voltage are accounted for in this treatment through the 'harshness coefficient', W. As harshness increases so do the two coefficients with the reaction rate coefficient progressively leading D resulting in constantly increasing value of W.

Solving the non-linear B.V.P. represented by Eqs. 54,55 along with the associated initial boundary conditions (Eqs. 54,55), the species concentrations, the aggressive and unstable ones included, are determined at every spatial node and for every time increment. The failure criterion is considered to be of a mechano-chemical nature because of the obvious interaction as seen from section 6.5. For the case of a weakened bond, the degraded interface is assumed to "debond" when the C.L.'s density diminishes

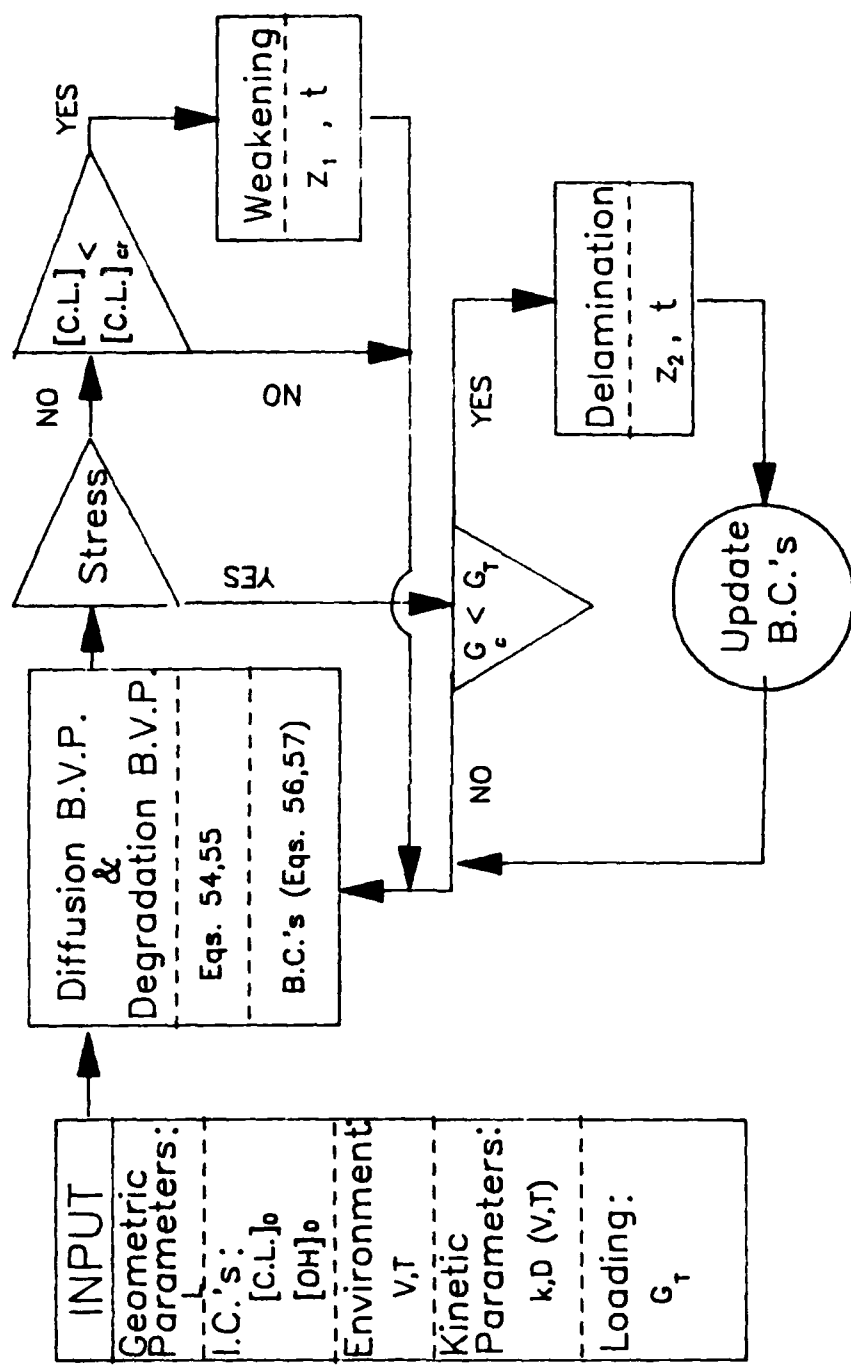


Figure 78. A Schematic of the Algorithm for Numerical Simulations.

to a trickle, $C.L_c = 5$ percent in this treatment. Depending on whether or not stress is applied, updating the boundary conditions becomes necessary if and when delamination takes place.

The numerical solution was attempted using the IMSL subroutine DPDES. A Fortran program was developed for the purpose of modelling the above example case in order to illustrate the trends associated with debonding. The algorithm follows the scheme that was illustrated in Figure 78, and a copy of the program is given in Appendix 3.

6.7 NUMERICAL PREDICTIONS

6.7.1 Weakening

An ASW environment with -1000 mV (SCE) and at 25 C was taken as a reference point and a control value of 1080 was used as a control for W. The reason for using the same value of W in these two cases is that the WBPR for the case above and for 1M NaOH at 25 C with no applied voltage was almost identical (chapter 3). The appropriate expression for the diffusion coefficient (Eq.19), control length, l, and c_f^∞ were used in Eq.58 to give

$$k_e = 8.41 \exp\left(\frac{-13002}{T}\right) \exp\left(\frac{1.376V}{T}\right)$$

with units of $(1/s)/(mole/cm^3)$. Note that the only variable that is left to be determined is the initial density of the critical linkage. This value was adjusted until a good fit to the control case in weakening (BDS) was found. As seen from the good fit in Figure 79, an appropriate value for $[C.L]_0$ was found to be about $1.5 \text{ mole}/\text{cm}^3$. Several other cases were run to verify this value. The figure also shows that the predictions fit the experimental results well except, perhaps, in the case of -1100 mV. An important observation is that the program predicts a "delay time" (time needed to debond the first nodal distance of about 0.254 mm) as a function of applied voltage which correlates well with experiments. The predicted delay times were 2.15, 1.08, and 0.137 days for -1000, -1100, and 1440 mV respectively compared to the linear regression values of about 1.96, 0.5 and 0 (Fig. 49).

An attempt was made to normalize the experimental data by using non-dimensional times of the form used in the above analysis. It is necessary to remember that the diffusion constants are a function of the independent variables: temperature and voltage. Non-dimensional distances were used as well. The resulting shifted data for the data in Figure 79 is presented in Fig.80 along with the predicted results. The apparent deviation in the experimental data of the -1100 mV case may explain the apparent lack of fit in Fig. 79 for this case. It is also interesting to note that the shifted predictions are parallel at large distances as we may have expected. The reason being that for these very harsh conditions, W increases proportional to k/D resulting in a high propagation rate at small distances while it tapers off as diffusion becomes the dominant process.

In order to verify the program further, other available weakening data in seawater at various voltages and temperatures was utilized as well. Stevenson's [8] data which was collected in seawater was plagued by considerable scatter but was plotted in a fashion similar to VPI's. Figure 81 shows some representative data points from Ref.8

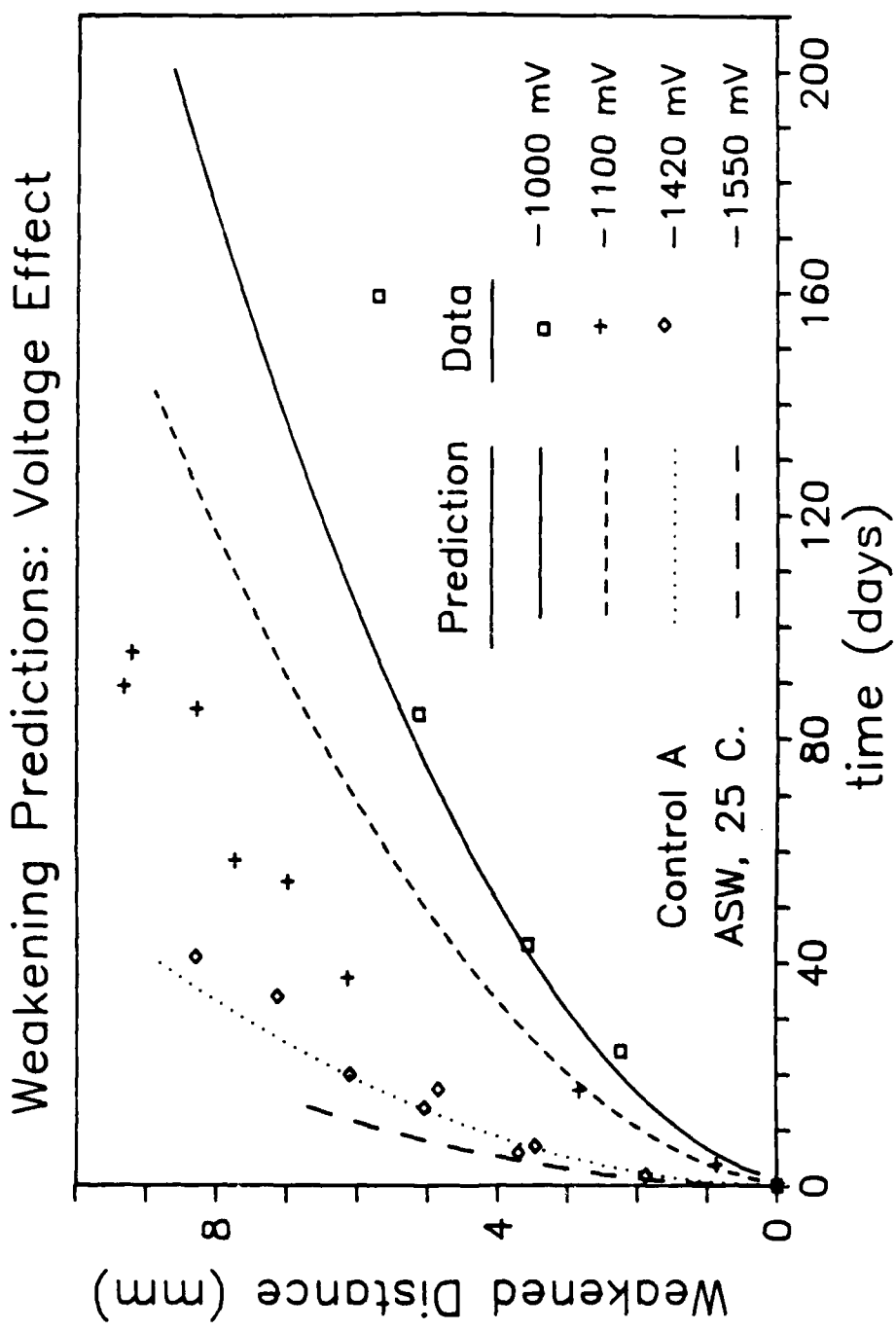


Figure 79. Numerical Predictions of Weakening in ASW at 25°C; Control A.

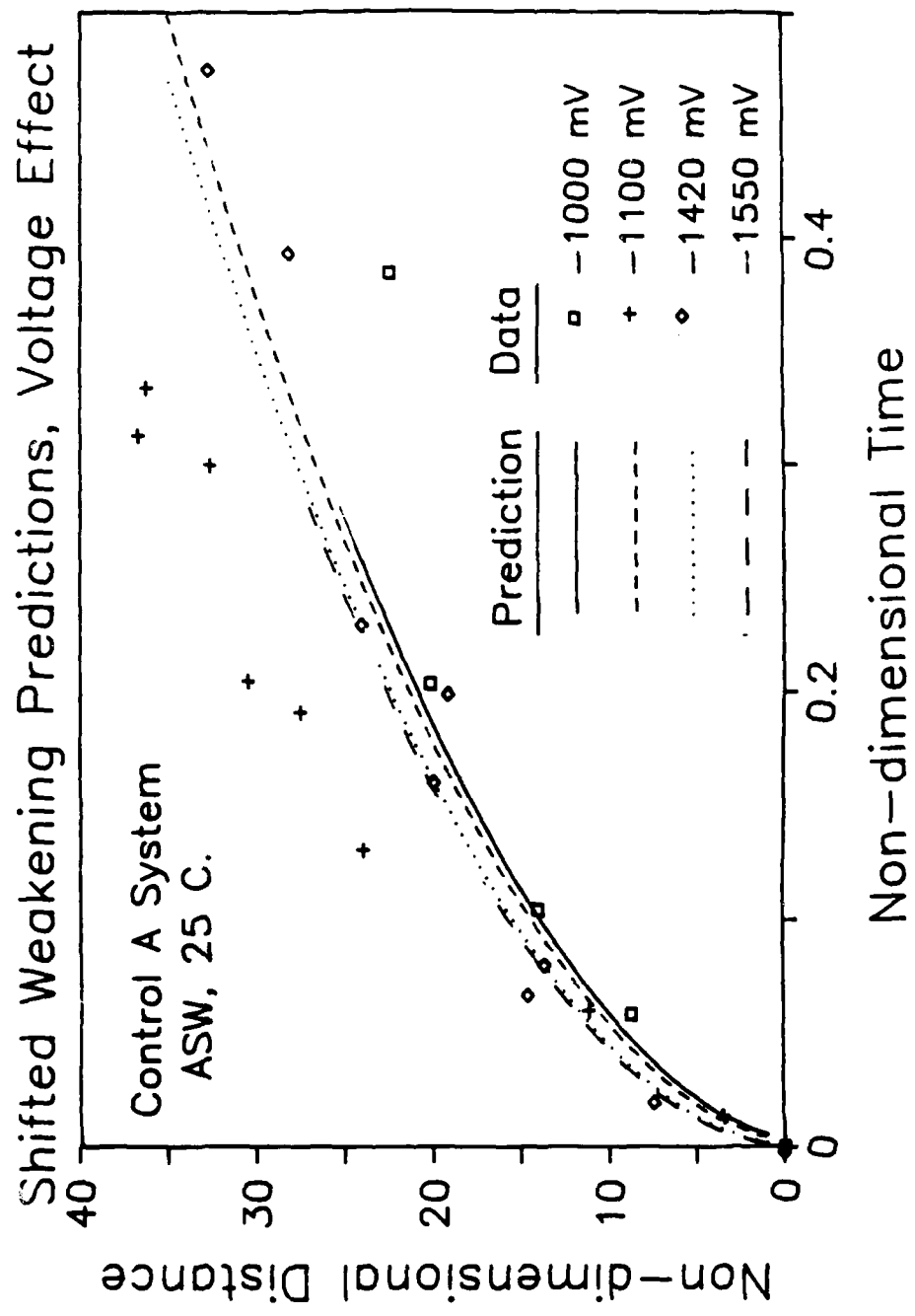


Figure 30. Shifted Numerical Predictions of Weakening in ASW at 25°C; Control A.

along with case B-4 from the test matrix at VPI. While the fit is reasonable for the higher voltages, the fit is somehow uncharacteristically poor for the lower ones. This may be explained by the fact that the data used here from Stevenson are merely an "expected" fit and may not be very accurate. Nevertheless, the predicted delay times agree very well with those reported in Ref [8]. Values of 1.98, 8.27, and 47.9 days were predicted for -1050, 850, and 610 mV respectively compared to about 1.2, 6.25, and 30 days by Stevenson. Again, the numerical predictions were plotted also in Fig.81 and show that non-dimensionalizing with respect to the diffusion coefficients plays the role of a "shift factor". And knowing that the chemical reaction rate dominates in the initial stages, Figure 82 shows that the initial slopes of the prediction curves differ while the rate is similar at long distances where diffusion dominates.

Similarly, the same value of $[C.L]_0$ (based on a 5 percent failure criterion for weakening) was used for NaOH modelling as well. Figure 83 shows the BDS data collected in 1M NaOH at 25 C for different voltages along with their numerical predictions. The fit is fairly good considering the amount of data scatter. Again a delay time associated with the "mild" harshness factor of 1080 is observed. The shifted data and their respective fits are shown in Figure 84. An interesting observation is that all the curves when voltage is applied are virtually superimposable. We believe that this is due to the extremely large values of W at these voltage levels. Also, the experimental data becomes banded in a fashion where the fit lines seem to be located around the mean value. This could be perhaps because the expressions for k and D are the same that were determined from the regression analysis.

Weakening Predictions: Comparisons

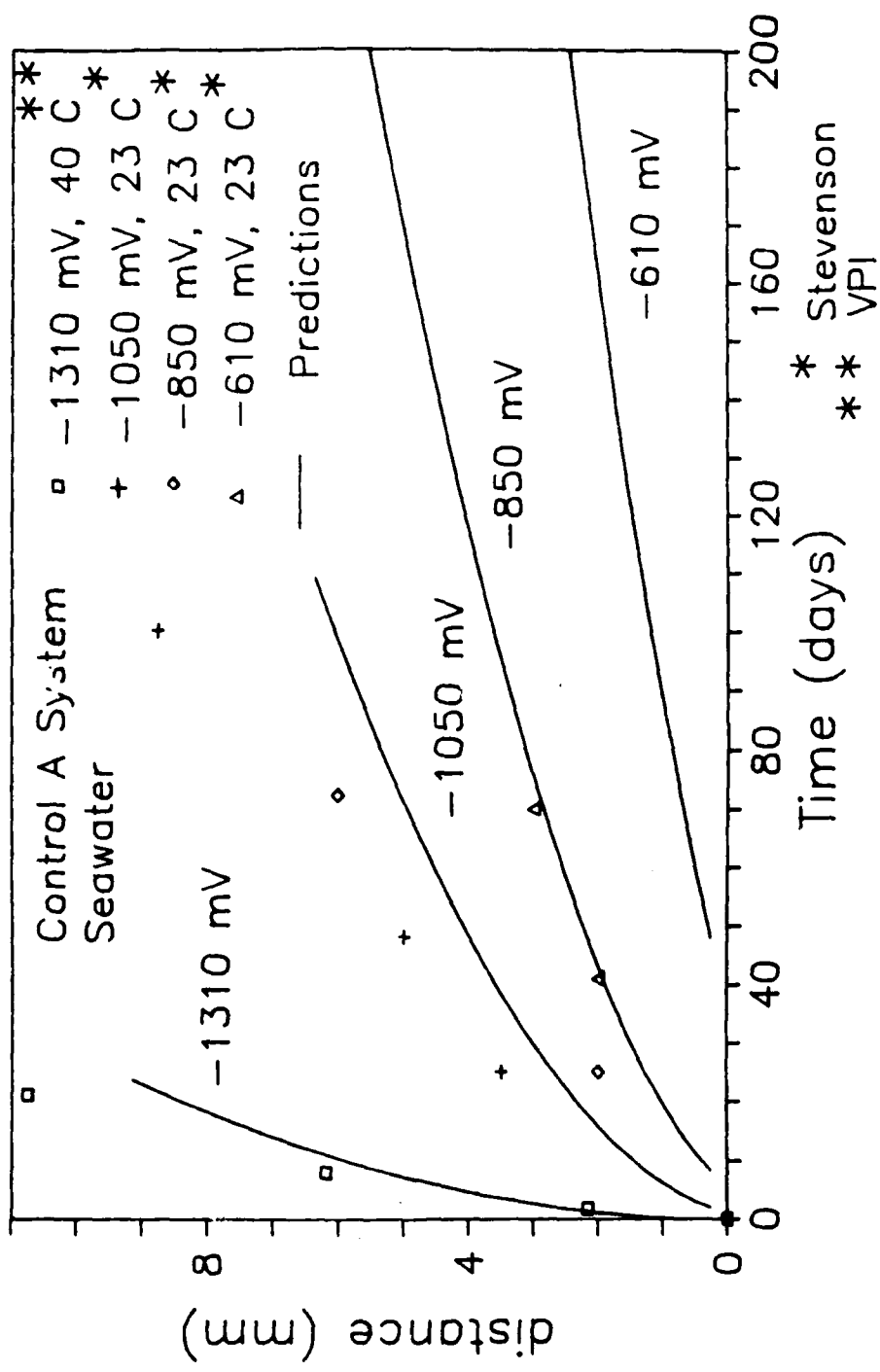


Figure 81. Predictions of Weakening in SW at different voltages and temperatures; Control A.

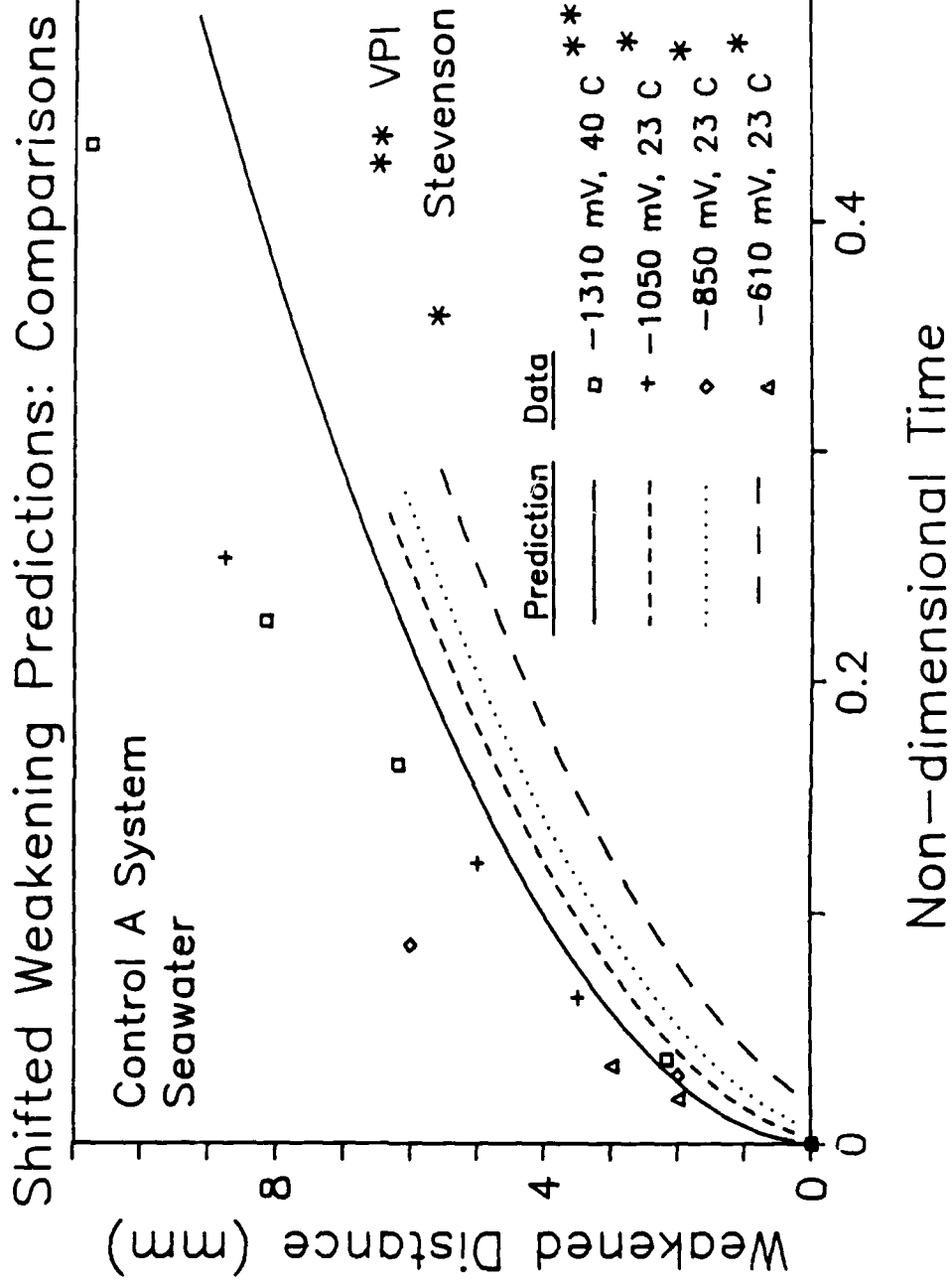


Figure 82. Shifted Predictions of Weakening in SW at different voltages and temperatures; Control A.

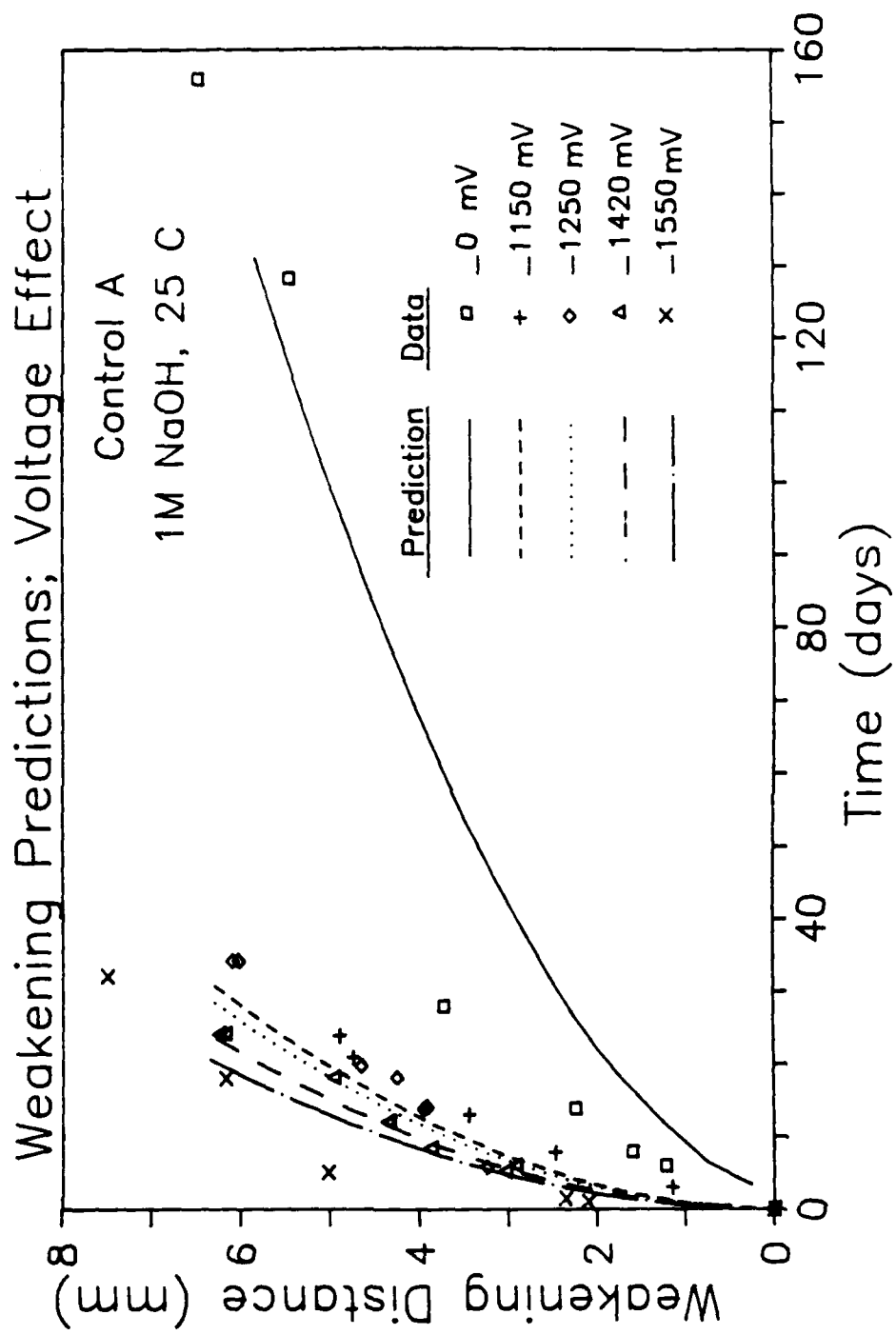


Figure 83. Predictions of Weakening in 1M NaOH at 25 C; Control A.

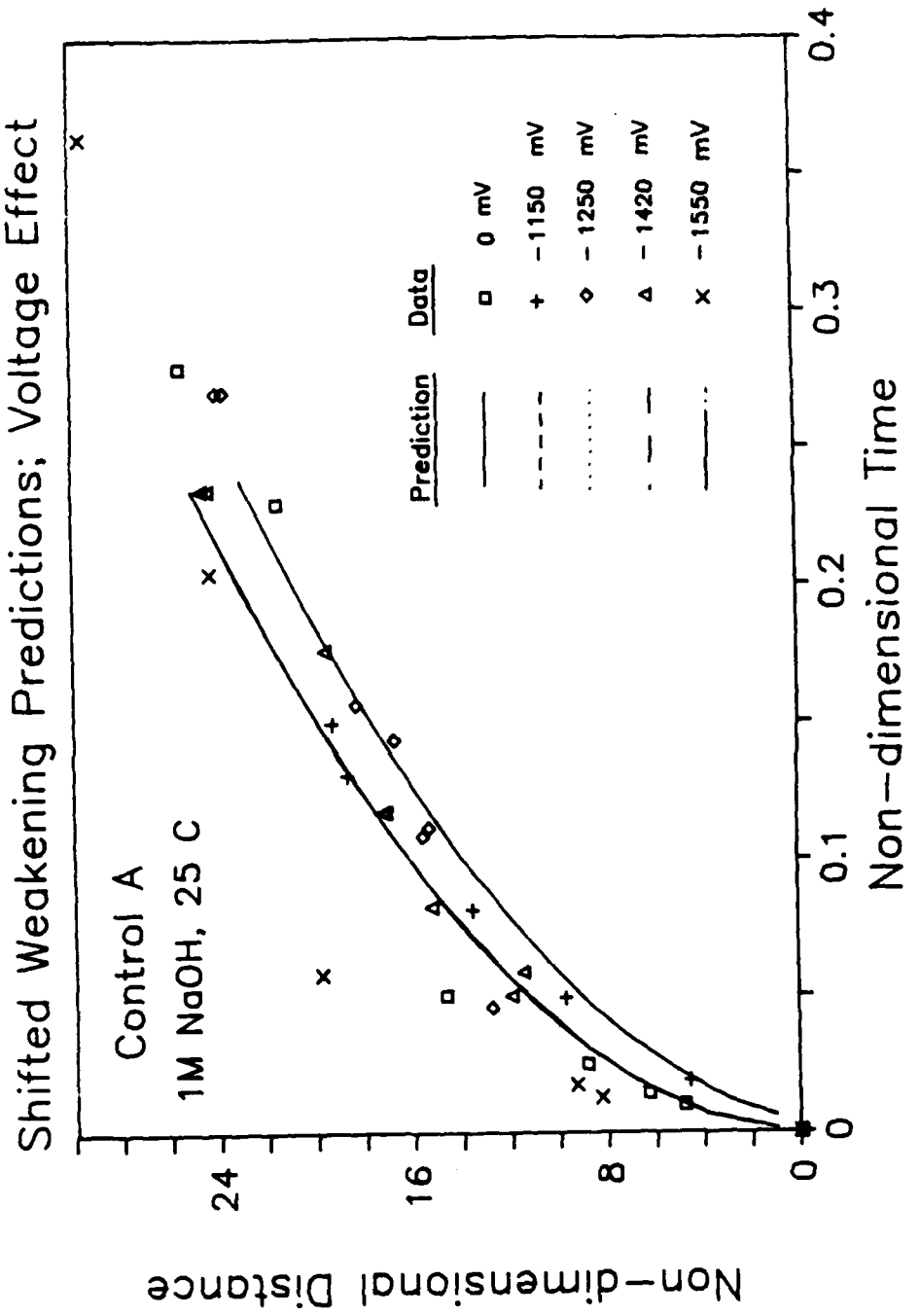


Figure 84. Shifted Predictions of Weakening in 1M NaOH at 25 C; Control A.

6.7.2 Delamination

One virtue of the model described above is that the number of parameters that are needed to determine the rate of delamination is reduced to two: W and G_{c0} , where the former is determined from the knowledge of k and D as discussed above. Another unknown factor is the decay behavior of G_c as a function of degraded critical linkages. Figure 85 gives some expressions for the hypothetical influence of degradation on G_c for three possible values of G_{c0} : 10, 50, and 100 kJ/m^2 . The major action for the case when the SBS is used is apparently limited to the lower right corner of the figure where G_c becomes small. Because an exact function of the shape of the decaying G_c versus [C.L.] is not available, a linear relationship was assumed in the model and the solution proceeded according to the algorithm. A value of G_{c0} of 100 kJ/m^2 was found to fit the data best.

Delamination results from the SBS in 1M NaOH at 25 C with and without potential were normalized with respect to their respective diffusion coefficients and are presented in Figure 86. Voltages of -1150, 1250, 1420 mV (SCE) along with a case without voltage are all included. Interestingly enough, the collapse of the experimental data along a straight line is indicative of the shifting capability of this technique and, perhaps, a sign that the experimental data for the Chemlok 205/220 system in NaOH solution is well behaved. A linear decaying function with an initial G_{c0} value of 100 kJ/m^2 was used and a good fit for the case of -1150 mV at 25 C (taken as a reference) was consequently arrived at. As seen from Figure 86, the resulting predictive curve is fairly linear (bends down slightly) with the initial slope most comparable to the experimental data. Similar fits were found for the other voltages were found to be virtually

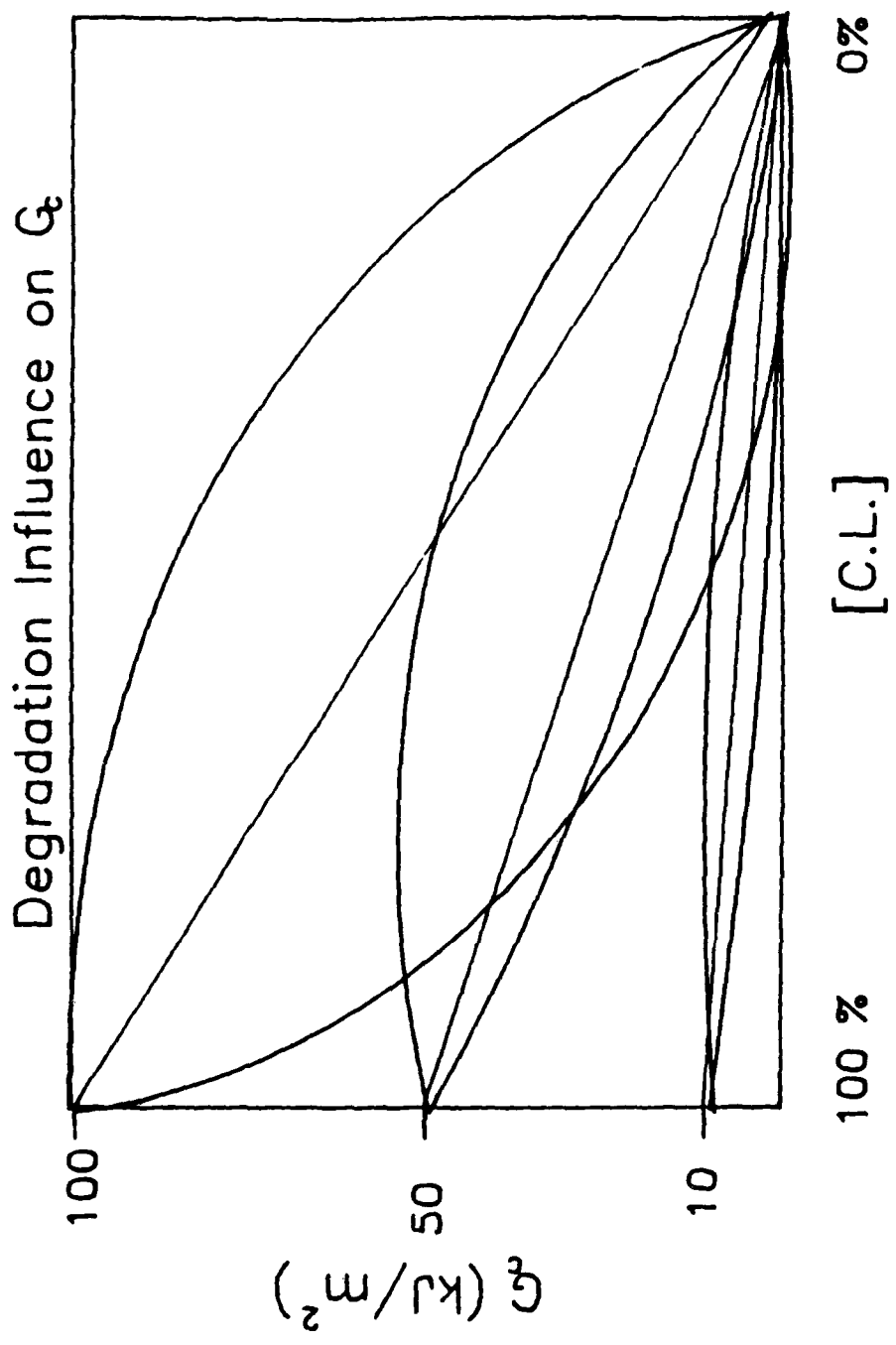


Figure 85. Influence of Degradation on Critical G.

superimposable with the exception of the case of no applied voltage (W for this case is considerably lower).

Figure 87 shows the delamination predictions in real time for the above mentioned environments. Reasonably good fits are obtained (except for the case of 0 mV) for up to about 12.7 mm delamination length (corresponding to G_T of about 0.4 kJ/m²) after which the model tends to over estimate the rates. This is not surprising since this value of G_T falls into the range within which the DBPRs decrease rapidly (region II).

Similarly, the delamination data for the control system in ASW at different voltages were shifted and are plotted in Figure 88. Some scatter is evident, and the data for -1000 mV is especially distant from other data. This is due to the fact that these data did not conform to the otherwise established accelerating effect of applied G as could be seen in Figure 96 in Appendix 2. Again, a G-decay expression identical to that used above is utilized resulting in a fairly linear predictions as shown in Figure 88. Except in the case of -1000 mV, the data is fitted nicely within the given range of given debond window. Figure 89 illustrates the data and the corresponding fit in real time. It is understandable that the predictions for the -1000 mV case are higher than the data due to the above mentioned anomaly.

6.8 CONCLUSIONS

The model described above is a useful tool to model debonding given that the appropriate parameters are used. Environmental failure of adhesive joints comes about

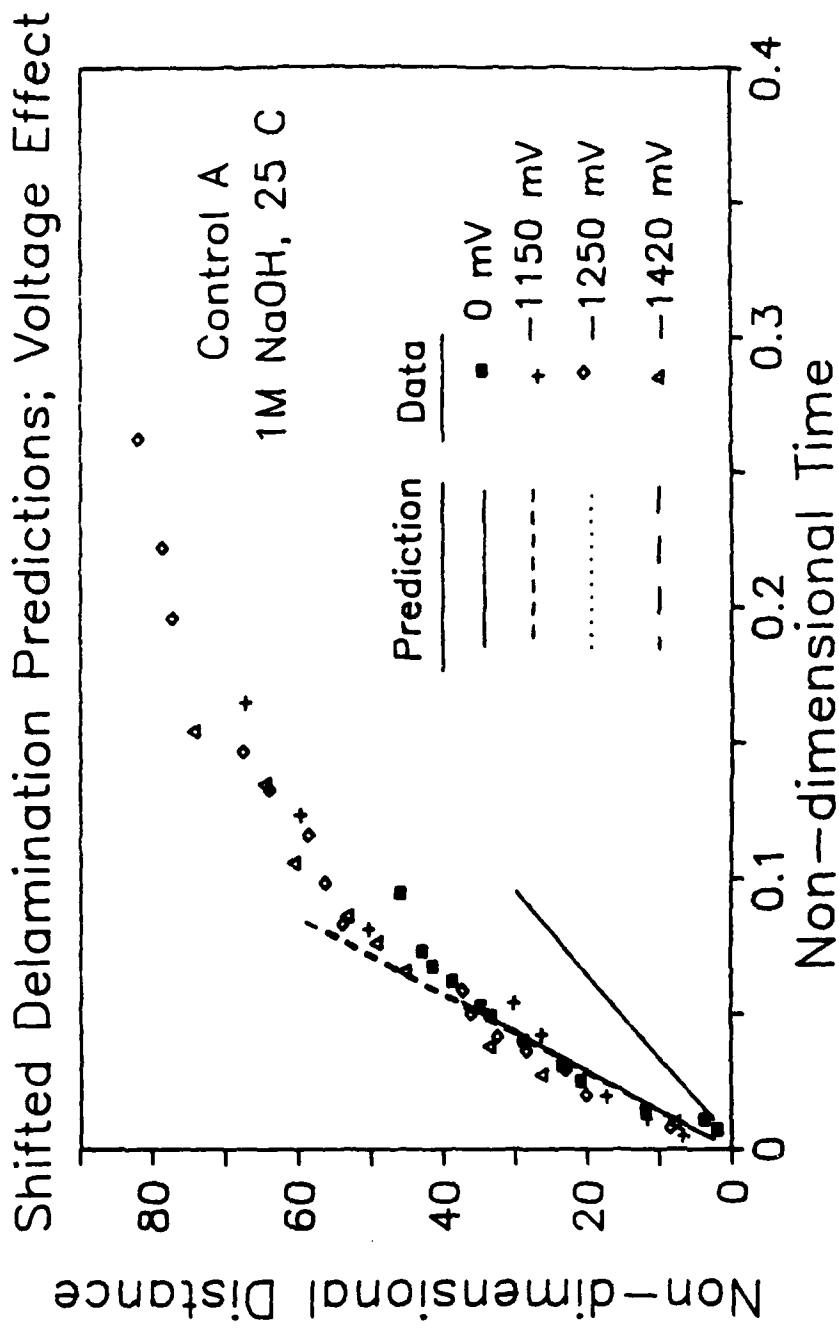


Figure 8c. Shifted Delamination Data and the Apparent fits; Control A; 1M NaOH, 25 °C.

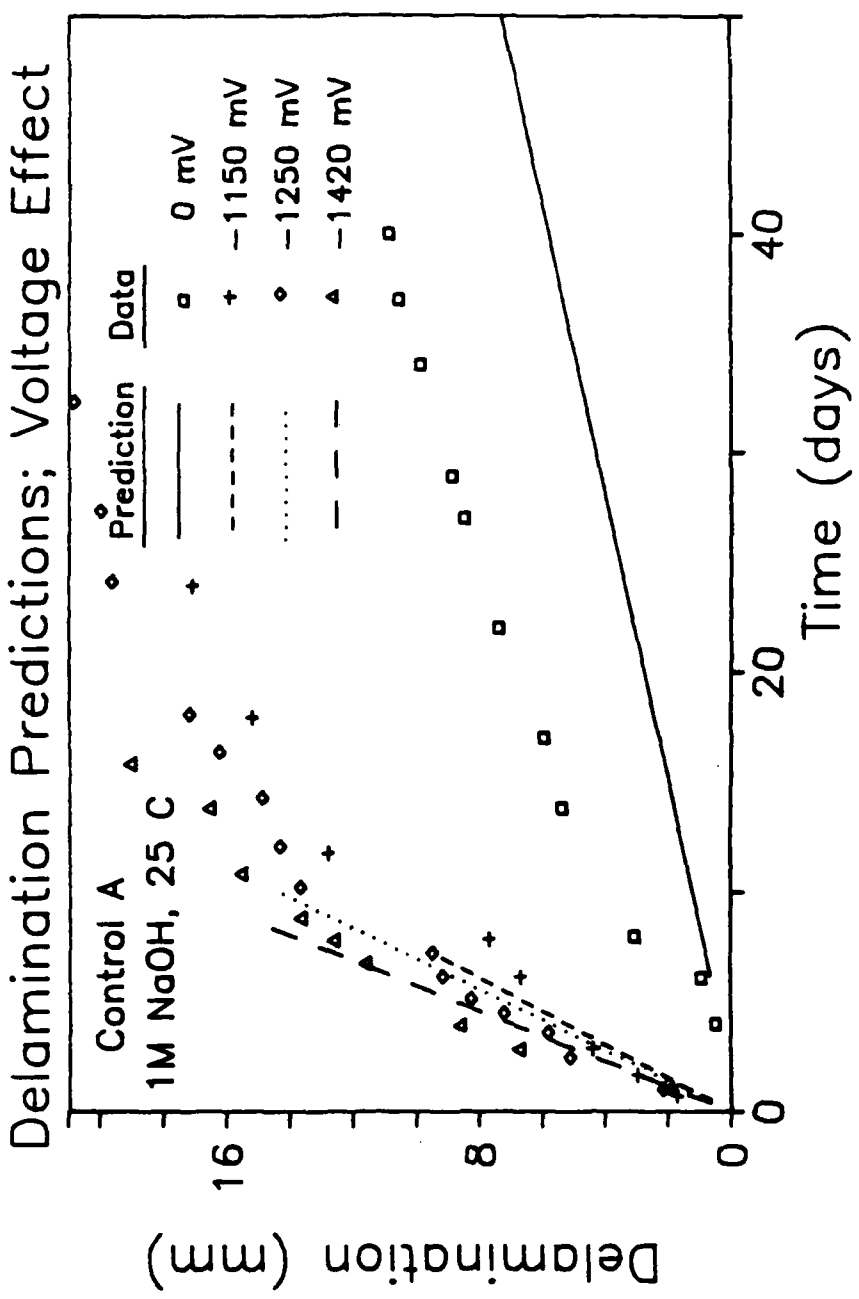


Figure 87. Delamination Predictions; Control A; 1M NaOH, 25 C.

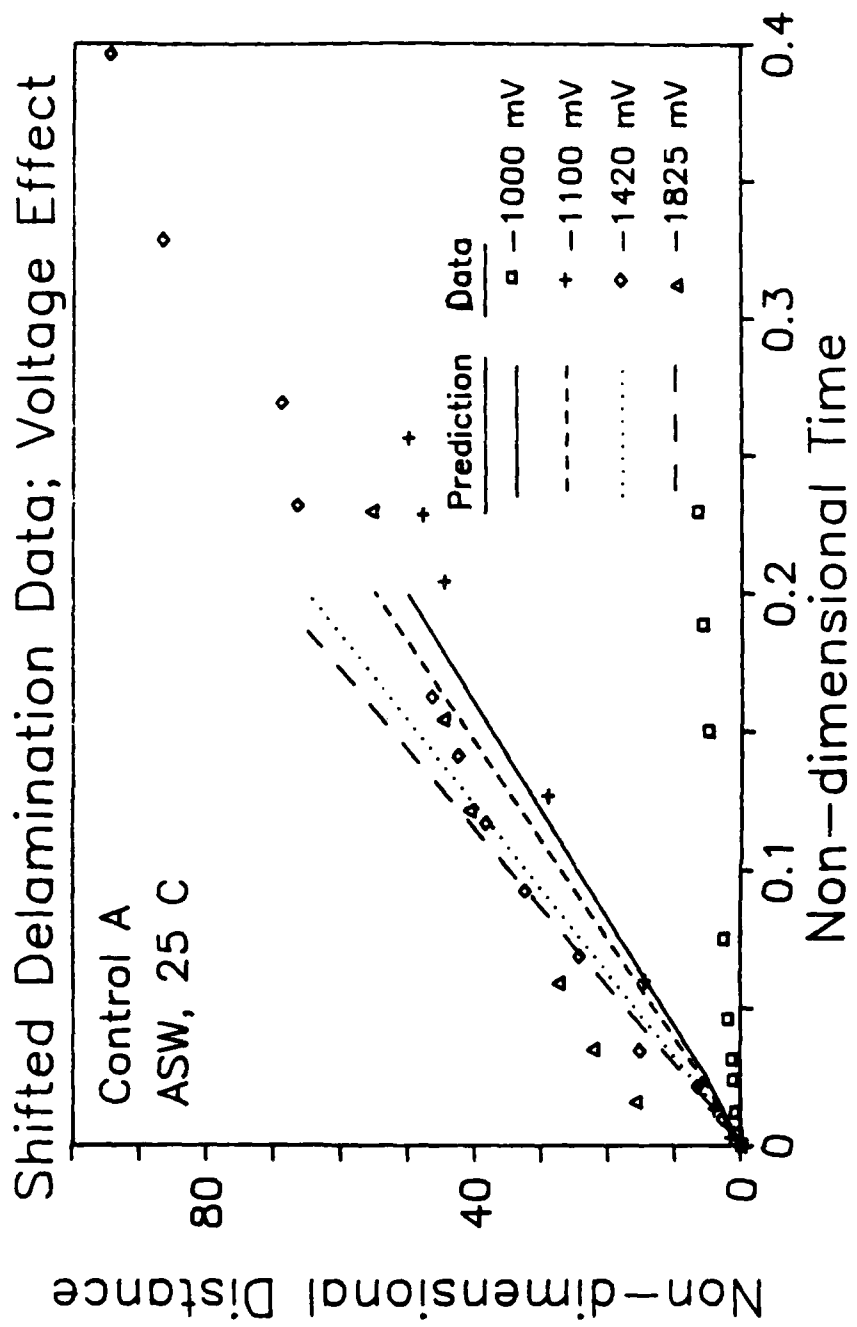


Figure 33. Shifted Delamination Data and Apparent Fits; Control A; ASW, 25 C.

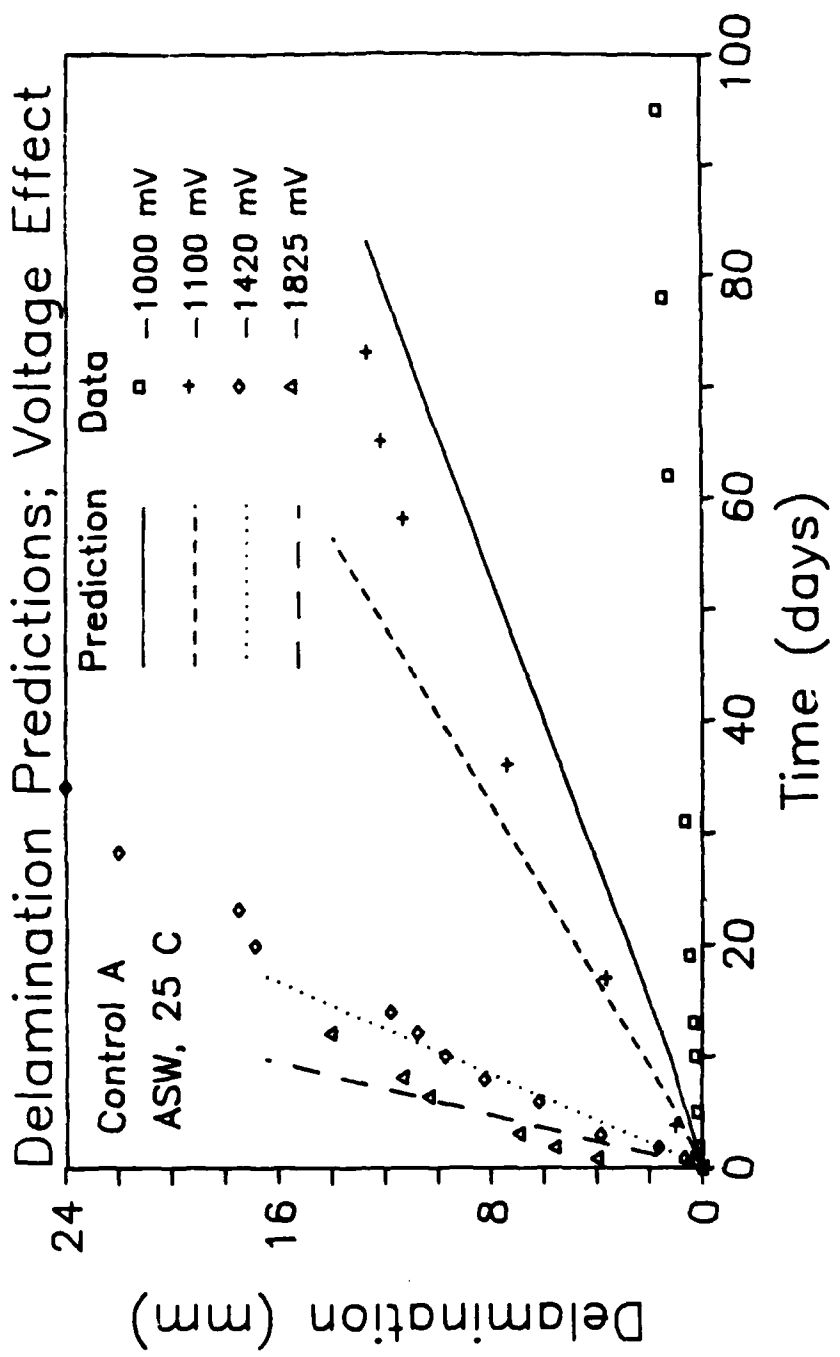


Figure 89. Delamination Predictions; Control A; ASW, 25 C.

as a result of the completion of a series of events. The characterization of a failure criterion serves to identify the climax of that closed-loop chain. The complexity of the various processes and their interaction requires more detailed study. Nonetheless, we were able to show the feasibility of such an approach without having to solve the fully developed problem of the form presented in Appendix 4. In summary we conclude that

- 1- The environment interaction with the bondline is modelled through the boundary value problem (Eq.54,55), subject to the appropriate BC's, which accounts for the proper generation and consumption terms.
- 2- The failure criterion for weakening depend on the concentration of the critical linkage [C.L] which is in turn a function of the surface concentration of the aggressive hydroxyl.
- 3- The failure criterion for delamination is a derivative of that for weakening into which updating of the boundary conditions was incorporated leading to a "marching boundary" phenomena.
- 4- Weakening was modelled exceptionally well and reasonable delay times were numerically determined and correlated with real data.
- 5- Predicting delamination was accomplished fairly successfully for large values of G, while the program overestimated delamination for relatively low G's.

7. INSIGHTS INTO THE MECHANISM(S) OF FAILURE

7.1. INTRODUCTION

Generally, characterization of the mechanism and locus of failures in adhesive bonds is a difficult task. Each and every interfacial (oxide/primer, primer/top coat, top coat/substrate) region is theoretically capable of de-adhesion given that the conditions are adverse. Also, degradation of the adhesive constituents (oxide solubilization, bulk adhesive attack) may take place as well. Another complication is that failures' mechanisms and modes are adhesive system sensitive and may vary (for the same system) considerably from one condition to the next. A review of the mechanism(s) of cathodic debonding of rubber from steel is addressed herein.

There is no question that bulk degradation may, and indeed does, occur due to the hydroxyl attack on the unsaturated bonds within the primer as shown by Boerio [23] and Hamadeh et al [26]. A wide range of bulk linkages are susceptible to attack by the

OH^- especially the molecular bridges i.e. methylene, ether, etc. The contribution of bulk integrity is crucial for bond durability in aggressive media thanks to diffusion resistance. The question that needs to be asked, however, is whether the deterioration in the bulk is the mechanism by which cathodic activity fails the bond.

7.2 THEORIES OF ADHESION

In order to develop a better understanding of de-adhesion, one needs to appreciate the nature of adhesion. Adhesion is a diverse phenomena in as far as the number of scientific fields involved and the complexity of the adhesive system. On a micro- level, adjacent atoms and molecules may develop either physical or chemical forces and frequently both. The collective work of those forces contribute to the macro properties of the bonded system i.e. the dry strength and durability, to name a few. Several theories have appeared to try to explain adhesion on the basis of inter-molecular forces that prevail at the interface. A wide range of those forces that operate at the interface can be polar or non-polar,i.e., van der Waals (physi-sorption) and covalent (chemi-sorption). Among the theories that relate to polymeric materials bonding to metal oxides are the following:

- 1) The Electronic Theory: Suggests that electrostatic forces arising from electron transfer between the adhesive and the substrate molecules provided contact occurs.

2) Theory of Mechanical Linking: This theory suggests that the interlocking of the molecules of the adhesive with the irregularities of the substrate is the source of adhesion. One drawback of this theory is that it does not explain the aging behavior, i.e., deterioration of bond.

3) The Adsorption Theory: Physical and chemical interactions are the primary force of attraction provided that adsorption of the adhesive molecules occur. Heat is needed to provide energy for the reactions and pressure aids the polymer to wet and physically absorb.

Bickerman [48] suggested the existence of a finite boundary layer composed of absorbed molecules that differ from those in the bulk adhesive phases. A Weak-Boundary Layer is, therefore, responsible for failure either because of inherent flaws during the bonding process or due to service conditions. The former category may be caused by a contaminated substrate, entrapment of air, incompatibility of the adhesive and the substrate. The induced WBL may form due to cohesively weak oxide layer or the chemical degradation between the polymer and the substrate.

7.3 **DISCUSSION**

The cooperation between VPI, TRI, UC, and UT over the past three years has amassed an extensive amount of data in support of bulk degradation. However, a question has been raised whether other mechanisms, i.e., interfacial, do exist. The implied suggestion is that the degradation process which takes place at the interface

could be different than that in the bulk and not simply an "accelerated process". Throughout this interdisciplinary study, several observations were made that may support either mechanism. As a result, we have accumulated the evidence that, we think, supports both arguments and have presented it in two separate groups entitled "Substantiating/Counterargument" for both the "bulk" and the "interfacial" proposed failure mechanisms as follows:

SUBSTANTIATING BULK	COUNTERARGUMENT
<ul style="list-style-type: none"> - XPS & IR show degradation of some linkages in bulk adhesive and that the cathodically failed surfaces show the same trend. Boerio [23], sighting IR study of bulk primer after exposure to NaOH solution, reported that the "methylene groups linking the benzene rings in the phenolic polymer rapidly decrease in intensity". He then suggested a possible failure mechanism by which the base-catalyzed oxidative degradation of the phenolic makes the resin more hydrophilic and eventually results in failure. A mechanism previously suggested by VPI [26] concludes that hydrolysis 	<ul style="list-style-type: none"> - Degradation of the phenolic resin is almost inevitable when exposed to the alkali. The contribution to durability of the joint depends on the rate of such mechanism in comparison to another interfacial mechanism. The similarity of the degraded peaks in bulk to those on the fracture surface may be explained as follows: <ul style="list-style-type: none"> i) XPS is not a very surface sensitive technique. The relatively deep penetration of the beam means that the interfacial components may have been masked. ii) The degradation of the polymer at the surface, as evidenced by similar peaks to those in the bulk, may have occurred as a result of exposure to the alkali

<p>of ether linkages in the backbone polymer leads to saponification of the adhesive. A secondary mechanism was the leaching of chlorine, as Cl^-, from the adhesive and possibly corroding the iron oxide.</p>	<p>after the bond has failed due to other mechanism (interfacial).</p>
<ul style="list-style-type: none"> - TRI reported no improvement in the DBPR when silane was used as surface preparation. <p>A question may be raised is that if failure is interfacial, why was the improvement limited to the case when the silane was added to the primer, while no positive effect on durability was seen when the A-1100 silane is added directly onto the oxide surface?</p>	<ul style="list-style-type: none"> - Others [49] have reported that the best improvement in durability occurred when silane was added as surface preparation. <p>One may suggest repeating the test for several possible reasons:</p> <ol style="list-style-type: none"> i) the silane might have been old, ii) insufficient data was collected, iii) or that proper interdiffusion and crosslinking between the silane and the primer were not accomplished. which may have resulted in shifting the locus of failure to silane/primer interface.
<ul style="list-style-type: none"> - The WBPR, the initial DBPR, and the rate of degradation of the free primer films in 1M NaOH are all comparable. This may suggest that 	<p>The rates being similar may simply indicate that the rate for the bulk degradation mechanism is comparable to that of the interfacial mechanism for these conditions.</p>

debonding is a direct result of bulk degradation.	This may not be true for the case when voltage is applied.
SUBSTANTIATING INTERFACIAL	COUNTERARGUMENT
<ul style="list-style-type: none"> - Failures always seem to occur near the oxide and that the analysis of the XPS results from the polished specimens show a much cleaner interfacial separation. Boerio [50] noted a substantial difference in delamination results with polished and etched substrates. For polished specimens, locus of failure was near the primer/oxide interface with little primer left on the substrate and little oxide remaining on the rubber. Hamadeh et al [26] used XPS to characterize both sides of failure of a polished rubber/steel joint exposed to 1M NaOH, natural potential of zinc, and 30 C. Compared with a rough substrate, much more chloride (originally in adhesive) was left on the rubber surface and much less iron, zinc, and lead (mostly from alloy) were observed. 	<ul style="list-style-type: none"> - It is reasonable to expect failure to occur near the cathode where pH is highest. Same componental composition on both sides of the fracture surfaces of rough substrates after exposure to cathodic activity. VPI [51] had reported that both the steel and rubber sides of the failure surfaces "appear to be quite similar in the broad window of ESCA even though the failure appears to be clean interfacial failure to the naked eye".

<ul style="list-style-type: none"> - In 1NaOH solution without voltage, Bond Propagation Rate depends on the oxide on the substrate. Stainless steel performed much worse than mild steel (without applied voltage). 	<ul style="list-style-type: none"> - Oxide may serve as a catalyst for the reaction on the surface.
---	--

Q: If bulk degradation is the governing mechanism, why are the rates so much different? (a)

<ul style="list-style-type: none"> - Following degradation of neat film specimens in 1M NaOH for a long period, the modulus and the strength of these specimens remained moderately high. A point could be made as to Why would the bond fail if the primer material retains high residual strength? 	<ul style="list-style-type: none"> - The in situ pH within the confined regions of the bond near the cathode could generate higher pH than occurs in 1M NaOH solutions.
---	--

a: Koehler [19] used an oleoresinous/steel coating system and showed a complete failure in ammonium hydroxide solution after 4 hours. He then used tinplate and 3004 aluminum for substrates and did not observe any detachment after exposure to the same solution ($\text{pH} = 11.7$). One explanation was that 'the dependence of the adhesion loss on both the coating and the metal is to be expected from a mechanism involving the acid/base nature of these entities and the pH of the interfacial solution'.

7.4 THE ATTACHMENT SITE THEORY

The adhesive joint could be looked upon as a composite that is made up of three major components: the inorganic metal substrate, the adhesive, and the rubber layer. If we look closely, one realizes that the final joint consists of several other layers. The hydrated oxide meets the adhesive in a 3-dimensional interphasal layer through which an internal structure of attachments develops. That is where the adhesive molecular segments are attached to the oxide. The properties of this layer are different than either the adhesive or the substrate: chains are highly organized in comparison with the bulk polymer. The molecules are closely aligned and oriented in such a way to fit with the morphology of the oxide. The attachment site theory of adhesive joint strengths was developed by Lewis [52] as an elaborate means to explain the contribution of the adhesive/adherend components to the strength of the adhesive system. Because the "dry" bond strength is indicative of the "cohesive" properties of the bulk adhesive, workers have not been able to directly measure the true "theoretical" interfacial strength of bonds. This theory offers an insight into the characteristic properties of the interface.

7.4.1 Geometry

Lewis and Saxon [53] found that when various controlled amounts of an adhesion promoting compound { bis(2-chloroethyl) vinyl phosphonate, BVCP} was radiation-grafted onto the surface of polypropylene, the existence of three conditions of

interfacial attachment was encountered. When very small quantities (less than 0.1 percent) of BVCP were used, low adhesive joint strengths were observed accompanied by complete interfacial failures signifying weak surface attachment. At somewhat higher grafting levels, 0.2 to 0.4 percent, mixed type failures were observed, accompanied by higher joint strengths. Finally at a particular grafting level, maximum joint strengths exhibiting cohesive type failures were observed.

Figure 90 shows the three regions that characterize the type of failure (strength) as a function of surface attachment (Z_e). Further increase in the degree of surface attachment does not enhance the mechanical joint strength due to the rheological aspects of the bulk adhesive, even though the effect of such increase may contribute to the environmental durability of such joints. It is assumed, then, that the joint strength, S_j , is the minimum value of S_c , the cohesive strength of the bulk adhesive, S_d , the cohesive strength of the bulk adherend, and S_b , strength of the interfacial boundary layer. That could be summarized by saying that

$$S_j = \min\{S_b, S_c, S_d\} \quad [63]$$

The curve in Fig. 90 can be fitted into a semi-empirical equation that relates the joint strength to the degree of surface attachment of the form:

$$S_j = S_c \left[1 - \exp\left\{-\sum_{i=1}^n \gamma_i Z_i^{q_i}\right\} \right]. \quad [64]$$

Where S_j is the joint cohesive strength, Z_i the density of AS (number/unit area), and γ_i and q_i are characteristic parameters.

One can separate the attachment sites into two groups: Z_e , number of effective sites, and Z_0 , number of inoperative sites. That yields,

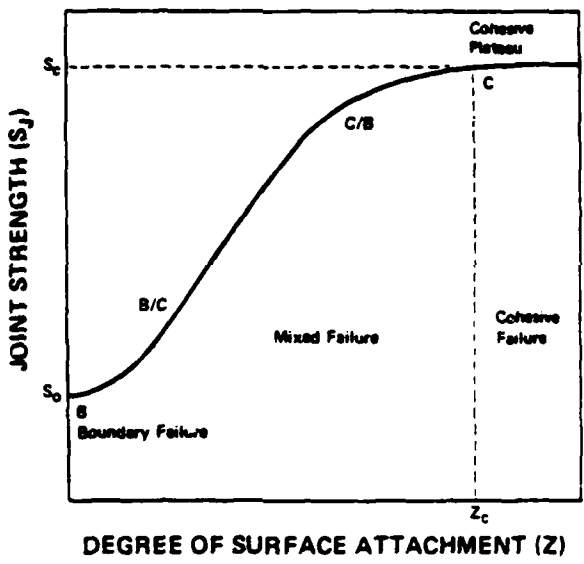


Figure 90. Semi-empirical Curve Representing the Adhesion (Joint Strength) as a Function of Surface Attachment (from [57]).

$$\sum_{i=1} \gamma_i Z_i^q = \gamma_0 Z_0^q + \gamma_e Z_e^q. \quad [65]$$

and normalizing by Z_0 ,

$$S_j = S_c \left[1 - \exp \left\{ \gamma_0 + \gamma_e \left(\frac{Z_e}{Z_0} \right)_e^q \right\} \right] \quad [66]$$

where γ_e and q_e are type dependent parameters.

$$\gamma_0 = - \ln \left(\frac{S_c - S_0}{S_c} \right) \quad [67]$$

since $Z_e = 0$ at $S_j = S_0$.

The derivation of the AS model was also developed using the principles of the phase transformation theory following Avrami [54-56] and by relating the volume of AS formed to the strength of the BL through a boundary layer ultimate strength, K^x such that,

$$S_b = k^x \left[1 - \exp \left\{ - (\gamma_0^x + \gamma^x Z^{qx}) \right\} \right] \quad [68]$$

where,

$$\gamma_0^x = - \ln \left(\frac{k^x - S_0}{k^x} \right). \quad [69]$$

Here, k^x is the ultimate "theoretical" Boundary Layer strength, γ^x is a rate constant (a kinetic term which is a function of AS geometry, growth rate effects as a function of AS concentration, and the potential nucleation site density), and q^x : the effective dimension of the AS growth model.

An attractive feature of this theory is that it is able to explain that different adhesively bonded joints perform differently due to the fact that "though the interfacial adsorption functionality of a given adhesive system remains constant, the number of effective AS's on the adherend will vary accordingly to its surface treatment" [57]. Another feature is the model's ability to explain the environmental attack on the adhesive system through the chemical degradation of the AS's. Figure 91 shows the phenomenon of de-adhesion. The bond fails when the environment attacks the effective sites (Z_e) converting them into inoperative ones (Z_0) thus reducing the strength of the BL, S_b , to where it can no longer resist the externally applied stresses. This environmental effectively shifts the locus of failure from cohesive in the adhesive to interfacial.

7.4.2 *Chemical Bonds*

Let us discuss the nature of those bonds that form the A.S.'s across the metal oxide. According to Fowkes [58], the interfacial acid-base bonding could span a wide range including the best known: hydrogen bonds with "interaction energies that are dependent on the acidity of the hydrogen donor and on the basicity of the hydrogen acceptor". He related the work of adhesion to exothermic interfacial energy changes while the bond is forming. Heats of adsorption were then correlated, through semi empirical parameters, with the adsorption of various polymers onto substrates. The strongest adsorption, for example, was found to take place when neutral solvents were used with PMMA (basic polymer) on silica (acidic) and that adsorption was diminished

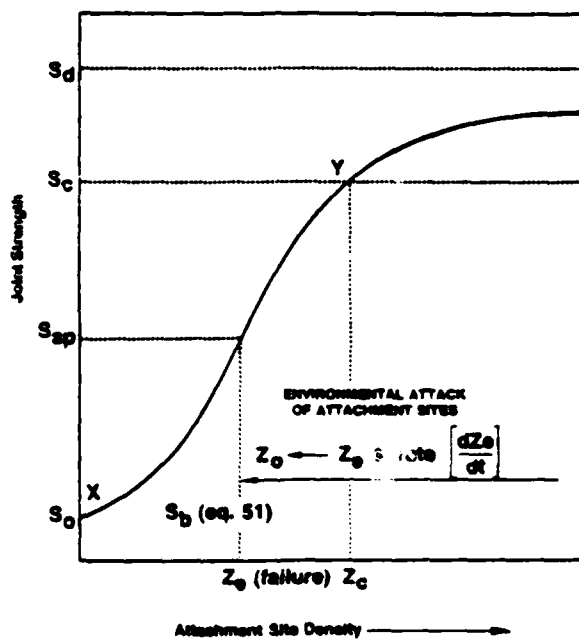


Figure 91. Semi-empirical Curve Representing the De-adhesion (Joint Strength) as a Function of Degraded Surface Attachment (from [57]).

when basic or acidic solvents were used. The reason for the lost adsorption is blamed on the competition between the acid and the base for the available sites. Fowkes goes on to suggest that silanes work well because they increase the basicity or the acidity (depending on type) of the substrate thus increasing bondability. Amino-Silane , APS, for instance, was found to make the surfaces quite basic as evidenced by its strong positive zeta-potential. This may be in agreement with work reported by Boerio and Williams [59] in which silane was deposited from solutions of pH 8.0 to 12.5. A considerable difference in residual bond strength under wet conditions was observed.

The addition of silane provides a water-resistant bond between an organic polymer and an inorganic metal as well as between organic polymers. Silanol groups may first form hydrogen bonds with the surface, but during drying they condense to-siloxane structures chemically bonded to the surface [60]. The overall joint strength and its resistance to moisture was found, however, to depend on the extent of cross linking of the silane primer and the interdiffusion of silane into the adhesive phase. The integrity of the 3-dimensional interphasal region is necessary to achieve both dry and wet strength.

7.4.2.a Aluminum Substrates

Adsorption studies [61] of phenolic (from a solvent blend) on a well characterized aluminum oxide surface show that the attachment density is very high for such an ideal system. The crystal structure of the oxide, contamination, and water vapor are mainly responsible for the considerably lower attachments in real life applications. Other components in the heterogeneous adhesive may also compete for the available sites as

well. The Al-O bond length affects the crystal structure of the Al oxide. About three attachments per phenolic molecule is theoretically feasible, and assuming that an average phenolic molecule takes up to $10\text{-}20 \text{ } \text{\AA}^2$, one site could theoretically be formed on $3\text{-}6 \text{ } \text{\AA}^2$. The nature of the bonds at these sites can range from Al-O to hydrogen bonds. An acid-base interaction can take place because the phenol is acidic and oxygen bonds to Al on the surface and attaches to it.

Jemian [62] used careful surface pretreatment of Al oxides to form hexagonal Bayerite ($\beta - Al_2O_3 \cdot 3H_2O$). He estimated the attachment density at the interface to be of the order of 10^{14} per cm^2 taking the molecular spacing to be approximately 1nm.

7.4.2.b Steel Substrates

The Chemlok 205 primer is phenolic-based and is primarily responsible for the quality of the interfacial attachments between the steel substrate and the other components in the bond (Chemlok 220 adhesive and Neoprene rubber). The cure conditions used with this system lead to the evolution of water via condensation reactions and are "precisely those that give the maximum probability of forming ether linkages between oxide surfaces and the resin" [63].

Gettings and Kinloch [64] used XPS & SIMS to investigate the durability of silane/steel adhesive joints. Mild steel substrates were used in their study and three different silanes were evaluated. They found that a γ - glycidoxylpropyltrimethoxy silane (GPMS) resulted in much better durability than either a styrene-functional amine hydrochloride silane (SAHS) or a γ - aminopropyltriethoxy silane (APES). The cause of the enhanced performance of the GPMS was attributed to the presence of a complex bonding, possibly between silicon, iron, and oxygen. The above peak was characterized

by a 4.8 eV shift in the iron $2p_{3/2}$ in the XPS spectra. Other differences between the above mentioned silane systems were revealed by SIMS. The radicals SiO_2H^- and SiO_2^- were observed at the primer/steel interface with the GPMS system but not for the other two. A significant difference, yet, was a strong evidence of the formation of a chemical bond, probably $Fe - O - Si =$, as evidenced by the detection of $FeSiO^+$ radicals at the interface.

7.5 LOCUS AND MECHANISM OF FAILURE

So far, we have established the feasibility of both the physical and chemical aspects of the attachment site theory as such. The applicability of the above to the STRIP problem will be discussed. Iron oxide may, or may not, be basic enough to accomplish the wide range of bonds that are associated with aluminum oxide. Nevertheless, Castle and Watts [4] used XPS to characterize polybutadiene coatings on metal. They suggest that the formation of the polar carbon peak in the position corresponding to $C=O$ may arise as a result of reaction of hydrocarbon with the iron oxide to yield $RCOOFe$. Using polished steel, they found that when debonding was induced by cathodic potential, a complete segregation between the polymer and the oxide was observed judging by the presence of bright Fe^0 . The residual adhesion was blamed for the considerable residue of organic carbon on the metal surface. They proceeded to conclude that the altered zone ahead of the debonded region to be active saponification, as proposed by Hammond, et al. [65]. Alkaline conditions certainly would hydrolyse the $FeOOCR$ salt which we proposed. Hydrolysis of the bond

adjacent to the oxide surface would account for the interphase separation. Saponification, of a near interface polymer zone, prior to complete hydrolysis of the bond, would account for the low energy cohesive failure ahead of the disbondment front" [4].

Gettings et al [66] have fractured epoxy/mild steel joints inside the XPS spectrometer, after environmental exposure, and found that the steel substrate had no adhesive remaining on the oxide and no traces of oxide on the adhesive side. Recently, Leidheiser [3] has abandoned his previous view that oxide dissolution is the cause of cathodic failure in coatings and has stated that "the delamination process occurs because of hydroxyl attack at the interface". He sites some IR studies to conclude that the most likely bond between the polymer and the oxide on steel is between the carboxyl group in the polymer and the -OH group on the oxide surface as follows:



He, then, assumes the presence of about 0.5×10^{15} surface bonds per cm^2 of geometric surface area and proceeds to assume that the interfacial degradation reaction is of the form



7.6 CONCLUSIONS

In light of the above theory, a possible explanation of cathodic delamination of the 205/220 system is that the bonds that form the A.S.'s are being displaced by the OH^- partly because the pH of the hydroxyl is more basic than the iron oxide. The hydroxyl (strong base) competes with the weak base (oxide) for the phenolic (acidic) breaking the bond and effectively rendering the originally effective site inoperative. The presence of the hydroxyl is both necessary and sufficient for the mechanism to proceed since the process is chemical-reaction-controlled. Upon modification with APES , the improvement is two fold: significant increase in substrate basicity that reduces the gap for the acid-base substitution reaction, and the diffusion and crosslinking of the silane in the primer has improved the environmental resistance of the bulk adhesive.

8. SUMMARY AND CONCLUSIONS

8.1 INTRODUCTION

Cathodic debonding of the 5109S Neoprene Rubber from ANSI-1026 steel appears to be a direct consequence of alkali attack. In principle, TRI, UT, and UC were involved in the surface preparation and durability improvement, characterization of the mechanical properties of the Neoprene rubber, and adhesive system characterization aspects respectively. VPI's assignment, on the other hand, was to determine the effects of the accelerating parameters on debonding, to develop an understanding for the failure mechanism(s), and to ultimately model the various involved processes. In retrospect, we feel that our major contributions could be summarized in this chapter as follows:

8.2 MECHANISM(S) OF DEBONDING

Because all the evidence has pointed to the primer/oxide interface as the locus of failure, we have performed a comprehensive study of the degradation mechanism(s) of alkali attack on free-standing primer adhesive films and on adhesively bonded specimens. The study was two fold: 1) net mass uptake studies of free coupons, and 2) surface characterization of degraded primer and failed bond surfaces using XPS.

Fig.6 has demonstrated the amount of physical and chemical damage that the primer underwent during exposure to 1M NaOH. A significant increase in mass uptake (compared to a similar coupon in ASW) is a clear indication of the above degradation. The chemical degradation of the phenol-formaldehyde-based Chemlock 205 is clearly illustrated in Fig. 5. The XPS analysis of the C 1s spectrum of the free film primer shows the rise of a carboxylate peak that is indicative of saponification. The increased hydrophilicity of the polymer may explain the unusually high percentages of mass uptake following exposure. The physical damage incurred may be deduced from the re-sorption portion of the mass uptake curves. Although the extent of water diffusion was insignificant for the unexposed primer, large percentages were observed following exposure. One explanation is that the physical structure of the polymer has been significantly altered after being degraded thus resulting in higher permeability. Another possibility is that the remaining hydroxyl ions inside the film and the unsaturated carboxylate ions act as a "sponge".

Figure 10 shows the same degradation trends for failed bonds and neat primer as seen by the curve-fit of the C 1s peak. Fig. 8 also illustrates the apparently similar composition of both sides (rubber side and metal side) of the fracture surface. But although the analysis of the XPS spectra of the failed bondline surfaces seems to suggest

a cohesive locus of failure close to the oxide, additional work on polished substrates favors an interfacial mechanism. Figs. 13 and 14 show a much cleaner interfacial break thanks to a lack of oxide roughness.

While both bulk saponification and interfacial linkage hydrolysis mechanisms are possible, Boerio [14] suggested another bulk degradation mechanism by which the methylene linkages are broken by the alkali. Therefore, two approaches were taken in order to improve durability: modification of the adhesive with silanes and zinc phosphate treatment of the steel. The former treatment improves the environmental durability of various systems due perhaps to better quality and higher density attachments at the adhesive/oxide interface. Figure 30 also shows that the A-1100 (Union Carbide) silane-modified primer possesses a better OH^- resistance capability. The treatment of the oxide with has resulted in considerably lower BBPR's at low voltages in ASW. The major contribution of the phosphate, we feel is due to a decrease in the catalytic activity of the oxide that may have retard the oxygen reduction reaction rate at the steel surface.

8.3 ACCELERATING PARAMETERS

As stated in the original Navy specifications, temperature, dissolved oxygen content, externally applied pushouts (stress), electrolyte, and cathodic voltage were all described as being variable parameters that may affect the performance of the transducer units in service. VPI was able to classify some of the above parameters as being dependent thanks to a polarization properties study of the ANSI-1026 steel. Dissolved

oxygen content, electrolyte, and voltage were correlated with the current density. Thus, the remaining independent parameters were identified as temperature, stress, and applied current density.

Early in this study, we were able to identify a form of debonding in stress-free specimens (see the BDS geometry in Fig. 1) in which the bondline weakens considerably after exposure without being detected by the "naked eye". This mode was referred to as "weakening" the rate of which is entirely dictated by the environment and is denoted by the weakened bond propagation rate (WBPR). The plot of the weakened distances against the square root of time gives a straight line. Figure 33 showed typical behavior of which the slope, WBPR, is the square root of the effective diffusion coefficient, D_e , that is in turn a function of temperature and voltage and can be described according to Equation 19

$$D_e = D_0 \left\{ \exp\left(-\frac{U_D^x}{RT}\right) \exp\left(-\frac{\beta(H^+)FE}{RT}\right) \right\}$$

U_D^x is the activation energy for diffusion. Weakening is a diffusion-controlled process where the ratio of the chemical degradation rate ratio to the diffusion coefficient is high.

Delamination, on the other hand, is a visible form of debonding that can be best described as a "post-weakening" phenomena. A typical degraded bondline showing the weakened and delaminated regions was shown in Figure 18. In essence, the process is similar to static stress corrosion of metals where applied tensile stresses were shown to accelerate the process. The transducer design, being a constant displacement geometry, has led the University of Texas to develop the SBS (see Fig 17) in order to measure delamination rates. Liechti et al. at UT, using a strain energy function following Peng [41] and the nonlinear code TEXPAC-NL, were able to determine that the applied strain energy release rate, G_T , decays as a function of delamination distance as described by Fig.

61. A typical delamination history was shown in Fig. 55. Note that the delaminated bond propagation rate (DBPR) varies as a function of G_T with the largest rate occurring at relatively large values of G. The process resembles that of a continuously "shrinking core" model where a diffusion-chemical reaction operates. Consequently, while the diffusion coefficient is described again by Eq. 19 the degradation rate could similarly be described by

$$k_e = k_0 \left\{ \exp\left(-\frac{U^*}{RT}\right) \exp\left(-\frac{\beta FV}{RT}\right) \right\}$$

where U^* is the activation energy barrier associated with the degradation mechanism. Note that as temperature or voltage is raised so would k_e and D_e with the ratio k_e/D_e becoming progressively larger for harsher environments, and thus favoring chemical-reaction control.

The influence of shear and compression was investigated in the context of stress effect on the WBPR's. The durability specimen (DS) was developed as a self loading and nearly constant shear geometry (see Fig. 16). A constant torque specimen (SS) was also developed for the same purpose. The linear distribution of shear stress along the rubber/steel bondline is designed to reveal any dependence of weakening rates on shear. Within the data range explored, no shear effect was observed from either geometry judging by comparable weakening propagation in all directions. Had shear been an accelerating parameter, one would have expected higher WBPR's in the loaded direction of the DS or a triangular weakening profile from the SS (see Fig. 54).

For the same purpose, the BDS was utilized in a compression mode using a spring loaded feature (Fig. 49). A noticeable reduction in the WBPR (compared with non-stressed BDS data) was observed after exposure to NaOH solutions with no applied voltage. However, no decelerating in debond rates was seen when cathodic voltage was

applied. One should recognize the fact that tensile stresses accelerates debonding mainly due to a "marching boundary" mechanism which may indicate that compressive stresses are capable of decelerating debonding given that they contribute to a reduction in diffusivity or wicking. The stiff adhesive, however, requires that very high compressive stress be applied before any appreciable decrease in the free volume be achieved. The decrease in the WBPR after pressure-exposure to the alkali may be due mainly to a reduction in "wicking" at the bondline. At high voltages (-1400 mV), no oxygen is needed for the electrochemical reaction and the driving force for ion migration is dominated by the applied potential rather than a slower "capillary action".

8.4 DEBOND MODELLING

8.4.1 Semi-empirical Model

Weakened (BDS) and delamination (SBS) data collected at VPI, TRI, and UT were used to fit semi-empirical models utilizing a multiple regression scheme. This model is based on theoretical considerations and is compared to a heterogeneous "shrinking core" model in which the chemical reaction rate is much larger than the rate of diffusion. Temperature influence on weakening rates is shown to obey an Arrhenius type dependency as could be seen in Figure 41. Applied current density was related to voltage for different solutions and temperatures through a transfer coefficient, β , and a rate constant, k, which are $[OH^-]$ - dependent.

The above mentioned model is of the general form given by equation 22 which describes a linear relationship between weakened distances and the square root of time. The activation energy barrier associated with weakening was estimated for both adhesive systems (Chemlok 205/220 and Modified B) in ASW and NaOH aqueous solutions. For example, a value of U_0 of 40 kJ/mole was estimated for the Chemlok system in 1M NaOH. Figure 44 illustrates a typical SAS fit for the control A system weakening data in 1M NaOH solution with different voltages.

The delamination data from the SBS were also analyzed and a semi-empirical model in which temperature and current density are accounted for in an environment-dependent chemical reaction rate, k , similar to the one shown above. Figures 65-68 present the delamination data plotted in a typical da/dt vs. G_T format. The clear trend is a decreased delamination rate as applied G decreased, and an increased rate rate as a function of increasing temperature and current density. An assumption was made that region II in a dz_2/dt vs. G (Figure 69) dominates the overall delamination behavior for moderate G ranges. Therefore, stress dependency of the DBPRs was accounted for through an exponential expression in G_T as shown in Eq. 35. A typical activation energy barrier for weakening was estimated to be about 100 kJ/mole which is consistent with degradation of polymers.

8.4.2 Numerical Model

Another means to model debonding, in both the weakening and the delamination modes, was through the use of a numerical model that takes into consideration the

environment effect on the strength of the bondline in a fashion similar to stress crack corrosion. The expressions used for the chemical reaction and diffusion constants are functionally identical to those determined using the SAS model. The conservation of mass of the aggressive species (OH^-) and the degraded critical linkage (C.L.) is represented in two partial differential equations (Eqs.54,55) which account for both generation and consumption of the involved species. The resulting boundary value problem is subject to the boundary conditions Eqs.56,57. In addition, a failure criterion was incorporated into the model by which failure of the bond commences whenever a crucial "critical linkage" concentration was reached as a result of the OH^- attack. For weakening to occur, it suffices that such a critical density is reached. Verification of the model was accomplished satisfactorily as shown in Figures 79, 81, and 83. Delay times were correlated nicely with the experimentally determined values at VPI and from Stevenson [8].

Delamination was modelled using the same numerical scheme described above although the failure mechanism is different. Local failure (delamination) is assumed to occur if and when the applied G exceeds the rapidly decaying G of the bond ahead of the running crack tip. For this purpose, a linearly decaying function of G_c as a function of decreasing [C.L] was utilized with a maximum value of $G_{c0} = 100 \text{ kJ/m}^2$. Delamination was predicted fairly well for high G ranges but overestimates were numerically calculated corresponding to low values of G 's as were shown in Figures 87 and 89.

BIBLIOGRAPHY

1. H. Leidheiser Jr., "Solid-State Chemistry as Applied to Cathodically Driven or Corrosion-Induced Delamination of Organic Coatings ", *Ind. Eng. Chem. Prod. Res. Dev.*, 20 , No.3, 547-551 (1981).
2. H. Leidheiser Jr. and W. Wang, "Some Substrate and Environmental Influence on the Cathodic Delamination of Organic Coatings ", *J. Coatings Tech.*, 53 , No.672, 77-84 (1981).
3. H. Leidheiser Jr., " Cathodic Delamination of Polybutadiene from Steel-A Review ", *J. of Adhesion Science and Technology*, 1 , 79 (1987).
4. J.E. Castle and J.F. Watts, "Cathodic Disbondment of Well Characterized Steel/Coating Interfaces ", *Corrosion Control by Organic Coatings*, Henry Leidheiser- Editor, NACE, 78-86 (1981).
5. R.A. Gledhill, A.J. Kinloch, "Environmental Failure of Structural Adhesive Joints ", *J. Adhesion*, 6 (1974) p.315.
6. C. Kerr, N.C. MacDonald, and S. Orman, "Effect of Hostile Environments on Adhesive Joints", *Brit. Polymer. J.*, 2 (1970) pp.67-72
7. A. Stevenson, " On the Durability of Rubber/Metal Bonds in Seawater ", *Int. J. Adhesion and Adhesives*, 5, No. 2, April 1985.
8. A. Stevenson, "The Effect of Electrochemical Potentials on the Durability of Rubber/Metal Bonds in Sea Water ", *J. Adhesion* , Vol. 21, 1987, pp.313-327.
9. A. Mahoon, *17th Annual Conference on Adhesion and Adhesives*, City Univ., London, March (1979).

10. H. Leidheiser Jr., W. Wang, and L. Igetoft, "The Mechanism for the Cathodic Delamination of Organic Coatings from a Metal Surface", *Progress in Organic Coatings*, 11, pp.19-40 (1981).
11. J.S. Hammond, J.W. Holubka, and R.A. Dickie, *J. Coatings Tech.*, 51, 45 (1979).
12. J. A. Williams, "Environmental Exposure and Accelerated Testing of Rubber-To-Metal Vulcanized Bonded Assemblies", *Journal of Applied Polymer Science: Applied Polymer Symposium*, 32, pp. 229-246 (1977).
13. J.J. Ritter and J. Kruger, "Studies of the Subcoating Environment of Coated Iron Using Qualitative Ellipsometric and Electrochemical Techniques", *Corrosion Control by Organic Coatings*, Henry Leidheiser- Editor, NACE, pp. 28-31 (1981).
14. F.J. Boerio, "Adhesive Systems-Surface Preparation, Primers, and Adhesives," *NRL Memorandum Report 5748*, April 1986, Work Unit II.A.3.a.
15. G. Odian, *Principles of Polymerization*, 2nd Ed., Wiley, N.Y., pp. 128-133 (1970).
16. R.A. Dickie, J.S. Hammond, and J.W. Holubka, "Interfacial Chemistry of the Corrosion of Polybutadiene-coated Steel", *Ind. Eng. Chem. Prod. Res. and Dev.*, 20 (2), pp.339-343 (1981).
17. J.S. Hammond, J.W. Holubka, J.E. DeVries, and R.A. Dickie, "The Application of X-ray Photoelectron-Spectroscopy to a Study of Interfacial Composition in Corrosion-Induced Paint De-adhesion", *Corrosion Science* 21 (3), pp.239-253 (1981).
18. D.H Smelt, "The Interaction of Chlorinated Rubber Based Lacquers with Abraded Mild Steel Substrates", *Corrosion Control by Organic Coatings*, NACE, 238-246 (1981).
19. E.L. Koehler, "The Mechanism of Cathodic Disbondment of Protective Organic Coatings- Aqueous Displacement at Elevated pH", *Corrosion-NACE*, 40, No. 1, pp.5-8, January (1984).
20. Hidemitsu Hojo, Ken Tsudu, Mitsuuhiko Koyama, "Corrosion Behavior of Glass Fiber Composites and Vinyl Ester Resin in Chemical Environments", *3rd International Conference in Org. Coat. Sci. and Tech.*, 221-234, (1977).
21. J.S. Thornton and R.W. Thomas, "Adhesive Systems- Durability Testing", *NRL Memorandum Report 5748*, April 1986, Work Unit II.A.3.b.
22. J.S. Thornton and R.W. Thomas, "Adhesive Systems- Durability Testing", *NRL Memorandum Report 5934*, October 1986, Work Unit II.A.3.b.
23. F.J. Boerio, "Adhesive Systems-Surface Preparation, Primers, and Adhesives," *NRL Memorandum Report 6068*, July 1987, Work Unit II.A.3.a.

24. A. Turnbull and D. H. Ferriss, " Mathematical Modelling of the Electrochemistry in Corrosion Fatigue Cracks in Structural Steel Cathodically protected in Sea Water ", *Corrosion Science* , 26, No. 8, pp.601-628 (1986).
25. A. Turnbull and D. H. Ferriss, " Mathematical Modelling of the Electrochemistry in Corrosion Fatigue Cracks", *Modeling Environmental Effects on Crack Growth Processes* , 1985.
26. R.F. Hamadeh, W.J. van Ooij, and D.A. Dillard, " A study of the Mechanism of Cathodic Debonding of Adhesively Bonded Neoprene Rubber from Steel ", *Journal of Adhesion Science and Technology* , 2, No 2, April 1988.
27. D.A. Dillard and H.F. Brinson, " Adhesive Systems-Characterization of Neoprene/Steel Debonding in Seawater," *NRL Memorandum Report 6068*, July 1986, Work Unit II.A.3.c.
28. G.F. Froment, K.B. Bischoff, *Chemical Reactor Analysis and Design* , pp239-70 (1979).
29. C.Y. Wen, "Noncatalytic Heterogeneous Solid Fluid Reaction Models", *Ind.-Eng. Chem.* , 60 , No. 9, 34 (1968).
30. J. Szekely, J.W. Evans, and H.Y. Sohn, *Gas-Solid Reactions*, Academic Press (1976).
31. K.J. Vetter, *Electrochemical Kinetics; Theoretical Aspects*, Translated by Scripta Technica, Inc., Academic Press, (1967).
32. R.P. Gangloff and A. Turnbull, " Crack Electrochemistry Modeling and Fracture Mechanics Measurement of the Hydrogen Embrittlement Threshold in Steel", *Modeling Environmental Effects on Crack Growth Processes* , The Metallurgical Society, Inc. (1985).
33. O. Buck and R. Ranjan, " Evaluation Of A Crack-Tip-Opening Displacements Under Stress-Corrosion Conditions ", *Modeling Environmental Effects on Crack Growth Processes* , pp.209-223 (1985).
34. D.W. Levi, "Durability of Adhesive Bonds to Aluminum ", *J. of Applied Polymer Science* , 32 , 189-199 (1977).
35. S.L. Bussa, N.J. Sheth, and S.R. Swanson, "Development of a Random Load Life Prediction Model", *Mater. Res. Stand.* , 12 (3) , 31 (1972).
36. A.N. Gent and E.A. Meinecke, " Compression, Bending, and Shear of Bonded Rubber Blocks ", *Polymer Eng. and Sci.* , 10 , 1 January (1970).
37. D.E. Glowe and S.L. Arnett, "The Application of Mechanical Clamps on the Portsmouth Connector", *NRL Momerandum 4602*, Naval Research Laboratory, Washington, D.C., November (1981).

38. D.R. Lefebvre, D.A. Dillard, and H.F. Brinson, "The Development of a Modified Double-Cantilever-Beam Specimen for Measuring the Fracture Energy of Rubber to Metal Bonds", *Exp. Mech.*, 28, 1, pp.38-44, March (1988).
39. K.M. Liechti, "Adhesive Systems-Stress Analysis," *NRL Memorandum*, 3Q May 1985, Work Unit II.A.3.d.
40. K.M. Liechti, E.B. Becker, C. Lin, and T.H. Miller, "A Fracture Analysis of Cathodic Delamination in Rubber to Metal Bonds", *Accepted for Publication in the Int. J. Fracture*, 1988.
41. S.J. Peng, "Nonlinear Multiaxial Finite Deformation Investigation of Solid Propellant", *AFRPL-TR-84-036* (1984).
42. G.P. Anderson, S.J. Bennett, and K.L. Devries, *Analysis and Testing of Adhesive Bonds*, Academic Press (1977).
43. R.W. Hertzberg, *Deformation and Fracture Mechanics of Engineering Materials*, John Wiley & Sons, p.439 (1976).
44. D.P. Williams and H.G. Nelson, "Embrittlement of 4130-Steel by Low-pressure-Gaseous Hydrogen", *Met. Trans.*, 1 (1), p.63 (1970).
45. Yu.V. Moiseev, G.E. Zaikov, *Chemical Resistance of Polymers in Aggressive Media*, p.180 (1987).
46. M. Pourbaix, *Lectures on Electrochemical Corrosion*, Plenum Press (1973).
47. E.H. Andrews, "Mechanical Measurement of Interatomic Bonding Energies at Interfaces", *Adhesive Joints, Formation, Characteristics, and Testing*, K.L. Mittal-Editor, Plenum Press, pp. 689-702.
48. J.J. Bickerman, *The Science of Ahesive Joints*, 2nd ed., Academic Press, N.Y. (1986).
49. C. Kerr and P. Walker, "Some Aspects of Silane Technology for Surface Coatings and Adhesives", *Adhesion 11*, K.W. Allen-Editor (1987).
50. F.J. Boerio, "Adhesive Systems-Surface Preparation, Primers, and Adhesives", *NRL Memorandum Report 5934*, Work Unit II.A.3.a.
51. D.A. Dillard and H.F. Brinson, "Adhesive Systems-Characterization of Neoprene/Steel Debonding in Seawater," *NRL Memorandum 5748*, 2Q86, Work Unit II.A.3.c.
52. A.F. Lewis and L.J. Ferrestal, "Chemical Nature of Polymer to Metal Adhesion", *ASTM Spec. Tech publ.*, 360, p.59 (1964).

53. A.F. Lewis and R. Saxon, "Epoxy Resins: Chemistry and Technology", *Epoxy-Resin Adhesives*, May, C.A. and Tanaka, Y.- Editors, Marcel Dekker, pp.373-450 (1973).
54. M. Avrami, *Kinetics of Phase Change I*, " J. Chem. Phys.", Vol 7, p1103 (1939).
55. M. Avrami, *Kinetics of Phase Change II*, " J. Chem. Phys.", Vol 8, p212 (1940).
56. M. Avrami, *Kinetics of Phase Change III*, " J. Chem. Phys.", Vol 9, p177 (1941).
57. A.F. Lewis and R.J. Natarajan Gounder, "Permanence and Endurance of Structural Adhesive Joints", *Treatise on Adhesion and Adhesives*, Patrick, R.L. -Editor, pp.313-381 (1981).
58. F.M. Fowkes, "Role of Acid-Base Interfacial Bonding in Adhesion", *Journal of Adhesion Science and Technology* , 1 , No. 1 (1987).
59. F.J. Boerio and J.W. Williams, "Applications of Surface Science", *North Holland Pub. Co.* 7 , 19 (1981).
60. M.K. Chaudhury, T.M. Gentle, and E.P. Plueddemann , "Adhesion Mechanism of Polyvinyl Chloride to Silane Primed Metal Surfaces", *Journal of Adhesion, Science and Technology*, 1 , No. 1 (1987).
61. R. Holmes- Farley, *Lord Corporation*, "Private Communications".
62. W.A. Jemian, "Structural Precursors to Fracture in Adhesive Joints", *Adhesive Joints : Formation, Characteristics, and Testing* , K.L. Mittal- Editor, Plenum Press, pp. 809-827.
63. A.J. Kinloch, "The Use of Modern Surface Techniques in Adhesion", *Adhesion* 6, K.W. Allen- Editor, p.95 (1982).
64. M. Gettings and A.J. Kinloch, "Surface Analysis of Polysiloxane-Metal Oxide Interfaces", *J. Mater. Science*, 12 (12), pp.2511-2519 (1977).
65. J.S. Hammond, J.W. Holubka, and R.A. Dickie, *A.C.S. Org. Coat. Plas. Chem.*, 39, p.506, 11 (1978).
66. M. Gettings, F.S. Baker, A.J. Kinloch, "Use of Auger and X-ray Photoelectron Spectroscopy to Study Locus of Failure of Structural Adhesive Joints", *J. Applied Polymer Sience*, 21, p.2375 2392(1977).
67. A. Turnbull and D.H. Ferriss," Mathematical Modelling of the Electrochemistry in Corrosion Fatigue Cracks ", *Modelling Environmental Effects on Crack Growth Process* , pp. 3-39 (1985).
68. A. Turnbull and J.G.N. Thomas, "A model of Crack Electrochemistry for Steels in the Active State Based on Mass Transport by Diffusion and Ion Migration", *J. Electrochemical Society* , pp.1412-1422, July (1982).

69. A. Turnbull and D. H. Ferriss, "Mathematical Modelling of the Electrochemistry in Corrosion Fatigue Cracks in Structural Steel Cathodically protected in Sea Water", *Corrosion Science*, 26, No. 8, pp.601-628 (1986).
70. G.H. Nancollas, T.F. Kazmierczak, and E. Schuttriger, *Crystal Growth of Calcium Carbonate; A Controlled Composition Kinetic Study*, "J. Physical Chemistry", 86, pp103-7 (1982).

1. POLARIZATION STUDIES OF ANSI-1026 MILD STEEL

Extensive work was done to determine the polarization properties of ANSI-1026 steel. Several solutions, temperatures, and voltage scan rates were involved. In voltammetry, a potential is varied linearly with time and the corresponding currents are measured. The potential is changed from an initial equilibrium value, E_1 , to a value E_2 , -2400 V (SCE) in this study, at which point the scan direction is reversed until a second potential E_3 is reached.

The conventional three-electrode system was used. The potential is applied across the working (steel) and the reference (calomel) electrodes by a wave front generator, a PAR Model 175 Universal Programmer, which programs a potentiostat, a PAR Model 371 Potentiostat/ Galvanostat, to control the potential limits, the initial potential, the initial scan direction, and the scan rate. The three electrodes are the working, reference, and counter electrodes. The working electrode, a 0.25" X 0.25" ANSI-1026 steel embedded in epoxy to hold it to a glass tube. Before each test run, the steel electrode was polished with 600-grit silicon carbide paper and then rinsed with double-distilled water. The reference electrode, a saturated calomel electrode was refilled regularly with saturated KCl solution while the counter electrode, a circular mesh made up of platinum wires, was cleaned prior to each test. Electrochemical cell, of capacity of 750 ml, was used throughout the testing process. Temperature was monitored using a mercury thermometer and room air was circulated through the cell using a pump.

Figures 92 and 93 show the loading and unloading polarization curves for the ANSI-1026 in 1M NaOH solution at 25 C, 40 C, and 55 C. A sweep rate of 2 mV/s was

used throughout the study except in one case where a rate of 10 mV/s was performed for comparison. The control case (rate = 2mV/s, Temperature = 25 C, and stirring = 5/max.) was run twice to check for reproducibility. Figures 94 and 95 show the corresponding curves for the 3.5 percent ASW environment. One can see that curves have shifted horizontally compared to the control curve. A shift to the right corresponds to an increase in current density for the same potential. A comparison of the various solutions is presented in Figure 96 and shows that there exists more than one voltage for every current density level.

The solutions with low concentrations (0.1 and 0.001M) can not support high current outputs because of the low electrolyte content. Table 3 (in chapter 4) summarizes the results of the study and the chosen cathodic voltages.

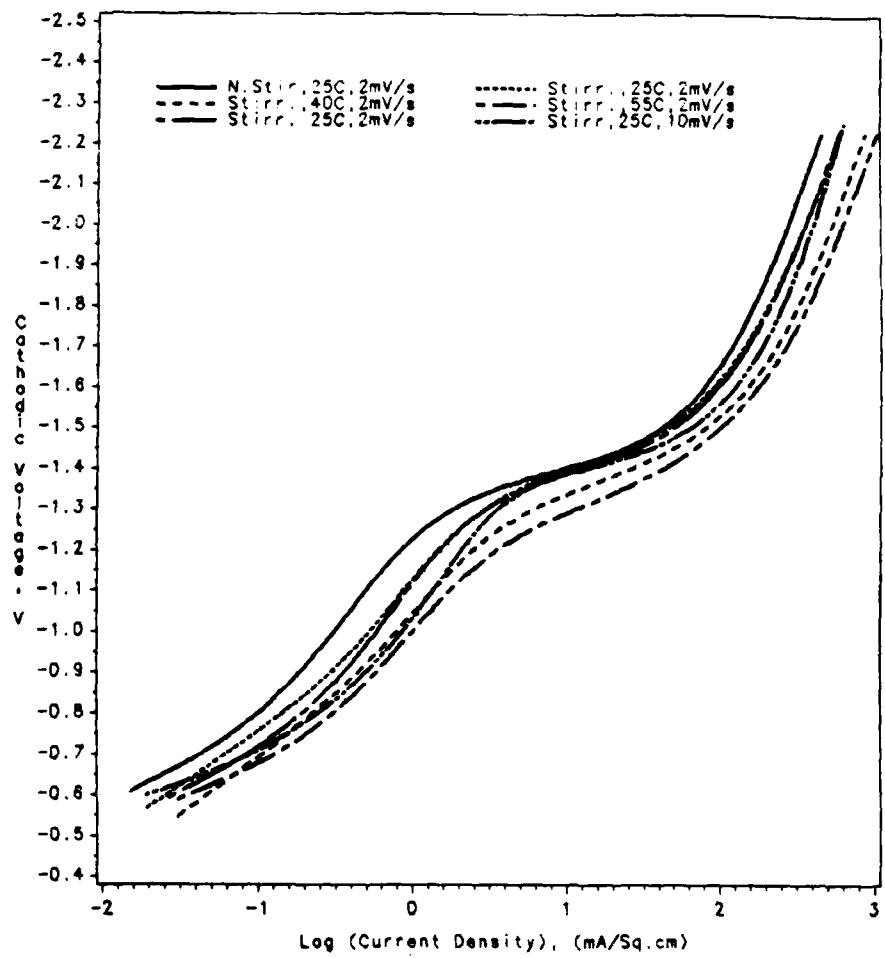


Figure 92. Loading polarization curves for ANSI 1026 steel in 1M NaOH.

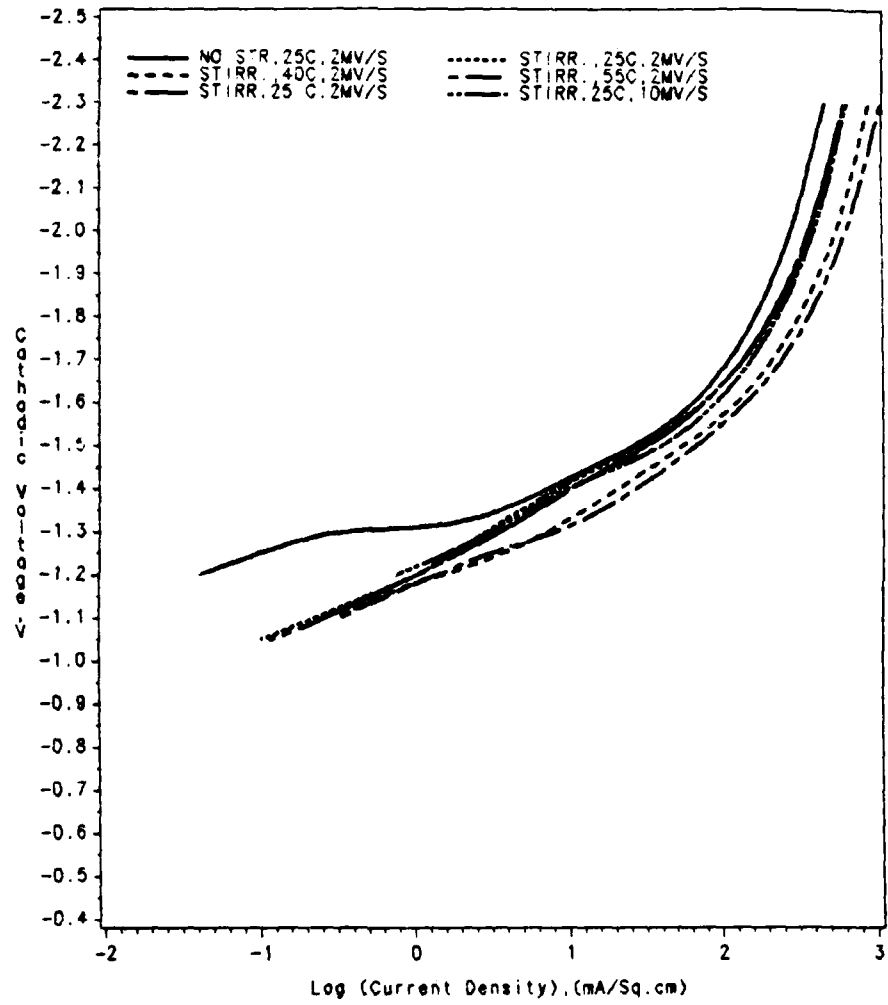


Figure 93. Unloading polarization curves for ANSI 1026 steel in 1M NaOH.

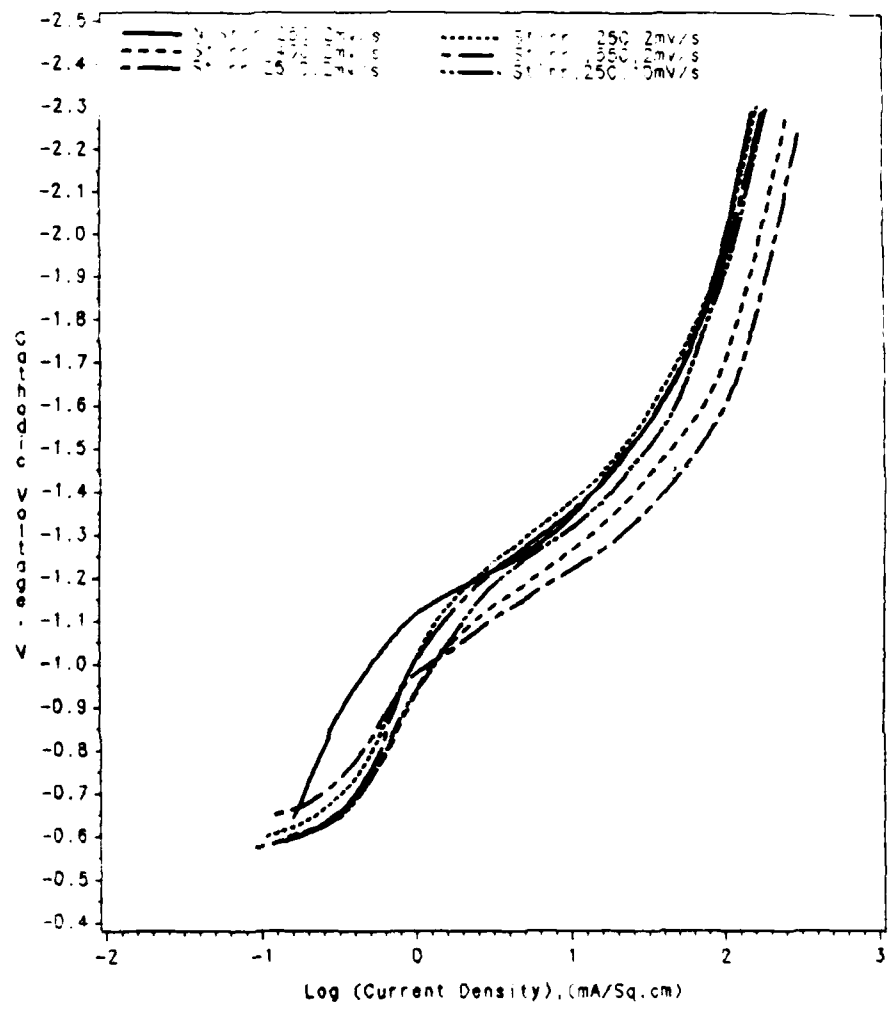


Figure 94. Loading polarization curves for ANSI 1026 steel in ASW.

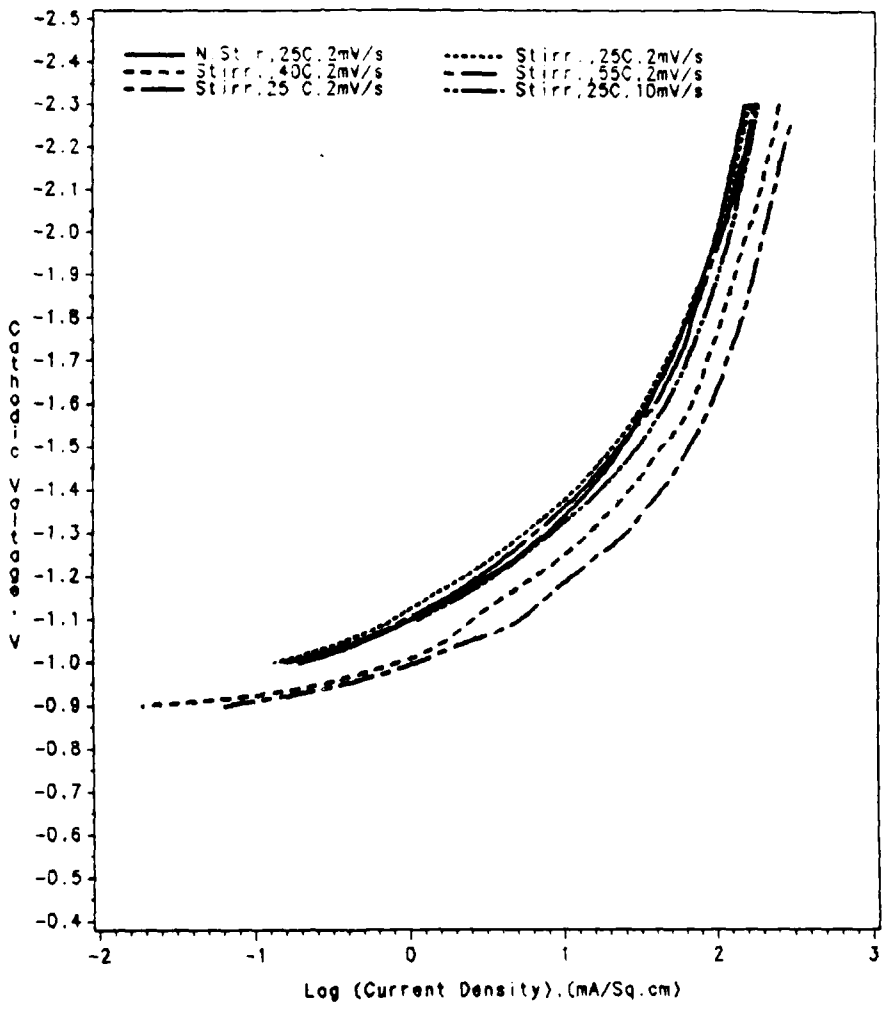


Figure 95. Unloading polarization curves for ANSI 1026 steel in ASW.

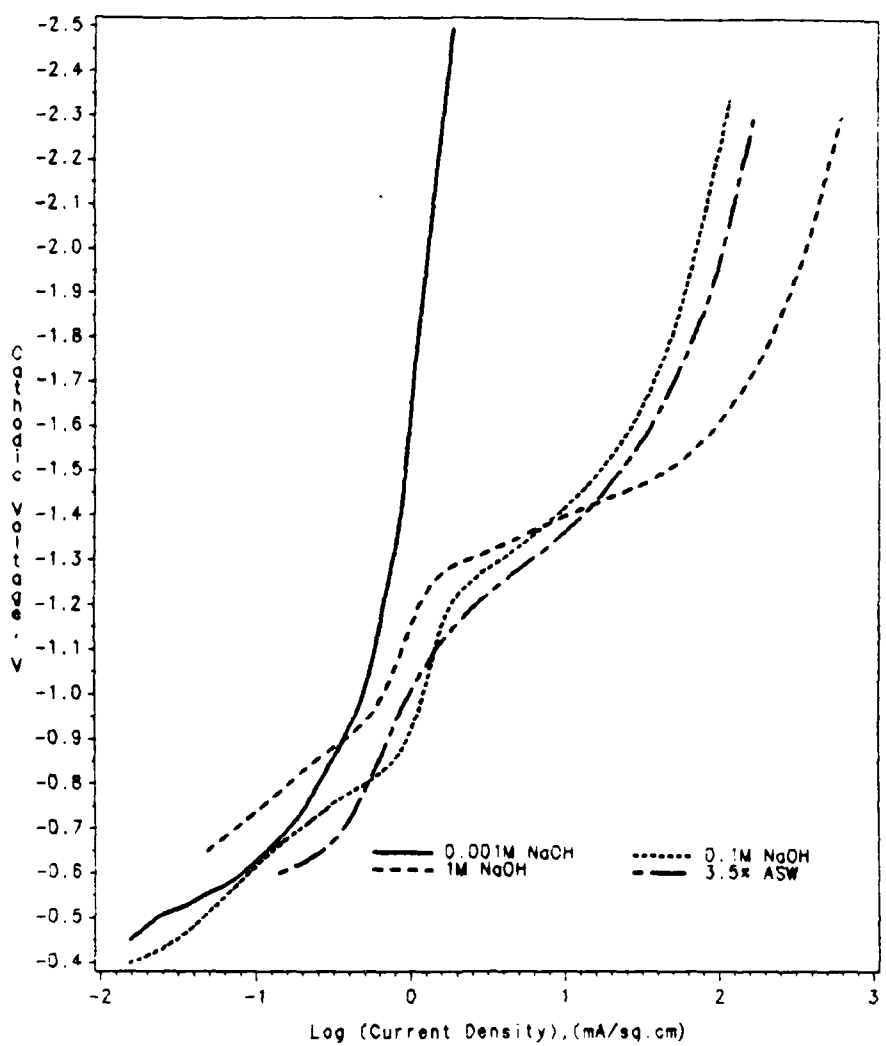


Figure 96. Comparison of polarization curves for ANSI 1026 in various environments.

2. DURABILITY DATA

Results of thirteen sets of data collected in different environments are presented below. The corresponding numbers on the Test Matrix (as shown in Table 2, chapter 4) are: A-2,5; D-1,5; B-4; C-4; E-4; and F-4. A large number of SBS and BDS's were involved in this effort. Every bath contained at least one specimen of each of the two adhesives: control and silane modified. In addition, zinc phosphate coated steel substrates were used as adherends for some SBS's which were tested in ASW environments. Both weakened and delaminated distances are presented where it is understood that delamination measurements are taken along the four loaded edges and represent the delaminated distance, z_2 , and do not include the weakened distance, z_1 .

Figure 97 shows the debond results for case A-2: ASW, at 25 °C, and an applied impressed voltage of -1000 mV (SCE). The data has been collected over a 162 day period at the end of which relatively little debond was observed. The phosphate system (#822) has outperformed both the control (#955) and the A-1100 modified (#60) systems. On average, the debond growth was .035, .064, .083 in. for the three systems respectively (or a ratio of 1/1.82/2.37). An interesting observation is that the weakened distances (#K15) are larger than the delaminated distances. This discrepancy was repeated in a few other instances and will be discussed below.

Debond growth data for A-3 (ASW, at 25 °C, and -1100 mV) are presented in Figure 98.

Delamination rates of the control (#196) and modified (#207) systems were significantly increased following an 100 mV increase in cathodic voltage (up to -1100mV) while the growth of the phosphated system was not affected at all by the voltage increase. The A-1100 modified system seems to perform slightly better than the control but was clearly

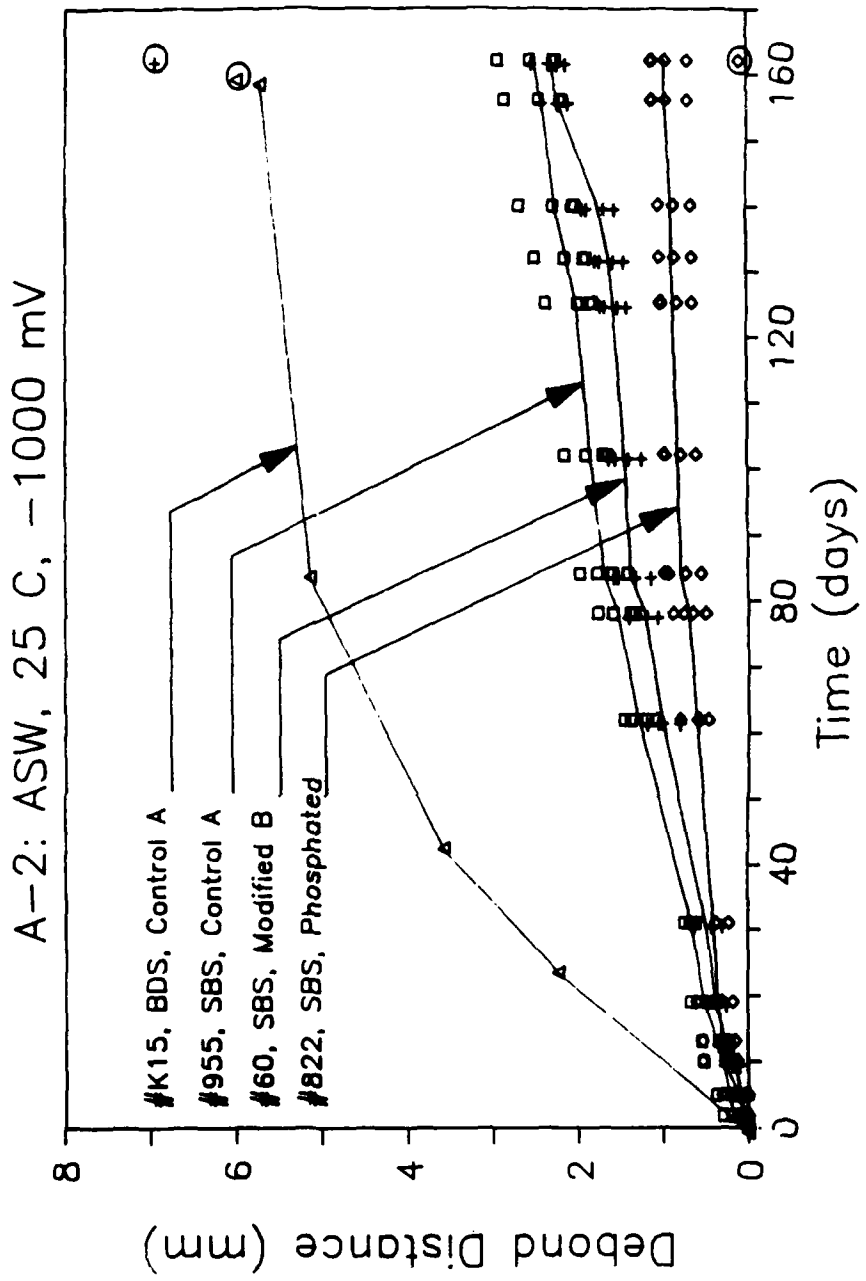


Figure 97. Debonding Data; Case A-2: ASW at 25 C and -1000 mV (SCE).

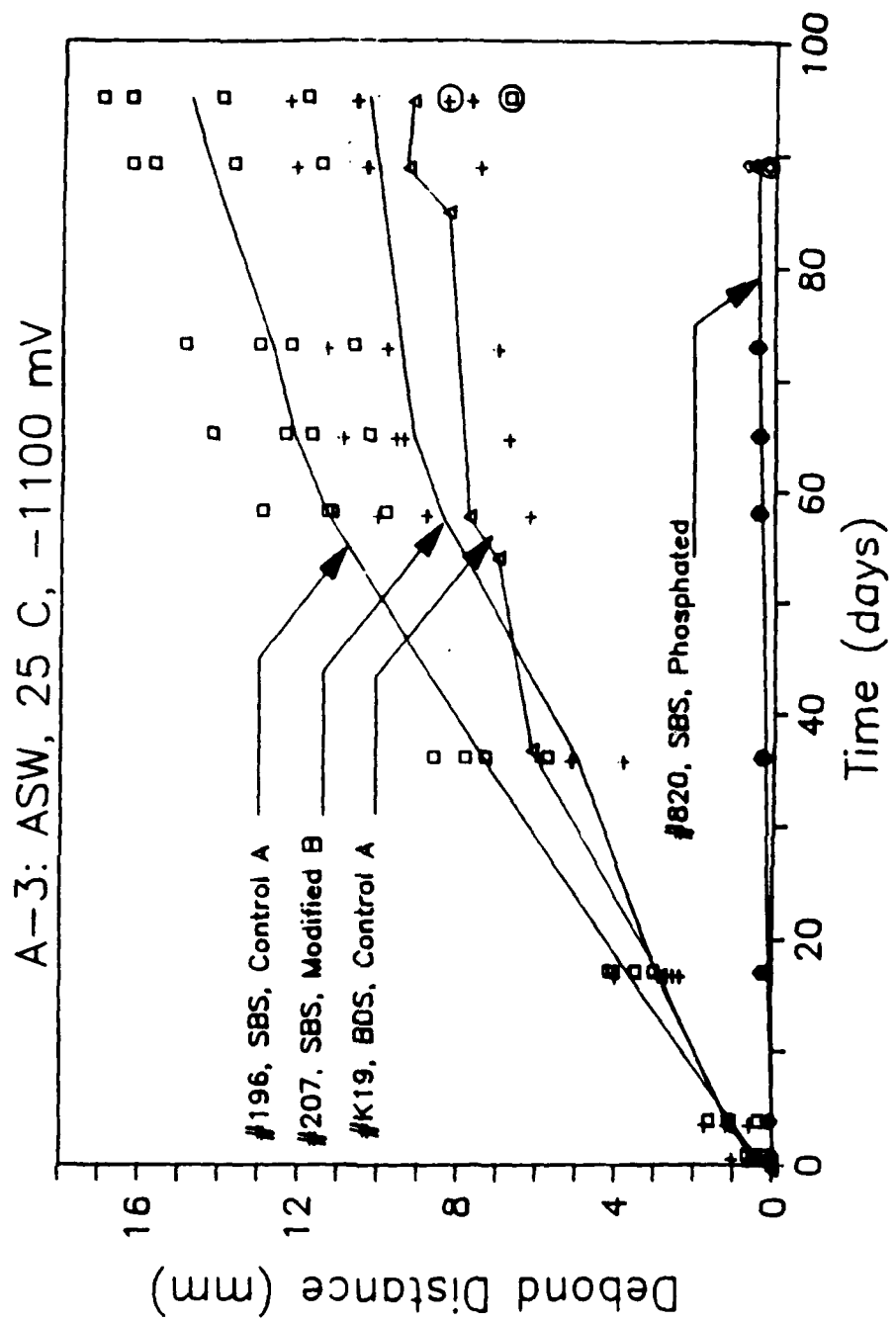


Figure 98. Delamination Data; Case A-3: ASW at 25 C and -1100 mV (SCE).

outperformed by the phosphate system. The specimens were pulled open after the experiment was concluded to compare the weakened (side) fronts for those systems. Again, the phosphate coated specimens outperformed the other systems. Weakened distances from the BDS specimens (#K19) were also plotted and show an interesting trend. For short distances, delamination and weakening are comparable while the difference becomes significant at longer distances when weakening becomes controlled by mass transfer.

Figure 99 presents the delaminated distances for A-4 (ASW, 25 C, and -1420 mV) plotted against time and shows the data for specimens #979, 45, and 827. The data seems to be linear in time for the 205/220 system up to about 0.4" of delamination after which it starts to level off slightly. A "delay" time of a few days seem to exist for the modified system after which delamination proceeds but considerably slower than the control system. The phosphate coated substrates show the most delay time and the least slope. The weakened bond for that system, on the other hand, was examined after the bond was pulled open using the side diffusion distances and it was found that distances z_1 were about the same as other systems. While the stresses tend to help the separation process and shorten the diffusion distance, shorter weakened lengths (in ASW) in front of the crack tip may reduce the pH at the interface thus slowing the debonding process. Another possible explanation is that at such high potentials dissolution of the iron oxide may be the failure mechanism.

Figure 100 presents the data for case A-5: ASW, 25 C, and -1825 mV. The control system A performed poorly in comparison with the other systems. The stress effect is very pronounced at this harsh potential (compare #1039 and #K17). The same observation concerning the poor performance of the phosphate system in the weakened state at -1420 mV was witnessed again at -1825 mV. Figures 101-105 present the data for cases D-1,2,3,4, and 5 respectively.

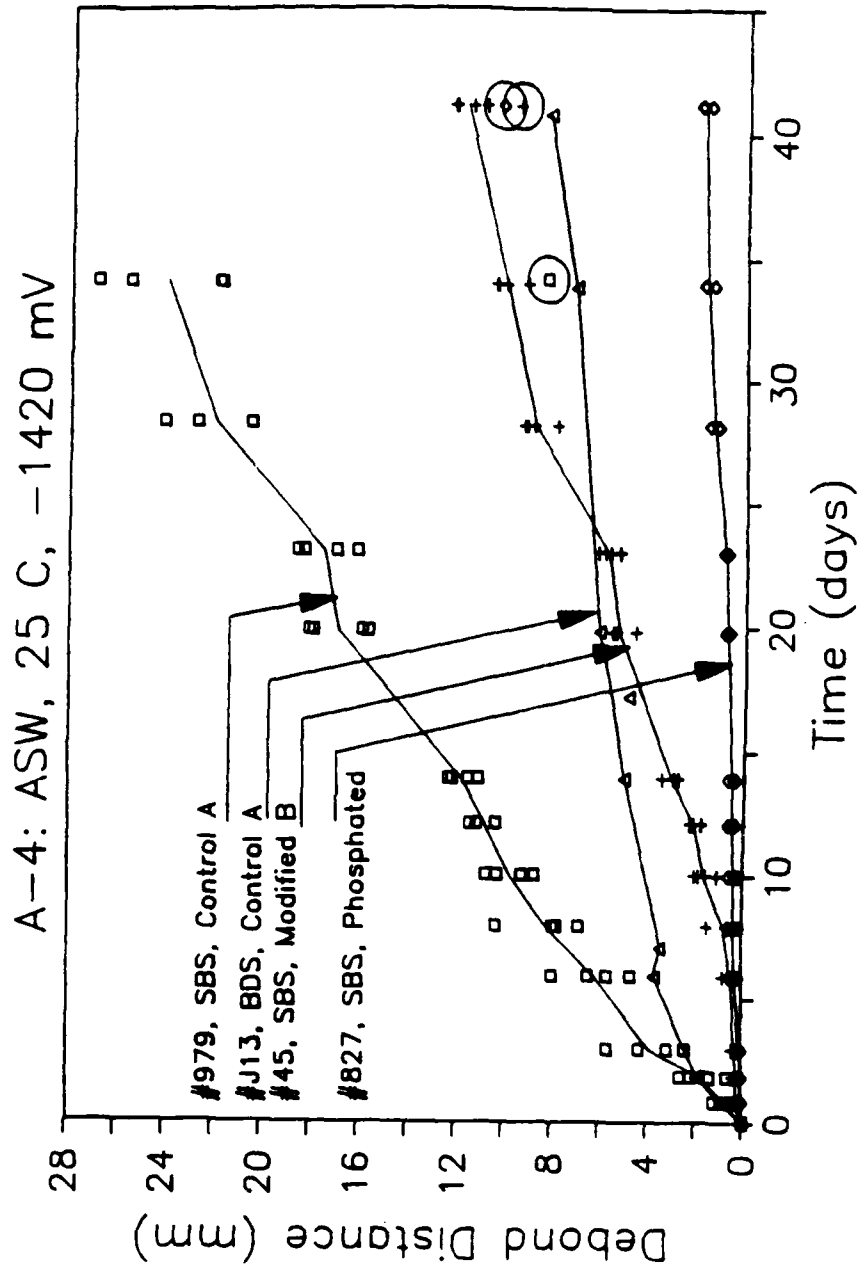


Figure 99. Delamination Data; Case A-4: ASW at 25 C and -1420 mV (SCE).

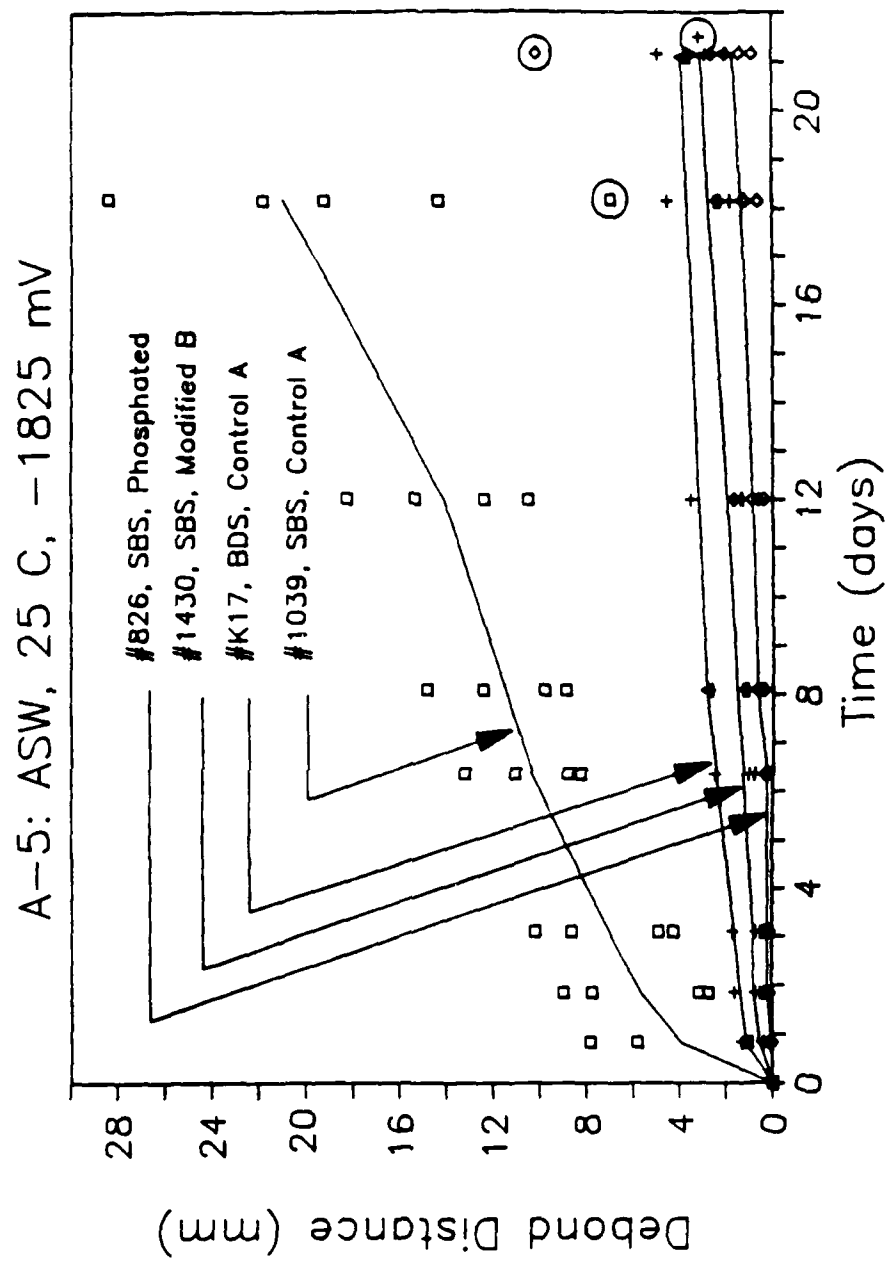


Figure 100. Delamination Date; Case A-5: ASW at 25 C and -1825 mV (SCE).

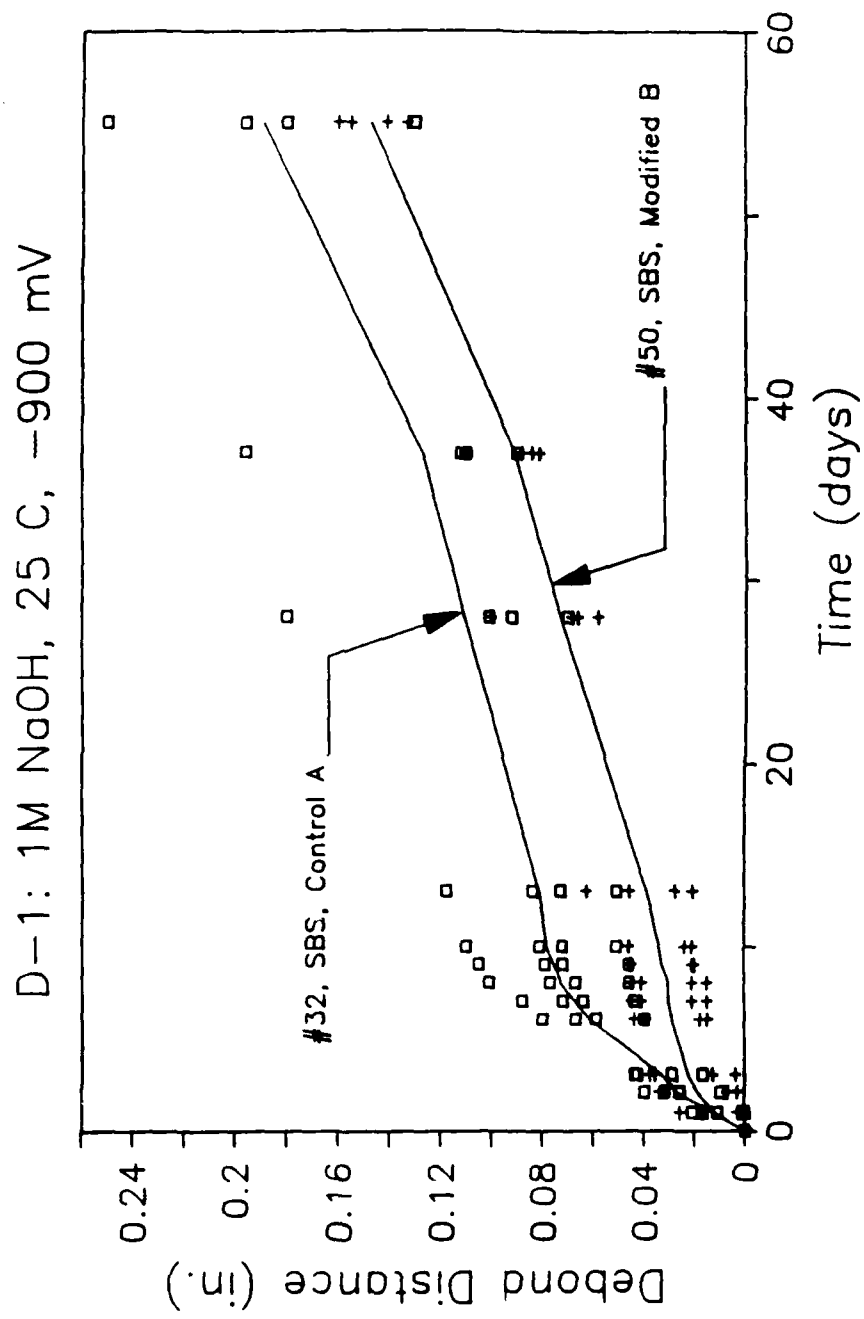


Figure 101. Delamination Data; Case D-1: 1M NaOH at 25 C and -960 mV (SCE).

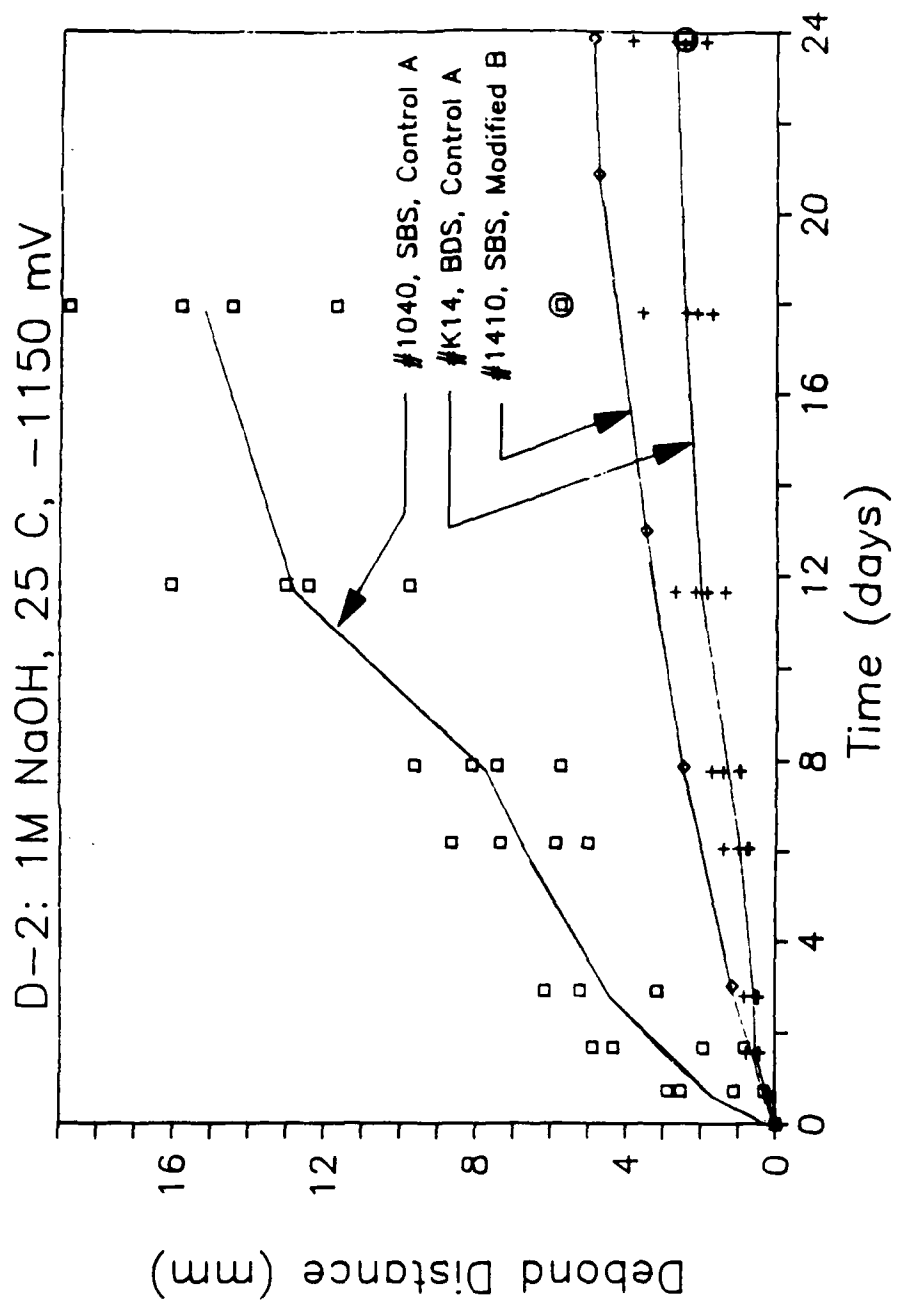


Figure 102. Delamination Data; Case D-2: 1M NaOH at 25 C and -1150 mV (SCE).

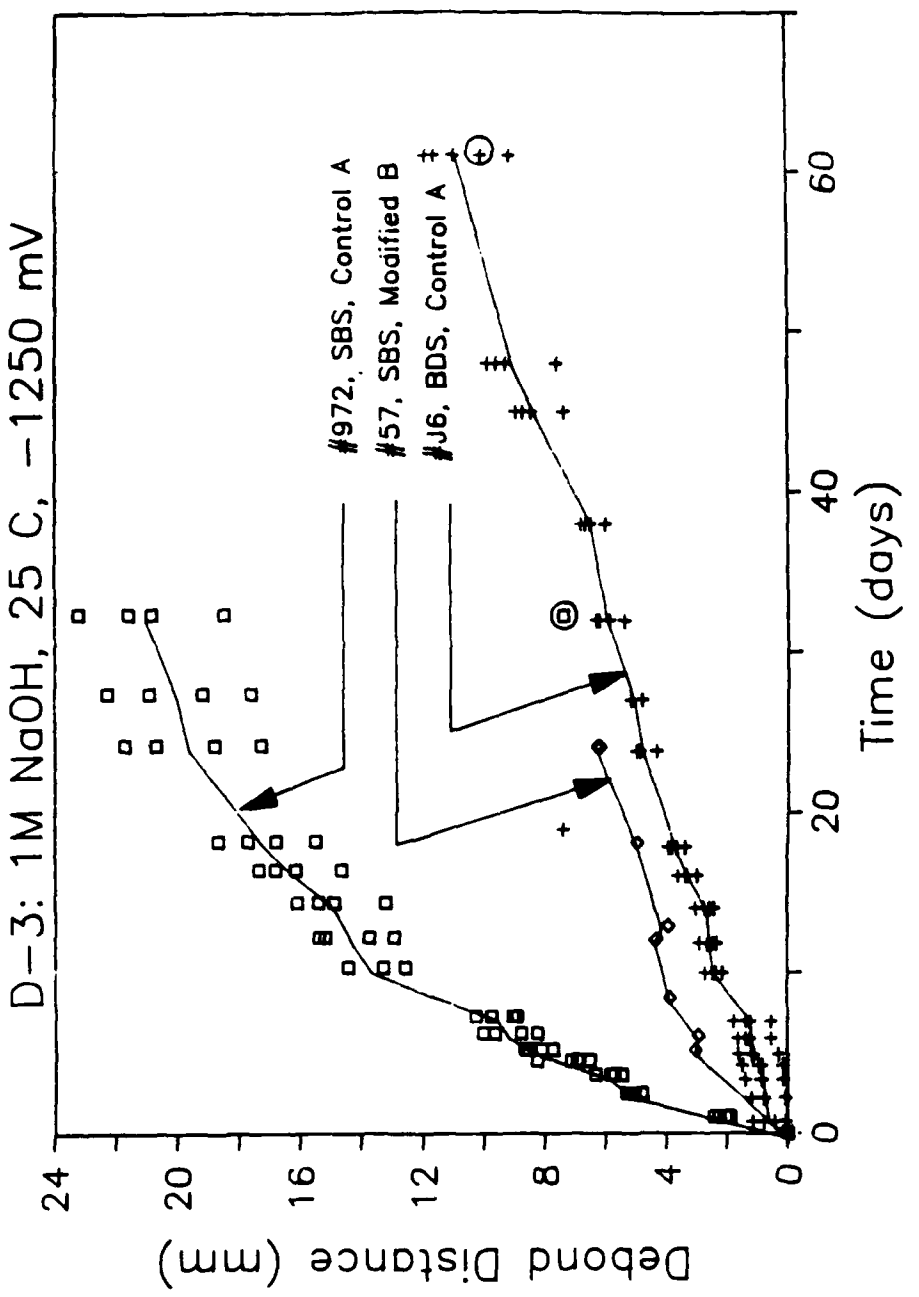


Figure 103. Delamination Data; Case D-3: 1M NaOH at 25°C and -1250 mV (SCE).

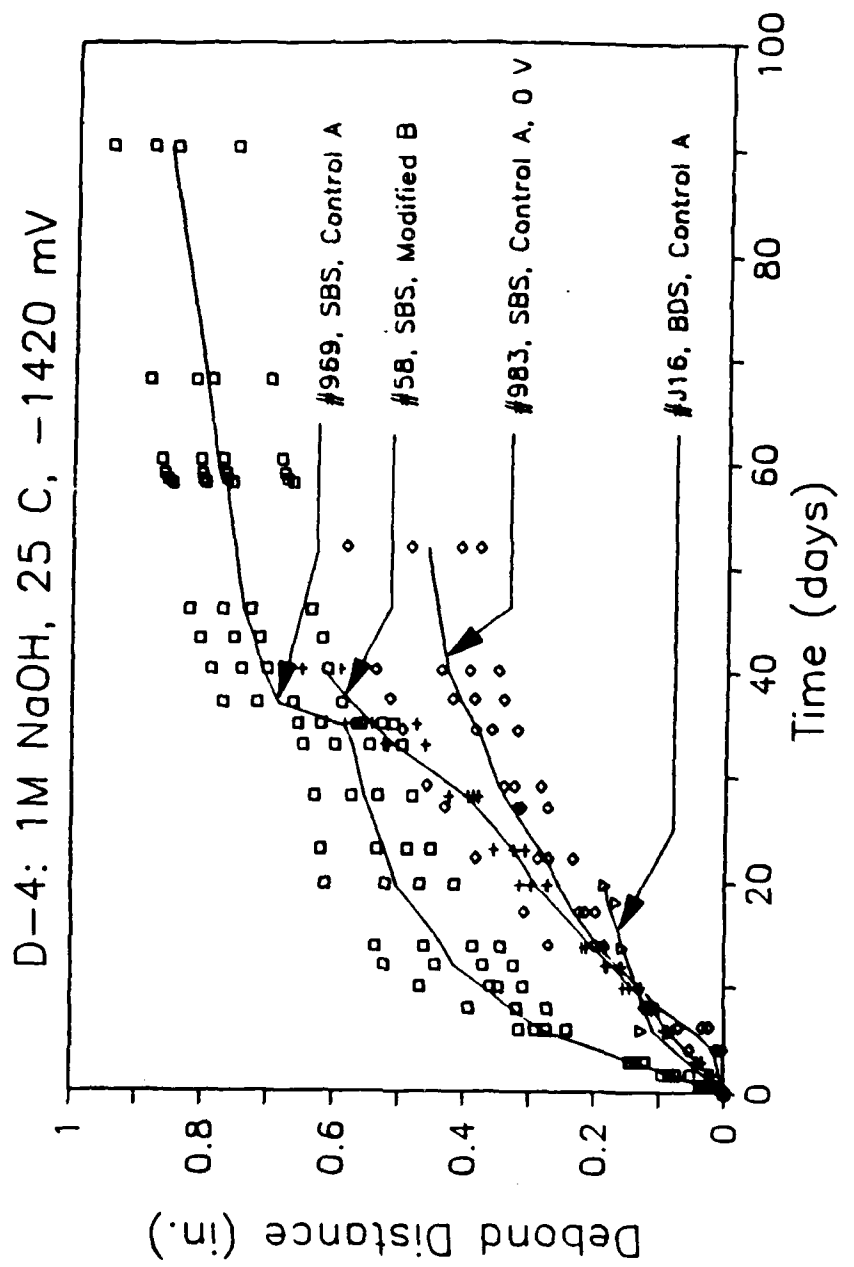


Figure 104. Debonding Data; Case D-4; 1M NaOH at 25 C and -1420 mV (SCE).

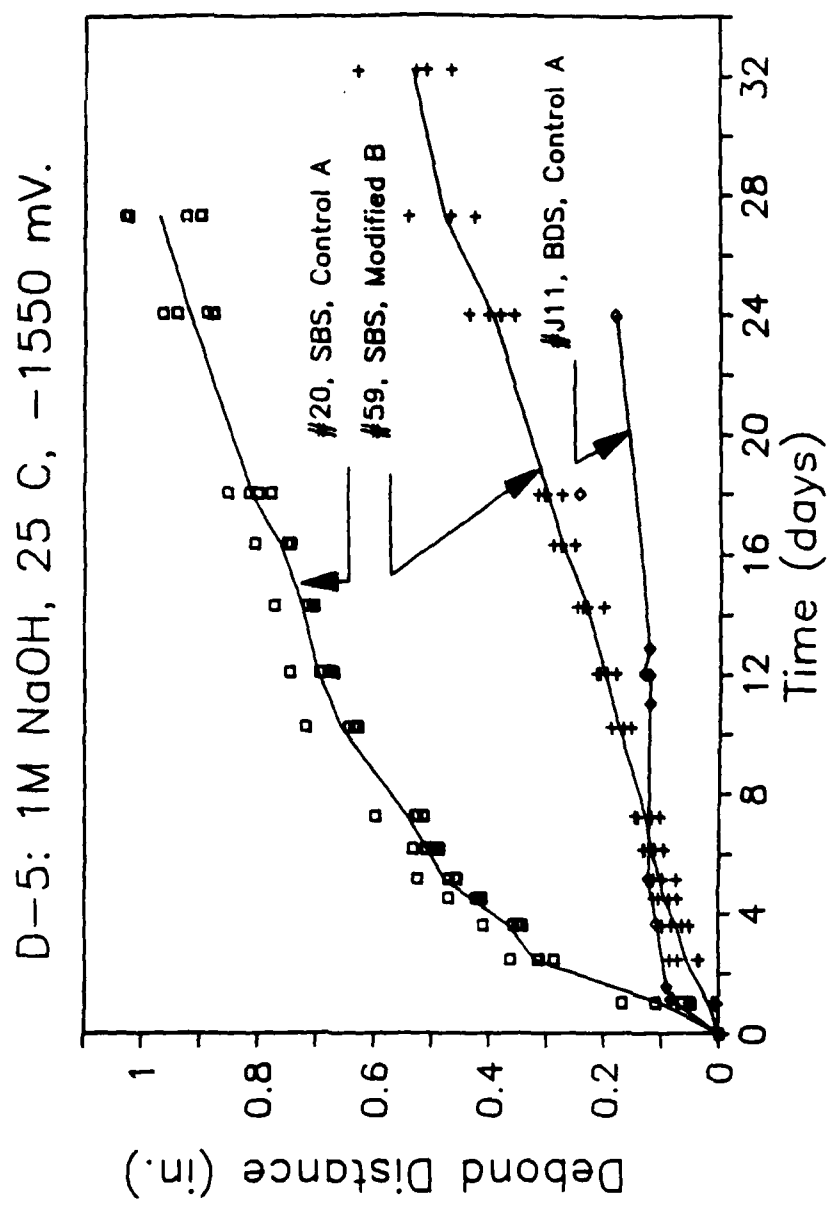


Figure 105. Delamination Data; Case D-5: 1M NaOH at 25 C and -1560 mV (SCE).

These cases correspond to 5 consecutive levels of current density in 1M NaOH solution at 25° C. In all five cases, the silane system outperformed the 205/220 by a wide margin. Scatter is low and repeatability of the various delaminated fronts is acceptable except, perhaps, in the case of specimen #32 of D-1 and #969 of D-4. The results for both adhesive systems show that the DBPR increases as the current density increases. An attempt was made to exclude cathodic potential from the process in the case of specimen #983 (205/220) thus coupling the effects of stress and the concentration. Figure 104 shows that the "delay" time has increased from almost zero to about 5 days when voltage was not applied. Afterwards, delamination proceeded in the same fashion as in those specimens exposed to current. The current, as we know, accelerates the debonding mainly by contributing to the pH increase.

Effect of tensile stress was again seen throughout the entire range as seen clearly by comparing the results from the BDS's and SBS's. An evidence for direct contribution of tensile stresses can also be seen in Figure 104 when the 3/8" dowel in specimen #969 was replaced by a larger dowel of 0.5" diameter after about 35 days of exposure. That change resulted in an appreciable increase in G which led to a large increase in the DBPR. At 60 days, the environment was replenished in hopes of segregating the influence of environment and stress. No effect was noticed at the same level of total strain energy release rate, G.

The effect of temperature as an independent parameter was demonstrated when choosing the voltage which correspond to the same current density for the 25 C case then running the tests at that voltage but at higher temperatures. Four cases were assigned for that purpose two of which were in ASW and the other two with 1M NaOH solution and are B-4, C-4, E-4, and F-4. Debond data for B-4 (ASW, 40 C, and at -1310 mV) and C-4 (ASW, 55 C, -1250 mV) is shown in Figures 106 and 107 respectively. Calcareous deposits buildup at the rubber/metal bondline constituted a major problem

at such high levels of applied voltage that may have resulted in some erroneous results especially at high temperatures, i.e. 55 C.

Figure 106 shows that the effect of stress at such a harsh environment is mostly restricted to the first few days where the DBPR is high due to the high applied G. The slopes of the weakening curve and that of the last portion of the delamination are comparable which is expected at long crack lengths (and lower G levels). The results for C-4 are presented in Figure 107 and show some interesting observations. The last portion of the curves show a steep rise that we believe is due to side diffusion that diminished the width of the bond ahead of the crack tip prior to failure. Although the data is scattered, partly due to a deposit build-up, the 205/220 and the 205/220/A 1100 adhesive systems seem to delaminate evenly at this high temperature. The 1" wide bond has been observed to have delaminated completely when the bond was opened. As a result, we were not able to compare the respective weakened distances on the sides. However, the fact that the final distances are close in value may imply that the weakened bond delamination rate (WBDR) is comparable. It is possible, then, that the silane does not enhance the durability at such high temperatures either because that the degradation rate is very high or that a different mechanism is taking place (oxide dissolution).

Figure 108 presents the results for case E-4 (1M NaOH, 40 C, -1360 mV). Again two specimens were tested: #20 (modified B) and #985 (control A). The data shows very low scatter for both systems except when comparing distances B,C and D,E of the modified system. The entire length of the control specimen delaminated in about one week at 40° C in 1N NaOH with -1.36V (SCE) apparently in a linear fashion up to 0.6". Delamination was much slower for the modified system. Again, notice the sudden increase in distances D and E just prior to failure which indicate side weakening effect.

Some problems were encountered with F-4 when the rubber layer in the control specimen was partially broken one day after starting the test. The damage occurred in

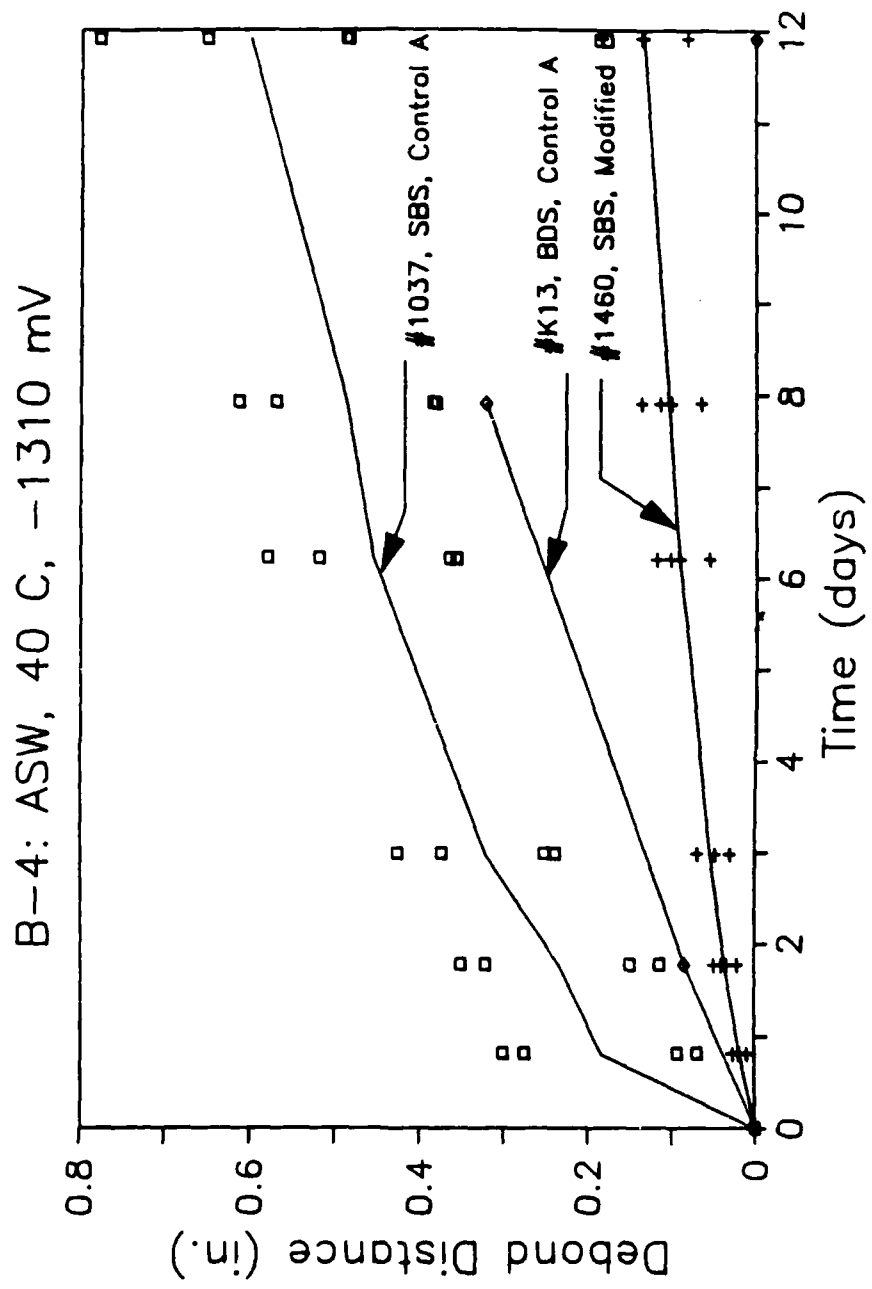


Figure 106. Debonding Data; Case B-4: ASW at 40 C and -1310 mV (SCE).

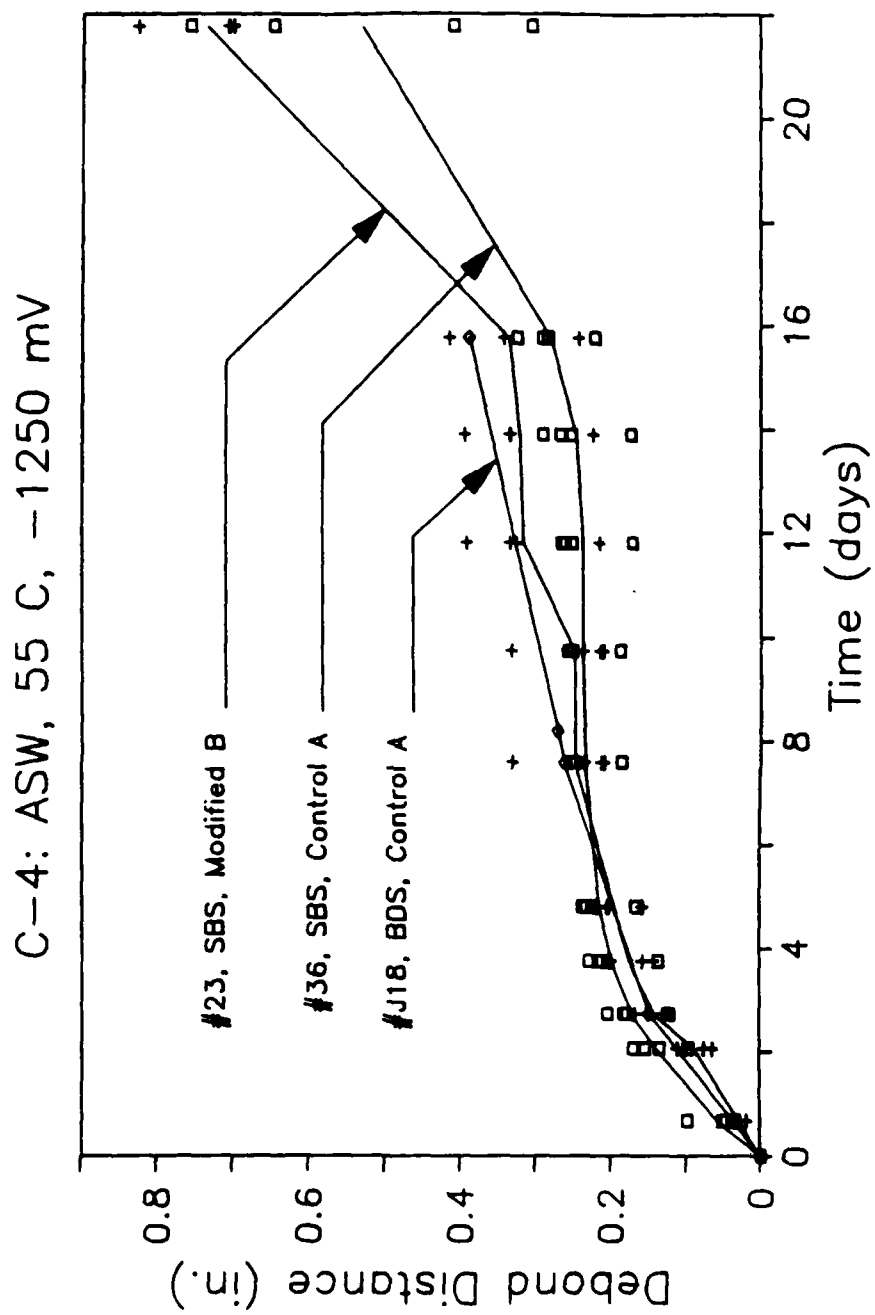


Figure 107. Delamination Date; Case C-4: ASW at 55 C and -1250 mV (SCE).

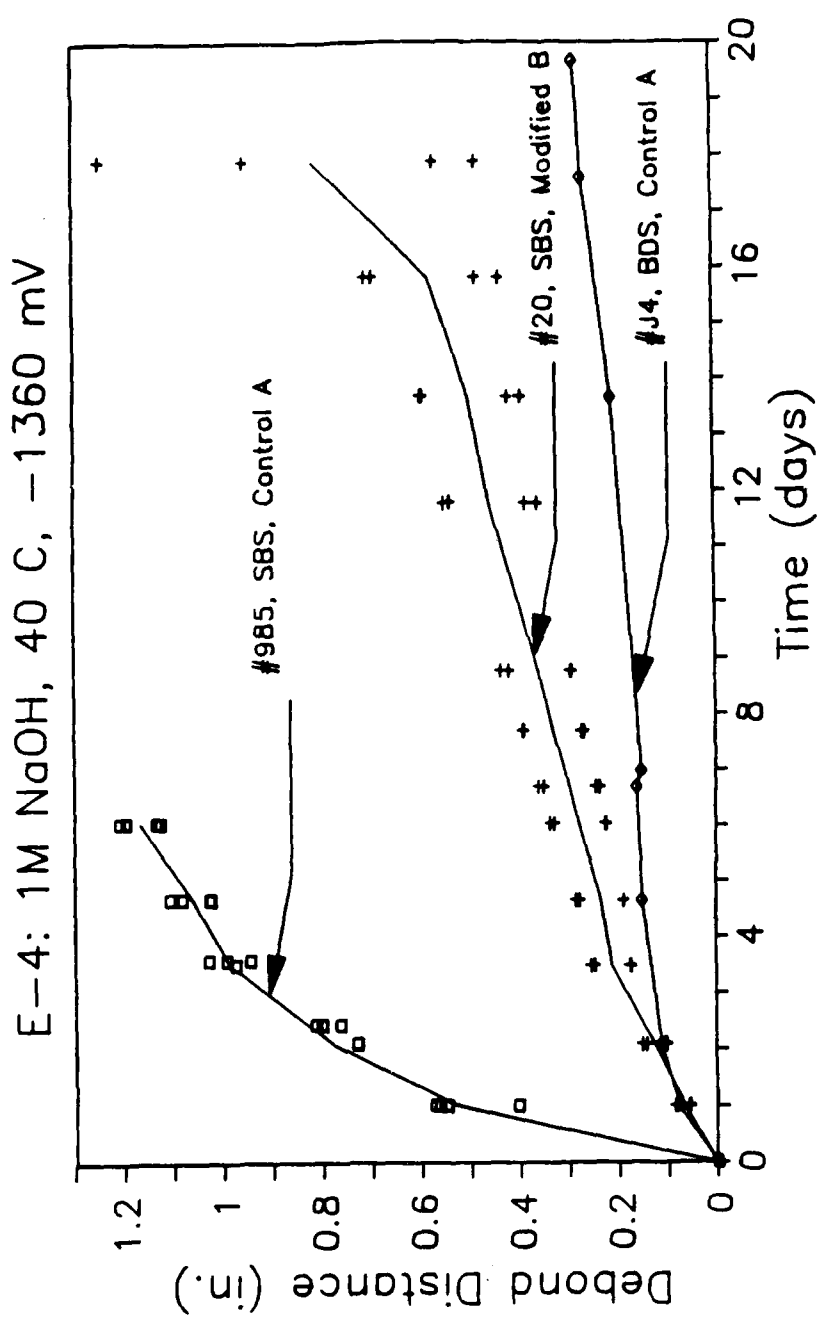


Figure 108. Delamination Date; Case E-4; 1M NaOH at 40 C and -1360 mV (SCE).

B and D at the crack tip where the stresses in the rubber are high and where the environment is very harsh (1N NaOH, 55 C, -1.31 V). That may have caused a decrease in the stresses at the delaminating front of C and E and possibly the delamination rate. The silane system outperformed its rival regardless of the fact that it was exposed to a higher initial value of G at the beginning. Where stresses were very low in the control system, i.e. fronts B and D, delamination rates were comparable to those of the silane. Notice that after the initial fast, and apparently linear stage, the delamination rate decreased significantly past 0.7 ". Note, also, that the slope of the silane system remains fairly constant presumably because the value of G is still relatively high.

2.1 Discrepancies in Debond Data

For case A-4 (ASW, 25 C, and -1420 mV) the phosphate system showed a superior performance with a very small delamination rate. However, upon fracturing the specimen after the test was concluded, it was noticed that the stressed front (delamination) in the phosphate coated specimen (#827) has propagated at a lower rate than the unstressed (side) weakened fronts. Figure 110 is a photograph showing the steel and rubber sides of the fracture surface and clearly show the calcareous deposits at and around the crack tip where the crack was arrested. Interestingly enough, similar and larger deposits were observed on specimen #979 (control system) where the delaminated front has outgrown the weakened front considerably. Table 7 compares the various delamination distances with their weakened counterparts.

For the phosphate coated specimen, the stressed front has grown only by 0.054" compared with 0.395" for the non-stressed front. The control system showed a clear stress effect that was reflected by increased delamination, while the silane modified

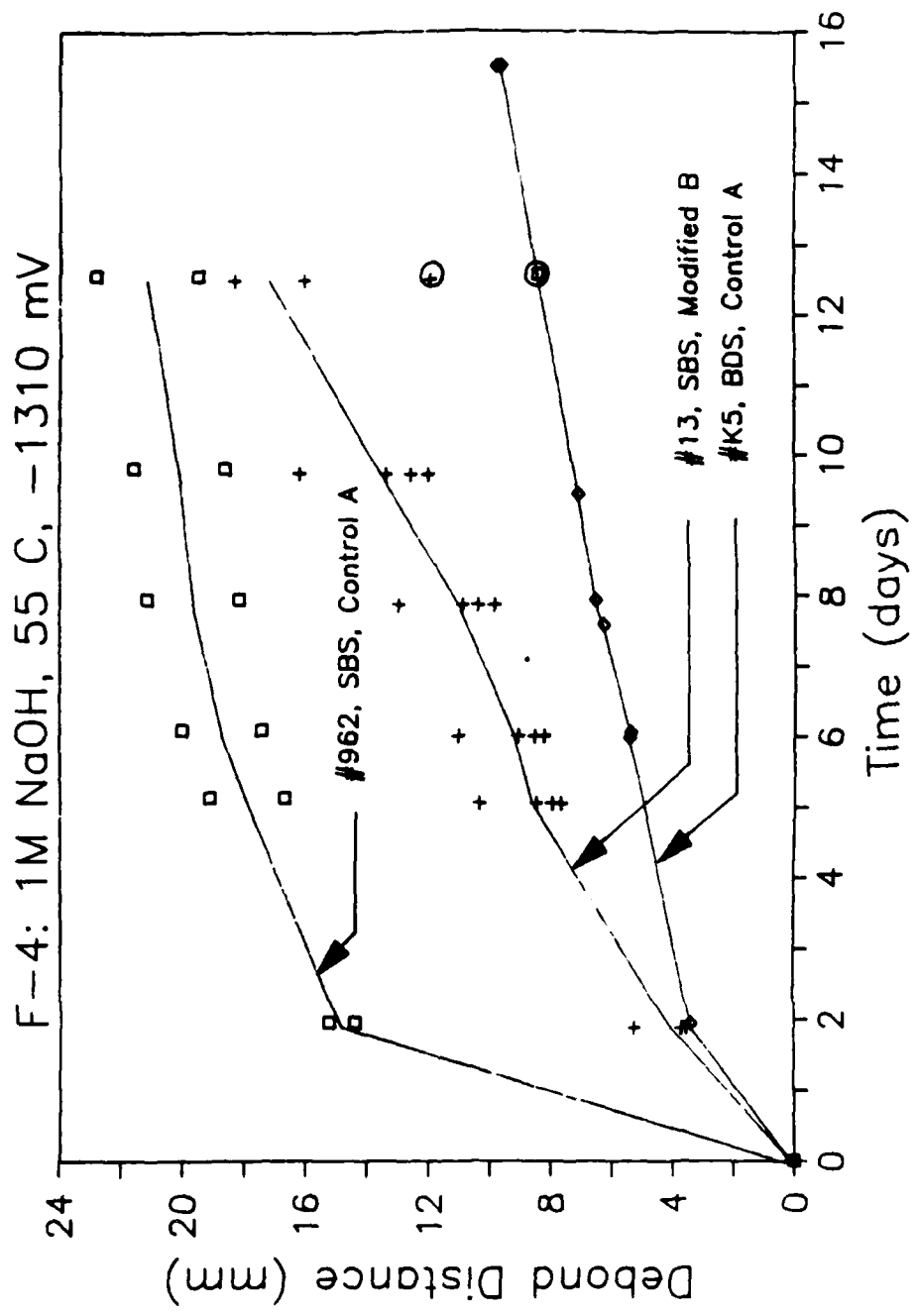


Figure 109. Delamination Data; Case F-4: 1M NaOH at 55 C and -1310 mV (SCT).



Figure 110. Photograph showing the calcareous deposits on SBS #827.

Table 7. Average Debond Growth (mm); A-4: ASW, 25 C, -1420 mV.

Specimen Number	Stressed Front (Delamination)	Stress-Free Front (Weakening)
#979	22	9.1
#45	8.7	10.
#827	1.4	10.

#979: 205/220/mild steel substrate

#45 : 205/A-1100/220 mild steel

#827: 205/220/phosphate coated mild steel

system did not show any stress effect (fronts are comparable). One can argue about a decelerating effect that calcareous deposits may have on diffusion and mass transfer of the aggressive species. Another possible explanation is a competition between the ever advancing delaminated front (due to stresses) and the crack pH. It was shown [67] that the OH^- concentration profile in a marine crack is a function of crack length with longer cracks resulting in higher tip pH. The weakened fronts retain their confinement (due to lack of external stresses) resulting in longer cracks than the stressed case. Generally speaking, higher pH levels result in higher debond rates. The fact that some systems (phosphate) seem to be severely affected by this phenomena while others (205/220 and 205/A-1100/220) do not, may lead us to conclude that the latter are less affected by a very high pH than by a simultaneous application of stresses and moderately high pH.

Another important observation concerning A-4 is the comparable weakened distances of all systems after 28 days. This is very surprising considering the wide difference in delamination performance. It is possible at such high pH levels in the constrained bond that the different bonds or adhesive types make little difference. More failure analysis will be performed on other matrix cases in order to determine whether or not the above conclusion holds.

3. THE FORTRAN PROGRAM USED IN THE ANALYTICAL MODEL

```
SJOB WATFIV,TIME=0.1,PAGES=1

IMPLICIT REAL*8 (A-H,O-Z)

INTEGER IER,INDEX,I,J,K,NIN,NOUT,NPDES,NX,IY,ICOUNT,NI,IGCR
REAL*8 H,TEND,TOL,T,WK(99999),X(100),Y(2,2,100),YY(2,2,100),
1     C1(100),C2(100),C1P(100),C2P(100),RI,RN,
2     W,ALPHA,PAR,COEF,DEL,W1,D12,D32,D42,BC2,W2,DELP,BC5,DS2,
3     YK1,L,EEXT,GUESS,D121,D321,D421,DS21,HE,ZE0,DOH,ZZ
4     GTOTAL,GCRITIC,CHECK,YNODAL,RADIUS,RADIUS4,YSQ,GUESS2
COMMON ALPHA,PAR,DEL,D12,D32,D42,BC2,DELP,BC5,DS2,
1     YK1,L,EEXT,GUESS,D121,D321,D421,DS21,HE,ZE0,DOH,IFLAG,
2     ICOUNT1,W

EXTERNAL FCN,BNDRY

PARAMETERS

CALL XUFLOW(0)

PAR = 60.D0

IFLAG = 1

IF (IFLAG.EQ.1) THEN

C ****
ASW ENVIRONMENT, SET D'S ACCORDINGLY
C ****
WRITE (*,*) ' ASW ENVIRONMENT'
C DOH = DIFFUSION COEFFICIENT OF OH IN ASW = 3.800*10-05
C DOH = 1.0D-06
ELSE
```

```

C *****
C NAOH ENVIRONMENT, SET D'S ACCORDINGLY
C *****
C ***** WRITE (*.*) 'NAOH ENVIRONMENT'
C DOH = DIFF. COEFF. OF OH IN NAOH = 1*10-08*(0.121 + 1.022*U(2))
C DOH = 1.0D-08*(0.121 + 1.022*U(2))
C ENDIF
C *****
C DIFFUSION COEFFICIENTS FOR THE ENVIRONMENTAL CRACK
C *****
C *****
C PARAMETERS FOR THE B V P
C *****
EEXT = -1.10D03
TEMP = 298.D00
CONST = 1.15D-07
D0 = 260406.7D00*CONST
D0 = EXP(12.47)*CONST
YK0 = EXP(23.2)
C1INF = 1.0D+06
D0 = EXP(20.69)*CONST
YK1 = (YK0)*EXP(-16500.D00/(TEMP))*EXP(-2.3469*EEXT/(TEMP))
DOH = (D0)*EXP(-7564.D0/(TEMP))*EXP(-1.1195*EEXT/(TEMP))
L = 1.27D0
HE = 1.0D-03
ALPHA = 1.0D00
DEL = -17.524D-03*EEXT
BC2 = 2.15D-09*L
DELP = -19.47182D-03*EEXT
BC5 = 3.280D-03*L
GUESS = 1.50D00
W = (YK1*L*L*C1INF)/(DOH)

```

```

PRINT 8,ALPHA,W,PAR,COEF,DEL,W1,D12,D32,D42,D52,W2,DELP
1     ,YK1,L,EEXT,GUESS,BC2,BC5,DOH
8 FORMAT(2X,'ALPHA = ',D10.4,2X,'W = ',D10.4,2X,'PAR = ',D10.4,2X,',
1     2X,'COEF = ',D10.4,2X,'DEL = ',D10.4,2X,'W1 = ',D10.4,2X,',
2     2X,'D12 = ',D10.4,2X,'D32 = ',D10.4,2X,'D42 = ',D10.4,2X,',
3     2X,'D52 = ',D10.4,2X,'W2 = ',D10.4,2X,'DELP = ',D10.4,2X,',
4     2X,'K1 = ',D10.4,2X,'L = ',D10.4,2X,'EEXT = ',D10.4,2X,',
5     2X,'GUESS = ',D10.4,2X,'BC2 = ',D10.4,2X,'BC5 = ',D10.4,2X,',
6     2X,'DOH = ',D10.4)

C *****
IGCR=0
ICOUNT=0
ISTOP=0
NPDES=2
NX=51
IY=2
RN=NX-1
DO 110 I=1,NX
RI=I-1
X(I)=RI/RN
YY(1,1,I)=1.D0*DEXP(-PAR*X(I))
YY(1,2,I)=-PAR*DEXP(-PAR*X(I))
YY(2,1,I)=GUESS
YY(2,2,I)=0.D0
110 CONTINUE
995 DO 10 I=1,NX
RI=I-1
X(I)=RI/RN
Y(1,1,I)=YY(1,1,I)
Y(1,2,I)=YY(1,2,I)
Y(2,1,I)=YY(2,1,I)
Y(2,2,I)=YY(2,2,I)

```

10 CONTINUE

Y(1,1,NX)=0.0D0

H=1.0D-08

TOL=1.0D-06

T=0.0D0

INDEX=1

DO 39 I=1,NX,25

WRITE (6,46) T,X(I),Y(1,1,I),Y(2,1,I)

46 FORMAT (2X,T=' ',D14.6,2X,X=' ',D14.6,2X,Y(I)=' ',D14.6,2X,

I 'Y(2)=' ,D14.6)

39 CONTINUE

GUESS2=GUESS/20.D00

DO 20 J=1,100

YNODAL=IGCR/RN

RADIUS=1.27D0+YNODAL

YSQ=Y(2,1,2)*Y(2,1,2)

GTOTAL=9.3042-9.2307*RADIUS+3.64695063*(RADIUS**2)-0.65197768*

I (RADIUS**3)+0.04348863*(RADIUS**4)

GTOTAL=13.712-10.9118*RADIUS+3.61936*(RADIUS**2)-0.561936*

I (RADIUS**3)+0.033878*(RADIUS**4)

IF (Y(2,1,2).GE.GUESS2) THEN

GCRITIC=15.0D0

ELSE

GCRITIC=0.2D01

END IF

ALP=100.0D0

GY=GUESS/2.0

IF (Y(2,1,2).GE.0.5) THEN

GCRITIC=15.0D0

ELSE

GCRITIC=0.02+5000.8*Y(2,1,2)

END IF

```

GUES2=GUESS**2
GCRITIC=(11.111/GUESS)*(Y(2,1,2)-10*GUESS)
GCRITIC=(10.526/GUESS)*(Y(2,1,2)-.05*GUESS)
GCRITIC=0.02+17.446*Y(2,1,2)-4.973*YSQ
GCRITIC=0.2+44.3*Y(2,1,2)
GCRITIC=0.2+66.533*Y(2,1,2)
GCRITIC=0.4098+8.852*YSQ
GCRITIC=0.2049+4.46*YSQ
GCRITIC=0.0000+4.66*Y(2,1,2)
GCRITIC=0.2000+66.65*Y(2,1,2)
GCRITIC=2.578+3.3*YSQ
GCRITIC=-0.144+4.236*YSQ
GCRITIC=-3.942+68.12*Y(2,1,2)-121.7*YSQ+102.38*YSQ*Y(2,1,2)-30.618
1      5*YSQ*YSQ
GCRITIC=25.59*Y(2,1,2)+0.9834*YSQ-7.5809*YSQ*Y(2,1,2)
GCRITIC=2.5D-03+(10.025D0/GUES2)*YSQ
GCRITIC=10.D0*DEXP(-0.5*Y(2,1,2))
CHECK=GCRITIC-GTOTAL
ZZ=Y(2,1,2)-ZEO
IF (ZZ.GE.0.1D-03) THEN
  IF (CHECK.GE.0.050D0) THEN
    TEND=J/10000.
    ICOUNT=ICOUNT+1
    CALL DPDES(NPDES,FCN,BNDRY,T,H,TEND,X,Y,IY,NX,TOL,INDEX,WK,
1                                IER)
113 DO 30 I=1,NX,25
*****
      WRITE (6,40) T,X(I),Y(1,1,I),Y(2,1,I),ICOUNT
40  FORMAT (2X,T=' ',D14.6,2X,'X=' ',D14.6,/2X,Y(1)=' ',D14.6,2X,
1      Y(2)=' ',D14.6,2X,ICOUNT=' ',I6)
30  CONTINUE
      WRITE(6,*)

```

```

ELSE
ISTOP=1
N1=NX-1
WRITE (*,*) ' QUIT, GAPPLIED > GCRITICAL !!!!!'
WRITE (6,41) GCRITIC,GTOTAL
41 FORMAT (2X,'GCRITIC = ',D14.6,2X,'GTOTAL = ',D14.6)
IGCR=IGCR+1
YY(1,1,1)=1.0D0
YY(1,2,1)=0.0D0
YY(2,1,1)=Y(2,1,2)
YY(2,2,1)=0.0D0
DO 991 JJ=2,NX
I=JJ+1
YY(I,1,JJ)=Y(I,1,I)
YY(I,2,JJ)=0.0D0
YY(2,1,JJ)=Y(2,1,I)
YY(2,2,JJ)=0.0D0
991 CONTINUE
YY(2,1,NX)=GUESS
WRITE(6,*) ' INITIAL CONDITIONS WERE UPDATED, NEW ROUND'
GOTO 995
END IF
20 CONTINUE
88 STOP
END
*****
SUBROUTINES
*****
SUBROUTINE FCN(NPDES,X,T,U,UX,UXX,UT)
IMPLICIT REAL*8 (A-H,O-Z)
COMMON ALPHA,PAR,DEL,D12,D32,D42,BC2,DELP,BC5,DS2,
1      YK1,L,EEXT,GUESS,D121,D321,D421,D521,HE,ZE0,DOH,IFLAG,

```

```

2   ICOUNT1,W
REAL*8  X,T,U(2),UX(2),UXX(2),UT(2),Y(2,2,100),
1   W,ALPHA,PAR,COEF,DEL,W1,D12,D32,D42,BC2,W2,DELP,BC5,DS2,
2   YK1,L,EEXT,GUESS,D121,D321,D421,DS21,HE,ZE0,DOH,ZZ
INTEGER  NPDES,IKK,IFLAG,ICOUNT1
.....
        UT(1)= UXX(1)
1       -ALPHA*W*U(1)*U(2)
        UT(2)= -W*U(2)*U(1)
RETURN
STOP
END
.....
BOUNDARY CONDITIONS
.....
SUBROUTINE BNDRY(NPDES,X,T,ALP,BET,GAMP)
IMPLICIT REAL*8 (A-H,O-Z)
COMMON ALPHA,PAR,DEL,D12,D32,D42,BC2,DELP,BC5,DS2,
1   YK1,L,EEXT,GUESS,D121,D321,D421,DS21,HE,ZE0,DOH,IFLAG,
2   ICOUNT1,W
INTEGER  NPDES,I
IF (X.GT.0.5D0) GO TO 10
        ALP(1) = 1.0D0
        BET(1) = 0.0D0
        GAMP(1) = 0.0D0
        ALP(2) = 0.0D0
        BET(2) = 1.0D0
        GAMP(2) = 0.0D0
RETURN 10    ALP(1) = 0.0D0
        BET(1) = 1.0D0
        GAMP(1) = 0.0D0
        ALP(2) = 0.0D0

```

BET(2) = 1.0D0
GAMP(2) = 0.0D0
RETURN CSENTRY
END

4. DEBONDING: A PROPOSED ANALYTICAL MODEL

4.1 Chemical And Electrochemical Reactions

In seawater, several species contribute to the hydroxyl generation at the crack tip. Oxygen, for instance, is needed for the oxygen reduction reaction at low voltages such that,



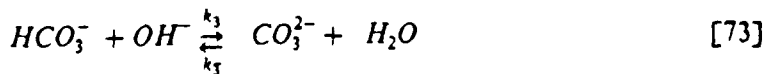
Water is needed as a medium for ions and dissolved oxygen diffusion, and, at higher voltages, is needed for its own reduction as follows



Na^+ and Cl^- ions, although not involved in any electrochemical reaction, satisfy charge neutrality through the transfer of current. While another reaction is the ionization of water itself,



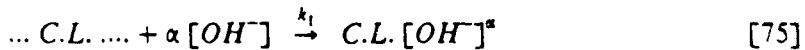
Bicarbonates play a buffering role when they react with OH^- as



Passivation of the metal surface results partly from calcium carbonate deposition due to the limited solubility of this species that results from



The chemical attack on the critical linkages (interfacial bond-creating or bulk adhesive linkages) is believed to be chemically activated, with α molecules of OH ions reacting with those linkages at the crack tip to form an activated complex thus forming an inactive site according to:



where the value of α determines the order of reaction and k_1 is the degradation rate constant. The reaction rate could be temperature dependent according to the Arrhenius relation in Equation 9.

4.2 Mathematical Modelling of the Environment

Unlike neutral particles, ions move under the action of their chemical potential gradient as well as an applied electric field. Therefore, the total flux of a given system could be written in the form of the Nernst- Planck ionic mobility equation:

$$\begin{aligned} \vec{J}_j &= \vec{i} \frac{v_j}{nF} \\ &= -D_j (\vec{\nabla}c_j \pm z_j c_j \frac{F}{RT} \vec{\nabla}\phi) \end{aligned} \quad [76]$$

Where i is the current, v_j are the stoichiometric factors (positive for the oxidized components and negative for the reduced components), n is the number of needed

electrons for the reaction, z is the charge, F is Faraday constant, and ϕ is the potential drop across the length. Notice that the migration flux component is dependent on the actual concentration of the species at the metal/environment interface and on the diffusion coefficients thus showing a clear dependence on the position in the crack.

The reason behind the lateral potential drop in a crack, for example, is that within the electrolyte outside the double layer the solution is electroneutral, while in that narrow layer of the solution, in the vicinity of the metal surface, both concentrations and the potential undergo sharp changes in a direction normal to the surface. The diffusion potential itself is responsible for the potential drop in the parallel direction, $\phi = E_{ext} - E(x)$, that results in an ion migration flux. For instance, in a simple univalent electrolyte- A^+B^- , in order to maintain electroneutrality, c_A must equal c_B . Thus the concentration gradient for both ions must be identical. B^- ions will migrate to the surface (governed by the diffusion coefficient with a flux), however, since these ions are not deposited, an electrical field forms which drives these ions from the surface at the same rate. With the same concentration gradient, A^+ ions also diffuse to the surface where they react electrochemically, however, the flux is different due to a different diffusion coefficient and, because the charge is opposite, the identical electrical field causes an additional migration to the surface. For simplicity, the influence of the ionic strength on the diffusion coefficients will not be considered.

The substances produced at the surface at the rate of $i v_i / n F$ must migrate through the diffusion layer. Therefore, the mass transfer through the diffusion layer must have the value $i v_i / n F = J_i$. This mass transport is composed of a diffusion component and a migration component which is a consequence of the electrical field. The migration component is given by

$$\frac{-|z_j| c_j \Lambda_j}{z_j F} \vec{\nabla} \phi \quad [77]$$

with the conductivity expressed as

$$\Lambda_j = \frac{|z_j| F^2}{RT} D_j. \quad [78]$$

Substituting the expression of Λ_j into Eq.77 results in the extra ionic migration component lumped into Fick's first law.

Several assumptions need to be made in order to reduce the system into a one-dimensional form and to simplify the model. Turnbull and Thomas [68] have used a similar approach to model an environmental crack under fatigue stresses in seawater. They assume that :

- a- The crack is of length L, thickness H, and width B and that the area of metal external to the crack is very much greater than the crack area such that changes in the conditions in the crack do not affect the potential of the specimen as a whole.
- b- The gravitational field is assumed to be in a direction parallel to the X-axis and directed toward the tip and hence natural convection resulting from density changes can be neglected.
- c- Mass transport in the through-thickness, Z direction, is neglected if the thickness dimension is larger than the crack length.
- d- The mass conservation equations can be reduced to a one-dimensional form by neglecting concentration and potential gradients between the walls of the crack.

The mass transport equations for the dissolved species are, then, those that relate the rate of transfer per unit area of section (flux) to the concentration and potential

gradient normal to the section. For a static crack in seawater environment, Turnbull [69] used the following flux relationships in a single coordinate cartesian system:

$$[H^-] \quad J_{1x} = - D_1 \frac{\partial c_1}{\partial x} - \frac{D_1 F}{RT} c_1 \frac{\partial \phi}{\partial x} \quad [79]$$

$$[OH^-] \quad J_{2x} = - D_2 \frac{\partial c_2}{\partial x} + \frac{D_2 F}{RT} c_2 \frac{\partial \phi}{\partial x} \quad [80]$$

$$[Na^+] \quad J_{3x} = - D_3 \frac{\partial c_3}{\partial x} - \frac{D_3 F}{RT} c_3 \frac{\partial \phi}{\partial x} \quad [81]$$

$$[Cl^-] \quad J_{4x} = - D_4 \frac{\partial c_4}{\partial x} + \frac{D_4 F}{RT} c_4 \frac{\partial \phi}{\partial x} \quad [82]$$

$$[O_2] \quad J_{5x} = - D_5 \frac{\partial c_5}{\partial x} \quad [83]$$

$$[HCO_3^-] \quad J_{6x} = - D_6 \frac{\partial c_6}{\partial x} + \frac{D_6 F}{RT} c_6 \frac{\partial \phi}{\partial x} \quad [84]$$

$$[CO_3^{2-}] \quad J_{7x} = - D_7 \frac{\partial c_7}{\partial x} + \frac{2D_7 F}{RT} c_7 \frac{\partial \phi}{\partial x} \quad [85]$$

$$[Ca^{2+}] \quad J_{8x} = - D_8 \frac{\partial c_8}{\partial x} - \frac{2D_8 F}{RT} c_8 \frac{\partial \phi}{\partial x} \quad [86]$$

The mass conservation equations of the electrolyte system constituents in a parallel-sided environmental crack could be written as follows:

$$\frac{\partial \bar{c}_i}{\partial t} = - \frac{\partial J_{ix}}{\partial x} - \frac{K \bar{c}_i}{H} \quad [87]$$

where,

$$K = \frac{i_1}{F} . \quad [88]$$

From chapter 6, the cathodic current density could be expressed as follows :

$$i_1 = - k c_i \exp - \left(\frac{BFE}{RT} \right) \quad [89]$$

It is to be noted that all the environmental concentrations in this treatment are average concentrations across the thickness, \bar{c} , where the "bar" was dropped for convenience. Equation 87 is based on concentration averaging between the walls of the crack or the polymer media, and it was obtained by integrating the two-dimensional governing equations in the transverse, y , direction as shown in Appendix 5 (after Turnbull). The fact that only one side of the crack is metal and the other is adhesive requires a special treatment at the boundaries. One side is electrochemically active (for generation or consumption of reactions) as opposed to two sides for the case of a homogeneous crack in the metal as used in the research by Turnbull. The same averaging technique with the parallel crack could be followed for those wedge-shaped cracks with small angle, θ . Additional terms associated with the slope of the wall are due to the fact that the normal direction to the crack's axis makes an angle with the normal to the wall. The resulting equations are of the form [69]:

$$\frac{\partial c_i}{\partial t} = - \frac{\partial J_{ix}}{\partial x} - \frac{K}{H} + \frac{\theta}{H} D \frac{\partial c_i}{\partial x} + \frac{\theta}{H} D \frac{\partial \phi}{\partial x} \quad [90]$$

Expanding and taking into account the chemical and electrochemical contributions mentioned above, the mass conservation equations for a single-dimension-parallel-sided crack or a polymeric media under similar conditions may be expressed as :

$$\frac{\partial c_1}{\partial t} = - \frac{\partial J_1}{\partial x} + (k_2 - k_{\bar{2}}) c_1 c_2 \quad [91]$$

$$\frac{\partial c_2}{\partial t} = - \frac{\partial J_2}{\partial x} + (k_2 - k_{\bar{2}}) c_1 c_2 + k_{\bar{3}} c_7 - k_3 c_2 c_6 + \frac{k^1 c_5}{HF} \exp \left[- \frac{B^1 F(E_{ext} - \phi)}{RT} \right]$$

$$+ \frac{k(c_1)}{HF} \exp \left[- \frac{B(c_1) F(E_{ext} - \phi)}{RT} \right] - \sum_{i=1} \alpha_i k_i c_i c_2 \quad [92]$$

$$\frac{\partial c_3}{\partial t} = - \frac{\partial J_3}{\partial x} \quad [93]$$

$$\frac{\partial c_4}{\partial t} = - \frac{\partial J_4}{\partial x} \quad [94]$$

$$\frac{\partial c_5}{\partial t} = - \frac{\partial J_5}{\partial x} - \frac{k^1 c_5}{HF} \exp \left[- \frac{B^1 F(E_{ext} - \phi)}{RT} \right] \quad [95]$$

$$\frac{\partial c_6}{\partial t} = - \frac{\partial J_6}{\partial x} + k_{\bar{3}} c_7 - k_3 c_2 c_6 \quad [96]$$

$$\frac{\partial c_7}{\partial t} = - \frac{\partial J_7}{\partial x} - k_{\bar{3}} c_7 + k_3 c_2 c_6 - \frac{1}{H} k^{\varphi} [(c_7 c_8)^{1/2} - (k_{so}^{\varphi})^{1/2}]^2 \quad [97]$$

$$\frac{\partial c_8}{\partial t} = - \frac{\partial J_8}{\partial x} - \frac{1}{H} k^{\varphi} [(c_7 c_8)^{1/2} - (k_{so}^{\varphi})^{1/2}] \quad [98]$$

where the subscripts 1 through 8 refer to H^+ , OH^- , Na^+ , Cl^- , O_2 , HCO_3^- , CO_3^{2-} , and Ca^{2+} respectively.

The last term in Equation 92 represents the reduction of concentration of the aggressive species OH^- due to such reactions as the interaction with the polymers' functional groups, hydration of the metal oxide, or direct attack (and subsequent

neutralization) on the attachment sites at the polymer/metal interface. Therefore, c_i is the concentration of functional groups in the polymer and at the interface which are capable of taking part in a complex-formation or substitution reaction; k_i is the rate of the complex formation or substitution reaction of the OH^- with the above groups. The above posed problem imposes a large burden of evaluating a large number of parameters for the various groups. Simplifying the problem could be achieved by reducing the total number of these groups with which the hydroxyl reacts to one critical linkage upon which the bond relies for strength (AS). This will reduce equation 86 into a simpler form

$$\frac{\partial c_2}{\partial t} = - \frac{\partial J_2}{\partial x} + (k_2 - k_{\bar{2}}) c_1 c_2 + k_{\bar{3}} c_7 - k_3 c_2 c_6 + \frac{k^1 c_5}{HF} \exp \left[- \frac{B^1 F(E_{ext} - \phi)}{RT} \right] \\ + \frac{k(c_1)}{HF} \exp \left[- \frac{B(c_1)F(E_{ext} - \phi)}{RT} \right] - \alpha k_1 C.L. c_2 \quad [99]$$

Nancollas, et al [70] suggested the kinetics of carbonate scale growth to be of the form used in Equation 98 as follows

$$\frac{\partial Ca^{2+}}{\partial t} = - k^\varphi \left[([Ca^{2+}][CO_3^{2-}])^{1/2} - (k_{so}^\varphi)^{1/2} \right]^2 \quad [100]$$

4.3 Initial and Boundary Conditions

Equations 91, 93-99, and 55 constitute a system of 9 coupled non-linear p.d.e's that constitute the boundary value problem which needs to be solved numerically subject to several initial and boundary conditions. For instance, electric neutrality suggests that

$$\sum_{i=1} z_i c_i = 0 \quad [101]$$

or,

$$c_1 - c_2 + c_3 - c_4 - c_5 - 2c_7 + 2c_8 = 0. \quad [102]$$

at $t = 0$,

$$c_1 = c_1(x,0) = 0, c_2 = c_2(x,0) = 0, c_3 = c_3(x,0) = 0,$$

$$c_4 = c_4(x,0) = 0, c_5 = c_5(x,0) = 0, c_6 = c_6(x,0) = 0,$$

$$c_7 = c_7(x,0) = 0, c_8 = c_8(x,0) = 0, C.L. = C.L.(x,0) = C.L_0, \phi = \phi(x,0). \quad [103]$$

at $t > 0$,

$x = 0$, at the crack mouth,

$$c_1 = c_1^\infty, c_2 = c_2^\infty, c_3 = c_3^\infty, c_4 = c_4^\infty, c_5 = c_5^\infty, c_6 = c_6^\infty,$$

$$c_7 = c_7^\infty, c_8 = c_8^\infty, \frac{\partial C.L.}{\partial x} = 0, \phi = 0. \quad [104]$$

$x = l$, at the crack tip,

$$J_1 = 0 \quad [105]$$

$$J_2 = \frac{k(c_1)}{F} \exp \left[- \frac{B(c_1)F(E_{ext} - \phi)}{RT} \right] + \frac{k^1 c_5}{F} \exp \left[- \frac{B^1 F(E_{ext} - \phi)}{RT} \right] \quad [106]$$

$$J_3 = 0 \quad [107]$$

$$J_4 = 0 \quad [108]$$

$$J_5 = -\frac{k^1 c_s}{F} \exp \left[-\frac{B^1 F(E_{ext} - \phi)}{RT} \right] \quad [109]$$

$$J_6 = 0 \quad [110]$$

$$J_7 = 0 \quad [111]$$

$$J_8 = 0 \quad [112]$$

$$\frac{\partial C.L.}{\partial x} = 0, \quad [113]$$

4.4 Assumptions and Simplifications

Several simplifying assumptions could be used to simplify the numerical model. The geometric configuration of the crack could be either parallel or wedge-shaped with the former assumed here. The voltage drop in the lateral direction is responsible for the migration component of the total flux. The significance of which is the attraction or repulsion from the crack of oppositely-charged and similarly charged ions respectively. The inclusion of the potential drop, ϕ , will add an nth variable to the system of n-1 equations thus complicating the problem considerably. Therefore, ϕ will be discarded in the treatment of the following simplified version. The error resulting from this assumption could be significant because the similar charge carried by the metal surface and the hydroxide will result in repulsion. The ion migration component of the flux may decrease the total flux considerably. That will act as a buffer resulting in lower pH at

the crack tip. The electrochemical process by which carbonate products get deposited on the surface is also excluded for the same reasons.

Taking into consideration the above assumptions yields a simpler form of the system of equations as follows:

$$\frac{\partial c_1}{\partial t} = \frac{\partial}{\partial x} (D_1 \frac{\partial c_1}{\partial x}) + (k_2 - k_{\bar{z}}) c_1 c_2 \quad [114]$$

$$\begin{aligned} \frac{\partial c_2}{\partial t} = & \frac{\partial}{\partial x} (D_2 \frac{\partial c_2}{\partial x}) + (k_2 - k_{\bar{z}}) c_1 c_2 + k_{\bar{z}} c_7 - k_3 c_2 c_6 + \frac{k^1 c_5}{HF} \exp \left[- \frac{B^1 F(E_{ext})}{RT} \right] \\ & + \frac{k(c_1)}{HF} \exp \left[- \frac{B(c_1) F(E_{ext})}{RT} \right] - \alpha k_1 C.L. c_2 \end{aligned} \quad [115]$$

$$\frac{\partial c_3}{\partial t} = \frac{\partial}{\partial x} (D_3 \frac{\partial c_3}{\partial x}) \quad [116]$$

$$\frac{\partial c_4}{\partial t} = \frac{\partial}{\partial x} (D_4 \frac{\partial c_4}{\partial x}) \quad [117]$$

$$\frac{\partial c_5}{\partial t} = \frac{\partial}{\partial x} (D_5 \frac{\partial c_5}{\partial x}) - \frac{k^1 c_5}{HF} \exp \left[- \frac{B^1 F(E_{ext})}{RT} \right] \quad [118]$$

$$\frac{\partial C.L.}{\partial t} = - k_1 (C.L._0 - C.L.) c_2 \quad [119]$$

The number of p.d.e.s in the above reduced system was reduced to a total of six. The associated boundary conditions are as follows: at $t=0$,

$$c_1 = c_1(x,0) = 0, c_2 = c_2(x,0) = 0, c_3 = c_3(x,0) = 0,$$

$$c_4 = c_4(x,0) = 0, c_5 = c_5(x,0) = 0, C.L. = C.L.(x,0) = C.L._0, \quad [120]$$

at $t > 0$,

$x = 0$, at the crack mouth,

$$c_1 = c_1^\infty, c_2 = c_2^\infty, c_3 = c_3^\infty, c_4 = c_4^\infty, c_5 = c_5^\infty, \frac{\partial C.L.}{\partial x} = 0, \quad [121]$$

$x = l$, at the crack tip,

$$J_1 = 0 \quad [122]$$

$$J_2 = \frac{k(c_1)}{F} \exp \left[- \frac{B(c_1)F(E_{ext})}{RT} \right] + \frac{k^1 c_5}{F} \exp \left[- \frac{B^1 F(E_{ext})}{RT} \right] \quad [123]$$

$$J_3 = 0 \quad [124]$$

$$J_4 = 0 \quad [125]$$

$$J_5 = - \frac{k^1 c_5}{F} \exp \left[- \frac{B^1 F(E_{ext})}{RT} \right] \quad [126]$$

$$\frac{\partial C.L.}{\partial x} = 0, \quad [127]$$

4.5 Characterization of parameters

The simplified model, equations 114-119 subject to 120-127, contains many parameters that vary: geometry of the crack and electrochemical coefficients to chemical reaction rates and diffusion coefficients. These parameters are identified here as:

$L, C_2^\infty, k_2, k_{\bar{2}}, k^1, k(c_1), B(c_1), E_{ext}, B^1, D_1, D_2, D_3, D_4, D_5$

k_1 , H , $C.L_0$, α .

Where the first group of parameters is either known, prescribed, or could be found in the literature. To obtain the second group, the question remains whether our interest lies in the degradation of the bulk adhesive (in which case α , k_1 , and the initial density of unstable bonds could be determined as discussed below) or of the interfacial bonds.

Corrosion literature contains some of the parameters which are needed to determine the rates of the mass transport processes. Diffusion coefficients that determine the transport rates in ASW are readily available and could be used in this model. However, these values are valid only in a delaminated bond where the metal ahead of the crack mouth becomes directly exposed to the electrolyte. Weakening of the bond, on the other hand, implies that the adhesive has not separated from the substrate, and that the mass transport may take place in the degraded polymeric media adjacent to the interface or through the weakened interface itself. Diffusion coefficients of the hydroxyl, for example, in the polymer could be determined from the re-sorption curves of the free film primer.

Environmental attack rates on the unstable linkages in the adhesive itself could be evaluated using a pool of available techniques. Some of these are: stress-chemical relaxation, pH measurements on both sides of a primer thin film of known thickness in electrolyte solution, and possibly the mass uptake studies on primer films. The latter may be the most practical where several adhesive films of different thicknesses are exposed to the same harsh environment. Thin films provide data about an almost pure chemical reaction control case. The slopes of the mass uptake are looked upon as equivalent to what is known as "conversion factor X" which indicates the degree of reaction. Several thicknesses need to be used in order to eliminate the role of diffusion as the distances get smaller and smaller.

However, the rates of chemical degradation reaction processes and the initial concentration of the attachment sites at the interface are hard to determine experimentally. Nonetheless, numerical schemes could be implemented to solve this problem using non-dimensional parameters similar to those mentioned above. We are proposing that appropriate values of the unknown parameters should be fed into the non-dimensional quantities thus creating a semi-empirical, yet reasonable, approach that will verify the trends associated with the real-life situation. Example problems could be solved numerically to correlate with real time data of debonding that is already known from experiments. Validation of the model should be done in a fashion that captures the major features of debonding, i.e. stress, temperature, and environment concentration effects. One should expect, for example, that the debond behaves linearly when plotted against the square root of time when applied stress is absent.

4.6 A Posed Sample Problem

Let us consider the deterioration of the adhesively bonded joint in an ASW environment with applied cathodic voltage. Diffusion of the moisture and the ions in the weakened region (environmental crack) is assumed to be uniform, and that mass transfer in the crack or the degraded adhesive proceeds at a constant rate. Upon normalizing the variables and the parameters with respect to those of species' 2 as follows:

$$t^{non} = \frac{D_2}{L^2} t, \quad c_i^{non} = \frac{c_i}{c_2^\infty}, \quad x_i^{non} = \frac{x_i}{L} \quad (i = 1, 2, \dots, n) . \quad [128]$$

where the superscript 'non' has been dropped in the following treatment for convenience, the boundary value problem reduces to:

$$\frac{\partial c_1}{\partial t} = D_{12} \frac{\partial^2 c_1}{\partial x^2} - W1 c_1 c_2 \quad [129]$$

$$\frac{\partial c_2}{\partial t} = \frac{\partial^2 c_2}{\partial x^2} - \alpha WC.L.c_2 + COEF \exp(DELPP) + W2 c_5 \exp(DELPP) - W1 c_1 c_2 \quad [130]$$

$$\frac{\partial c_3}{\partial t} = D_{32} \frac{\partial^2 c_3}{\partial x^2} \quad [131]$$

$$\frac{\partial c_4}{\partial t} = D_{42} \frac{\partial^2 c_4}{\partial x^2} \quad [132]$$

$$\frac{\partial c_5}{\partial t} = D_{52} \frac{\partial^2 c_5}{\partial x^2} - W2 c_5 \exp(DELPP) \quad [133]$$

$$\frac{\partial C.L.}{\partial t} = - W (C.L._0 - C.L.) c_2 \quad [134]$$

The non-dimensional parameters used in the above treatment capture the characteristic properties of the physical problem. The rates of the diffusion and the deterioration problems, the geometric properties, and the electrochemical generation and depletion kinetics have all been absorbed into the following parameters:

$$W = k_1 \frac{L^2}{D_2} c_2^\infty .$$

$$W1 = (k_2 - k_2) \frac{L^2}{D_2} c_2^\infty .$$

$$W2 = \frac{k^1}{F H} \frac{L^2}{D_2}$$

$$COEF = \frac{k(c_1)}{HF} \frac{L^2}{D_2 c_2^\infty}$$

$$DELP = -\frac{B(c_1) F(E_{ext})}{R T}$$

$$DELPP = -\frac{B^1 F(E_{ext})}{R T}$$

$$D12 = \frac{D_1}{D_2}, D32 = \frac{D_2}{D_2}, D42 = \frac{D_4}{D_2}, D52 = \frac{D_5}{D_2}, \quad [136]$$

In the above treatment, H is the height of the crack, L is the crack length, and D_2 is the diffusion coefficient of the hydroxyl in the polymer or the environmental crack. The initial and boundary conditions for this reduced problem are derived from the more generalized system and are shown below:

at $t = 0$,

$$c_1 = c_1(x, 0) = 0, c_2 = c_2(x, 0) = 0, c_3 = c_3(x, 0) = 0,$$

$$c_4 = c_4(x, 0) = 0, c_5 = c_5(x, 0) = 0, C.L. = C.L.(x, 0) = C.L._0, \quad [137]$$

at $t > 0$,

$x = 0$, at the crack mouth,

$$c_1 = \frac{c_1^\infty}{c_2^\infty}, c_2 = \frac{c_2^\infty}{c_2^\infty}, c_3 = \frac{c_3^\infty}{c_2^\infty}, c_4 = \frac{c_4^\infty}{c_2^\infty}, c_5 = \frac{c_5^\infty}{c_2^\infty}, C.L. = \frac{C.L._0}{c_2^\infty}, \quad [138]$$

$x = 1$, at the crack tip,

$$\frac{\partial c_1}{\partial x} = 0. \quad [139]$$

$$\frac{\partial c_2}{\partial x} = BC2 \exp(DEL_P) + BC5 c_5 \exp(DEL_{PP}) \quad [140]$$

$$\frac{\partial c_3}{\partial x} = 0 \quad [141]$$

$$\frac{\partial c_4}{\partial x} = 0 \quad [142]$$

$$\frac{\partial c_5}{\partial x} = BC5 c_5 \exp(DEL_{PP}) \quad [143]$$

$$\frac{\partial C.L.}{\partial x} = 0. \quad [144]$$

Where

$$BC5 = \frac{k^1 L}{F D_5}, \quad BC2 = \frac{k(c_1) L}{F D_2 c_2^\infty}. \quad [145]$$

Solving a similar version of the electrochemical system in a crack in seawater, Turnbull was able to model the pH profile as a function of crack length. Figure 111 shows that the predicted values of pH reach high values, 12 in that case, regardless of the bulk pH of the electrolyte solution.

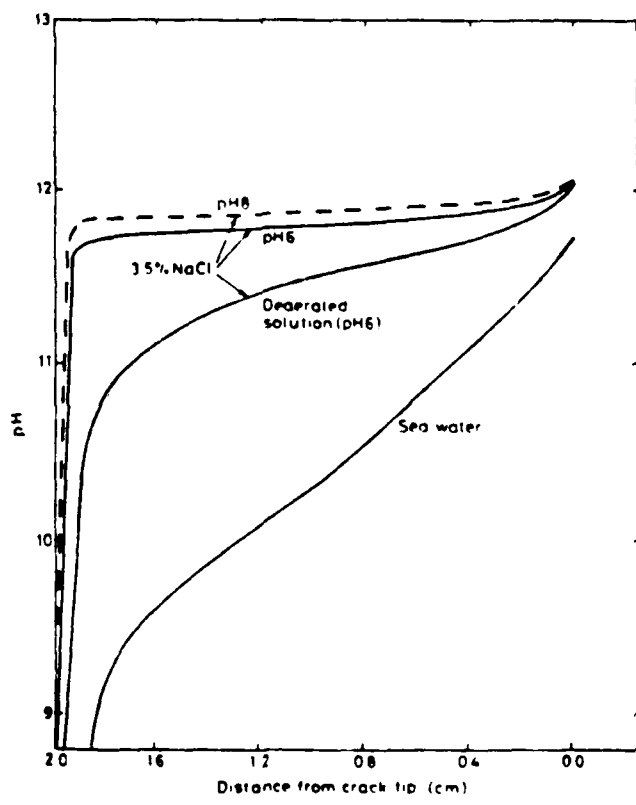


Figure III. pH profiles as a function of crack length.

5. MATHEMATICAL TREATMENT OF CONCENTRATIONS

The average concentrations for the environmental species are used in this study in order to reduce the problem to a single-dimension system. Neglecting the side diffusion in the z-direction, Equation 45 is expressed using cartesian coordinates, in the lateral, x, and transverse, y, directions as follows:

$$\frac{\partial c}{\partial t} = - \frac{\partial J_x}{\partial x} - \frac{\partial J_y}{\partial y}. \quad [146]$$

Integrating over the thickness for a crack of height H,

$$\int_{-H/2}^{+H/2} \frac{\partial c}{\partial t} dy = - \int_{-H/2}^{+H/2} \frac{\partial J_x}{\partial x} dy - \int_{-H/2}^{+H/2} \frac{\partial J_y}{\partial y} dy \quad [147]$$

and substituting the expression for the flux in the previous equation yields

$$\int_{-H/2}^{+H/2} \frac{\partial c}{\partial t} dy = \int_{-H/2}^{+H/2} \frac{\partial}{\partial x} (D \frac{\partial c}{\partial x}) dy + \int_{-H/2}^{+H/2} \frac{\partial}{\partial y} (D \frac{\partial c}{\partial y}) dy \quad [148]$$

Upon evaluating the second integral on the right hand side of the previous equation, it becomes

$$\int_{-H/2}^{+H/2} \frac{\partial c}{\partial t} dy = \int_{-H/2}^{+H/2} \frac{\partial}{\partial x} (D \frac{\partial c}{\partial x}) dy + D \frac{\partial c}{\partial x} \Big|_{-H/2} - D \frac{\partial c}{\partial x} \Big|_{H/2} \quad [149]$$

But the flux on the adhesive side ($y = +H/2$) is assumed to be identically zero due to the absence of electrochemical reaction, which implies that:

$$- D \frac{\partial c}{\partial x} \Big|_{H/2} = 0 \quad [150]$$

Now, using the averaging concept for the concentrations,

$$\bar{c}(x,t) = \frac{1}{H} \int_{-H/2}^{+H/2} c(x,y,t) dy \quad [151]$$

that results in

$$\frac{\partial}{\partial x} \left(\frac{\partial \bar{c}(x,t)}{\partial x} \right) = \frac{1}{H} \int_{-H/2}^{+H/2} \frac{\partial}{\partial x} \left(D \frac{\partial c(x,y,t)}{\partial x} \right) dy. \quad [152]$$

Therefore,

$$\int_{-H/2}^{+H/2} \frac{\partial c}{\partial t} dy = H \frac{\partial}{\partial x} \left(D \frac{\partial \bar{c}}{\partial x} \right) + D \frac{\partial c}{\partial y} \Big|_{-H/2}. \quad [153]$$

Dividing by H on both sides of the equation,

$$\frac{1}{H} \int_{-H/2}^{+H/2} \frac{\partial c}{\partial t} dy = \frac{\partial}{\partial x} \left(D \frac{\partial \bar{c}}{\partial x} \right) + \frac{D}{H} \frac{\partial c}{\partial y} \Big|_{-H/2} \quad [154]$$

Note that the term on the left hand side is the derivative of the right hand side of Equation 151, the previous equation becomes:

$$\frac{\partial \bar{c}(x,t)}{\partial t} = \frac{\partial}{\partial x} \left(D \frac{\partial \bar{c}(x,t)}{\partial x} \right) + \left. \frac{D}{H} \frac{\partial c}{\partial y} \right|_{-H/2} \quad [155]$$

The flux at the wall is given previously as:

$$D \frac{\partial c}{\partial y} = - \frac{i_1 c(y=a)}{F} \quad [156]$$

resulting in the expression given above in Equation 87 where the bar has been dropped for convenience:

$$\frac{\partial \bar{c}(x,t)}{\partial t} = \frac{\partial}{\partial x} \left(D \frac{\partial \bar{c}(x,t)}{\partial x} \right) - \frac{i_1 \bar{c}}{FH} \quad [157]$$

where $c(y=a)$ was assumed to be equal to \bar{c} .

BIBLIOGRAPHIC DATA SHEET	1. Report No.	2.	3. Recipient's Accession No.
4. Title and Subtitle An Interdisciplinary Study of Cathodic Debonding in Elastomer/Metal Adhesive Bonds		5. Report Date 10/17/88	6.
7. Author(s) Hamadeh, Ramzi F., Dillard, D. A.		8. Performing Organization Rept. No. VPI-F-88-30 CASS/ESM-88-10	
9. Performing Organization Name and Address Virginia Polytechnic Institute and State University Center for Adhesive & Sealant Science Department of Engineering Science and Mechanics Blacksburg, VA 24061		10. Project/Task/Work Unit No. N00014-85-K0185	
12. Sponsoring Organization Name and Address Office of Naval Research 800 N. Quincy Street Arlington, VA 22217		13. Type of Report & Period Covered 1/85 - 10/88	
15. Supplementary Notes		14.	
16. Abstract An interdisciplinary study concerning the durability of adhesively elastomer/metal bonded joints in marine environments is reported. The generation of OH-ions at the bondline due to an imposed cathodic current from an external source is suspected to be the predominant cause of failure. A surface analysis study was performed early in this research for the purpose of identifying the cause(s) of failure. Characterization of the rubber and the metal failure surfaces with XPS (X-ray Photoelectron Spectroscopy) showed similar composition on both sides and to that of the bulk degraded primer component of the adhesive. Saponification of the adhesive and the leaching of chlorine (forming HCl that attacks the oxide) are identified as two possible failure mechanisms. The locus of failure is believed to be very close to the adhesive/oxide interface. The exposure of bulk adhesive free-standing films to different environments showed that the hydroxyl is detrimental in continued			
17. Key Words and Document Analysis. 17a. Descriptors			
17b. Identifiers/Open-Ended Terms			
17c. COSATI Field/Group			
18. Availability Statement Unlimited		19. Security Class (This Report) UNCLASSIFIED	21. No. of Pages 283
		20. Security Class (This Page) UNCLASSIFIED	22. Price

16. Abstracts continued

the environmental durability of these specimens judging by the percentage of net mass uptake. An alternate interfacial failure mechanism is also presented where the neutralization of the adhesion-promoting attachment sites (A.S.) at the interface leads to de-adhesion and whereby OH-ions chemically break-up the -COOH-Fe bond forming a non-operative activated complex at the degraded crack tip.

Debond, or loss of adhesion, can exist in two modes. Weakening denotes debond growth which takes place undetected to the naked eye, and is governed by a diffusion-control degradation process that gives a straight line when plotted against the square root of time. Delamination, on the other hand, is a "post weakening" process. Debond rates in this mode are influenced by the applied total strain energy release rate, G_T , and by the environment and can be described by an exponential function in G_T . The effect of shear stress on debond acceleration was determined to be minimal. While compressive stresses seem to be beneficial in slowing the ingress of the bulk hydroxyl into the bondline, no noticeable improvement was detected when an imposed current was used. The use of zinc phosphate-coated steel substrates is shown to improve bond durability significantly at low voltages. Similar trends are observed when silane (γ -aminopropyltrimethoxy) modified primer were used in bonding.

Two approaches are used in order to model debonding: empirical and analytical. Statistical Analysis System (SAS) is used to fit the empirical model which draws heavily on the functional dependencies of debond rates on the accelerating parameters, i.e., temperature, stress, and applied voltage. An Arrhenius relationship is shown to model the effect of temperature very well. Also, voltage effect is correlated with the corresponding current densities which, in turn, were found to obey an exponential relationship with debonded rates. SAS fits of the experimental data are shown to model the process accurately and could be utilized for life predictions. Integration of delamination rates in real time is a feasible method to predict durability as well.

A generalized analytical model for debonding is also developed, and it draws on the similarities between this application and corrosion fatigue of metals. The model is based on the conservation of mass of the involved species and is composed of a system of partial equations and their associated boundary conditions. Furthermore, temperature and voltage-dependent diffusion coefficients and reaction rate constants were used. The resulting boundary value problem amounts to a diffusion-chemical reaction mechanism into which a mechano-chemical failure mechanism is incorporated. A simplified version of the full scale analytical model is solved numerically and some interesting conclusions concerning the failure criterion are drawn. The model also simulates the weakening and delamination behavior and allows for temperature and voltage treatment as well. Delay times are also predicted as a function of the applied voltage and temperature. A particularly important conclusion is that the "marching boundary" phenomena seems to account for most of the accelerating influence of applied G .